JEMS

JOURNAL OF ETA MARITIME SCIENCE

Volume: 12 Issue: 3

September 2024

E-ISSN: 2148-9386

www.jemsjournal.org

JEMS
JOURNAL OF ETA MARITIME SCIENCE
2024 / Volume ▪ 12 - Issue ▪ 3

Editorial Board

JEMS
JOURNAL OF ETA MARITIME SCIENCE
2024 / Volume • 12 - Issue • 3

Editorial Board

Journal Info

Please refer to the journal's webpage (www.jemsjournal.org) for " About Us", "Aim and Scope", "Guide for Authors" and "Ethical Policy".

JEMS is currently indexed in Web of Science Emerging Sources Citation Index (ESCI), Tubitak Ulakbim Science Database, Transport Research International Documentation (TRID), Directory of Open Access Journals (DOAJ), EBSCO, J-Gate, Scopus and CNKI.

Owner UCTEA The Chamber of Marine Engineers

Address: Sahrayıcedit Mah. Halk Sk. Golden Plaza No: 29 C Blok K:3 D:6 Kadıköy/İstanbul - Türkiye
Web: gemimo.org **E-mail:** bilgi@gemimo.org **Phone:** +90 216 747 15 51
Fax: +90 216 747 34 35

Publisher Galenos Publishing House
Address: Molla Gürani Mah. Kaçamak Sk. No: 21/1 34093 İstanbul, Türkiye
Phone: +90 (530) 177 30 97 **E-mail:** info@galenos.com.tr **Web:** www.galenos.com.tr

E-ISSN: 2148-9386

Online Publication Date:
September 2024

Journal website:
www.jemsjournal.org

Submit Article:
jag.journalagent.com/jems

Cover Photo:

2024/ Volume 12 / Issue 3
BASBÖYÜK Ö. (2020) Mersin International Port, Türkiye

JEMS
JOURNAL OF ETA MARITIME SCIENCE
2024 / Volume ▪ 12 - Issue ▪ 3

Contents

DOI: 10.4274/jems.2024.84704

Journal of ETA Maritime Science 2024;12(3):237

Selçuk Nas

Dokuz Eylül University Maritime Faculty, Department of Maritime Education and Training, İzmir, Türkiye

Dear Readers,

I am delighted to introduce JEMS 12 (3) to our valued readers. We are following with great pleasure the increase in the internationality of our publications in each issue. We also see a tendency towards marine engineering topics in the publications. Despite the intensive article submissions, we try to be selective and limit ourselves to 10 article publications in each issue. There are some worthwhile and intriguing studies in this issue. There is little question that these investigations will be beneficial to the maritime area.

I express my gratitude to the authors, who diligently followed our publication guidelines to generate publications of the highest caliber; the editorial board; the section editors; and the reviewers whose perceptive studies were accepted for publication in this issue.

Prof. Dr. Selçuk NAS
Editor in Chief

Address for Correspondence: Selçuk Nas, Dokuz Eylül University Maritime Faculty, Department of Maritime Education and Training, İzmir, Türkiye
E-mail: snas@deu.edu.tr
ORCID iD: orcid.org/0000-0001-5053-4594

Received: 23.09.2024
Accepted: 23.09.2024

ORIGINAL RESEARCH (AR) DOI: 10.4274/jems.2024.79836

Journal of ETA Maritime Science 2024;12(3):238-252

Quasi-2DH Modeling of the Shoreline Evolution Around an Offshore Breakwater

Cüneyt Baykal, Can Özsoy

Middle East Technical University Faculty of Engineering, Department of Civil Engineering, Ankara, Türkiye

Abstract

In the present study, a quasi-two-dimensional (2D) numerical model developed to model shoreline evolution under wave action near various coastal defense implementations is applied to laboratory experiments on shoreline evolution around an offshore breakwater. The model uses a spectral wave model based on the energy balance equation with wave breaking and diffraction terms. A method is proposed to distribute bulk longshore sediment transport rates over the surf zone for 2D applications. The proposed method agrees with the one-dimensional methods and 2D laboratory measurements. The model also comprises cross-shore and swash zone transport modules for maintaining the equilibrium profile, which is tested using a theoretical case governed solely by cross-shore transport. The test shows that the cross-shore transport module can restore any user-defined equilibrium beach profile. For the laboratory experiments, the model results for the nearshore wave heights and bottom contours agree well with the experimental results, especially for the initial cases of laboratory experiments. As the salient progresses through the offshore breakwater and a tombolo forms, the wave approach and local orientation angles increase, and the computed bottom contours begin to differ from the measured contours.

Keywords: Sediment transport, Shoreline change model, Quasi-2DH, Offshore breakwater

1. Introduction

The ever-increasing development and human interventions in coastal areas have led to significant shoreline changes. Hence, it is imperative to determine shoreline evolution in a specific condition or state to comprehend the associated processes and address them effectively. With recent advancements in computing technology, numerical modeling has become more convenient than ever before. Numerical modeling of shoreline evolution began with the pioneering work of Pelnard-Considere [1]. He defined a mathematical model for predicting the shoreline's position near a groin. This model assumes that nearshore seasonal variations, such as bar formation and storm-induced accretion/erosion, are negligible in the long-term (yearly, decadal) progress of the shoreline. Additionally, equilibrium beach profile represents the entire shoreline, and longshore sediment transport (LST) is the governing process. Price et al. [2] first numerically implemented the one-line theory, followed by many others [3-10].

Wave transformation computations mainly depend on parametric and geometrical relationships in one-line models. Thus, when coastal structures with complicated geometries and conditions are present in the nearshore region, such wave transformation computations become excessively convoluted in one-line models. Nonetheless, two- and three-dimensional numerical models can solve many equations with numerous input parameters, but they suffer from a significant increase in computational complexity. These models may not provide quick/interim solutions for designing and testing the effectiveness of coastal defense measures in time-sensitive studies such as coast restoration projects. However, one-line models may also not be sufficient for modeling highly complex coastal structures, sediment transport in curved shorelines, the effect of topographical conditions, and cross-shore transport, and for predicting tombolo formation, accretion, and erosion around structures such as Y-heads, T-head groins, or combinations of structures. Researchers have applied several methods and models to improve the

Address for Correspondence: Cüneyt Baykal, Middle East Technical University Faculty of Engineering, Department of Civil Engineering, Ankara, Türkiye
E-mail: cbaykal@metu.edu.tr
ORCID iD: orcid.org/0000-0002-8514-2758

Received: 25.12.2023
Last Revision Received: 20.03.2024
Accepted: 12.05.2024

To cite this article: C. Baykal, and C. Özsoy. "Quasi-2DH Modeling of the Shoreline Evolution Around an Offshore Breakwater." *Journal of ETA Maritime Science*, vol. 12(3), pp. 238-252, 2024.

computation of wave transformation around complex structures and bathymetry in one-line models. Hoan [11] coupled the EBED [12] wave model, solving the energy balance equation, with a one-line model to compute wave transformation in the nearshore. Smith [13] used an N-LINE model, in which the model is coupled with the SWAN wave model [14]. Similarly, Kristensen et al. [15] computed the sediment transport fluxes with MIKE21 [16] and integrated those fluxes over the surf zone to compute the sediment transport in the one-line model. Dang [17] incorporated an N-LINE model with RCPWAVE [18], a simple linear wave model, to compute wave characteristics in a large domain. To include the cross-shore transport effects, Hanson et al. [19] and Hanson and Larson [20] added cross-shore modules to one-line models, Larson et al. [21] coupled a beach profile model with a one-line model, Hanson and Larson [22], Dabees and Kamphuis [23], and Dang [17] developed multiple-line models, and Shimizu et al. [24] and van den Berg et al. [25]. Robinet et al. [10,26] developed a grid-based one-line approach using a 2D wave refraction model and a cross-shore transport module. The researchers also studied one major drawback of the one-line models: the shoreline's irregularities tend to smooth out, and curved shorelines become straight. Hanson et al. [27] surpassed this by introducing a stable representative coastline. Larson et al. [28,29] defined a regional shoreline to make the local shoreline progress in alignment with the regional shoreline. They also included a geometric wave transformation tool that transforms the waves into a representative contour. Kaergaard and Fredsoe [30] introduced a vector-based approach to model the evolution of shorelines with significant curvature. They performed detailed computations on sediment transport rates using spectral wave, hydrodynamic, and sand transport models. Several other researchers have also developed more detailed 2D depth-averaged horizontal (2DH) models to resolve the nearshore currents and associated transport rates [31-35]. However, these models required significantly higher computation times than the simple one-line models [36].

The present study investigates a shoreline evolution modeling approach with a more precise computed nearshore wave field around complex coastal structures compared with one-line models while demanding a smaller number of input parameters and less computational source compared with complex 2DH and 3D models, eliminating intense nearshore circulation and advection-diffusion computations. For this purpose, a depth-averaged quasi-2-dimensional shoreline evolution numerical model (Q-2DH hereafter) is constructed on the basis of the 2DH Beach Evolution Model [35] and following the simplified approach of van den Berg et al. [25] to compute nearshore sediment transport. The model is then applied to the laboratory experiments of Gravens and Wang [37] on the shoreline evolution around a detached breakwater, and the computed nearshore wave fields and post-test bathymetries are quantitatively compared with the measurements. This study is compiled from the thesis of the second author.

The paper is organized as follows. Section 2 describes the theoretical background of the Q-2DH model, its structure, and its main assumptions. Section 3 describes the model setup and the simulations conducted. Here, the model is applied to a cross-shore transport-related theoretical benchmark case and to Gravens and Wang's [37] laboratory experiments to investigate morphological changes around a detached breakwater. Finally, in section 5, the results are discussed, and the study conclusions are drawn.

2. Materials and Methods

In this chapter, the theoretical background of the Q-2DH model is described in detail.

2.1. Model Structure

The Q-2DH model is comprised of three main modules: a nearshore spectral wave (NSW) model [38], a sediment transport module (STD), and a morphology evolution module (MEV). MATLAB® is employed to develop the model, which operates on a rectangular grid and utilizes finite difference schematization to solve the governing equations. The Q-2DH model considers several input parameters, such as bottom topography, structural information, average bottom slope in the surf zone, wave parameters, hydrodynamic and morphodynamic time steps, material properties, sediment transport, and morphology options.

The first step of the Q-2DH model involves the computation of nearshore wave heights and mean directions, which are kept constant for a given hydrodynamic time step until bathymetrical changes affect the wave characteristics. The user defines the hydrodynamic time step (Δt). In the second step (STD), the bulk LST rate computed using the extended CERC formula [39] is distributed over the surf zone. Additional transport mechanisms, namely cross-shore, swash zone, and alongshore diffusivity, are utilized herein to maintain the equilibrium beach profile, restrain the growth of small-scale noise, and consider the swash zone profile. In the final step (MEV), the bathymetry is updated using the computed sediment fluxes in a continuity equation. The model structure is shown in Figure 1a. The Q-2DH model uses three different computational grids: i) a primary grid system to compute morphological changes and wave parameters, ii) a staggered grid system interpolated from the primary grid to compute the topographical orientation of the primary grid and the local wave approach angle, and iii) a face-center grid to define sediment influxes and outflux in the x- and y-directions. The grid system is shown in Figure 1b.

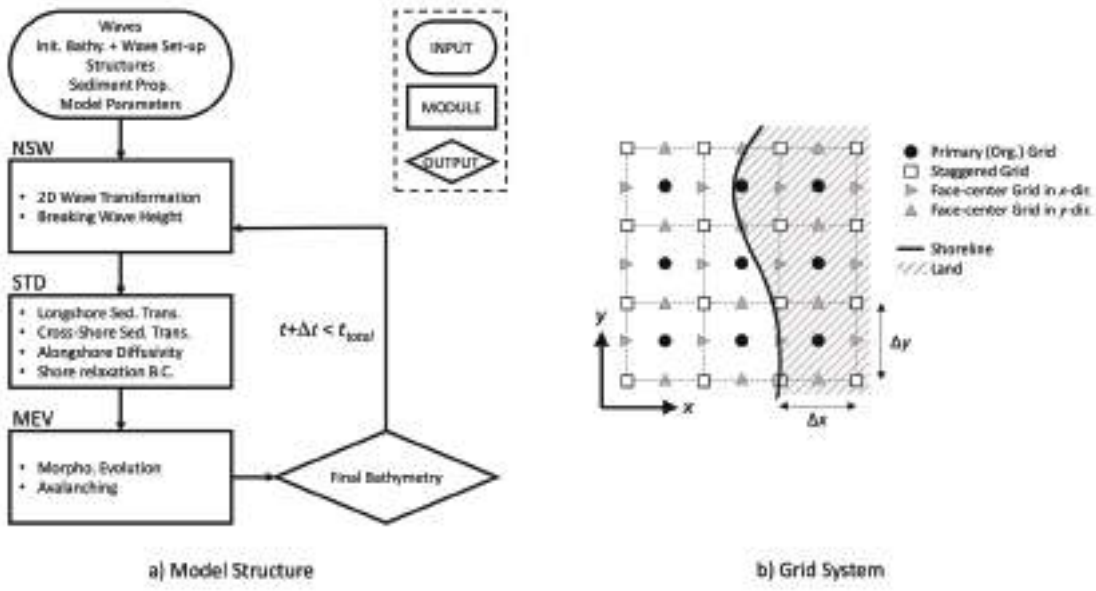

Figure 1. *a) Q-2DH model structure and b) grid system*

NSW: Nearshore spectral wave, STD: Sediment transport distributions, MEV: Morphology evolution, 2D: Two-dimensional

The directional domain is discretized into finite angular grids to describe the spectral density [40].

2.2. Wave Transformation (NSW)

NSW is a phase-averaged 2D spectral wave model [35,38,40], which only solves the energy balance equation in the spatial and directional (-π/2 to π/2) domains. The model considers the following essential processes: linear wave shoaling and refraction, random wave breaking [41], and diffraction [12]. The numerical solution scheme, boundary conditions, and benchmark studies conducted for the module are already given in the literature [35,38,40]. Therefore, they are not provided here for brevity.

2.3. Sediment Transport Distributions

The STD module is where the Q-2DH model's sediment transport computations are carried out. The bulk LST in the module is distributed over the surf zone from the shoreline to the closure depth. The cross-shore sediment transport is computed to preserve the equilibrium beach profile on a relatively long-time scale. Alongshore diffusivity transport is used to restrain the growth of small-scale noise in the MEV module. Furthermore, shore relaxation boundary condition mimics swash zone transport, favoring the profile at the shoreline to evolve to the equilibrium profile.

2.3.1. Longshore sediment transport

The longshore sediment transport (LST) is the primary mechanism in the Q-2DH model. It is calculated following the extended CERC formula [39], which includes the breaking wave height's alongshore gradients [42]:

$$Q = \mu H_{rms,b}^{5/2}\left(\sin(2\beta_b) - \frac{2r}{m}\cos(\beta_b)\frac{\partial H_{rms,b}}{\partial y}\right) \quad (1)$$

Here, Q is the bulk LST, μ is a constant taken as 0.2 $m^{1/2}/s$ (within a range of 0.06-0.45 $m^{1/2}/s$, given by Komar [39]), $H_{rms,b}$ is the root-mean-square breaking wave height, β_b is the angle between the breaking wave approach angle and the bottom contour, the r is a constant equal to 1.0, m is the mean bottom slope at the surf zone, and y is the alongshore distance of the model domain.

The above-given transport formula predicts the bulk LST along the cross-shore profile; thus, it is not directly applicable in a 2D model. The present model is modified to give an order of magnitude for LST at a given point in the computational domain. First, the angle between the breaking wave angle and shoreline (β_b) is replaced with the angle $(\beta = \theta - \alpha)$ between the local wave angle (θ) and the local bottom orientation angle (α) in the model. Figure 2 shows the local bottom orientation (α), local incoming wave angle (θ), and relative incoming angle (α).

Second, the root-mean-square breaking wave height, $H_{rms,b}$, is defined as the most offshore wave height that conforms $H_{rms} \geq \gamma_b \cdot d$ condition, where H_{rms} is the local root mean square wave height. As for the root-mean-square breaking wave height used in the gradient term in Equation (1), the local root-mean-square wave heights are used. The γ_b is the breaking wave index (the ratio of breaking wave height to the breaking water depth) computed using Nairn [43], and d is the local water depth. H_{rms} is the local root-mean-square wave height, calculated using Battjes and Groenendijk [44]

using the significant wave height (H_s) computed by the NSW module at each computational point.

$$\gamma_b = 0.39 + 0.56 \cdot \tanh\left(\frac{33H_{rms,0}}{1.56T_s^2}\right) \quad (2)$$

$$H_{rms} = \left(0.6725 + 0.2025\left(\frac{H_s}{d}\right)\right)H_s \quad (3)$$

Here, $H_{rms,0} = H_{s,0}/\sqrt{2}$ is deep water root-mean-square wave height and T s is significant wave period. Following the above-given computations for bulk LST in the computational domain, the local orientation of the bottom contours, wave height, and approach angle variations due to structures or bathymetric features are considered. van den Berg et al. [25] assumed that the cross-shore distribution of LST roughly follows the longshore current profile and utilized the equation introduced by Komar [39]. However, this approach does not apply to complex coastal defense systems. Therefore, to confine the LST from the shoreline to the closure depth and compute the longshore sediment fluxes at the face centers of the primary grid around the coastal structures, Komar's [39] equation is approximated as follows:

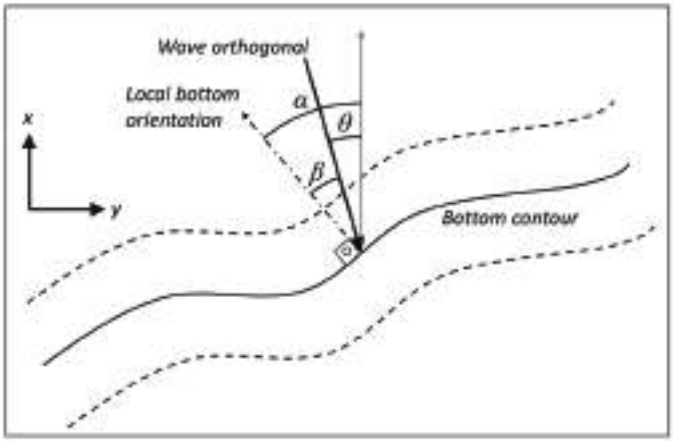

Figure 2. *Angle between local wave angle and local bottom orientation*

$$q_{lst,x} = -Q_{lst} \cdot \overline{C_3} \cdot sin\,(\alpha) \quad (4)$$

$$q_{lst,y} = Q_{lst} \cdot \overline{C_3} \cdot \cos\,(\alpha) \quad (5)$$

$$C_3 = (C_1)^4 \cdot C_2 \quad (6)$$

$$C_1 = \frac{d_c - d}{d_c} \quad (7)$$

$$C_2 = \left(\frac{H_{rms}}{H_{rms,b}}\right)^{5/2} \quad (8)$$

Above, $q_{lst,x}$ and $q_{lst,y}$ are the LST rates computed at each face-center grid location in the x- and y-directions, respectively, depending on the orientation of bottom contours (i.e., for straight parallel bottom contours aligned in the y-direction, $q_{lst,x}$ values become null), d_c is the depth of closure computed with [45] using deep water

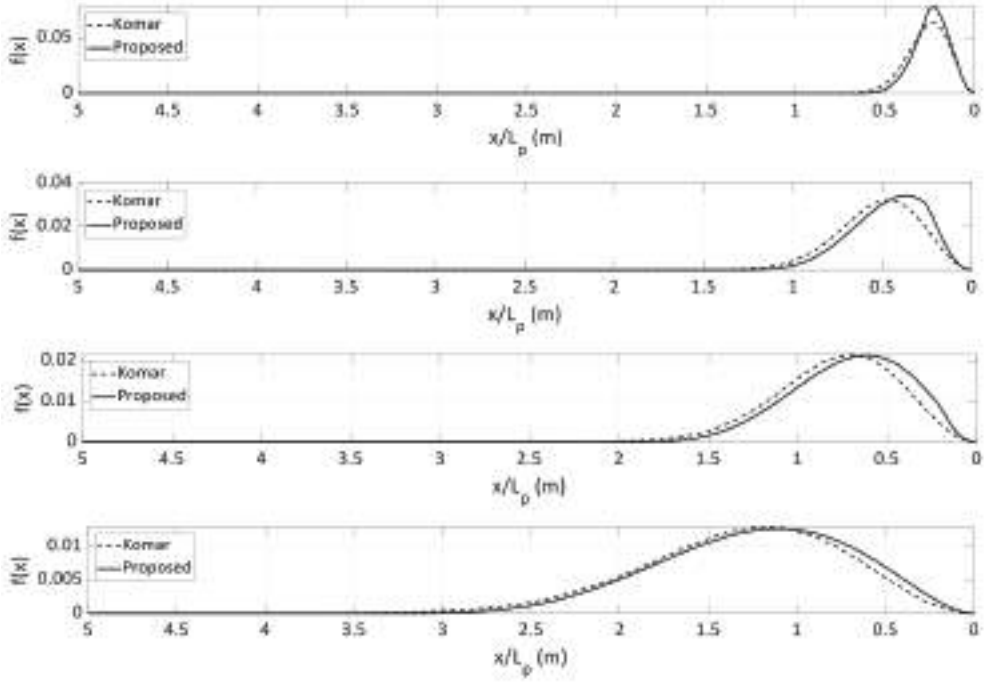

Figure 3. *Comparison of the proposed and Komar [39] (1998) distribution: a) 1/10 slope, b) 1/20 slope, c) 1/30 slope, and d) 1/50 slope*

significant wave height and respective significant period, $\overline{C_3}$ is the normalized distribution over the surf zone. Figure 3 shows the proposed and Komar's distributions [39] for a straight parallel beach with 1/10, 1/20, 1/30, and 1/50 bottom slopes. Here, the $f(x)$ represents the density function of the LST distribution over the surf zone.

In Figure 3, for the bottom slopes of 1/10 and 1/20, the proposed distribution gives slightly higher peak densities than Komar [39] by approximately 20% and 7%, respectively. Both distributions are almost identical qualitatively and quantitatively for the bottom slopes of 1/30 and 1/50. Equations (6-8) agree with Komar [39] with a coefficient of correlation, $R^2 = 0.993$, and a mean absolute error of 5.9% for the above-given bottom slopes. Further study could be conducted to validate these equations using laboratory and field data available in the literature. However, such a study has been kept out of scope in this study.

2.3.2. Cross-shore sediment transport

In the Q-2DH model, cross-shore sediment transport is defined to preserve the equilibrium profile, as given in [25]. The analyses of short- and medium-term events such as storm-induced erosion and breaches or winter and summer profiles are not focused in the Q-2DH model. The parameterization of the cross-shore sediment transport is given as follows:

$$q_{crs} = -\gamma_x \left(\frac{\partial (d - d_e)}{\partial x} \right) \tag{9}$$

$$\gamma_x = \varepsilon_x \gamma_b^{-1/6} g^{1/2} H_{rms,b}^{11/6} X_b^{-1/3} \varphi(x) \tag{10}$$

$$\varphi(x) = \frac{1 + b + \tanh\left(\frac{X_l - x}{L_d}\right)}{1 + b + \tanh\left(X_l / L_d\right)} \tag{11}$$

in which, d is the local depth, d_e is the assumed equilibrium profile depth, γ_x is cross-shore diffusivity constant, ε_x is a non-dimensional constant, γ_b is breaking wave index, g is the gravitational acceleration, $H_{rms,b}$ is the breaking root-mean-square wave height, X_b is the width of the surf zone ($X_b = H_{rms}/(\gamma_b \cdot m)$), $\varphi(x)$ is the shape function. The shape function, $\varphi(x)$, peaks in the surf zone and reduces to a residual value (b) almost equal to zero. The b is a constant controlling the residual magnitude beyond the closure depth, $X_l = 2X_b$, x is the distance to the shoreline in the x-direction, L_d and controls the length scale decay until X_l. The above approach indicates that if the initial profile is identical to the user-defined equilibrium profile, the cross-shore transport is null at the start of the simulation. If the cross-shore profile differs from the equilibrium profile, this profile is altered to the equilibrium profile with non-null cross-shore sediment fluxes.

2.3.3. Alongshore diffusivity

The alongshore diffusivity transport is defined by [25] to mitigate the morphodynamic instabilities in the MEV module. This transport mechanism is based on the local bathymetrical orientation and depth variation in the x- and y-directions. The alongshore diffusivity transport is given below;

$$q_d = -\gamma_y \left(\frac{\partial d}{\partial x} sin(\alpha) + \frac{\partial d}{\partial y} cos(\alpha) \right) \tag{12}$$

where, γ_y is the alongshore diffusivity term, which is similar to the cross-shore diffusivity term, γ_x. The alongshore diffusivity constant is calculated using Equation (10); where ε_x is used instead of ε_y.

2.3.4. Swash zone dynamics

Two distinct methodologies were employed to represent the dynamic behavior of the swash zone in the model. First, a shore relaxation boundary condition is introduced at the shoreline [25], which moves the sediment from wet to dry or in the opposite direction at the shoreline. This boundary condition ensures the preservation of the equilibrium profile at the shoreline so that the bed slope between the wet cell at the shoreline and the adjacent dry cell matches the equilibrium profile. Such a boundary condition is implicitly present in the cross-shore transport definitions of Kristensen et al. [15] and Arriaga et al. [46], which preserve the equilibrium beach profile in their models. Second, a wave-induced setup is calculated using [47] and applied to the entire model domain, leading to the inundation of the swash zone and activating the transport mechanisms in this domain. Such a definition further extends the preservation of the equilibrium onshore, similar to the definition of the berm height limit in Kristensen et al. [15] or the swash zone width in Arriaga et al. [46]. While the first method replicates the behavior of the swash zone, the latter causes the shoreline to move toward the land during wave conditions, thus preserving the equilibrium profile.

Shore relaxation defines sediment transport from wet to dry grid points when the swash zone slope is gentler than the equilibrium slope at the shoreline. As a result, the shoreline advances in the offshore direction. In contrast, if the equilibrium slope is milder than the swash zone slope, sediment transport occurs from dry to wet grid points, resulting in the shoreline retreating landward. The shore relaxation transport is given by;

$$q_{rel} = -\gamma_s \left(\frac{\partial d}{\partial x} cos(\alpha_s) - \frac{\partial d}{\partial y} sin(\alpha_s) + m_s \right) \tag{13}$$

$$q_{rel,x} = -q_{rel} \cdot cos(\alpha_s) \quad (14)$$

$$q_{rel,y} = -q_{rel} \cdot sin(\alpha_s) \quad (15)$$

where, γ_s is the shore relaxation coefficient proportional to $(\Delta x^2)/T_r$, T_r is the relaxation time, d is the local water depth, α_s is the local orientation angle at the shoreline, and m_s is the local bottom slope at the shoreline. Goda [47] provides a relationship to compute the wave-induced setup for a uniform bottom slope range of 1/10-1/100, a wave steepness range of 0.005-0.08, and a wave approach angle range of 0°-70°. The formula is not given here for brevity.

2.4. MEV

In the MEV module, sediment transport rates computed in the STD module at the face centers are used to compute the depth changes:

$$\frac{\partial d}{\partial t} = m_f \left(\frac{\partial q_x}{\partial x} + \frac{\partial q_y}{\partial y} \right) \quad (16)$$

Above, t is time, m_f is the morphological acceleration factor, q_x is the total sediment flux in the x-direction, and q_y is the total sediment flux in the y-direction, where both include the bed porosity factor. The MEV module also has an avalanching algorithm adopted from [38]. The algorithm ensures that the bottom slopes over the computational domain are lower than the critical slopes defined by the user for wet and dry grid points. The default values for the wet and dry critical slopes are 1:6 and 1:5, respectively. Further details are provided in the latter reference.

2.5. Boundary Conditions

The local orientation angles (α) are refined in the model to smoothen the sediment transport direction locally, considering the overall transport direction around a local grid point. This particularly helps to handle cases where the shoreline evolves, having a curvature leading to minimal values of wave approach angles near the shoreline and variations in the sediment transport direction. For the computation of the orientation of the coastline, van den Berg et al. [25] suggested using the mean bathymetric orientation in the surf zone rather than the shoreline orientation or the respective contour orientation. They compute each grid point's mean orientation within a user-defined moving box. Such a moving box filter is applied in the Q-2DH model similarly to [25] to represent the overall sediment transport more accurately. The user defines the moving filter box's dimensions in the order of the surf zone width (X_b), where the default values are two times in the cross-shore direction and four times alongshore.

In the STD module, sediment transport fluxes are computed at the face centers of the primary grid. The most offshore limit of the transport modes is the closure depth. Beyond the closure depth, sediment transport is assumed to be null. On land, the wet cells above a minimum depth (including wave set-up) defined by the user are the most onshore limit of the sediment transport, except for the shore relaxation term. This is intentionally defined in the exact position of the shoreline. The model implements a Courant-Friedrichs-Lewy type [25] numerical stability criterion to control the time increment (Δt) as given below,

$$\Delta t = c H_{rms}{}^{-3/2} \frac{(min\{\Delta x, \Delta y\})^2}{max\{\varepsilon_x, \varepsilon_y\}} \quad (17)$$

where c is a calibration constant with a default value of 0.13, Δx, and Δy are spatial resolutions in the x and y directions, respectively, ε_x and ε_y are non-dimensional constants in Equation (17) with default values of 0.05.

3. Model Application

This section introduces the theoretical case for testing the cross-shore module, the laboratory experiments [37] to which the Q-2DH model is applied, and the methodology for evaluating the differences between the computed and measured results.

Before applying the model to laboratory experiments [37], the model's cross-shore module is first tested with a theoretical case study. A randomly determined initial bed profile is introduced in the model. A LST is absent (perpendicular wave approach), and default values are used for all parameters. The evolution of the initial bottom profile is evaluated. Later, the Q-2DH model was applied to a series of laboratory experiments [37], which were specifically conducted to gather data sets for validating sediment transport relationships and developing computational model algorithms to estimate tombolo processes near headland structures such as offshore breakwaters and T-groins. The experiments consisted of five series of physical model experiments, each including several subseries in which waves and currents were generated on a movable bed in the wave basin. The experiments collected wave heights, current velocities, mean water elevations, bulk sediment transport rates, and bathymetrical data. Among the series, those conducted to obtain data sets for tombolo development at the lee-side of an offshore breakwater are "test 1" and "test 2". In this study, the Q-2DH model is applied to "test 1" only. The "test 1" cases were studied in a subseries of eight simulations (T1C1 through T1C8), with each subseries approximately 190 min long. The cases were conducted on a natural beach with a 4-m-long rubble mound offshore breakwater located 4 m from the initial shoreline and at the center in the alongshore direction (Y=26 m to Y=22 m).

The experiments demonstrated the initiation of a salient in T1C1 and to inspect the advancement of the salient between cases T1C1 and T1C7. In case T1C8, the formation of a tombolo was observed. Furthermore, an additional simulation started from the beginning of case T1C1 and continued almost until the end of case T1C2 without interruption due to any stability problem. Wave-induced longshore currents were recirculated in the basin from downstream to upstream using pumps. Following subseries T1C2 (time=6 hours) and T1C5 (time=15 hours), the sediment traps at the downstream are cleared, and the equilibrium beach profile is reconstructed. The sediment bottom is composed of well-sorted quartz sand with a median grain size of 0.15 mm. The properties of all simulations are given in Table 1. This simulation is named as T1C1-T1C2. The layout of the "Test 1" case is shown in Figure 4.

Table 1. *Benchmark cases*

Case name	$H_{s,0}$ (m)	T_s (s)	θ_0 (°)	Duration (min)	Purpose
Cross-shore transport	0.27	1.43	10	334	Preservation of the equilibrium profile
T1C1	0.27	1.43	10	185	Formation of the salient (model calibration)
T1C2				181	Advancement of the salient
T1C3				185	″
T1C4				192	″
T1C5				176	″
T1C6				189	″
T1C7				191	″
T1C8				184	Formation of the tombolo
T1C1-T1C2				366	Formation of the salient

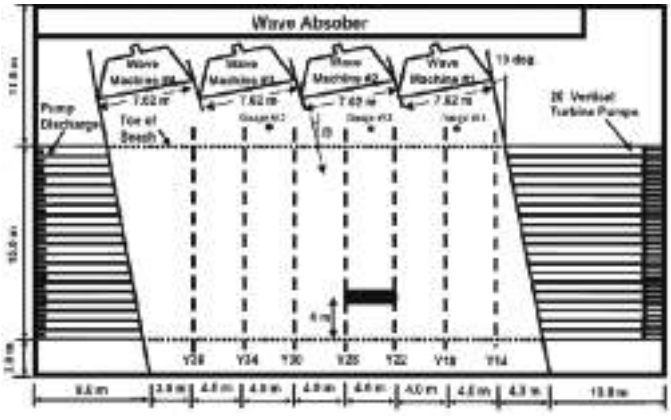

Figure 4. *Initial layout of Test 1 (adopted from Gravens and Wang [37] 2007)*

The computed wave heights were assessed using an aerial mean absolute percent error (MAPE) definition. The results of beach evolution were evaluated using both MAPE and Brier Skill Score (BSS) [48]. For morphological evaluations, the MAPE is computed separately for the shoreline change and bathymetry. MAPE is given in Equation 18:

$$MAPE = \frac{1}{n}\sum_{i=1}^{n}\left|\frac{y_i - x_i}{x_i}\right| \tag{18}$$

where y_i is the predicted value, x_i is the true value, and n is the total number of data points.

BSS is a score function commonly used in sediment transport and beach evolution modeling. It computes the mean squared difference between the observed and predicted values. A BSS score equal to one gives an excellent correlation, which worsens as the value decreases below zero. The BSS is given by Equation 19:

$$BSS = 1 - \frac{\sum_{i=1}^{n}\sum_{j=1}^{k}\left(d_{i,j}^{p} - d_{i,j}^{m}\right)^2}{\sum_{i=1}^{n}\sum_{j=1}^{k}\left(d_{i,j}^{b} - d_{i,j}^{m}\right)^2} \tag{19}$$

with $d_{i,j}^{p}$ is the predicted depth at the (i, j)th cell, $d_{i,j}^{m}$ is the measured depth at the (i, j)th cell and $d_{i,j}^{b}$ is the initial depth at the (i, j)th cell. According to van Rijn et al. [49] (2003), the performance of a morphologic simulation is considered as "bad" when $BSS<0.0$, "poor" when $0.0<BSS<0.1$, "reasonable/fair" when $0.1<SS<0.2$, "good" when $0.2<BSS<0.5$, and excellent" when $0.5<BSS<1.0$. In the BSS computation, only the offshore breakwater's lee side is considered. van Rijn et al. [49] state, "BSS is susceptible to small changes when the denominator is low". When considering the entire model domain, depths with minimum differences in the model and measurements lead to lower BSS scores. Therefore, BSS is calculated for three different depth intervals (0-0.08 m, 0.08-0.16 m, and 0-0.16 m), which will be addressed further as BSS1, BSS2, and BSS3, respectively, in each case. BSS3 gives a score for the entire region at the lee side of the breakwater.

The T1C1 case lasted 185 min with waves and wave-induced currents. The Q-2DH model is first calibrated for the T1C1 case, and the calibrated parameter values are used in subsequent cases. The model domain area is discretized with an equal grid spacing of 0.2 m in both the alongshore and cross-shore directions following Nam et al. [50] and Baykal et al. [35]. To sustain the longshore currents in the model area, the model area is extended 20 m in the upstream and downstream directions. These extended lateral boundaries are not considered in the MAPE and BSS computations. The

model domain is also extended in the offshore direction by extrapolating the water depths from the most offshore depth of T1C1 as 0.7 to an offshore depth of 1.69 m to satisfy the offshore wave conditions of Test 1. In summary, the model area is composed of a total of 113 cells (X-range=1.6 to 24) in the x-direction and 301 cells (Y-range=-6 to 54) in the y-direction. Other model parameters are listed as follows: $H_{s,0}$=0.27 m, $T_{s,0}$=1.42, θ_0=10°, γ_b=0.78, s_{max}=10, ε_x=0.5, ε_y=0.5, γ_s=6.24*10-6, m_f=0.37, μ=0.20, d_c=0.37 m and Δ_t=0.2 s. The $H_{s,0}$, $T_{s,0}$, θ_0, γ_b and s_{max} are adjusted to assure the offshore wave conditions of T1C1. The parameters ε_x, ε_y, γ_s and m_f are calibrated by trial and error until the computed shoreline agrees quantitatively and qualitatively with the measured shoreline in T1C1. As mentioned earlier, the Δ_t is the hydrodynamic time step satisfying the stability criterion. For the computation of the mean orientation of the coastline, the dimensions of the moving box filter are introduced as two times the surf-zone width in the alongshore direction and one surf-zone width in the cross-shore direction.

4. Results and Discussion

The results of the simulations introduced in the preceding section are given and discussed in this section.

4.1. Cross-Shore Transport

In the Q-2DH model, a parametrized expression for cross-shore sediment transport is applied rather than a process-based method. This parameterized expression restores or preserves the predefined equilibrium profile on a relatively long-time scale. Here, the simulation results are given, where the sediment transport is in the cross-shore direction only and the alongshore transport is not present. The bottom profiles of different time steps are shown in Figure 5, where the black solid line represents the initial profile, the black dashed line represents the bottom profile at the respective time step, and the red dashed line represents the user-defined equilibrium profile.

In Figure 5a (t=0 seconds), the initial and final profiles are identical, as cross-shore sediment transport has not yet started. In Figure 5b (t=1000 seconds), the profile approximately takes the shape of the equilibrium profile. In Figure 5c (t=10000 seconds), the final profile is almost identical to the equilibrium profile. In Figure 5d (t=20000 seconds), the final and equilibrium profiles are similar. It can be inferred that the magnitudes of the fluxes are much higher in the earlier steps of the simulation and gently decrease to null.

4.2. Laboratory Experiments

In the simulations of the laboratory experiments, the model is first applied to the case T1C1. The variation of significant wave heights in the cross-shore direction for the Y30 and Y24 profiles, the alongshore direction for the X5.2 profile, and the a LST flux variation for the Y24 profile are shown in Figure 6.

Figure 6 shows that the computed significant wave heights agree with the measurements. The wave heights in the shadow zone right behind the breakwater are underestimated

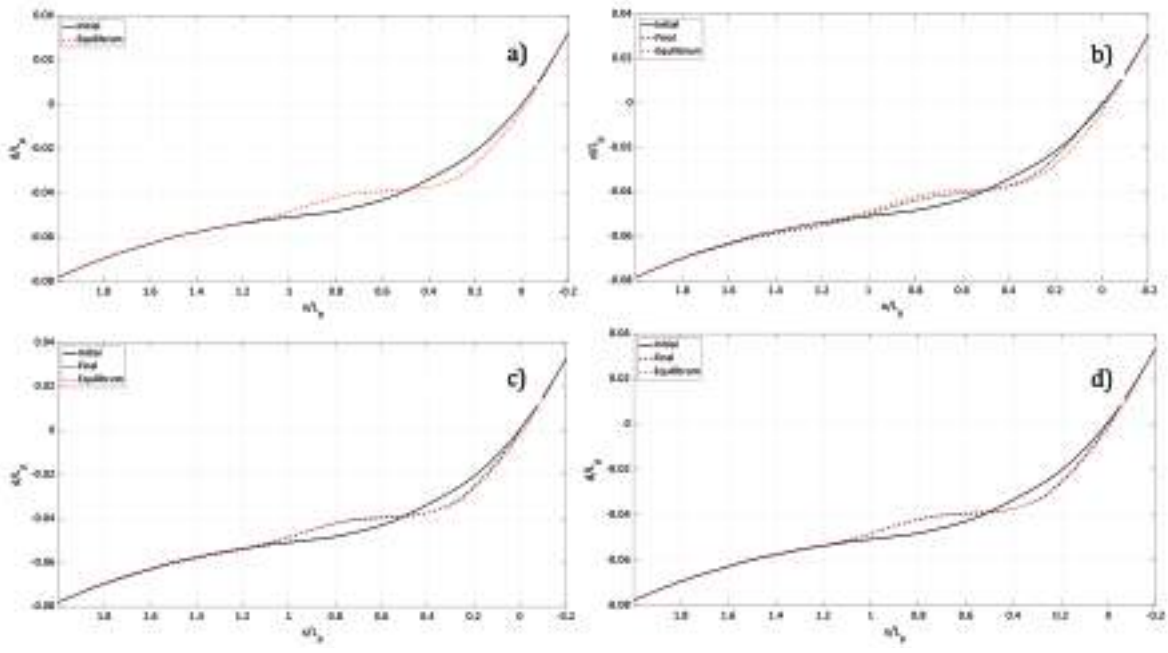

Figure 5. *Evolution of bottom profile under cross-shore sediment transport a) t=0 s, b) t=1000 s, c) t=10000 s, and d) t=20000 s. The solid line is the initial bottom profile, the red dashed line is the equilibrium bottom profile, and the black dashed line is the intermediate bottom profile*

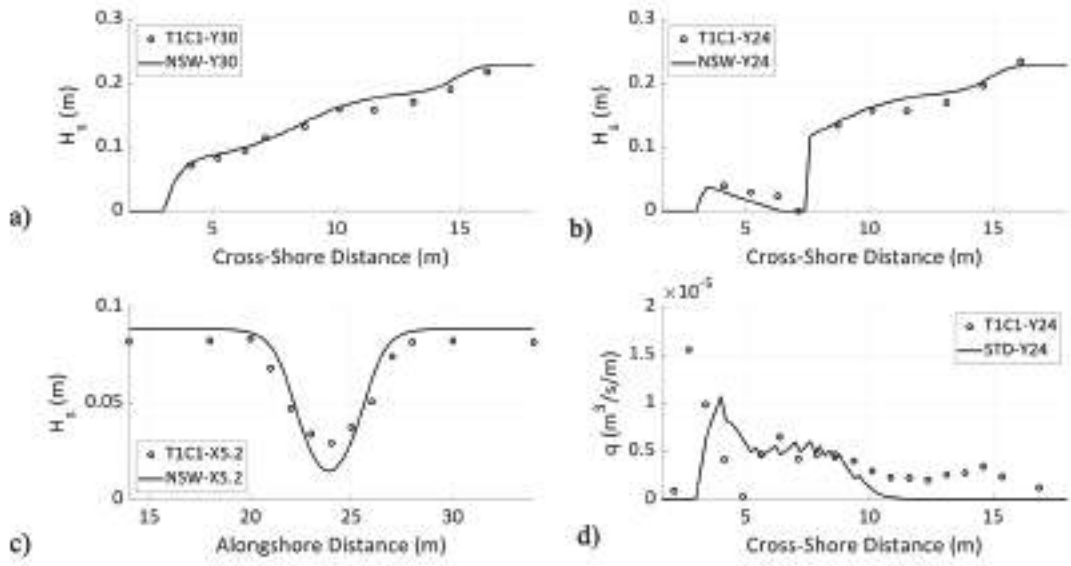

Figure 6. *a) Significant wave heights along Y30, b) Y24, c) X5.2, and d) longshore sediment fluxes at Y24. The circles represent the measurements. The solid line is computed*

NSW: Nearshore spectral wave, STD: Sediment transport module

by almost 20% on average (22 m<Y<26 m). Meanwhile, they are slightly overestimated by 5% on average in the illuminated zone (Y<22 m and Y>26 m). The MAPE for the significant wave heights for T1C1 is computed as 12%. The alongshore bulk sediment fluxes are in relatively good agreement with the measurements around the offshore breakwater; however, they are underestimated close to the shoreline and further offshore. For the other tests (T1C2-T1C8), the computed significant wave heights are compared with the measurements in Figures 7 and 8. The MAPE values were calculated for the significant wave heights, shoreline, and bathymetry, the BSS scores computed for various depth ranges, and the relative maximum shoreline retreat and advancement (R_{rel} and A_{rel}, respectively) in shore-normal directions computed and measured for all simulations are shown in Table 2. The values of the shoreline retreat and advancement given in Table 2 are determined for each simulation from the initial and final positions of the shoreline in each case.

In Figures 7 and 8, solid black lines are the equal height contours of significant wave heights measured by [37], gray dotted lines are computed by the Q-2DH model, and blue dotted lines are the initial bottom contours of the respective tests. As seen from the figures, the computed significant wave heights agree well with the observations around the structure both quantitatively and qualitatively. For all cases, the wave heights in the shadow zone of the breakwater (4<X<6 m and 22<Y<26 m) are slightly underestimated, whereas in the illuminated zone, they are overestimated. Overall, the MAPE values varied between 11% and 18% (see Table 2), where the maximum differences are observed for T1C7 and T1C8 (final stages of salient before tombolo formation), and the minimum discrepancies are observed for T1C3 and T1C2 (early stages of salient).

The morphological changes computed by the Q-2DH model are compared with the measurements in Figures 9 and 10 for the cases T1C1-T1C8. In the figures, the solid black lines are the bottom contours measured by [37], the gray dotted lines are the computed bottom contours by the Q-2DH model, and the blue dotted lines are the initial bottom contours of the respective tests. In Figure 9a, for the T1C1 case, the shoreline and 0.1 m contour computed by the model match well with the measured contours. There are some irregularities in the bottom contours at the sides of the salient and offshore breakwater. Moreover, the 0.1 m contour is aligned toward the left in the measurements, whereas the computed contour is more symmetrical. Figure 9b shows that the Q-2DH model overpredict the accretion at the shoreline in the T1C2 case, whereas the computed 0.1 m contour is close to the measurement. In the T1C3 case (Figure 9c), the computed shoreline is identical to the experimental results. Both the computed and measured 0.1-m contours merge with the 0.1-m contour around the breakwater on the left side of the breakwater. In the T1C4 case (Figure 9d), the contour lines are quantitatively and qualitatively similar at the lee side of the breakwater. More scour occurs on the left and right sides of the breakwater than in the observations. In T1C5 (Figure 10a), the shoreline recedes more in the model results than in the experiments. Figure 10b shows that the shoreline and 0.1 m contour are similar to the observations of T1C6. At the updrift (left) part, the shoreline and 0.1 m contour are much more accreted than in the model, whereas erosion are

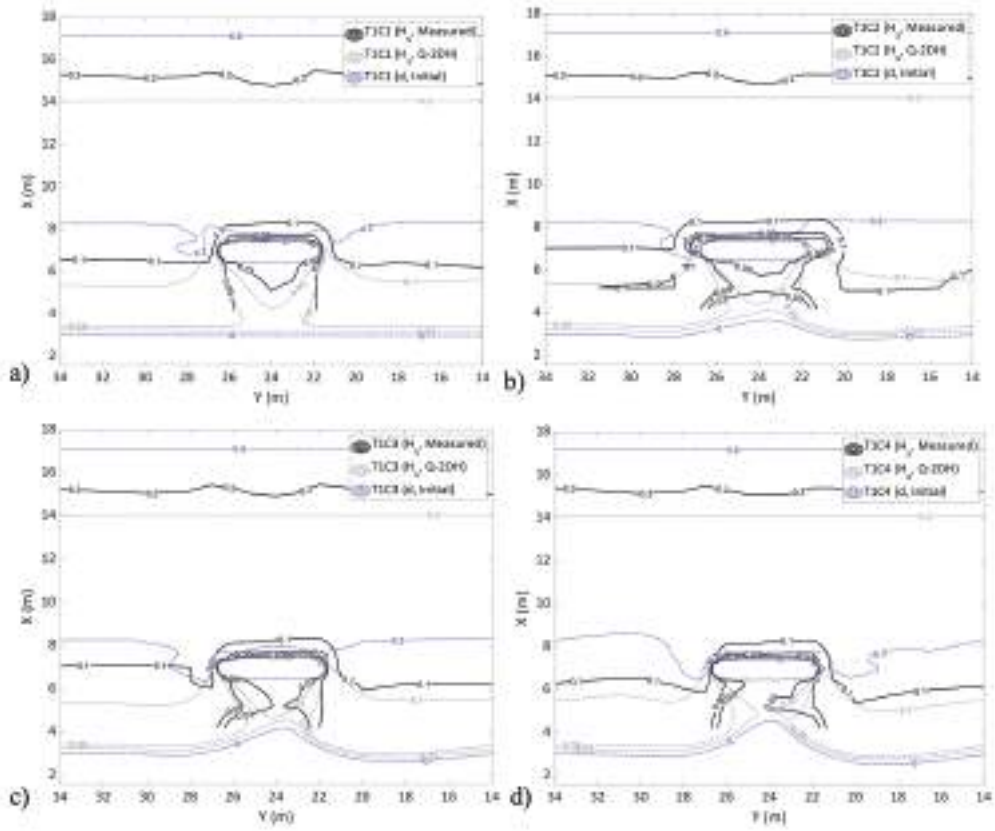

Figure 7. *Measured and computed significant wave heights for the tests: a) T1C1, b) T1C2, c) T1C3, and d) T1C4. (Solid black lines are measured by Gravens and Wang [37], gray dotted lines are computed by the Q-2DH model, and blue dotted lines are the initial bottom contours)*

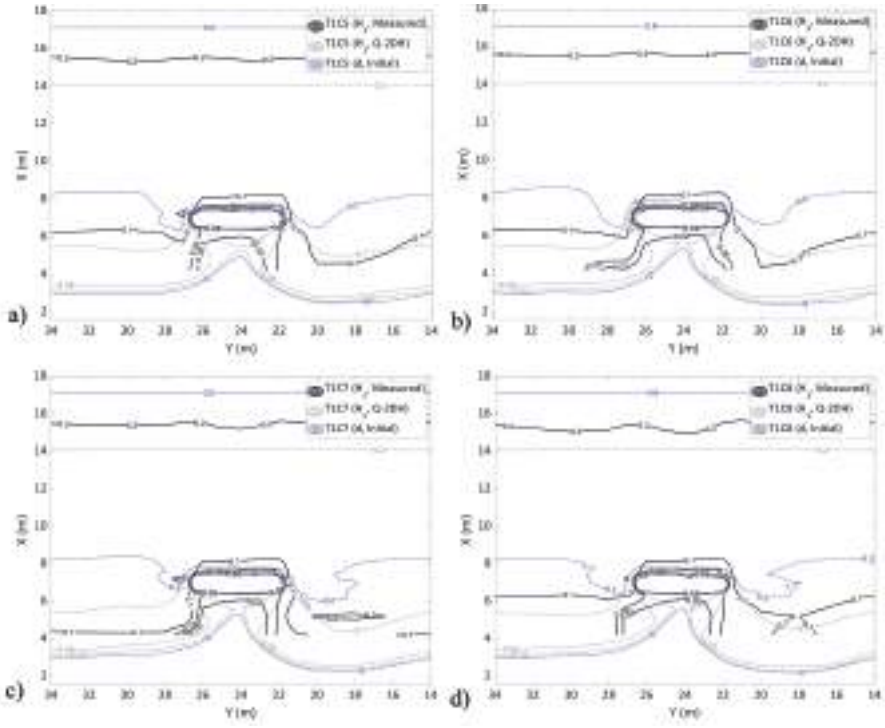

Figure 8. *Measured and computed significant wave heights for the tests: a) T1C5, b) T1C6, c) T1C7, and d) T1C8. (Solid black lines are measured by Gravens and Wang [37] 2007; gray dotted lines are computed by the Q-2DH model, and blue dotted lines are the initial bottom contours)*

Table 2. *MAPE for significant wave heights, bathymetry and shoreline, BSS scores, and shoreline retreat and advancement near the breakwater*

Case name	MAPE			BSS1*	BSS2**	BSS3***	Measured		Computed	
	H_s	Bathymetry	Shoreline				R_{rel} (m)	A_{rel} (m)	R_{rel} (m)	A_{rel} (m)
T1C1	0.12	0.26	0.0024	0.83	0.62	0.71	0.29	0.88	0.39	0.83
T1C2	0.12	0.37	0.0011	0.71	-0.45	0.50	0.34	0.48	0.25	1.00
T1C3	0.11	0.29	0.0026	-1.26	0.07	-0.42	0.11	0.43	0.24	0.85
T1C4	0.14	0.22	0.0068	-1.45	-0.03	-0.65	0.14	0.43	0.33	0.72
T1C5	0.16	0.29	0.0019	-2.93	-0.91	-2.00	0.25	0.38	0.30	0.41
T1C6	0.15	0.22	0.0067	-2.78	-1.21	-2.22	0.47	0.13	0.37	0.15
T1C7	0.18	0.28	0.0036	-8.47	-2.99	-6.43	-	-	-	-
T1C8	0.16	0.31	0.0100	-7.93	-2.95	-6.07	-	-	-	-
T1C1-T1C2	0.12	0.37	0.0015	0.85	0.58	0.74	0.38	1.27	0.52	1.21

*: Calculated for 0-0.08 m depth range, **: Calculated for 0.08-0.16 m depth range, ***: Calculated for 0-0.16 m depth range MAPE: Mean absolute percent error, BSS: Brier Skill Score

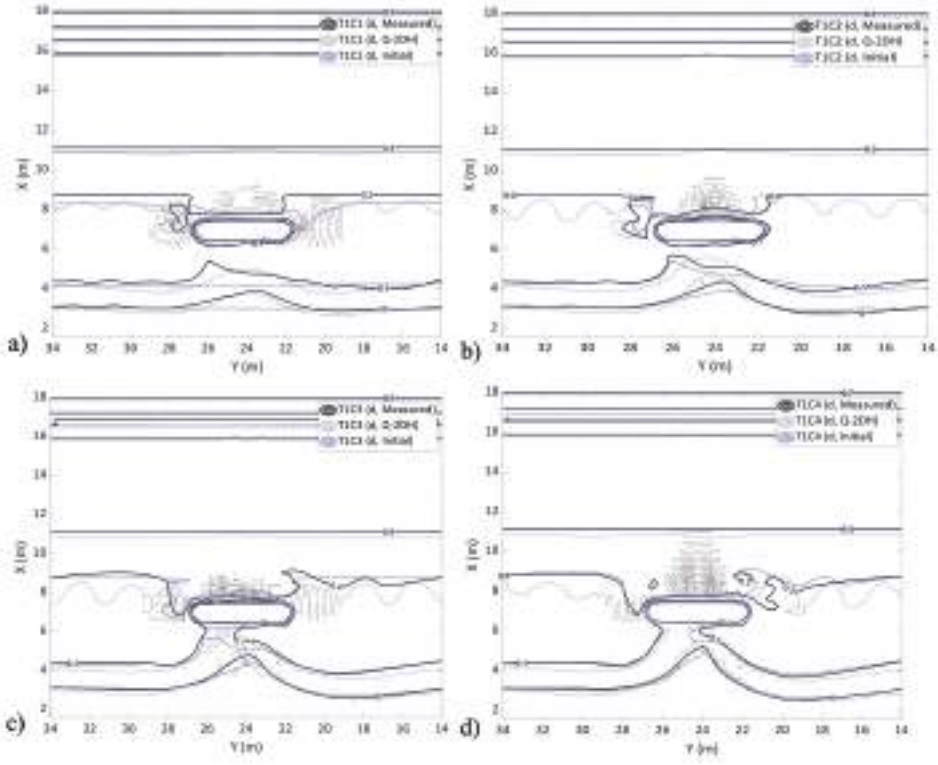

Figure 9. *Measured and computed bottom contours for the tests: a) T1C1, b) T1C2, c) T1C3, and d) T1C4. (Solid black lines are measured by Gravens and Wang [37], gray dotted lines are computed by the Q-2DH model, and blue dotted lines are the initial bottom contours)*

similar at the downdrift part (right side). In the T1C7 case (Figure 10c), the model results show that the shoreline does not progress toward the breakwater; its alongshore width increases. The computed 0.1 m contour is similar to the experimental result. Finally, for the T1C8 case (Figure 10d), the computed shoreline is a partial tombolo formation with some discontinuities. On the other hand, the computed 0.1 m contour is close to the observation.

As a general tendency, the MAPE values computed for the shoreline for all cases increase with the case number, similar to the wave heights. However, the MAPE values computed for the nearshore bathymetry do not have such a trend and vary between 22% and 37%, with an average value of 28%. BSS scores are more sensitive than MAPE values for areal changes. They follow a similar trend to the MAPE values computed for wave heights. As the number of cases increases,

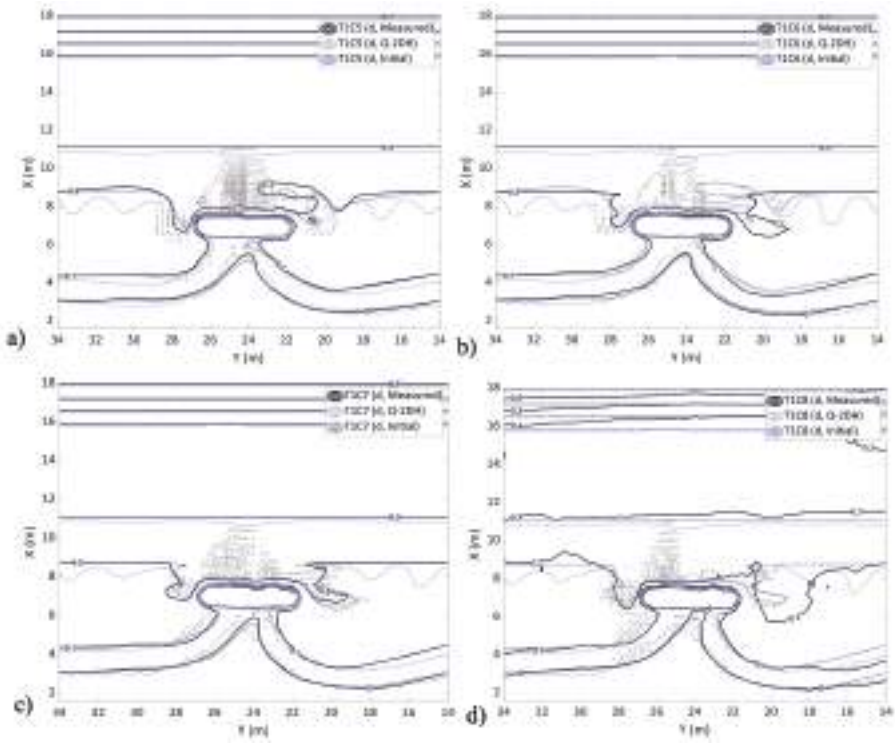

Figure 10. *Measured and computed bottom contours for the tests: a) T1C1, b) T1C2, c) T1C3, and d) T1C4. (Solid black lines are measured by Gravens and Wang [37], gray dotted lines are computed by the Q-2DH model, and blue dotted lines are the initial bottom contours)*

the model's prediction performance decreases, and the BSS values are reduced. This is related to the high orientation angles of the bottom contours occurring as the shoreline advances in the offshore direction toward the breakwater. The highest BSS values were observed in T1C1, T1C2, and T1C1-T1C2, which could be classified as "excellent". The smallest values were obtained for the T1C7 and T1C8 cases. In addition, BSS1 (computed within 0-0.08 m depths) and BSS2 computed within 0.08-0.16 m depths) values computed for all the cases imply that the model performance on computing the morphological changes close to the shoreline (within 0-0.08 m depths) is slightly better than the rest of the nearshore domain. Table 2 shows that the model predicts the maximum relative shoreline retreat and advancement in the shore-normal direction with relatively good accuracy for the T1C1 case and the continuous run T1C1-T1C2. However, as the shoreline advances in the normal direction, the computed values become larger than the measured. This might be attributed to the wave heights being underestimated in the shadow zone, thus resulting in larger alongshore transport gradients moving the sediment toward the lee side of the breakwater. After the 0.1-m contour merges toward the detached breakwater, the retreat and advancement values become close again.

The Q-2DH model is also run from the start of the experiments (T1C1) with the same settings and parameter

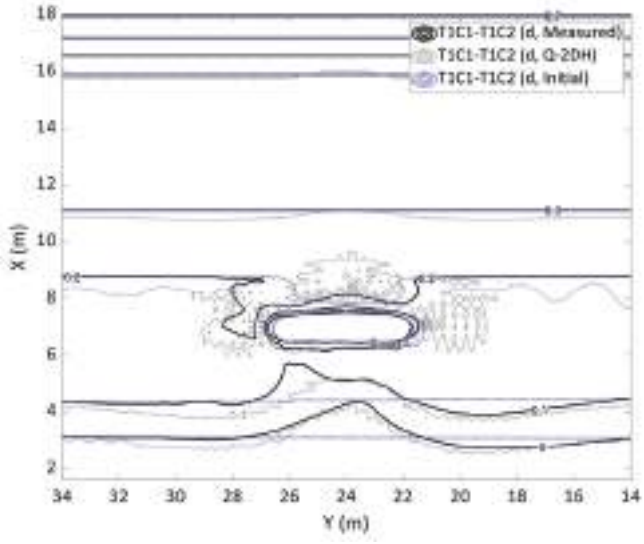

Figure 11*. Comparison of bottom contours for T1C1-T1C2 (measured) and T1C1-T1C2 (Q-2DH).*

values until it is interrupted due to an instability error, which is almost equivalent to the end of T1C2. The run is named T1C1-T1C2. The total model run time is 366 min. The computed bathymetry was compared with the experimental results (T1C2 final bathymetry). The computed significant wave heights for this run are almost the same as those for the T1C1 case, as shown in Figure 7a. A comparison of the

measured and computed bottom contours for the T1C1-T1C2 simulation is given in Figure 11.

Figure 11 shows that the shoreline and 0.1 m contour are similar to the observations. At the updrift (left) part, the two measured contours accreted more than the model. At the downdrift part (right side), erosion are similar; however, around Y18, the measured contours are positioned offshore compared to the computed ones.

5. Conclusion

In the present study, a quasi-2-dimensional numerical model developed to simulate both medium- and long-term shoreline changes under wave action near coastal structures is applied to the experimental dataset of [37] on shoreline evolution behind an offshore breakwater. The model provides a more precise wave transformation computation than the one-line models. At the same time, it demands a smaller number of input parameters and fewer computational sources compared with complex 2DH and 3D models, eliminating complex nearshore circulation and advection-diffusion computations.

The model computes the wave field in the vicinity of structures using a spectral wave model [38] rather than geometric/parametric computations as in one-line models. Thus, the accuracy of the wave field is comparable to that of complex models. Then, it computes the distributed LST based on nearshore wave characteristics. The model also incorporates a cross-shore sediment transport algorithm, alongshore diffusivity, and shore relaxation terms [25]. The cross-shore sediment transport algorithm preserves the equilibrium profile. The alongshore diffusivity term eliminates the growth of high-approach angle stability errors. The shore relaxation term mimics swash zone transport. In addition, a wave setup term is adopted from [47] to represent the mean water level variations at the wet/dry interface of the bathymetry and to extend the active zone of sediment transport further onshore (similar to the definition of equilibrium beach profile), which is handled by solving non-linear shallow water equations in complex models and promoting sediment transport around the shoreline.

The model is first applied to a theoretical case in which cross-shore transport is the only governing mode of transport. The cross-shore transport module can restore any user-defined equilibrium beach profile, which is a major assumption of the one-line-based models. Later, the model was applied to laboratory tests [37]. The present study studies the experiments from T1C1 to T1C8 using the Q-2DH model. When the cases are individually studied, the Q-2DH model quantitively and successfully estimates the nearshore wave field and bathymetrical changes for all cases. The MAPE values computed for the shoreline BSS scores give that the model thrives, especially in T1C1, T1C2, and the continuous run T1C1-T1C2 cases. However, in further cases (T1C3 to T1C8), the performance of the Q-2DH model is reduced. As the shoreline progresses toward the offshore breakwater, high local orientation angles and high incoming wave angles occur, resulting in irregularities in morphological computations. As these irregularities accumulate over time, they result in a highly varying bathymetry, which leads the model to fail.

Further studies are required to resolve the high-wave approach and high local orientation angle-led problems. Such studies will enable us to simulate shoreline changes more accurately around shore-normal structures like shore-normal or angled groins and T-groins. Moreover, the curved shorelines/pocket beaches with/without the presence of structures, sand sources/sinks, tides, and currents also stand as further challenges for simpler models like the Q-2DH model.

Authorship Contributions

Concept design: C. Baykal, and C. Özsoy, Data Collection or Processing: C. Baykal, and C. Özsoy, Analysis or Interpretation: C. Baykal, and C. Özsoy, Literature Review: C. Baykal, and C. Özsoy, Writing, Reviewing and Editing: C. Baykal, and C. Özsoy.

Funding: The authors declare that no funds, grants, or other support was received during the preparation of this manuscript.

References

[1] R. Pelnard-Considere, "*Essai de Theorie de L'Evolution des Form de Rivage en Plage de Sable et de Galets*". 4th Journess de l'Hydraulique, Les Energies de la Mer, Question III, Rapoort No. 1, 1956, pp. 289-298.

[2] W. A. Price, D. W. Tomlinson, and D. H. Willis, "*Predicting changes in the plan shape of beaches*". Proceedings of the 13th International Conference on Coastal Engineering, 1973, ASCE.

[3] H. Hanson, and N. C. Kraus, "*Genesis: generalized model for simulating shoreline change*". Technical Report CERC-89-19, Report 2 of a Series, Workbook and User's Manual. US Army Corps of Engineers, Waterways Experiment Station, Vicksburg, MS, 1989, USA.

[4] M. A. Dabees, and J. W. Kamphuis, "*Oneline, a numerical model for shoreline change*". Proceedings 27th International Conference on Coastal Engineering, ASCE, Copenhagen, 1998. pp. 2668-2681.

[5] I. Şafak, "*Numerical modeling of wind wave induced longshore sediment transport*". M.Sc. Thesis, METU, Ankara, Turkey, 2006.

[6] S. S. Artagan, "*A one line numerical model for shoreline evolution under the interaction of wind waves and offshore breakwaters*". M.Sc. Thesis, METU, Ankara.

[7] C. Baykal, "*Numerical modeling of wave diffraction in one-dimensional shoreline change model*". M.Sc. Thesis, METU, Ankara, Turkey, 2006.

[8] M. Esen, "*An implicit one-line numerical model on longshore sediment transport*". M.Sc. Thesis, METU, Ankara, Turkey, 2006.

[9] A. M. Elghandour, "*Efficient Modelling of coastal evolution. Development, verification and validation of ShorelineS model*". Delft: IHE Delft Insitute for Water Education, 2018.

[10] A. Robinet, B. Castelle, D. Idier, M. D. Harley, and K. D. Splinter, "Controls of local geology and cross-shore/longshore processes on embayed beach shoreline variability". *Marine Geology* vol. 422, 106118, Apr 2020.

[11] L. X. Hoan, "*Long-term simulation of coastal evolution*". Ph.D. Thesis, Lund, Sweden, 2010.

[12] H. Mase, "Multidirectional random wave transformation model based on energy balance equation," *Coastal Engineering Journal,* vol. 43, pp. 317-337, May 2001.

[13] G. A. Smith, "*Wave induced sediment mobility modelling: bedforms, sediment suspension and sediment transport*". Ph.D. Thesis, Swinburne University, 2012.

[14] N. Booij, R. sC. Ris, and L. H. Holthuijsen, "A third-generation wave model for coastal regions: 1. model description and validation". *Journal of Geophysical Research: Oceans,* vol. 104, pp. 7649-7666, Apr 1999.

[15] S. E. Kristensen, N. Drønen, R. Deigaard, and J. Fredsoe, "Hybrid morphological modelling of shoreline response to a detached breakwater". *Coastal Engineering,* vol. 71, pp. 13-27, Jan 2013.

[16] DHI, Danish Hydraulic Institute. "*MIKE 21/3 Coupled Model FM. Technical Documentation*". Shoreline Morphology Module, Lyngby, Denmark, 2005.

[17] V. T. Dang, "Development of a mathematical n-line model for simulation of beach *changes*". Ph.D Thesis. University of New South Wales, 2006.

[18] B. A. Ebersole, M. A. Cialone, and M. D. Prater, "*Regional coastal processes numerical modeling system: Report 1: RCPWAVE - a linear wave propagation model for engineering use*", Technical Report CERC 86-4. US Army Corps of Engineers, CERC. Vicksburg, Miss., 1986.

[19] H. Hanson, M. Larson, N. C. Kraus, and M. Capobianco, "*Modeling of seasonal variations by cross-shore transport using one-line compatible methods*", Proceedings, Coastal Dynamics '97, ASCE, pp. 893-902, 1997.

[20] H. Hanson, and M. Larson, "*Seasonal shoreline variations by cross-shore transport in a one-line model under random waves*". Proceedings of 26th International Coastal Engineering Conference, ASCE, pp. 2682-2695, 1998.

[21] M. Larson, N. C. Kraus, and H. Hanson, "*Decoupled numerical model of three-dimensional beach range*". Proceedings 22nd Coastal Engineering Conference, ASCE, pp. 2173-2185, 1990.

[22] H. Hanson, and M. Larson, "*Simulating coastal evolution using a new type of N-line model*". Proceedings 27th Coastal Engineering Conference ASCE, pp. 2808-2821, 2000.

[23] M. A. Dabees, and J. W. Kamphuis, "*NLINE: efficient modeling of 3-D beach change*". Proceedings 27th Coastal Engineering Conference ASCE, pp. 2700-2713, 2000.

[24] T. Shimizu, T. Kumagai, and A. Watanabe, "*Improved 3-D beach evolution model coupled with the shoreline model (3D-shore)*". Proceedings 25th Coastal Engineering Conference ASCE, pp. 2843-2856, 1996.

[25] N. van den Berg, A. Falqués, and F. Ribas, "Long-term evolution of nourished beaches under high angle wave conditions". *Journal of Marine Systems,* vol. 88, pp. 102-112, Oct 2011.

[26] A. Robinet, D. Idier, B. Castelle, and V. Marieu, "A reduced-complexity shoreline change model combining longshore and cross-shore processes: the LX-Shore model". *Environmental Modelling & Software,* vol. 109, pp. 1-16, Nov 2018.

[27] H. Hanson, M. Larson, and N. C. Kraus, "A new approach to represent tidal currents and bathymétrie features in the one-line model concept," Proceedings Coastal Dynamics '01, ASCE, pp.172-181, 2001.

[28] M. Larson, N. C. Kraus, and H. Hanson, "*Simulation of regional longshore sediment transport and coastal evolution - the 'Cascade' model*". Proceedings of 28th Coastal Engineering Conference, World Scientific Press, Singapore, pp. 2612-2624, 2002.

[29] M. Larson, N. C. Kraus, and K. J. Connell, "*Cascade version 1: Theory and model formulation*," ERDC TNSWWRP-06-7. Vicksburg, Mississippi: U.S. Army Engineer Research and Development Center, 2006.

[30] K. Kaergaard, and J. Fredsoe, "*A numerical shoreline model for shorelines with large curvature*". Coastal Engineering, vol. 74, pp. 19-32, Apr 2013.

[31] A. Militello, C. W. Reed, A. K. Zundel, and N. C. Kraus, "*Two-dimensional depth-averaged circulation model M2D: Version 2.0, Report 1: Documentation and user's guide*," ERDC/CHL TR-04-02, U.S. Army Engineer Research and Development Center, Vicksburg, MS, 2004.

[32] A. M. Buttolph, et al. "*Two-dimensional depth-averaged circulation model CMS-M2D: Version 3.0, report 2*". Sediment Transport and Morphology Change. Technical Report ERDC/CHL TR-06-9, Coastal and Hydraulics Laboratory, US Army Engineer Research and Development Center, Vicksburg, MS, 2006.

[33] N. Bruneau, P. Bonneton, R. Pedreros, F. Dumas, and D. Idier, "A new morphodynamic modelling platform: application to characteristic sandy systems of the aquitanian coast, France". *Journal of Coastal Research,* vol. 50, pp. 932-936, 2007.

[34] D. Roelvink, A. Reniers, A. van Dongeren, J. van Thiel de Vries, R. McCall, and J. Lescinski, "Modelling storm impacts on beaches, dunes and barrier islands". *Coastal Engineering,* vol. 56, pp. 1133-1152, Nov-Dec 2009.

[35] C. Baykal, A. Ergin, and I. Güler, "Two-dimensional depth-averaged beach evolution modeling: case study of the Kizilirmak River Mouth, Turkey". *Journal of Waterway Port Coastal and Ocean Engineering,* vol. 140, 2014.

[36] D. Roelvink, B. Huisman, A. Elghandour, M. Ghonim, and J. Reyns, "Efficient modeling of complex sandy coastal evolution at monthly to century time scales". *Frontiers in Marine Science,* 7, 2020.

[37] M. B. Gravens and P. Wang, "*Data report: Laboratory testing of longshore sand transport by waves and currents; morphology change behind headland structures*," Technical Report, ERDC/CHL TR-07-8, Coastal and Hydraulics Laboratory, US Army Engineer Research and Development Center, Vicksburg, MS, 2007.

[38] C. Baykal, "*Two-Dimensional Depth-Averaged Beach Evolution Modelling*," Ph.D. Thesis, METU, Ankara, Turkey, 2012.

[39] P. D. Komar, "Beach Processes and Sedimentation," 2nd Edition. Prentice Hall, Englewood Cliffs, N.J., 1998.

[40] C. Baykal, "Development of a numerical 2-dimensional beach evolution model". *Turkish Journal of Earth Sciences,* vol. 23, pp. 215-231, 2014.

[41] T. T. Janssen, and J. A. Battjes, "A note on wave energy dissipation over steep beaches". *Coastal Engineering,* vol. 54, pp. 711-716, Sep 2007.

[42] H. Ozasa, and A. H. Brampton, "Mathematical modelling of beaches backed by seawalls". *Coastal Engineering,* vol. 4, pp. 47-63, 1980-1981.

[43] R. B. Nairn, "*Prediction of cross-shore sediment transport and beach profile evolution*". Ph.D Thesis, Imperial College, London, 1990.

[44] J. A. Battjes, and H. W. Groenendijk, "Wave height distributions on shallow foreshores". *Coastal Engineering,* vol. 40, pp. 161-182, Jun 2000.

[45] R. J. Hallermeier, "*Uses for a calculated limit depth to beach erosion*". Proceedings 16th International Conference on Coastal Engineering ASCE, New York, pp. 1493-1512, 1978.

[46] J. Arriaga, J. Rutten, F. Ribas, A. Falqués, and G. Ruessink, "Modeling the long-term diffusion and feeding capability of a mega-nourishment". *Coastal Engineering,* vol. 121, pp. 1-13, Mar 2017.

[47] Y. Goda, "Wave setup and longshore currents induced by directional spectral waves: prediction formulas based on numerical computation results". *Coastal Engineering Journal*, vol. 50, pp. 397-440, 2008.

[48] G. W. Brier, "Verification of forecasts expressed in terms of probability". *Monthly Weather Review*, vol. 78, pp. 1-3, Jan 1950.

[49] L. C. van Rijn, D. J. R. Walstra, B. Grasmeijer, J. Sutherland, S. Pan, and J. P. Sierra, "The predictability of cross-shore bed evolution of sandy beaches at the time scale of storms and seasons using process-based profile models". *Coastal Engineering,* vol. 47, pp. 295-327, Jan 2003.

[50] P. T. Nam, M. Larson, H. Hanson, and L. X. Hoan, "A numerical model of nearshore waves, currents, and sediment transport". *Coastal Engineering,* vol. 56, pp. 1084-1096, Nov-Dec 2009.

ORIGINAL RESEARCH (AR) DOI: 10.4274/jems.2024.81567

Journal of ETA Maritime Science 2024;12(3):253-262

Formal Safety Assessment of the Connection of the Sunda Strait and Java Sea Through the Implementation of IMO Routeing Measures

Taufik Fajar Nugroho, Ketut Buda Artana, Anak Agung Bagus Dinariyana, Zayyan Fakhri Suwardana, Febro Helios Javanica

Institut Teknologi Sepuluh Nopember, Department of Marine Engineering, Surabaya, Indonesia

Abstract

Safety management of maritime traffic is crucial for archipelagic states such as Indonesia, especially in areas like the connection between the Sunda Strait and the Java Sea. This study proposes a traffic lane design using the IMO routeing measures, employing the Formal Safety Assessment scientific method. The study recommends implementing Traffic Separation Schemes (TSS), precautionary areas with a recommended counterclockwise route, and inshore traffic zones. Results indicate that TSS is more effective in reducing collision frequency compared with two-way routes, with a counterclockwise flow further mitigating crossing situations. The proposed measures, particularly Risk Control Option 3, show a 54% reduction in collision frequency compared with the existing conditions. However, despite improvements, collision frequencies remain intolerable, necessitating additional strategies. The total collision frequency for all proposed measures is deemed unacceptable, requiring further methods to enhance safety. The economic evaluation shows potential savings, with estimated values for Gross Cost of Averting Fatality and Net Cost of Averting Fatality at US$ 3.21 million and US$ 2.9 million, respectively. Thus, while the proposed measures demonstrate some efficacy, additional strategies are imperative to adequately address collision risks in the designated area.

Keywords: IWRAP, maritime traffic, collision frequency, routeing measures

1. Introduction

Safety is a certain priority for all maritime operations, and it certainly has an effect on human lives, the environment, or the continuity of the operation. The concept of maintaining safety aspects aligns with the intention to avert a certain risk. In the case of maritime traffic, any effort to prevent risks should be addressed to all maritime operations related to vessels' movement from one significant place to another in a region that involves other vessels. However, the rights for ships to pass through a region of waters should essentially not be limited until there is a concern of accidents that may occur. Therefore, the idea of establishing maritime traffic lanes in some regions has always been influenced by the concern of safety in the area, and it is intended to prevent unwanted threats to human lives, the environment, or the vessels' operation. The necessity of maintaining the safety of maritime traffic goes along with the efforts of managing the traffic. Consider that managing maritime traffic is a certain way to keep the continuity of the traffic out of any obstruction. An example of managing traffic in Indonesia is through the enforcement of Indonesia's Archipelagic Sea Lanes (IASL), which, originally before its establishment, are naturally diverse and uncontrollable. The reason is that the waters have a strategic position to have many accesses for international shipping to pass through. Therefore, IASL was established through the United Nations Convention on the Law of the Sea in 1982 as procedures for international shipping to only pass through three separated main routes, in which each route has directions in passing among archipelago according to the situation in each area. However, IASL is only able to manage the entrance and exit that ships are allowed to access in and out of Indonesian waters, while the concern of an accident occurring is not in the context of its establishment. Therefore, maritime traffic lane establishment is the solution for preventing accidents. Accident cases that should be avoided in maintaining

Address for Correspondence: Anak Agung Bagus Dinariyana, Institut Teknologi Sepuluh Nopember, Department of Marine Engineering, Surabaya, Indonesia
E-mail: kojex@its.ac.id
ORCID iD: orcid.org/0000-0002-6624-2577

Received: 05.03.2024
Last Revision Received: 14.05.2024
Accepted: 22.05.2024

To cite this article: T. F. Nugroho, K. B. Artana, A. A. B. Dinariyana, Z. F. Suwardana, and F. H. Javanica, "Formal Safety Assessment of the Connection of the Sunda Strait and Java Sea Through the Implementation of IMO Routeing Measures." *Journal of ETA Maritime Science*, vol. 12(3), pp. 253-262, 2024.

the continuity of maritime traffic include grounding and collision. To prevent grounding, it can be done by managing the direction of traffic flow that intentionally directs the passing ships out of shallow areas. To prevent collisions, efforts are quite varying, such as managing the traffic direction, reporting, and monitoring system through Vessel Traffic Service (VTS), or the separation of opposing traffic. Because collisions can be defined as when more than one moving vessel collides with each other in significant ways. The connection between the Sunda Strait and the Java Sea became the main focus of this study because of the location of IASL-1, where specifically IASL-1 passes through the Sunda Strait from the Java Sea toward the Indian Ocean on the south of Indonesia. The establishment of IASL is certainly to accommodate passages that are considered to have higher traffic density to allow international vessels to pass legally. Then, the Traffic Separation Scheme (TSS) of the Sunda Strait is established to prevent collisions in the area. The consideration for its establishment apart from the high traffic density is the existing traffic flow in the area. Where other than the traffic of vessels that are going south from Java Sea toward Indian Ocean and the other way around, there is also traffic that crosses the strait from the ports and terminals around Suralaya Water toward the Island of Sumatra. The most frequent vessel to cross the strait is the traffic of crossing ferries from the Port of Merak bound to the Port of Bakauheni and the other way around. Because of this crossing situation of different traffic flow, which at least has five crossing points in the area [1], the TSS of the Sunda Strait was established to prevent collisions in the crossing traffic.

There has been a case of collision that occurred in the area before the TSS of the Sunda Strait was established. In 2012, a collision between MV Bahuga Jaya and MT Norgas Cathinka in the Sunda Strait occurred on September 26th. At 03.05 local time, MV Bahuga Jaya was on its route from Port of Merak bounded to Port of Bakauheni with a speed of 10 knots, which usually takes 2 h. While MT Norgas Cathinka was approaching the Sunda Strait from the southern side heading toward the northeast direction of its position with a speed of 12 knots. At 04.44 local time, the collision occurred where the port bow of MT Norgas Cathinka collided with MV Bahuga Jaya's starboard side. With the TSS of the Sunda Strait being established, the effectiveness of maritime traffic lane was proven with reduced frequency of ship-to-ship collision. However, this study took a further step toward this concern through the evaluation of maritime traffic lane design that might be needed in the northern counterpart of the Sunda Strait, considering that there is no maritime traffic lane established in the area despite its high traffic density [2].

Despite the various kinds of efforts that can be implemented to prevent the risk, it is certain that each solution has its own concern, which will need relevant considerations. This study focuses on the effort in preventing ship-to-ship collision through the establishment of maritime traffic lanes by precisely considering the right designs based on the regulations for IMO Routeing Measures, which then compare the reduced frequency of collision and the economic benefits obtained by each design. Even though the real cases show that the efforts would only be effective if they are implemented altogether as a combination, such as the implementation of VTS along with maritime traffic lanes, which proves that implementing only one of them may not be effective.

2. Methods

A maritime traffic lane is an example of making and establishing a regulation that should be obeyed by the targeted parties, specifically because the purpose of a maritime traffic lane is to manage traffic through procedures of navigation. The consideration to establish maritime traffic lanes is also guided by the rules of IMO on Ships' Routeing that are already standardized and certainly align with other rules of IMO. Therefore, this study requires a method that is acceptable for evaluating a regulation with its existing situation and comparing it to possible development of the regulation. This necessity aligns with the purpose of Formal Safety Assessment (FSA) [3]. By conducting FSA for this study, this research could thoroughly determine the risk, provide possible solutions, calculate detailed cost requirements, and obtain recommendations for decision makers.

The study is carried out in sequence as shown in Figure 1. The flowchart is a modified version of the original flowchart for FSA as determined by the IMO [3]. However, its modification is intended to achieve a more suitable method that corresponds to the aim of this study. Since FSA is designed to evaluate safety and risk concerns, important criteria such as hazard, frequency, and consequences of accidents are the assessed parameters. In this case, the frequency of collision was designed to be the prioritized assessment to determine the number of collisions per year or the interval between collisions to occur.

Basically, finding the frequency of collision in an area can be carried out through a calculation method or using simulation software. This study used software called the International Association of Marine Aids to Navigation and Lighthouse Authorities (IALA) Waterway Risk Assessment Program (IWRAP) as a simulation tool to obtain the frequency of collisions in the area. This software has been endorsed by the IALA to evaluate the risk of ship collision prior to implementing a new maritime traffic lane. The reason is that

the tool is considered to be the most advanced methodology with its ability to assess the frequency based on the existing traffic records using the recorded Automatic Identification System (AIS) data.

3. Results and Analysis

3.1. Hazard Identification (FSA Step 1)

As part of identifying the hazard, this research collected some reports from The National Transportation Safety Committee, the National Shipping Court, and local news that reviewed some incidents that had occurred. It was found that from 2010 until 2023, there were nine incidents of collision that occurred in the focused area of this research. However, the nine incidents were limited to those that occurred around the Sunda Strait and extended to the area of Jakarta Bay; therefore, any collision incidents that occurred in the Java Sea but were outside of the limitation are not included in Table 1.

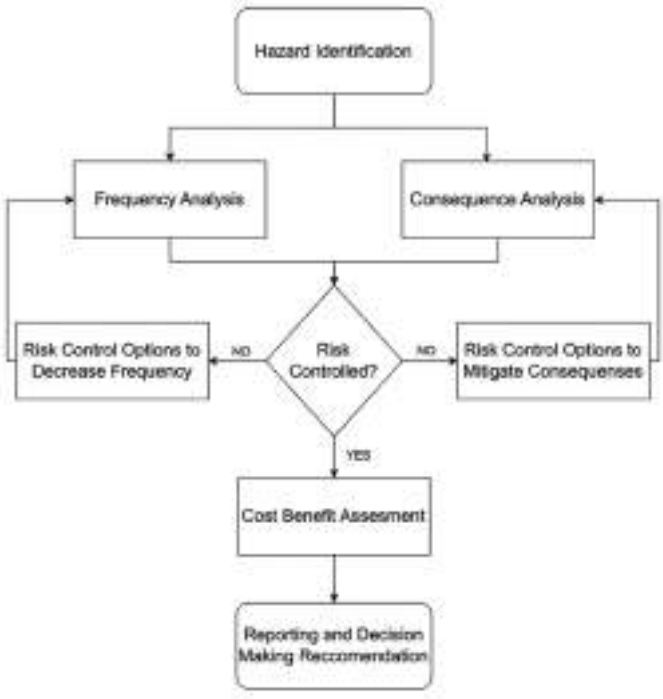

Figure 1. *Methodology for the study*

The incidents are categorized on the basis of the type of collisions, which are head-on, overtaking, and crossing collisions. The incidents are categorized on the basis of the collision scenario, as mentioned in their reports. However, three incidents are not categorized into any of the types since the reports stated them as bumping situations.

At the beginning of the study, hazard identification is important to specifically define the risk of each hazard. In this case, it is found that every type of collision scenario has a specific consideration in mitigating the risk, such as the need to separate opposing traffic to avoid a head-on collision. In this study, type of collisions are categorized before assessing the risk because each collision scenario is assessed differently when simulated in IWRAP. Some incidents that were not classified as one of them, such as bumping between ships, are neglected because the collision occurred because of extreme weather conditions and none of the ships were sailing or maneuvering during the incidents.

3.2. Risk Assessment (FSA Step 2)

After identifying the hazards, the study continued with risk assessment, which assessed the collision frequency using the IWRAP. One year interval of AIS data was collected from the VTS of Tanjung Priok, Indonesia. The data were imported in AIS RAW message format and underwent configuration for heatmap and density plot setup to assess the collision frequency and displayed accurately in the software. Specific setups were configured to limit the area of interest. The results are shown in a density plot indicating high-traffic areas. Legs are defined based on density plots of the highest traffic density at intervals of two weeks, although yearly intervals were also considered to accurately capture the overall frequency. Then, the frequency of collision is calculated on the basis of the specific traffic located in

Table 1. *Historical records of collision incidents in Sunda Strait and part of Java Sea*

No.	Date	Time	Collision Types	Waters	Weather Condition
1	19/05/2010	22:50:00	Head-on	Java Sea	Unstated
2	26/09/2012	4:44:15	Head-on	Sunda Strait	Soft Wind
3	31/05/2013	21:12:30	Head-on	Java Sea	Cloudy
4	7/4/2017	1:30:00	Crossing	Java Sea	Sunny
5	5/7/2017	18:32:00	Overtaking	Sunda Strait	Sunny
6	29/08/2017	17:10:00	Collision	Sunda Strait	Extreme Weather
7	23/6/2020	5:40:00	Collision	Sunda Strait	Harsh Current
8	22/4/2019	16:31:28	Overtaking	Sunda Strait	Cloudy, Soft Wind and Current
9	1/4/2023	6:55:00	Collision	Sunda Strait	Harsh Current

the legs and waypoints, as shown in Figure 2. The 2-week interval with the highest traffic indicated that the highest frequency is on Leg 5 and Waypoint 2. This study aims to compare the existing risk on Leg 5 and Waypoint 2 and the risk when several adjustments are made on both areas of interest. However, the obtained frequencies are classified on the basis of the individual risk acceptance criteria to consider the classification of risk into either tolerable, intolerable, or As Low As Reasonably Practicable. Based on the classification, the frequency on Leg 5 and Waypoint 2 are already classified as intolerable risk in which risk mitigation is needed to reduce the frequency.

3.3. Risk Control Option (FSA Step 3)

Risk Control Option (RCO) is required in an FSA study to define what suitable risk mitigation should be taken to reduce the risk. In this study, risk mitigation are arranged in the form of IMO routeing measure implementation [4]. The implementation of routeing measures as determined by the IMO is considered based on the specific hazard. Therefore, there are certain conditions that have to be met as a requirement to proposed routeing measure implementation. As an example, there must be an international seagoing vessel passing the area to implement TSS.

The result of the risk assessment indicates that the highest values are located in Leg 5 and Waypoint 2, which are considered to be intolerable risks and require further mitigation to reduce the frequency. Specifically, the assessment identified that Leg 5 has the highest frequency for head-on and overtaking collisions, while Waypoint 2 has the highest frequency for crossing collisions, and all of them are classified as intolerable. As for selecting the right routeing measures to mitigate the risk, the consideration was based on the requirement of each ships's routeing as regulated in [5] Ministerial Regulation 129 Year 2016 of the Indonesian Directorat General of Maritime Affairs.

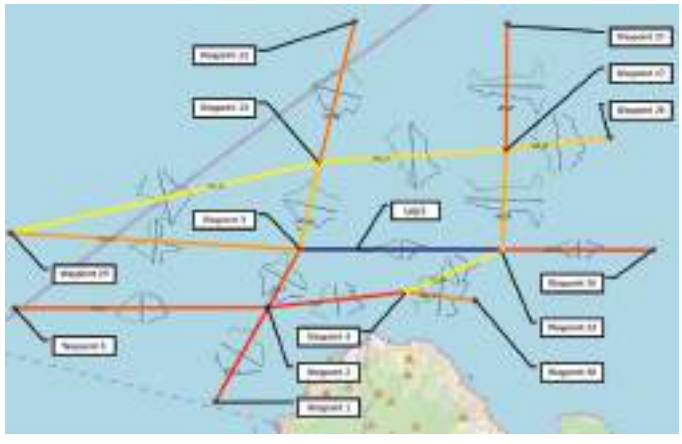

Figure 2. *Relative frequency analysis on each leg and waypoint plotting in IWRAP*

IWRAP: IALA Waterway Risk Assessment Program

Table 2 shows the proposed routeing measures as the chosen suitable routeing measures in addressing the identified hazard. As an example, in mitigating head-on collision at Leg 5, there are two possible routeing measures to implement: Traffic Separation by Separation Zone and Line or Two-Way Routes with One-Way Sections. In the case of mitigating the risk of crossing collision at Waypoint 2, the possible routeing measures to implement are either roundabouts or precautionary areas with recommended traffic flow. Then, several RCOs are determined as the combination of the proposed routeing measures in the design to thoroughly mitigate all the risks. A similar case to which this study also reflected to similar routeing measures selection and design is the implementation in the Sunk Area and Northern Approach to the Thames Estuary, as shown in Figure 3.

In most cases, in establishing any regulations or procedures, there must be an evaluation of the regulation's relevance to its application. Therefore, this study also evaluated its implementation assuming that the implementation of routeing measures will be established for 25 years of application. The most important consideration to this evaluation is regarding the traffic volume in the area that will certainly grow. The assumption for this consideration is based on the growth of traffic volume in the area over the last decade, and the growth rate is used to forecast the growing traffic for 25 years in the future. Therefore, the proposed RCOs are differentiated based on the implementation for the present and the forecasted traffic volume, in which the traffic in 2022 has an hourly traffic of 1.65 ships/hour and the escalated traffic on the same location in 2047 has an hourly traffic of 6.79 ships/hour.

Table 2. *Proposed routeing measures based on identified hazard*

Hazard Identification	Frequency	Proposed Routeing Measures
Head-on collision at Leg 5	4.69E-04	• Traffic separation by separation zone and line
		• Two-way routes (with one-way sections)
Overtaking collision at Leg 5	1.91E-04	• Traffic separation by separation zone and line
Crossing collision at waypoint 2	2.68E-04	• Roundabouts
		• Precautionary area with recommended traffic flow

The consideration to propose TSS and two-way routes is to accommodate the opposing traffic in Leg 5, which is theoretically able to minimize the risk of both head-on and overtaking collisions, and the consideration to implement roundabouts is to minimize the crossing situation in Waypoint 2. As for overtaking collision, efforts can be made by adjusting the width of a fairway, where a greater width of a fairway will provide better space for an overtaking scenario and consequently prevent collision. For inshore traffic zone, this measure is considered in this study as a recommendation from the Navigation District of Tanjung Priok. Inshore traffic zones might be needed due to the frequent port activity in Suralaya Waters, even though no assessment using IWRAP was conducted for evaluating inshore traffic zones.

An additional step of the design process is required in this study, although it is not included as a step of FSA. The design process is conducted after the RCOs have been determined. Each RCO is a combination of routeing measures in the design of a maritime traffic lane. With the planned designs, the next consideration is the dimension of the lane, which certainly could affect the frequency of collision. The length of a fairway is adjusted to the length of conventional routes, while the width of the fairway is determined based on the existing width of the passage, ship dimensions, and traffic volume in the area [6]. In this case, the existing situation in the area of interest is located in an open sea with few natural obstructions. However, the width of the fairway essentially determines the standard deviation of the traffic distribution [7].

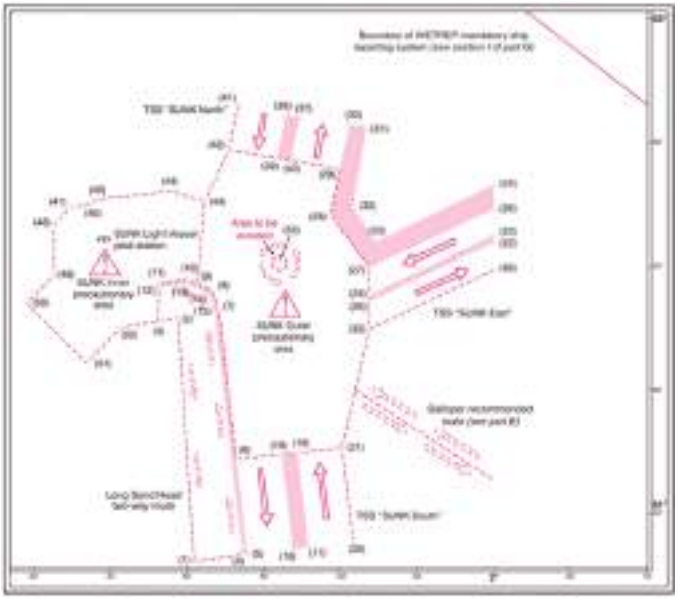

Figure 3. *Routeing measures implementation in the sunk area and northern approach to thames estuary*

Source: IMO Ships Routeing, 2010

The decision to determine the width of a fairway based on the existing traffic volume refers to the guidelines of the Permanent International Association of Navigation Congresses and a study from the Maritime Research Institute Netherlands. The study recommends that the minimum width of a fairway is 4 L for areas with the number of annual trips less than 4400, 6 L for areas with the number of annual trips between 4400 and 18000, and 8 L for annual trips above 18000, where L is 98.5% of the length overall of the largest vessel passing through.

Because the length of the planned fairways is adjusted to the length of the conventional routes, the required fairways are assumed to have the same length as the defined legs, as shown in Figure 2. Then, they are adjusted to prevent overlapping of any obstructions nearby, other fairways, and adjusted to the safety and maneuver margin [8]. An example for Leg 1 in Figure 2, when a fairway is designed to have the same length as the leg, it will overlap the route of crossing the ferry Merak-Babakauheni. Therefore, the traffic lane on the leg should be shortened to the north.

Roundabouts that need to reduce the frequency of crossing collisions at Waypoint 2 require a vast area to accommodate ships for maneuvering, and this study arranges the location of the center of the roundabout to be exactly at Waypoint 2. However, as the condition led to overlapping between the roundabout and the nearby anchorage areas in Suralaya Waters, the location is shifted a little bit toward the northwest for 60° from the North for 2 km. The final designs are four different traffic lane designs with various dimension and routeing measures selection. An example of RCO 3 is shown in Figure 4, which shows the location of the proposed RCO, TSS Sunda Strait, and nearby anchorage areas in Suralaya Waters.

In duplicating the design of RCOs and the forecasted traffic volume for simulation, additional configurations are required in IWRAP (Table 3). The intention is to modify

Table 3. *List of RCO*

RCO	Routeing Measures	Traffic Analysis
1	Roundabouts, two-way routes, and inshore traffic zone	RCO for traffic analysis in 2022
2	Roundabouts, traffic separation scheme, and inshore traffic zone	RCO for traffic analysis in 2047
3	Roundabouts, two-way routes, and inshore traffic zone	RCO for traffic analysis in 2022
4	Roundabouts, traffic separation scheme, and inshore traffic zone	RCO for traffic analysis in 2047

the existing traffic to adjust the natural characteristics with the mannered version as the impact of the establishment of routeing measures. The modification in IWRAP is by scaling the traffic volume specifically on each leg depending on the growth of the traffic, the distance between opposing routes, and the traffic distribution. Assuming the traffic is in a form of normal distribution, the distribution has a standard deviation of 40% of the width of a fairway, which is an approach as explained in the module of IWRAP theory.

The results from IWRAP are the frequency of each type of collision obtained in four different scenarios with each value of frequency and in total, as shown in Table 4, and the value of reduction rate, as shown in Table 5. Even though the only applicable one is RCO 3 as it is the only one able to reduce the frequency of collision, none of them did not show any potential to be implemented as all their frequencies are still classified as intolerable.

3.4. Cost Benefit Analysis (FSA Step 4)

Although all RCOs have been assessed using IWRAP, the selection of RCO was not only based on the effectivity of the RCO in reducing the risk but also should be seen from an economical perspective, in which this FSA study considered the selection of RCO through cost-benefit assessment. This step assessed the cost per ship for the implementation of each RCO, the reduced risk, and the expense cost from a fatality,

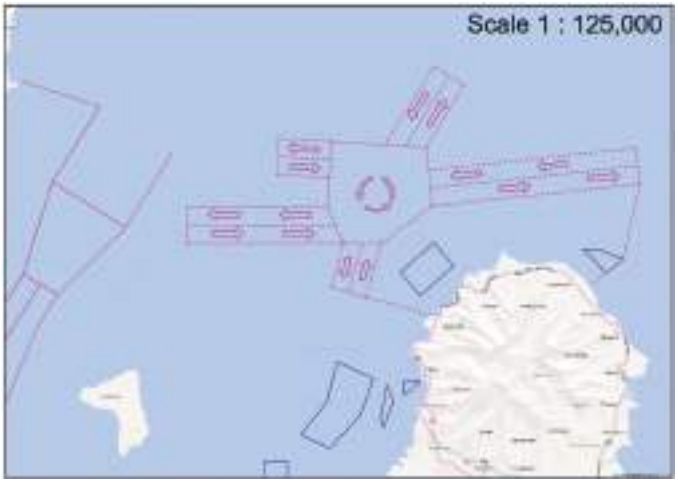

Figure 4. *Design of traffic lane proposed as RCO 3*

RCO: Risk Control Option

which is assumed to be averted through the implementation of the RCOs. The parameters used to select the RCO based on the three components are the value of Net Cost of Averting Fatality (NCAF) and Gross Cost of Averting Fatality (GCAF), which consist of the three assessed factors. The formulas to calculate NCAF and GCAF are, respectively, shown below:

$$GCAF = \frac{\Delta C}{\Delta R} \quad (1)$$

where ΔC is the cost per ship of the RCO under consideration while ΔR stand for risk reduction per ship, implied by RCO.

$$NCAF = \frac{(\Delta C - \Delta B)}{\Delta R} \quad (2)$$

Where ΔB is an economic benefit per ship resulting from the implementation of RCO.

All three components should be determined by the objective of the research itself. In this study, ΔC was defined as the total survey cost on the area of research with the cost required for additional fuel due to the extended distance of the ship accessing the routes, ΔB was the cost of averted fatality, which in this study is assumed for the case of an oil spill occurring in the area due to ship collision. The value of ΔR is the difference between the frequency of collision on the existing assessment and the frequency assessed with each RCO implementation.

The calculation of ΔC was based on survey cost which estimated about USD. 133,422 by the District Navigation of Tanjung Priok, adding up to the additional operating cost of the ship due to the additional voyage duration.

The calculation of the additional operating cost was based on the length of the route, which led to the increase in voyage duration, assuming that the ship was traveling at the same average speed. In calculating the extended distance of the ships to pass through, a list of dominant routes that mostly pass by are determined based on the existing traffic. Where 11 routes are defined as in Figure 5, and Table 6 shows the difference between each RCO. It selected the most frequent trajectories for vessels to pass the area, and the total distance

Table 4. *Frequency of collision of all RCOs*

	RCO 1	RCO 2	RCO 3	RCO 4
Overtaking	8,91E-04	1,18E-02	2,80E-04	3,94E-03
Head-on	8,73E-04	1,24E-02	4,36E-04	1,08E-02
Crossing	8,60E-04	1,45E-02	4,39E-04	7,22E-03
Total	2,59E-03	3,87E-02	1,15E-03	2,20E-02

of each trajectory is represented by the summation of several connecting legs located nearest to the actual trajectories of the ships.

The value of ΔB is based on the assumption that the amount of oil spill was from an oil product tanker with the characteristics shown in Table 7, where the amount of oil spilled is assumed to be the volume of an oil cargo tank located in the midship section of the vessel. The estimation method used in this study is based on an approach conducted by [9] because most cargo tanks located in the midship section have more volume than the others. Therefore, the approach used to calculate the cargo tank volume is based on the formula as follows.

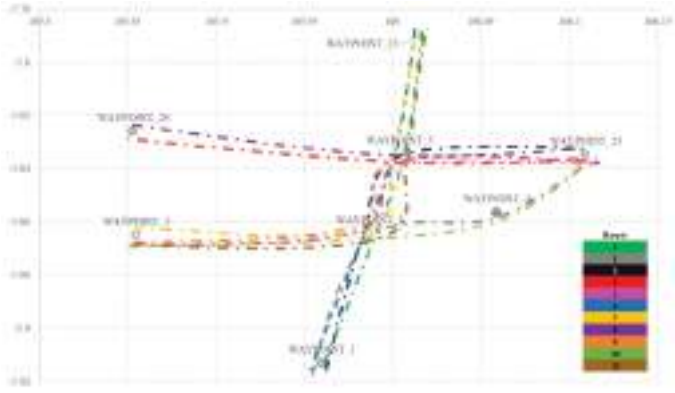

Figure 5. *Dominant routes of ships passing through Suralaya Waters*

$$B_T = \frac{B - 2w}{m} \quad (3)$$

where B_T is the breadth of cargo tank compartment (m), B is the breadth of vessel (m), w is the double hull width (m), and m is the number of tanks in the transverse direction.

$$D_T = D - h \quad (4)$$

where D_T is the draught of the cargo tank compartment (m), D is the draught of the vessel (m), and h is the height of the double bottom (m).

The double hull width and the height of the double bottom are calculated using the rules determined by Det Norske Veritas (DNV) in the DNV Rules for Classification Part 5 Chapter 5 that specifically regulate the requirements for tankers. The formula is specifically targeted to ships of 600 DWT to 5000 DWT and ships above 5000 DWT. The selected vessel is classified as ships of above 5000 DWT, which means the formula is applicable for the sample, and the estimation method is for general conventional design of monohull tankers with double skin. The following are the

Table 5. *Reduction rate of all RCOs*

	RCO 1	RCO 2	RCO 3	RCO 4
Overtaking	-78%	-2259%	44%	-689%
Head-on	37%	-832%	67%	-711%
Crossing	-43%	-2312%	27%	-1105%
Total	-6%	-1489%	53%	-804%

Table 6. *Extended distance due to RCO implementation*

Routes	Existing 2022			RCO 1	RCO 2	RCO 3	RCO 4
	Course (waypoint to waypoint)	Course (leg to leg)	Route distance (m)	Route distance (m)	Route distance (m)	Route distance (m)	Route distance (m)
1	1,2,5,13	1,4,10	15069	17058	17058	16896	17065
2	1,2,4,23	1,3,31	20223	21049	21049	20658	20374
3	1,2,5,23	1,4,5	21598	21049	21049	20658	20374
4	23,5,29	5,30	28378	29322	29322	29473	29854
5	23,5,2,3	5,4,2	30059	32780	32780	32667	33518
6	13,5,2,1	10,4,1	15069	17667	17667	17971	17894
7	13,5,2,3	10,4,2	23530	23753	23753	23301	23548
8	29,5,23	30,5	28378	33049	33049	31818	31921
9	3,2,5,23	2,4,5	30059	29327	29327	28986	28855
10	3,2,4,23	2,3,31	28684	29327	29327	28986	28855
11	3,2,5,13	2,4,10	23530	25336	25336	25224	25546

equations used for calculating double hull width and height, respectively.

$w = 0.5 + \frac{DW}{20000}$ or $w = 2.0$, whichever is lesser, but not less than 1.0 m (5)

$h = \frac{B}{15}$ or $h = 2.0$, whichever is lesser, but not less than 1.0 m (6)

The length of the cargo tank compartment L_T was estimated using the following equation (7).

$$L_T = \frac{L - L_A - L_F}{n} \quad (7)$$

The values of LA and LF are based on the vessel's DWT and length, as shown in Table 8.

After all the above components have been calculated, which indicate the dimensions of a cargo tank compartment, the formula below can be applied to calculate the specific volume for the cargo tank located in the midship section.

$$V_i = C_i \times L_T \times B_T \times D_T \quad (8)$$

where, V_i is volume of a cargo tank (m^3) and C_i is the volumetric coefficient (equal to midship coefficient for cargo tank located at midship section).

As the volume of the cargo tank has been calculated, the estimation of the oil spill response cost per unit (US$/ton), C_u, is based on the weight of the spilled oil from the calculated volume of the cargo tank. Where the weight is obtained by assuming the density of the oil spilt to be 0.86 ton/m^3, and the response cost is basically the estimated cleanup cost (US$), C multiplied by the cost modifiers and the amount of oil spilt, as discussed in a previous study [10]. The estimated cleanup cost, C_e (US$), refers to a study [11] where the estimation is classified based on the amount of oil spilt, the type of oil, and the location of the oil spill scenario. Then, the total cleanup cost is obtained by linear regression of the classification.

The cleanup cost was modified by considering cost factors [12] such as oil type, spill size, location type, primary method cleanup, and shoreline oiling modifiers to obtain the response cost per unit. Therefore, the total response costs are obtained by multiplying the response cost per unit with the amount of oil spilt. The estimation of the total response cost is considered the benefit due to the averted fatality, which would cost when an oil spill scenario occurs. The response cost per unit and the estimated total response cost are given in Equations (9) and (10).

$$C_U = C \times l \times t \times o \times m \times s \quad (9)$$

Where l is a local location, t is an oil type modifier, o is a shoreline oiling modifier, m refers to cleanup methodology, and s is the size of the oil spill.

$$C_e = C_u \times A \quad (10)$$

where A is the specified spill amount for scenario (ton).

Then, the estimated cost of ΔB is divided by the number of trips passing through the area to obtain the cost for each ship. The resulting ΔB for RCOs analyzed in 2024 uses the same value, while for RCO 2 and RCO 4, the result is escalated as an impact of inflation through the years, and the same adjustment is also taken for ΔC.

The ΔR is only based on the frequency of collision assessed by using IWRAP, as discussed previously. The results of ΔC, ΔB, and ΔR to calculate the value of NCAF and GCAF are shown in Table 9. The main consideration in selecting the RCOs through cost-benefit assessment is based on the comparison of NCAF and GCAF between each RCO. In most cases, the selected RCO is simply the RCO with the lowest GCAF and highest ΔR. However, any RCO would only be accepted when both NCAF and GCAF are below

Table 7. *Ship characteristics of the selected vessel*

Ship data and characteristics		
Name : Rosa Dini	Loa : 182.55 m	Δ : 45118.137 ton
IMO : 9240718	LPP : 175 m	∇ : 44017.68 m^3
MMSI : 525119081	Beam : 27.74 m	Am : 304.734 m^2
DNV id : 9240718	Breadth : 27.34 m	Cb : 0.789
Flag : Indonesia	Depth : 16.7 m	Cp : 0.794
Type : Products Tanker	Draught : 11.216 m	Cm : 0.994
GT (ITC 69) : 23217	Height : 46 m	Cwp : 0.867
NT (ITC 69) : 11217	Cargo Tanks : 14	Δ : 45118.137 ton
DWT : 37155	TPC : 46.1	∇ : 44017.68 m^3

Table 8. L_A *and* L_F *of tankers based on DWT*

	Below 35k DWT	35k-50k DWT	50k-80k DWT	Above 80k DWT
L_A	0.24 L	0.22 L	0.21 L	0.195 L
L_F	0.06 L	0.055 L	0.055 L	0.05 L

Table 9. Summary of cost benefit assessment

RCO	ΔR	ΔC (US$ m)	ΔB (US$ m)	ΔC - ΔB (US$ m)	GCAF (US$ m)	NCAF (US$ m)
RCO 1	-0.0002	0.0100	0.0095	0.0005	(65.33)	(3.44)
RCO 2	-0.0565	0.0290	0.0029	0.0261	(0.51)	(0.46)
RCO 3	0.0013	0.0080	0.0095	(0.0015)	6.25	(1.18)
RCO 4	-0.0196	0.0254	0.0029	0.0225	(1.30)	(1.15)

US$ 3 million based on the US$ 3 million criterion, and this condition also the effect of the reduced frequency of collision where the reduced frequency of RCO 3 is considered too low and not effective enough.

3.5. Recommendation for Decision Making (FSA Step 5)

The recommendations obtained from this study conducted through FSA are addressed to the authority in the establishment of maritime traffic lanes. The result shows the inefficient effort to establish a maritime traffic lane in this specific case. This is due to the increasing traffic that will not be accommodated in the near future, thus requiring additional efforts in managing the traffic. Therefore, further evaluation that could affect the causation probability and not only from the geometric number perspectives like traffic volume, traffic direction, traffic lane width, and traffic distribution.

4. Conclusion

The traffic volume in the designated area has 14492 ship trips passing through in 2022, with the number of ships being 1928 vessels having a total collision frequency of 2.43E-03, while the frequency of head-on collisions, overtaking collisions, and crossing collisions is 1.34E-03, 4.99E-04, and 5.99E-04, respectively. The main priority in selecting routeing measures is to avoid head-on, crossing, and overtaking collisions. Both head-on and overtaking collisions can be prevented through the implementation of two-way routes or TSS, and the frequency of crossing collisions can be prevented by implementing roundabouts or precautionary areas with recommended counterclockwise traffic flow. However, routeing measures that have been assessed are not effective enough to support their implementation considering the insignificant reduction rates to prevent the risk. This study shows the limitation of reducing the risk of collision by only affecting the geometric number. Thus, future studies should discuss efforts to reduce the frequency of collision by the influence of both geometric number and causation probability for a more efficient solution.

Acknowledgment

The authors would like to sincerely thank the Vessel Traffic System of Tanjung Priok, operated by the Navigation District of Tanjung Priok, Indonesia, for their valuable contribution to this work.

Authorship Contributions

Concept design: T. F. Nugroho, K. B. Artana, A. A. B. Dinariyana, Data Collection or Processing: T. F. Nugroho, K. B. Artana, A. A. B. Dinariyana, Z. F. Suwardana, and F. H. Javanica, Analysis or Interpretation: T. F. Nugroho, K. B. Artana, A. A. B. Dinariyana, Z. F. Suwardana, and F. H. Javanica, Literature Review: T. F. Nugroho, K. B. Artana, A. A. B. Dinariyana, Z. F. Suwardana, and F. H. Javanica, Writing, Reviewing and Editing: T. F. Nugroho, K. B. Artana, A. A. B. Dinariyana, Z. F. Suwardana, and F. H. Javanica.

Funding: The authors received no financial support for the research, authorship, and/or publication of this article.

References

[1] F. I. Prastyasari, and T. Shinoda, "Ship's collision frequency assessment for introducing traffic separation scheme in Sunda Strait in Indonesia". *Navigation,* vol. 211, pp. 17-18, 2020.

[2] S. Sunaryo, A. Arif Priadi, and T. Tjahjono, "Implementation of traffic separation scheme for preventing accidents on the Sunda Strait". *International Journal of Technology,* vol. 6, pp. 990-997, 2015.

[3] International Maritime Organization. *Revised Guidelines for Formal Safety Assessment (FSA) For Use in The IMO Rule-Making Process*. MSC-MEPC.2/Circ.12/Rev.2, Apr 2018.

[4] International Maritime Organization (Ed.), Ships' Routeing (2010 ed., 10th ed). International Maritime Organization, 2010.

[5] Kementrian Perhubungan Republik Indonesia, Peraturan Menteri Perhubungan tentang Alur-Pelayaran di Laut dan Bangunan dan/atau Instalasi di Perairan. Retrieved from Permenhub No. 129

Tahun 2016 tentang Alur-Pelayaran di Laut dan Bangunan dan/atau Instalasi di Perairan [JDIH BPK RI], 2016.

[6] Y. S. Park, "Basic study on design guideline of traffic separation scheme". *Journal of Navigation and Port Research,* vol. 31, pp. 173-178, 2007.

[7] P. Friis-Hansen, *IWRAP Mk II, Basic modelling principles for prediction of collision and grounding frequencies,* (working document), Technical University of Denmark, 2008.

[8] Y. Mulyadi, T. F. Nugroho, K. Sambodho, and E. Pratiwi, "Kajian traffic separation scheme di Wilayah Perairan Teluk Bintuni". *IPTEK Journal of Proceeding Series,* 2018.

[9] F. Goerlandt, "A model for oil spill scenarios from tanker collision accidents in the Northern Baltic Sea". *50 Scientific Journals of the Maritime University of Szczecin,* vol. 122, pp. 9-20, 2017.

[10] C. A. Kontovas, and H. N. Psaraftis, "*Marine environment risk assessment: a survey on the disutility cost of oil spills*". 2nd International Symposium on Ship Operations, Management and Economics, SNAME Greek Section, Athens, September 2008.

[11] M. A. Cohen, "The costs and benefits of oil spill prevention and enforcement". *Journal of Environmental Economics and Management,* vol. 13, pp. 167-188, Jun 1986.

[12] D. S. Etkin, "*Worldwide analysis of marine oil spill cleanup cost factors*". Presented at: Arctic and Marine Oilspill Program Technical Seminar (June 2000).

DOI: 10.4274/jems.2024.03789

Journal of ETA Maritime Science 2024;12(3):263-276

In Search of a Linkage Between Personality Traits and Interpersonal Behaviour During the COVID-19 Pandemic: A Case Study on Indian Marine Engineers Using Structural Equation Modelling

Toorban Mitra

Indian Maritime University - Kolkata Campus, School of Maritime Management, Kolkata, India

Abstract

Building and maintaining social and interpersonal relationships are crucial for mental health. However, due to the unique characteristics of jobs, building and maintaining such interpersonal relationships with colleagues as well as others may not be as similar to off-shore employees like shore-based ones. On the contrary, preference towards exhibiting interpersonal relationship behaviour is another area that needs attention in the maritime sector. Such preferences may be unique while individuals pass through uncertain situations like the coronavirus disease-2019 (COVID-19) pandemic. Against the backdrop of the COVID-19 pandemic, this study investigates the linkages between personality traits and interpersonal relationship behaviours among Indian marine engineers. Data was gathered through snowball sampling from 385 marine engineers utilising the Big Five Inventory and the Fundamental Interpersonal Relationship Orientation-Behavior™ framework after necessary adaptations of these instruments. Results show that conscientiousness is linked to expressed inclusion and wanted control. Extraversion is linked with all behaviours except wanted control, while agreeableness is associated with expressed control. Neuroticism shows linkages with wanted inclusion, expressed control, and wanted control. This study fills critical research gaps by examining the missing links between personality traits and interpersonal relationships in a high-stress environment like the maritime sector and that too during the COVID-19 pandemic. These insights emphasise the need for effective communication and teamwork in high-stress maritime environments.

Keywords: Personality traits, Interpersonal relationship, COVID-19, Structural equation modelling

1. Introduction

Since the beginning of human civilisation, building relationships with others has been considered to be an important aspect of survival. There are diverse opinions towards the developing relationships among people. While some people can establish relationships with others at ease, others may struggle to do so. Cheek and Buss [1] have shown that sociability and the development of interpersonal relationships are linked to emotional wellbeing. Though the mechanisms behind it are not clear, it is generally accepted that interpersonal relationship has an impact on an individual's health [2].

Martino et al. [3] carried out a thorough review of existing literature and concluded that building and maintaining relationships with others has significant impacts on health and weight management, diabetes, cardiovascular diseases and even cancer. However, with the advent and mass penetration of the internet and smartphones, connecting with others has become far easier than in earlier days. The massive usage of social networking sites accelerated the pace of getting connected further. At the same time, social media has been found to be responsible for degrading social skills and, thereby, avoidance of face-to-face interactions [4]. Research also indicates that the use of social media impacts the interpersonal relationships of individuals [5,6]. Two studies by Humphreys and Hardeman [7] and Bhattacharjee and Begum [8] indicated that the use of mobile phones significantly impacts interpersonal communication as well as the quality thereof.

While interpersonal relationships have been adversely impacted nowadays, Sullivan [9] viewed "personality",

Address for Correspondence: Toorban Mitra, Indian Maritime University - Kolkata Campus, School of Maritime Management, Kolkata, India
E-mail: tmitra@imu.ac.in
ORCID iD: orcid.org/0000-0002-9189-987X

Received: 09.02.2024
Last Revision Received: 14.05.2024
Accepted: 22.05.2024

To cite this article: T. Mitra. "In Search of a Linkage Between Personality Traits and Interpersonal Behaviour During the COVID-19 Pandemic: A Case Study on Indian Marine Engineers Using Structural Equation Modelling." *Journal of ETA Maritime Science*, vol. 12(3), pp. 263-276, 2024.

which is a unique way of thinking, feeling and behaving, as a relatively stable pattern of interpersonal behaviours arising from interaction with others, especially during critical developmental periods. Such personality gradually develops since their childhood and through the interactions between their biological, environmental and psychological factors. While people carry out day-to-day activities associated with their jobs in an organisational setup, their personality traits play crucial roles in creating and maintaining connections with others.

The maritime industry is one of the oldest industries in human history and operates, among others, through different types of merchant ships, sailing of which largely depends on proper intra-department as well as inter-department coordination and cohesive teamwork. The Director General of Shipping, Government of India, has indicated two types of commercial ships, viz., "cargo ship" and "passenger ship" [10]. While the passenger ships are broadly divided into (i) ferry ships and (ii) cruise ships, which carry passengers [11], the cargo ships are broadly categorised as (i) dry cargo ships, which are used to transport dry cargo of different kinds, (ii) liquid cargo ships for carrying liquid bulk cargo including liquid gases like LNG, and (iii) specialised cargo ships for transporting extremely heavy or bulky objects [12]. Like an organisation, a cargo ship also sails due to the concerted effort of seafarers of three departments, viz., (i) deck department, in which the deck officers are responsible for the safe navigation of the ship; (ii) engine department, where the marine engineers are responsible for repair and maintenance of ship's engines and equipment and (iii) saloon department, which takes care of preparation and serving food and allied services to the crew members. On the other hand, while for a cruise ship, the functioning of the deck department and engine department are similar, the hotel department, which is not seen on cargo ships, is the largest department and takes care of food, entertainment, medical necessities, etc., for the passengers [13]. Therefore, working on a ship is associated with certain unique features which are rarely alike shore-based jobs. In this backdrop, the present study is an attempt to explore the association between personality traits and interpersonal relationships in an onboard environment.

1.1. Review of Literature

The job characteristics of maritime professionals are unique in nature. They need to sail the ships with a handful number of personnel without holidays/leave and stay away from family members for months together. Day-to-day interactions are mostly among the onboard fellow seafarers only, who are generally multinational as well as multicultural in nature. At the same time, seafarers join ships on short-period contracts, which mostly vary between 3 to 6 months. According to Staniulienė and Kučinskaitė [14], the personal relationship among employees, which develops over time while working together, has a greater impact on the employees and organisation compared to working relationships. However, the development of such personal relationships onboard may not be easy as crew members keep on signing off after the completion of respective short contract periods.

On the other hand, several researchers have highlighted seafaring profession is associated with a higher level of psychological stress [15-18]. Studies also confirmed that healthy interpersonal relationships among employees could contribute towards lowering stress levels [19,20]. According to Bowlby [21], developing and maintaining positive interpersonal relationships are important determinants of mental wellbeing. Stewart and Harkness [22] opined that poor interpersonal relationships are responsible towards developing negative emotions. Therefore, based on the above studies, it can be presumed that positive interpersonal relationships may play an important role in reducing stress levels among seafarers and helping them towards positive mental health.

As indicated above, a healthy interpersonal relationship may lead to reduced levels of stress; several studies have also found that an important factor which impacts organisational teamwork is the opportunity for interaction among team members [23-25]. Interpersonal relationships have been found necessary for fostering teamwork, sharing ideas and overcoming unpleasant work experiences [26]. As the number of onboard seafarers is limited and there is an utmost necessity to sail the ship in time time-bound manner, proper teamwork among the employees of all departments is an absolute necessity.

In continuation to the positive aspects of healthy interpersonal relationships, several studies indicate that positive interpersonal relationships at workplaces improve job satisfaction, job commitment, perceived organisational support, etc. [27-32].

As interpersonal relationships have been found to be a strong determinant of psychological stress, teamwork, job statifaction as well as job commitment, Stoetzer [33] argued that personality traits of the employees majorly govern interpersonal relationships in the workplace. Some of the studies have indicated that while some personality traits are responsible for forming unhealthy relationships, others intend to form positive ones [34-36].

Previous studies have shown that a person with a dominant extraversion trait develops positive interpersonal relationships compared to other traits [37-41]. According to Craenen et al. [42], personality traits influence human-human interactions through engaging and disengaging behaviours. Based on several studies, it is argued that while some personality traits

contribute towards healthy interpersonal relationships, others lead to unhealthy/toxic relationships [41,42]. Lewis [39] opined that while friendship between two individuals with dominant extrovert personality traits may develop to have fun together, such a friendship between two introverts may develop to share their emotions and feelings. Bang and Sim [43] researched nursing students who experience a higher level of occupational stress and found a significant correlation between personality and interpersonal relationships.

The interpersonal relationship has been seen to be affected during the coronavirus disease-2019 (COVID-19) pandemic situation by some of the studies. According to Lee [44], the social and interpersonal relationship was found to be tense. A survey conducted by the University of Minnesota revealed that 39% of the respondents felt that the COVID-19 pandemic had influenced their interpersonal relationships with family members and friends to some extent, while 30% of respondents felt such influence to a great extent [45]. Ades [2] has identified that during the pandemic, interactions were affected, including among family members. Existing studies also reveal that as the duration of the COVID-19 pandemic extended, social connections and social capital declined [46,47].

Though the maritime sector was one of the least disrupted compared to many other industries during the COVID-19 pandemic, the seafarers, who are the backbone of this industry, had to go through a series of unhappy moments. As it is well established that seafarers lack the opportunity to interact with the people at the shore in general, the COVID-19 pandemic snatched away whatever little opportunity they have by way of restrictions on shore leave as well as crew changes. A number of studies conducted on the impacts of the COVID-19 pandemic on seafarers clearly indicate their plights. 40% of the respondents in a study stated that they felt symptoms of depression, and 50% reported that they experience anxiety on a regular basis almost every day [48]. On the other hand, studies also indicate that during the pandemic, seafarers were anxious about getting infected by their fellow crew members [49]. Thereby, seafarers were in a situation where, due to restrictions on shore leaves, neither they could disembark during port stays nor they could go back to their families, and on top of that, the anxiety of getting infected was always there. Another study by Erdem and Tutar [50] found that anxiety among seafarers during the COVID-19 pandemic significantly impacts work stress. Therefore, there are enough pieces of evidence to cite that the COVID-19 pandemic posed a number of ill effects on seafarers worldwide.

1.2. Research Gaps

The existing studies elaborated that personality traits are associated with developing interpersonal relationships among individuals. Most of the studies focus on either individuals in general or employees performing jobs with moderate levels of stress. On the other hand, the prevalent studies directed towards personality and interpersonal relationships are carried out during situations under normal circumstances. Though some of the studies aimed at finding out the impact of the COVID-19 pandemic on interpersonal relationships, such studies are scanty in the maritime sector. At the same time, though some of the studies in this area, i.e., the linkages between personality and interpersonal relationship [Fundamental Interpersonal Relationship Orientation-Behavior™ (FIRO-B®)], are available and are conducted based on responses from students, the linkages are rarely explored for working professionals.

In view of the above, the researcher has identified the following research gaps.

- Existing studies support the theory that interpersonal relationship has an impact on lowering stress levels, but studies on whether, during stressful situations, people tend to develop better interpersonal relationships are hardly available.
- Research in the areas of personality and interpersonal relationship behaviours involving employees engaged in jobs responsible for higher levels of occupational stress, like seafaring, is limited, and
- The linkage between personality traits and interpersonal relationship behaviours among seafarers during uncertainties like the COVID-19 pandemic is hardly explored.

1.3. Objectives of the Study

This study aims to identify linkages between the personality traits of Indian marine engineers and their interpersonal relationship behaviours during uncertain periods. In the present study, the period of the COVID-19 pandemic has been considered an uncertain period.

1.4. Research Question

The following research question is framed with reference to the COVID-19 pandemic period.

RQ_1: Do interpersonal relationship behaviours among Indian marine engineers differ across job ranks?

RQ_2: During the COVID-19 pandemic, do Indian marine engineers' personality traits have a significant linkage with their interpersonal behaviours?

2. Materials and Methods

2.1. Sampling and Data Collection

Given the specialised nature of marine engineering as a profession and its global dispersion, as well as the absence of a defined sample frame, the researcher opted for the snowball sampling method. The snowball sampling method

has been recognised as a viable method of collecting data if the target participants are not easily accessible or not known to the researcher [51-54]. In the case of snowball sampling, new respondents are included in the sample by the existing respondents. Following the ethical research practices, prior to data collection, consents from the respondents were obtained, and a questionnaire was shared with them. While sharing the questionnaire, details about the use of the data were clearly stated, and the respondents voluntarily participated in the survey.

The major limitation of snowball sampling is that those who have a network are included in the survey, and excluding those who do not have a network, thereby, there can be a chance of biases among the respondents while responding. With an intention to overcome such an issue, this study considers respondents who have a large network and who do not have that large network. Therefore, this study attempts to limit biases found in results, which are generally found in studies based on snowball sampling. On the other hand, as the sample distribution follows a normal curve (the distribution of the data has been indicated at a later stage of this paper), the parametric statistical tests, which in general are more powerful than non-parametric tests [55], are applied to achieve the study objectives.

As the population is large, Cochran's formula, which is considered especially appropriate in situations with large populations [56], is used in the present study to determine sample size. According to Cochran, the minimum sample size should be 385 (95% confidence interval and 5% margin of error), as calculated below.

$n = \{p (1 - p) z2\}/e2$

n = sample size

p = the population proportion (if unknown, p=0.50) [57]

e = acceptable sampling error (e=0.05)

z = z value at reliability level or significance level. Reliability level 95% or significance level 0.05; z = 1.96.

An online survey was carried on, and data was collected from 385 Indian marine engineers during February 2021 and July 2022 who had experience on various types of vessels and had sailed both before and during the COVID-19 pandemic. Each rank, including "Chief engineer", "Second engineer", "Third engineer", and "Fourth engineer", contributed responses.

While responses are obtained from all job ranks, their representations in the sample are carried out keeping in mind the day to day interactions they need to carry out due to the nature of the job and responsibilities. Though the chief engineers are overall in-charge of the ships' engine departments, in practice, it is the second engineers who are continuously in direct contact and interaction with all employees of the engine department, and the chief engineers rely heavily on the second engineers. On the other hand, as the third engineers are next in the rank to second engineers as well as more experienced than the fourth engineers, interactions between them are also more compared to the fourth engineers, who are junior most in the ranks and are mostly engaged with maintenance of a limited number of equipment/machine.

2.2. Tools Used for Data Collection

The following instruments were used to collect data:

i) Socio-demographic variables:

Data on age, gender, marital status, job experience, and more were gathered through a structured questionnaire focusing on socio-demographic aspects. Descriptive statistics were applied to analyse the collected data.

ii) The Big Five Personality Traits:

The Big Five Inventory, also known as the OCEAN model of personality, is the most widely used and empirically supported model of personality traits [58-60], which consists of 44 items, employs a five-point Likert scale (ranging from 1, "Strongly Disagree", to 5, "Strongly Agree"). According to the theory, individual differences in five personality dimensions account for the ways people think, feel, and interact with others. This instrument was developed by Goldberg [61] and assessed an individual's personality across five dimensions: (i) "Extraversion", encompassing qualities such as assertiveness and sociability; individuals with lower extraversion tend to be more reserved. (ii) "Agreeableness", reflecting friendly behaviour and flexibility in interactions; individuals with lower agreeableness may display rigidity in their dealings with others. (iii) "Conscientiousness", characterised by qualities like orderliness, responsibility, and dependability. (iv) "Neuroticism", which pertains to emotional stability and the extent to which individuals experience stress, anxiety, anger, and depression. (v) "Openness", encompassing attributes such as acceptance of new ideas, curiosity, and imagination. Researchers are increasingly using the Big Five factors to gain insights into psychological disorders like anxiety and depression.

The present study uses the above Big Five Inventory in an adapted form after identifying factor loads, internal consistency and validity of the scale, which are shown in the next section. The adapted form of the Big Five Inventory used in the present study consists of 35 items.

iii) Fundamental Interpersonal Relationship Orientation-Behavior™ (FIRO-B®):

The theory of Fundamental Interpersonal Relationship Orientation focuses on the interpersonal relationships of individuals based on their intention to interact with others. The FIRO-B®, developed by Schutz [62], a widely used six-

point Likert scale tool [63], has garnered recognition and acceptance among scholars, researchers, and practitioners for comprehending how individuals manifest behaviour driven by their interpersonal behaviours. This assessment evaluates an individual's interpersonal conduct by considering their inclination to engage with others, as proposed by Schutz [62] in 1958. The FIRO-B assesses behaviours related to interpersonal needs, as outlined by Hammer and Schnell [64], focusing on three distinct dimensions: (1) inclusion, (2) control, and (3) affection, which can sufficiently explain most of the human interactions [65]. Such needs are again driven by an individual's two different interpersonal behaviours, viz., "expressed behaviours" and "wanted behaviours", while the expressed behaviours reflect the extent an individual shows such behaviour, e.g., "affection" towards others, wanted behaviours are the manifestation of that individual to what extent he/she expects others to show affection towards him/her. Thereby, the FIRO-B® instrument can reveal three different interpersonal needs and six interpersonal behaviours associated with such needs.

The researcher in the present study adapted the FIRO-B® instrument after assessing its factor loads, reliability and validity, which are shown in the next section. The adapted form of this instrument used in this present study consists of 45 items.

2.3. Internal Consistency and Validity of the Instruments

While using the Big Five Inventory and FIRO-B® scales for this present study, the respective instrument's reliability and validity were assessed and compared the same with the original scales. Such a task led towards the exclusion of items that did not meet the validity criteria from the final questionnaire. The Cronbach's alpha score for the reliability of the scale BFI with its original data for all dimensions was above 0.90 [61], and that for FIRO-B® was between 0.85 to 0.96 [62]. The final questionnaire comprises questions and statements related to (i) socio-demographic variables (consisting of 5 questions), (ii) the Big Five Inventory (comprising 35 items), and (iii) the FIRO-B® (comprising 45 items). Confirmatory factor analysis was carried on, and the factor loadings are shown in Tables 1A and 1B. Items having a factor loading of 0.50 or higher were retained in the instrument, with the exception of item 21 in the Big Five personality traits instrument, where the factor loading was almost 0.50. The reliability and validity scores for the validated instruments are presented in Tables 2A and 2B.

All variables exhibit Cronbach's alpha values exceeding 0.70, thereby confirming the strong internal consistency of both instruments. As per the criteria outlined by Fornell and Larcker [66], it is acceptable for the Average Variance Explained (AVE) to be below 0.50 as long as the Composite Reliability (CR) exceeds 0.60. The scores for CR, AVE, and Heterotrait-Monotrait Ratio of Correlations collectively demonstrate satisfactory discriminant and convergent validity.

2.4. Data Analysis Using "R"

In the present study, the programming language "R" is used to analyse the data. R is a programming language used generally for statistical analysis. For the purpose of answering the research question RQ_1, ANOVA is performed to understand if significant differences exist with regard to interpersonal relationship needs among Indian marine engineers across job ranks. On the other hand, to answer the research question RQ_2, Structural Equation Modelling (SEM) with Diagonally Weighted Leasts Square is used.

***Table 1A**. Factor loads of big five personality instrument*

Item no.	Factor	Factor load	Item no.	Factor	Factor load	Item no.	Factor	Factor load	Item no.	Factor	Factor load
1	E	0.71	12	A	0.63	23	C	0.70	34	N	0.60
2	A	0.31	13	C	0.64	24	N	0.30	35	O	0.73
3	C	0.33	14	N	0.72	25	O	0.59	36	E	0.65
4	N	0.66	15	O	0.55	26	E	0.43	37	A	0.67
5	O	0.83	16	E	0.51	27	A	0.88	38	C	0.67
6	E	0.67	17	A	0.73	28	C	0.54	39	N	0.62
7	A	-0.43	18	C	0.55	29	N	0.57	40	O	0.58
8	C	0.59	19	N	0.67	30	O	0.54	41	O	0.65
9	N	-0.26	20	O	0.21	31	E	0.51	42	A	0.63
10	O	0.32	21	E	0.49	32	A	0.56	43	C	0.65
11	E	0.50	22	A	0.78	33	C	0.31	44	O	0.70
E: Extraversion, A: Agreeableness, C: Conscientiousness, N: Neuroticism, O: Openness											

***Table 1B**. Factor loads of FIRO-B® instrument*

Item no.	Factor	Factor load	Item no.	Factor	Factor load	Item no.	Factor	Factor load	Item no.	Factor	Factor load	Item no.	Factor	Factor load	Item no.	Factor	Factor load
1	eI	0.78	10	wC	0.85	19	eA	0.37	28	wI	0.76	37	wI	0.84	46	wA	0.44
2	wC	0.79	11	eI	0.88	20	wC	0.71	29	wA	0.90	38	wA	0.82	47	eC	0.63
3	eI	0.80	12	eA	0.73	21	eA	0.65	30	eC	0.85	39	wI	0.38	48	wI	0.60
4	eA	0.61	13	eI	0.56	22	wC	0.34	31	wI	0.73	40	wA	0.60	49	wA	0.74
5	eI	0.55	14	wC	0.14	23	eA	0.74	32	wA	0.93	41	eC	0.19	50	eC	0.53
6	wC	0.81	15	eI	0.87	24	wC	0.62	33	eC	0.83	42	wI	0.73	51	wI	0.71
7	eI	0.76	16	eI	0.77	25	eA	0.79	34	wI	0.83	43	wA	0.33	52	wA	0.71
8	eA	0.63	17	eA	0.26	26	wC	0.77	35	wA	0.88	44	eC	0.82	53	eC	0.70
9	eI	0.86	18	wC	0.79	27	eA	0.77	36	eC	0.89	45	wI	0.24	54	eC	0.79

eI: Expressed Inclusion, eA: Expressed Affection, eC: Expressed Control, wI: Wanted Inclusion, wA: Wanted Affection, wC: Wanted Control, FIRO-B®: Fundamental Interpersonal Relationship Orientation-Behavior™

***Table 2A**. Reliability and validity of big 5 personality questionnaire*

Variables	Cronbach's alpha	AVE	CR	HTMT				
				Extravert	Agreeableness	Conscientiousness	Neuroticism	Openness
Extravert	0.74	0.41	0.82					
Agreeableness	0.81	0.35	0.81	0.64				
Conscientiousness	0.83	0.38	0.84	0.77	0.69			
Neuroticism	0.85	0.48	0.85	-0.60	-0.59	-0.62		
Openness	0.78	0.48	0.82	0.69	0.51	0.50	-0.50	

***Table 2B**. Reliability and validity of FIRO-B® questionnaire*

Variables	Cronbach's alpha	AVE	CR	HTMT					
				eI	eA	eC	wI	wA	wC
eI	0.906	0.54	0.91						
eA	0.888	0.62	0.92	0.74					
eC	0.869	0.52	0.88	0.41	0.41				
wI	0.958	0.72	0.72	0.96	0.72	0.44			
wA	0.822	0.59	0.88	0.63	0.87	0.42	0.73		
wC	0.865	0.46	0.87	0.02	0.04	0.15	0.05	0.04	

HTMT: Heterotrait-Monotrait Ratio of Correlations, AVE: Average Variance Explained, CR: Composite Reliability

As described by Bentler and Chou [67], SEM is a statistical approach which adopts a hypothesis-testing perspective for the examination of a structural theory pertaining to a particular phenomenon. SEM encompasses two key facets: (i) the use of a series of regression equations to depict the causal processes under investigation and (ii) the ability to visually model these structural equations to enhance the conceptualisation of the theory being studied. The constructed model undergoes testing, and if it demonstrates satisfactory goodness of fit, it suggests reasonable relationships among the variables.

3. Results

3.1. Descriptive Statistics

3.1.1. Demographic profile of the respondents

Table 3 below shows the demographic profile of the participants. Except for 1 female, all 384 respondents were male only.

Table 4 below shows that skewnesses of almost all of the variables are less than 1, and all are below 2. According to George and Mallery [68], the value of skewness and kurtosis ±2 is accepted to be considered a normal distribution. Table 4 below indicates that skewness and kurtosis are close to zero; hence, the responses are considered a normal distribution [68,69].

Table 3. *Descriptive statistics of the respondent's demographic profile*

	Job rank							
	Chief engineer		Second engineer		Third engineer		Fourth engineer	
Age (Years)	Count	%	Count	%	Count	%	Count	%
21-25	0	0.00	0	0.00	1	0.26	17	4.42
26-30	2	0.52	30	7.79	48	12.47	50	12.99
31-35	14	3.64	94	24.42	34	8.83	2	0.52
36-40	31	8.05	32	8.31	3	0.78	0	0.00
41-45	9	2.34	2	0.52	0	0.00	0	0.00
46-50	8	2.08	1	0.26	1	0.26	0	0.00
51-55	3	0.78	1	0.26	0	0.00	0	0.00
56-60	1	0.26	0	0.00	0	0.00	0	0.00
61-65	0	0.00	0	0.00	0	0.00	0	0.00
66-70	1	0.26	0	0.00	0	0.00	0	0.00
Total	69	17.92	160	41.56	87	22.60	69	17.92

Source: Table adapted from primary data collected by the author

Table 4. *Skewness and kurtosis of data (n=385)*

	Job ranks →	Chief engineer		Second engineer		Third engineer		Fourth engineer	
	Variables ↓	Skewness	Kurtosis	Skewness	Kurtosis	Skewness	Kurtosis	Skewness	Kurtosis
Big Five Personality Traits	Openness	-0.37	0.15	0.00	-0.25	-0.40	-0.14	-0.18	-0.15
	Conscientiousness	-0.22	-0.88	-0.53	-0.54	-0.51	-0.14	-0.23	-0.50
	Extraversion	-0.32	-0.17	-0.58	0.94	-0.17	-0.73	-0.14	0.06
	Agreeableness	-0.41	-0.09	-0.61	0.88	-0.51	-0.29	-0.19	-0.35
	Neuroticism	0.27	-0.51	0.35	-0.33	0.65	0.37	0.21	-0.55
FIRO-B®	Expressed inclusion	-0.32	-0.38	-0.65	0.18	-0.20	-0.65	-0.69	0.47
	Expressed affection	-0.46	-0.48	-0.27	-0.43	0.23	-0.68	-0.38	-0.50
	Expressed control	-0.18	0.04	-0.40	0.20	0.08	-0.28	-0.07	-0.22
	Wanted inclusion	-0.18	-0.67	-0.56	0.15	-0.21	-1.01	-1.05	1.79
	Wanted affection	-0.24	-0.37	-0.19	0.03	0.23	-0.38	-0.02	-0.87
	Wanted control	0.72	0.46	0.54	-0.15	1.18	1.94	0.18	-0.39

Source: Developed by the author from proprietary datasets

FIRO-B®: Fundamental Interpersonal Relationship Orientation-Behavior™

Table 5. *Levene's test of homogeneity of variance*

Variable	Df	F	p-value
Expressed inclusion	3	2.2169	0.0857
Expressed control	3	1.3087	0.2712
Expressed affection	3	0.7982	0.4954
Wanted inclusion	3	1.1156	0.3426
Wanted control	3	1.2662	0.2857
Wanted affection	3	0.8278	0.4792

3.1.2. Interpersonal relationship needs across job ranks

RQ_1: Do interpersonal relationship needs among Indian marine engineers differ across job ranks?

Levene's test for homogeneity of variance as shown in Table 5 above indicates test statistics in connection with "inclusion", "control" and "affection" across job ranks.

Based on the F values and corresponding p-values in Table 5 above, the assumption of homogeneity of variances is established. Thereby, ANOVA is performed to obtain the answer to the above research question, and the test result is shown in Table 6A below.

Except for expressed control, the p-values (Pr>F) associated with the ANOVA, as shown in Table 6A, are all well above 0.05, revealing no significant difference among Indian marine engineers with regard to their interpersonal relationship behaviours on expressed inclusion, expressed affection, wanted inclusion, wanted control and wanted affection across job ranks. As a significant difference is identified regarding expressed control behaviour on the basis of job ranks, a post-hoc test is carried on to identify the specific job ranks in this regard and the output is shown in Table 6B, which indicates that chief engineers and fourth engineers differ significantly in their expressed control behaviours.

Table 6A. *ANOVA on interpersonal needs based on job ranks*

Expressed inclusion	**Df**	**Sum. Sq**	**Mean. Sq**	**F.value**	**Pr(>F)**
Job rank	3	339	113.12	1.597	0.19
Residuals	381	26993	70.85		
Expressed control	**Df**	**Sum. Sq**	**Mean. Sq**	**F.value**	**Pr(>F)**
Job rank	3	526	175.50	3.908	0.00
Residuals	381	17106	44.90		
Expressed affection	**Df**	**Sum. Sq**	**Mean. Sq**	**F.value**	**Pr(>F)**
Job rank	3	121	40.26	0.755	0.520
Residuals	381	20327	53.35		
Wanted inclusion	**Df**	**Sum. Sq**	**Mean. Sq**	**F.value**	**Pr(>F)**
Job rank	3	141	47.12	0.537	0.657
Residuals	381	33458	87.82		
Wanted control	**Df**	**Sum. Sq**	**Mean. Sq**	**F.value**	**Pr(>F)**
Job rank	3	266	88.60	1.549	0.201
Residuals	381	21790	57.19		
Wanted affection	**Df**	**Sum. Sq**	**Mean. Sq**	**F.value**	**Pr(>F)**
Job rank	3	316	105.24	2.571	0.054
Residuals	381	15596	40.93		
ANOVA: Analysis of Variance					

Table 6B. *Post-hoc test for expressed control behaviour*

Job ranks	Difference	Lower bound	Upper bound	p-value
Second eng. Viz-a-viz. Chief eng.	-0.68	-3.17	1.81	0.89
Third eng. Viz-a-viz. Chief eng.	-2.47	-5.25	0.32	0.10
Fourth eng. Viz-a-viz. Chief eng.	-3.14	-6.09	-0.20	0.03
Third eng. Viz-a-viz. Second eng.	-1.78	-4.09	0.52	0.19
Fourth eng. Viz-a-viz. Second eng.	-2.46	-4.96	0.029	0.05
Fourth eng. Viz-a-viz. Third eng.	-0.68	-3.47	2.11	0.92

In addressing RQ_2, the current research examines the linkages between five distinct personality traits and three different interpersonal relationship needs among Indian marine engineers during the period of the COVID-19 pandemic.

RQ_2: During the COVID-19 pandemic, do Indian marine engineers' personality traits have a significant linkage with their interpersonal behaviours?

R programming language is used to perform Structural Equation Modeling (SEM) along with creation of a path diagram, and the results are displayed in Figure 1 and Table 7 below.

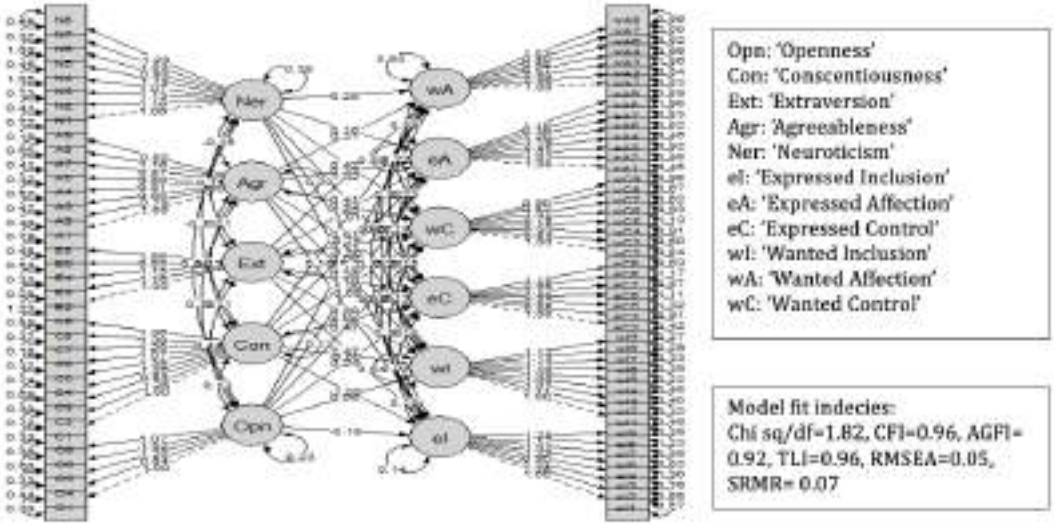

Figure 1. *Structural Equation Path model: Linkages between personality traits and interpersonal relationship needs*

Table 7. *Regression coefficients of personality traits (independent variables) and interpersonal relationship behaviours (dependent variable)*

Independent var.	Dependent var.	Estimate	Std. Err.	z-value	p-value	Std	Std.all
Openness	eI	-0.164	0.260	-0.632	0.527	-0.099	-0.099
	wI	0.062	0.283	0.219	0.827	0.031	0.031
	eC	0.245	0.250	0.978	0.328	0.131	0.131
	wC	0.469	0.307	1.529	0.126	0.223	0.223
	eA	-0.081	0.269	-0.300	0.764	-0.042	-0.042
	wA	0.579	0.344	1.682	0.093	0.257	0.257
Conscientiousness	eI	-1.052	0.480	-2.192	0.028	-0.481	-0.481
	wI	-0.599	0.522	-1.147	0.251	-0.229	-0.229
	eC	0.383	0.503	0.763	0.446	0.155	0.155
	wC	-1.394	0.650	-2.145	0.032	-0.504	-0.504
	eA	-0.556	0.556	-1.001	0.317	-0.220	-0.220
	wA	-1.011	0.645	-1.568	0.117	-0.340	-0.340
Extraversion	eI	2.474	0.544	4.547	0.000	1.242	1.242
	wI	2.025	0.541	3.742	0.000	0.849	0.849
	eC	1.105	0.407	2.716	0.007	0.492	0.492
	wC	0.510	0.426	1.199	0.230	0.202	0.202
	eA	1.619	0.439	3.686	0.000	0.702	0.702
	wA	1.320	0.500	2.637	0.008	0.487	0.487

Table 7. Continued

Independent var.	Dependent var.	Estimate	Std. Err.	z-value	p-value	Std.lv	Std.all
Agreeableness	eI	0.296	0.280	1.058	0.290	0.167	0.167
	wI	0.237	0.286	0.828	0.408	0.112	0.112
	eC	-0.753	0.277	-2.720	0.007	-0.377	-0.377
	wC	0.432	0.337	1.283	0.199	0.193	0.193
	eA	0.333	0.306	1.088	0.276	0.162	0.162
	wA	0.210	0.338	0.623	0.534	0.087	0.087
Neuroticism	eI	0.149	0.132	1.121	0.262	0.110	0.110
	wI	0.506	0.158	3.199	0.001	0.314	0.314
	eC	0.406	0.137	2.968	0.003	0.267	0.267
	wC	0.422	0.153	2.760	0.006	0.248	0.248
	eA	0.165	0.138	1.193	0.233	0.106	0.106
	wA	0.256	0.153	1.675	0.094	0.140	0.140

Source: Author-generated estimates based on structural equation modelling

var.: Variables, Std. Err.: Standard error

The above path diagram and Table 7 show, during the period of the pandemic,

• Openness is the only personality trait which is not liked with any of the interpersonal relationship behaviours.

• Conscientiousness has significant linkages with expressed inclusion and wanted control behaviours.

• Extraversion trait is linked with all interpersonal relationship behaviours except wanted control.

• The agreeableness trait is linked to expressed control behaviour.

• Neuroticism personality trait is linked to wanted inclusion, expressed control as well as wanted control.

4. Findings and Discussion

One of the findings of the study is that, except one, for all interpersonal relationship behaviours, viz., expressed inclusion, expressed affection, wanted inclusion, wanted control and wanted affection, there is no significant difference among the Indian marine engineers across job ranks. However, significant differences are visible across job ranks with respect to expressed control behaviours. Such a finding partially supports an existing study which found a significant difference across job ranks with regard to expressed inclusion, wanted inclusion, expressed control and wanted control [70]. The findings also reveal that the highest difference with regard to expressed control behaviour is between fourth engineers and chief engineers, while the least is between second engineers and chief engineers, as well as between fourth engineers and third engineers. The job rank of "Chief Engineer" onboard is similar to a Head of the Department, and that of "Second Engineer" is second in command. They both work in a managerial capacity, actively associated with onboard problem-solving and decision-making. It is already established that onboard activities are carried out in coordination with all team members, in which their active participation is an absolute necessity. The persons who are responsible for getting the job done through the team members, i.e., the chief engineers and the second engineers, take utmost care in proper coordination of the team and continuously keep track of the team functioning. On the other hand, as the fourth engineers and third engineers carry out the instructions given by the chief engineers and second engineers and rarely make crucial decisions, the expressed control behaviour is found least for the fourth engineers and also less for the third engineers.

The number of studies available in the areas of exploring the interplay between personality traits and interpersonal relationship behaviours is scanty. This present study is probably the first of its kind, which reveals the linkages between Big Five personality traits and FIRO-B® constructs among Indian marine engineers. A study on 192 students by Mahoney and Stasson [71] found extraversion personality trait is a pervasive aspect of relationships. The study also revealed a positive relationship between neuroticism and wanted control. Such a finding supports the present study, which explored significant linkages between extraversion and almost all interpersonal relationship behaviours, except wanted control. Furnham and Crump [72] in a study on MBTI personality types and FIRO-B®, found positive correlations between extraversion and expressed inclusion, wanted inclusion, as well as expressed affection. Hence, it supports the present study. Therefore, it can be concluded that irrespective of the situation, Indian marine engineers

with dominant extraversion traits behave in similar ways regarding their interpersonal relationship behaviour, i.e., uncertainties like the COVID-19 pandemic do not impact the way they behave. On the other hand, characteristics like assertiveness, which is a byproduct of the dominant extraversion trait, may be responsible towards a non-significant impact on wanted control behaviour. The result of this study also matches to a great extent with an earlier study by Furnham [73], which was carried out on middle to senior-level managers of a multinational communication organisation. The said study found, similar to the present one, that a significant linkage between the openness trait and any of the FIRO-B® constructs is absent. In the case of extraversion trait too, the findings of the present study exactly match with Furnham [73], i.e., except "wanted control", all interpersonal relationship behaviours are linked to a positive extent with extraversion.

The agreeableness trait is represented through characteristics like being sympathetic, cooperative, etc. The findings of the present study with respect to the "agreeableness" trait also align with the above study of Furham [73], wherein the "expressed control" behaviour is negatively linked, which implies Indian marine engineers with agreeableness traits exhibit similar kinds of interpersonal behaviour with respect to expressed control even during the pandemic. However, there are certain findings which contradict the above study. A high level of conscientiousness trait of the Indian marine engineers is found to have a negative linkage with wanted control behaviour, which does not support the above study by Furnham [73]. The said study did not find any significant relationship between neuroticism traits and any of the FIRO-B® constructs. However, the present study revealed positive linkages between neuroticism and "wanted inclusion", "expressed control" and "wanted control". The conscientiousness traits are expressed as being responsible, careful, diligent, etc. The COVID-19 pandemic posed itself as an unprecedented, extraordinary situation for which human civilisation was not prepared at all. The guidelines for safe sailing issued from time to time by the respective shipping companies were often not consistent. The chief engineers, though, were always in touch with their companies at the shore for necessary instructions; however, such instructions were often difficult to implement due to higher levels of diligence and orderliness, which is the probable reason that a higher level of conscientiousness leads to a significantly lower level of wanted control among Indian marine engineers. On the other hand, a higher level of conscientiousness trait leads to a higher level of sense of responsibility, and the majority of the respondents (almost 60%) are in the job ranks of either chief engineers or second engineers, who are working in the managerial capacity, carrying out their jobs in a responsible way during such an uncertain situation. The habit of being responsible and adhering to the guidelines may put extra pressure on Indian marine engineers with dominant conscientiousness. Apart from that, maintenance of the COVID-19 protocol may be another area of concern for them. Such factors may have contributed to a significantly negative impact on expressed inclusion behaviour.

Another study by Sharma [74], which was conducted on 912 management students, revealed that except for wanted inclusion, significant positive correlations exist between extraversion and interpersonal relationship behaviours. The said study also found a positive significant correlation between neuroticism traits and wanted control. Such a finding matches to a great extent with the present study. The neuroticism trait is associated with negative emotions like distress, dissatisfaction, self-doubt, etc. The resemblances of the findings of this study with the above one indicate that Indian marine engineers with dominant neuroticism personality traits continue to exhibit wanted control behaviour towards others even during the pandemic. At the same time, new dimensions in their interpersonal relationship behaviours, viz., "wanted inclusion" and "expressed control", have been seen during the pandemic. However, the present study contradicts the said study in certain dimensions, viz., while in the present study, conscientiousness has been found to be negatively linked with expressed inclusion and wanted control, Sharma [74] found a positive correlation among them.

On the other hand, the present findings align to some extent with a study carried out on 219 students of business courses [75], which found positive correlations between extraversion and expressed as well as wanted inclusion and expressed affection. Similarly, the openness trait did not get any statistical significance towards any of the FIRO-B® constructs. Similarity is also seen in the relationship between agreeableness and expressed control.

The above findings can be seen as opportunities for intervention by the shipping companies towards better utilisation of the onboard manpower. As it is clear from the above findings, which either strengthen the existing body of knowledge or, while contradicting existing literature, bring out new theories, particularly during the COVID-19 pandemic and Indian context, can be examined by the shipping companies in devising plans and strategies while selecting marine engineers based on their personality traits and interpersonal relationship skills. Such an act may facilitate the marine engineers in culminating cohesive teams onboard and thereby carrying out their day to day activities with ease [76]. On the contrary, a good blend of personality traits onboard may facilitate the marine engineers to interact with each other especially during the

periods like the COVID-19 pandemic. Such interactions may act as social buffer and assist them in reducing their anxiety and stress to a great extent [77]. Similarly, a team consisting of marine engineers collating complementary interpersonal relationship behaviours may be fruitful during crises in improved job performance [25] as well as emotional support [78] onboard.

5. Study Limitations

Like many other studies, this study is also not free from limitations. First of all, due to the lack of a sample frame, a non-random sampling method was followed for data collection, and hence, the findings of this study may not be generalised. Secondly, the responses are based on the perception of the respondents, which may be subject to bias, such as social desirability or memory bias, which may affect the accuracy of the results obtained.

This present study is probably the first of its kind, which reveals the linkages between personality traits and interpersonal relationship behaviours of Indian marine engineers during the COVID-19 pandemic. Thus, this study can be a guiding star for many researchers to explore further. This study, being exploratory in nature, has identified available linkages between personality traits and interpersonal relationship behaviours and points out some of the probable reasons. Therefore, future studies in this regard can lead to acceptance/rejection of the stated reasons as well as identifying additional factors in this regard. Further, considering this study as a point of reference, a similar kind of study can lead towards revealing the fact whether the interpersonal relationship behaviours of Indian marine engineers are consistent or not irrespective of external situations, i.e., during periods of normalcy and periods of uncertainty. In addition, in continuation to the present study, the perception of the shipping companies on the suggestions prescribed can be explored.

6. Conclusion

While seafarers are the backbone of international trade, the seafaring profession is characterised by a number of unique features. The optimum utilisation of the onboard resources largely depends on effective teamwork, while such an effective, to a great extent, depends on interpersonal relationships among the team members. This present study reveals significant linkages between certain personality traits and interpersonal relationship behaviours exhibited by Indian marine engineers. In this regard, while selecting a marine engineer for an onboard job, this study can assist the recruiter in understanding the way the prospective marine engineer can exhibit interpersonal relationships onboard. The recruiter can have guidance from this study regarding placing the "right person at the right place", which is expected to form a more cohesive team onboard. On the contrary, measures of shipping companies may be focussed towards providing marine engineers with necessary training like, on relationship building, teamwork and team building, cultural competency, emotional intelligence, conflict resolution, etc. At the same time, especially during uncertain periods like the COVID-19 pandemic, the seafarers who are away from their families need to be taken care of with compassion, and every possible support should be provided to them and their family members, which in turn makes the seafarers feel satisfied and less anxious. Such a mental state is likely to contribute towards a better interpersonal relationship onboard.

Funding: The author received no financial support for the research, authorship, and/or publication of this article.

References

[1] J. M. Cheek, and A. H. Buss, "Shyness and sociability". *Journal of Personality and Social Psychology*, vol. 41, pp. 330-339, 1981.

[2] A. Ades, "The quality of family interpersonal communication during COVID-19". *The Open Public Health Journal,* vol. 14, pp. 304-310, Aug 2021.

[3] J. Martino, J. Pegg, and E. Pegg Frates, "The connection prescription: using the power of social interactions and the deep desire for connectedness to empower health and wellness. *American Journal of Lifestyle Medicine,* vol. 11, pp. 466-475, Nov/Dec 2017.

[4] K. R. Subramanian, "Influence of social media in interpersonal communication". *International Journal of Scientific Progress and Research*, vol. 38, pp. 70-75, Aug 2017.

[5] J. García-Manglano, et al. "Social media and mental health: The role of interpersonal relationships and social media use motivations, in a nationally representative, longitudinal sample of Spanish emerging adults". *Journal of Social and Personal Relationships,* vol. 41, pp. 1157-1182, Mar 2024.

[6] G. Gupta, "Mobile usage and its impact on interpersonal relationships and work efficiency". *South Asian Research Journal of Business and Management*, vol. 3, pp. 23-33, Jan-Feb 2021.

[7] L. Humphreys, and H. Hardeman, "Mobiles in public: Social interaction in a smartphone era". *Mobile Media & Communication,* vol. 9, pp. 103-127, Jan 2021.

[8] R. Bhattacharjee, and S. Begum, "Impact of mobile phone on interpersonal communication among student of Assam agricultural university". *The Pharma Innovation*, vol. 11(6S), 1071-1076, 2022.

[9] H. S. Sullivan, *The Interpersonal Theory of Psychiatry*. Edited by Harry Stack Sullivan. Routledge, 2013.

[10] https://dgshipping.gov.in/Content/PageUrl.aspx?page_name=PARTIPreliminary accessed on 02.04.2024

[11] https://www.marineinsight.com/cruise/what-are-passenger-ships/ accessed on 02.04.2024

[12] https://www.oneocean.com/insights/vessel-types-explained accessed on 02.04.2024

[13] İ. Ç. Kolçak, and M. S. Solmaz, "Difficulties preventing Turkish officers from working on cruise ships and suggestions for solution". *Journal of Urban Academy,* vol. 14, pp. 842-852, Sep 2021.

[14] S. Staniulienė, and B. Kučinskaitė, "Research on employees' interpersonal and work relationships in Lithuanian companies". *Management of Organisations: Systematic Research*, vol. 77, pp. 119-136, Jun 2017.

[15] A. W. Parker, L. M. Hubinger, S. Green, and L. S. BA. *A Survey of the health, stress and fatigue of Australian seafarers.* Australian Maritime Safety Authority, Australian Government. 1997. https://www.amsa.gov.au/sites/default/files/health-stress-and-fatigue-study-1997.pdf

[16] M. Jezewska, I. Leszczyńska, and B. Jaremin, "Work-related stress at sea self estimation by maritime students and officers". *International Maritime Health*, vol. 57, pp. 66-75, 2006.

[17] M. Oldenburg, H. J. Jensen, and R. Wegner, "Burnout syndrome in seafarers in the merchant marine service". *Int Arch Occup Environ Health,* vol. 86, pp. 407-416, 2013. doi: 10.1007/s00420-012-0771-7, indexed in Pubmed: 22526089.

[18] M. Oldenburg, H.-J. Jensen, U. Latza, and X. Baur, "Seafaring stressors aboard merchant and passenger ships". *International Journal of Public Health*, vol. 54, pp. 96-105, Mar 2009.

[19] J. Gaines, and M. J. Jermier, "Emotional exhaustion in a high stress organization". *Academy of Management Journal*, vol. 26, pp. 567-586, Dec 1983.

[20] M. P. Leiter, and C. Maslach, "The impact of interpersonal environment on burnout and organisational commitment". *Journal of Organizational Behavior*, vol. 9, pp. 297-308, Oct 1988.

[21] J. Bowlby, "Disruption of affectional bonds and its effects on behavior". *Journal of Contemporary Psychotherapy*, vol. 2, pp. 75-86, Dec 1970.

[22] J. G. Stewart, and K. L. Harkness, "Testing a revised interpersonal theory of depression using a laboratory measure of excessive reassurance seeking". *Journal of Clinical Psychology*, vol. 73, pp. 331-348, Mar 2017.

[23] J. P. Meyer, and L. Herscovitch, "Commitment in the workplace: toward a general model". *Human Resource Management Review*, vol. 11, pp. 299-326, 2001.

[24] J. Yoon, and S. R. Thye, "A dual process model of organizational commitment". *Work and Occupations*, vol. 29, pp. 97-124, 2002.

[25] T. C. Wijayanti, "Influence of interpersonal communication and teamwork on organization to enhance employee performance: a case study." *Proceedings of the 1st UMGESHIC International Seminar on Health, Social Science and Humanities (UMGESHIC-ISHSSH 2020)*, vol. 585, pp. 425-431, Oct 2021.

[26] P. L. Curşeu, R. Ilies, D. Vîrgă, L. Maricuţoiu, and F. A. Sava, "Personality characteristics that are valued in teams: Not always "more is better"?" *International Journal of Psychology*, vol. 54, pp. 638-649, Oct 2019.

[27] C. Cherniss, "Career commitment in human service professionals. A biographical study". *Human Relations*, vol. 44, pp. 419-437, 1991.

[28] K. A. Jehn, and P. P. Shah, "Interpersonal relationships and task performance: An examination of mediation processes in friendship and acquaintance groups". *Journal of Personality and Social Psychology*, vol. 72, pp. 775-790, 1997.

[29] C. M. Riordan, and R. W. Griffeth, "The opportunity for friendship in the workplace: An underexplored construct". *Journal of Business and Psychology*, vol. 10, pp. 141-154, Dec 1995.

[30] S. E. Robinson, S. L. Roth, and L. L. Brown, "Morale and job satisfaction among nurses: What can hospitals do?" *Journal of Applied Social Psychology,* vol. 23, pp. 244-251, 1993.

[31] S.-H. Song, and D. Olshfski, "Friends at work: a comparative study of work attitudes in Seoul City government and New Jersey State government". *Administration & Society,* vol. 40, pp. 147-169, Apr 2008.

[32] T. J. Zagenczyk, K. D. Scott, R. Gibney, A. J. Murrell, and J. B. Thatcher, "Social influence and perceived organisational support: A social networks analysis". *Organisational Behavior and Human Decision,* vol. 111, pp. 127-138, Mar 2010.

[33] A. Stoetzer, *Interpersonal Relationship at Work*. Karolinska Institutet, Stockholm, 2010.

[34] D. L. Paulhus, and K. M. Williams, "The dark triad of personality: narcissism, machiavellianism, and psychopathy". *Journal of Research in Personality*, vol. 36, pp. 556-563, Dec 2002.

[35] K. V. Petrides, P. A. Vernon, J. A. Schermer, and L. Veselka, "Trait emotional intelligence and the dark triad traits of personality". *Twin Research and Human Genetics*, vol. 14, pp. 35-41, Feb 2011.

[36] A. S. Umair, W. Zhang, Z. Han, and S. H. U. Haq, "Impact of logistics management on customer satisfaction: a case of retail stores of Islamabad and Rawalpindi". *American Journal of Industrial and Business Management*, vol. 09, pp. 1723-1752, Aug 2019.

[37] F. J. Neyer, and J. B. Asendorpf, "Personality-relationship transaction in young adulthood". *Journal of Personality and Social Psychology,* vol. 81, pp. 1190-1204, 2001.

[38] F. J. Neyer, and J. Lehnart, "Relationships matter in personality development: Evidence from an 8-year longitudinal study across young adulthood". *Journal of Personality,* vol. 75, pp. 535-568, 2007.

[39] D. Lewis, "Personality, self-esteem, interpersonal relationships and friendships". *XULAneXUS*, vol. 7, pp. 3-11, Dec 2009.

[40] J. Lehnart, F. J. Neyer, and J. Eccles, "Long-term effects of social investment: The case of partnering in young adulthood". *Journal of Personality*, vol. 78, pp. 639-670, 2010.

[41] P. Viswanath, "Personality and interpersonal skills in college youth". *The International Journal of Indian Psychology*, vol. 7, pp. 796-800, Jul-Sep 2019.

[42] B. Craenen, A. Deshmukh, M. E. Foster, and A. Vinciarelli, "Do we really like robots that match our personality? The case of big-five traits, godspeed scores and robotic gestures". *2018 27th IEEE International Symposium on Robot and Human Interactive Communication (RO-MAN)*, pp. 626-631, 2018.

[43] M. Bang, and S. Sim, "The relationship among personality, interpersonal relations and stress of clinical practice of nursing students". *International Journal of Advanced Nursing Education and Research,* vol. 1, pp. 67-72, 2017.

[44] S. Lee, "Subjective well-being and mental health during the pandemic outbreak: exploring the role of institutional trust". *Research on Aging*, vol. 44, pp. 10-21, Jan 2022.

[45] https://www.sph.umn.edu/sph/wp-content/uploads/2021/04/c-eat-relationship-brief.pdf accessed on 04.04.2024

[46] D. Folk, K. Okabe-Miyamoto, E. Dunn, and S. Lyubomirsky, "Did social connection decline during the first wave of COVID-19?: The role of extraversion". *Collabra: Psychology*, vol. 6, pp. 1-13, 2020.

[47] B. Yu, M. Luo, M. Liu, J. Zhou, S. Yang, and P. Jia, "Social capital changes after COVID-19 lockdown among youths in China: COVID-19 impact on lifestyle change survey (COINLICS)". *Frontiers in Public Health*, vol. 9, pp. 1-8, Aug 2021.

[48] B. Pauksztat, M. Grech, M. Kitada, and R. B. Jensen, (2020). Seafarers' experiences during the COVID-19 pandemic: Report. Dec 2020.

[49] M. Kaptan, and B. Olgun Kaptan, "The investigation of the effects of COVID-19 restrictions on seafarers". *Australian Journal of Maritime & Ocean Affairs*, vol. 15, pp. 25-37, 2023.

[50] A. T. Erdem, and H. Tutar, "Impact of COVID-19 anxiety on work stress in seafarers: the mediating role of COVID-19 burnout and intention to quit". *International Maritime Health*, vol. 73, pp. 133-142, Oct 2022.

[51] Marcus, B., Weigelt, O., Hergert, J., Gurt, J., & Gelléri, P. "The use of snowball sampling for multi source organizational research: Some cause for concern". *Personnel Psychology,* vol. 70, pp. 635-673, 2017.

[52] M. Naderifar, H. Goli, and F. Ghaljaie, "Snowball sampling: A purposeful method of sampling in qualitative research". *Strides in Development of Medical Education,* vol. 14, Article 367670, Sep 2017.

[53] L. Reagan, et al. "Integrative review of recruitment of research participants through Facebook". *Nursing Research,* vol. 68, pp. 423-432, Nov/Dec 2019.

[54] A. R. Wohl, et al. "Project engage: Snowball sampling and direct recruitment to identify and link hard-to-reach HIV-infected persons who are out of care". *Journal of Acquired Immune Deficiency Syndromes,* vol. 75, pp. 190-197, Jun 2017.

[55] N. R. Smalheiser, Data literacy. How to Make your Experiments Robust and Reproducible. Academic Press, pp. 157-167, 2017.

[56] W. G. Cochran, Sampling Technique. 2nd Edition, John Wiley and Sons Inc., New York. 1963.

[57] https://medium.com/@josephajire/how-to-determine-sample-size-for-human-based-study-population-a52a651407c8 accessed on 11.04.2024

[58] M. S. Chmielewski, and T. A. Morgan, Five-Factor Model of Personality. In: Gellman, M.D., Turner, J.R. (eds.) Encyclopedia of Behavioral Medicine. Springer, New York, NY, 2013.

[59] M. L. Smith, and D. Hamplová, J. Kelley, and M. D. R. Evans, "Concise survey measures for the big five personality traits". *Research in Social Stratification and Mobility* vol. 73, 100595, Jun 2021.

[60] Y.-Y. Tang, and R. Tang. "Chapter 2 - Personality and meditation". *The Neuroscience of Meditation. Understanding Individual Differences*, vol. 15-36, 2020.

[61] L. R. Goldberg, "The development of markers for the Big-Five factor structure". *Psychological Assessment,* vol. 4, pp. 26-42, 1992.

[62] W. C. Schutz, FIRO: A three-dimensional theory of interpersonal behavior. Rinehart. 1958.

[63] https://eu.themyersbriggs.com/-/media/Files/PDFs/Book- Previews/FI0036e_preview.pdf Accessed on 13.05.2024.

[64] A. L. Hammer, and E. R. Schnell, FIRO-B Technical Guide. California: CPP, Inc. 2000.

[65] https://www.thesweden.se/files/FIRO-overview_element_b.pdf accessed on 13.05.2024

[66] C. Fornell, and D. F. Larcker, "Evaluating structural equation models with unobservable variables and measurement error". *Journal of Marketing Research,* vol. 18, pp. 39-50, Feb 1981.

[67] P. M. Bentler, and C.-P. Chou, "Practical issues in structural modeling". *Sociological Methods & Research,* vol. 16, pp. 78-117, Aug 1987.

[68] D. George, and P. Mallery, "*IBM SPSS statistics 25 step by step: A simple guide and reference*". 15th ed. Routledge, New York, 2018.

[69] J. F. Hair, G. T. M. Hult, C. M. Ringle, M. Sarstedt, N. P. Danks, and S. Ray, "*Partial least squares structural equation modeling (PLS-SEM) using r: A workbook*". Springer, 2021.

[70] A. Furnham, and J. Crump, "Personality and management level: traits that differentiate leadership levels". *Psychology*, vol. 06, pp. 549-559, 2015.

[71] J. M. Mahoney, and M. F. Stasson, "Interpersonal and personality dimensions of behavior: FIRO-B and the big five". *North American Journal of Psychology,* vol. 7, pp. 205-216, Jun 2005.

[72] A. Furnham, and J. Crump, "Relationship between the MBTI and FIRO—B in a large British sample". *Psychological Reports*, vol. 101, pp. 970-978, Dec 2007.

[73] A. Furnham, "Psychometric correlates of FIRO-B scores: locating the FIRO-B scores in personality factor space". *International Journal of Selection and Assessment,* vol. 16, pp. 30-45, Jan 2008.

[74] E. Sharma, "Personality mapping wand to organisational performance". *Journal of Business Theory and Practice,* vol. 2, 13, 2014.

[75] W. R. Forrester, A. Tashchian, and T. H. Shore, "Relationship between personality and behavioral intention in student teams". *American Journal of Business Education (AJBE),* vol. 9, pp. 113-118, 2016.

[76] Y. Bai, Y. Hu, Z. Zhou, X. Du, Y. Shi, and L. You, "Rise above prejudice against personality: Association with personality and interactive collaboration in team creativity performance". *Thinking Skills and Creativity,* vol. 52, 101539, Jun 2024.

[77] M. Gründahl, M. Weiß, K. Stenzel, J. Deckert, and G. Hein, "The effects of everyday-life social interactions on anxiety-related autonomic responses differ between men and women". *Sci Rep,* vol. 13, 9498, Jun 2023.

[78] X. Chen, B. Huang, and W. Lin, "The effect of interpersonal relationship and epidemic attention on negative emotion among medical students: the mediating role of social satisfaction". *BMC Psychiatry,* vol. 23, 610, Aug 2023.

ORIGINAL RESEARCH (AR) DOI: 10.4274/jems.2024.46693

Journal of ETA Maritime Science 2024;12(3):277-286

Blade Stress of Carbon Fiber B-Series Marine Propellers Based on Numerical Analysis

Firly Irhamni Ahsan, I Made Ariana, Aguk Zuhdi Muhammad Fathallah

Institut Teknologi Sepuluh Nopember, Department of Marine Engineering, Surabaya, Indonesia

Abstract

In the maritime world, carbon composite material has been used as a propeller on ships. Research on the use of carbon composite materials began in the early 2000s. With features including reduced cavitation and pressure fluctuations, improved acoustic attenuation, corrosion resistance, lower maintenance costs, enhanced efficiency, and longer propulsion system service life, carbon composite materials offer several benefits. The propeller's strength and performance should increase with the use of carbon composite materials. This research uses the Fluid Structure Interaction method by conducting computational fluid dynamic simulations followed by finite element analysis. This study analyzed the deformation and stress on the propeller blades by comparing epoxy carbon fiber that was woven and unidirectional with quasi-isotropic laminate; additionally, it will be compared with other metal materials like bronze, titanium alloy, and copper alloy. Through the process of study and observation of the numerically derived data, which represent the propeller blade's maximum deformation and equivalent stress. By comparing two types of carbon fiber, it can be analyzed from the results of maximum deformation and equivalent (Von-Mises) stress using the fluid structure interaction method. The results show that the epoxy carbon fiber is five times lighter than the copper alloy material, and the stress distribution has a similar pattern, but the deformation results of the two epoxy carbon fiber materials differ from those of the metal materials.

Keywords: Marine-propeller, CFRP propeller, Carbon fiber, Open water test, Fluid-structure interaction

1. Introduction

Composite propellers are more technologically advanced than traditional metal propellers because they have better acoustic attenuation, less cavitation and pressure fluctuations, less magnetic interference, lower maintenance costs, and longer propulsion system service lives. Examples of these composite propellers are those made of manganese-nickel-aluminum bronze and nickel-aluminum bronze [1-3]. Aside from all of these advantages, a particular alignment of the fibers can improve the propeller's flexibility and weight-carrying capacity. This prevents flapping by enabling the propeller to autonomously modify its form based on flow conditions and rotational speed [4]. A computational fluid dynamics (CFDs) approach was used for a number of propeller analyses, such as determining how a pre-duct affects ships with Propeller-Hull Interactions, altering the trailing edge shape to make it less likely to singe, assessing the propeller's performance, and using numerical methods to find cavitation noise in marine skew propellers [5-7].

The propeller's complex shape and loading conditions make structural analysis challenging. The propeller's structure can be studied using two main methods: analytical techniques and numerical analysis. The theories of curved beams, plates, and shells, and Taylor's approach, are examples of analytical techniques [8]. The numerical method computes the displacement and stresses quantitatively using finite element method (FEM) solvers [9]. Researchers at Bureau Veritas, a classification society, have recently developed an analytical method tailored to composite propellers. Based on the cantilever beam method, this method produces findings that are quite similar to numerical ones [10]. Compared with numerical methods, the ten analytical methods are faster, simpler, and easier to use. However, because of the assumptions made to simplify the problem, the solutions

Address for Correspondence: Firly Irhamni Ahsan, Institut Teknologi Sepuluh Nopember, Department of Marine Engineering, Surabaya, Indonesia
E-mail: firlyiahsan@gmail.com
ORCID iD: orcid.org/0000-0001-7843-6320

Received: 04.01.2024
Last Revision Received: 25.04.2024
Accepted: 05.06.2024

To cite this article: F. I. Ahsan, I. M. Ariana, and A. Z. M. Fathallah, "Blade Stress of Carbon Fiber B-Series Marine Propellers Based on Numerical Analysis." *Journal of ETA Maritime Science*, vol. 12(3), pp. 277-286, 2024.

are less precise. On the other hand, numerical procedures produce greater precision but require more time and money to process computationally.

Using the commercial program ANSYS Workbench, we investigated the hydrodynamic and structural characteristics of a large screw, seven-bladed composite propeller. Their findings demonstrated that it is critical to consider the effects of FSI when analyzing flexible composite propellers [11]. Using numerical modeling in one-way coupled situations, it is possible to forecast the fatigue life of the two naval propellers. In addition, they used coupled FSI assessments for various currently used materials, including stainless steel and aluminum alloy [12]. The bidirectional FSIs of glass fiber composite propellers and nickel-aluminum bronze propellers is calculated using finite element software and CFDs based on viscous flow theory [13]. Numerous studies that evaluated copper and composite propellers discovered that the latter are more vulnerable to hydrodynamic loads [14-16].

Propeller blades can be made of a composite material consisting of fibers and resin to lessen the cavitation impact (up to 70 percent) [17]. Composite materials can decrease cavitation damage while simultaneously enhancing fatigue resistance, corrosion resistance, and damping performance [18]. After several studies on the potential of carbon fiber in marine propellers, many more potentials need to be investigated. One such potential is the use of carbon fiber in patrol boats or fast boats, for which the stress on the material when it meets the pressure generated by the rotating propeller needs to be examined. As a result, CFDs and lifting surface theory can be used to assess thrust performance. Metallic materials such as bronze, titanium alloy, and copper alloy will be used for comparison.

2. Methodology

2.1. Geometrical Propeller B-5 Series

This study used the Wageningen B-5 Series propeller. An illustration of the propeller geometry can be seen in Figure 1.

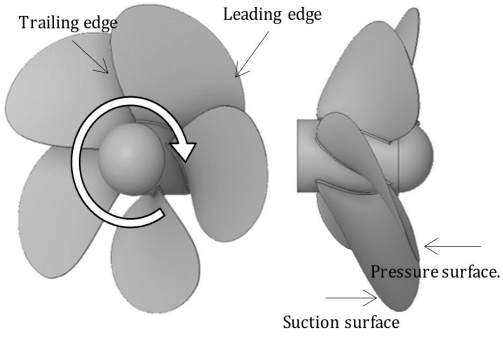

Figure 1. *Geometry of the propeller B-5 series*

Data can be found in Table 1, and it will be used as a research object for analyzing their effect using CFD simulation using the Open Water Test method from J=0 until J=1. By using this method, the pressure distribution will be produced on the propeller blade. In this study, only one blade representing the propeller will be analyzed. The blade model on the propeller is in Figure 2.

Table 1. *Geometrical parameters of the propeller B-5 series*

Parameter	Value
Diameter (mm)	290
AE/AO	1.05
P/D	1.1
Propeller Orientation	Right-hand Rotation
Number of Blades (Z)	5
Rotational Speed (RPM)	600

Figure 2. *Geometry of the blade propeller*

2.2. Propeller Theory

Hydrodynamic characteristics are a set of dimensionless coefficients that express a propeller's relative performance with respect to its mechanical attributes and fluid conditions. These parameters were designed to allow different propeller sizes and types to be compared. The propeller model was tested in open water to determine the intrinsic propeller performance while the ship was moving forward without the distribution of the ship. The terms thrust (T), torque (Q), and efficiency (η) are frequently used to describe the CFD results. With the torque coefficient (KQ) and thrust coefficient (KT) dimensionless and plotted against the advance ratio, the performance statistics are given in (J). The following non-dimensional terms are used to express the performance [19]:

$$K_t = \frac{T}{\rho n^2 D^4} \quad (1)$$

$$K_q = \frac{Q}{\rho n^2 D^5} \quad (2)$$

where n is the speed at which the propeller rotates, the propeller diameter is D, the fluid density is r, T is thrust, and

Q is torque. Furthermore, the advance ratio J, a dimensionless coefficient, is used to show the ratio of propeller speed Va to propeller tip speed:

$$J = \frac{V_a}{nD} \tag{3}$$

Finally, the propeller's open-water efficiency can be calculated as follows:

$$\eta = \frac{J}{2\pi}\frac{K_t}{K_q} \tag{4}$$

where ρ is the water density, n the number of propeller rotations per second (RPS)D is D the propeller diameter, and va represents water advance velocity (m/s).

2.3. Hydrodynamic Analysis

The flow around a marine propeller was effectively solved using Fluent, an unstructured mesh finite volume solution. The finite volume method applies Newton's second law in a model of fluid flow. The problem was resolved using the linear momentum conservation principle in the global Navier-Stokes equation. A few identities that are highly helpful for converting an equation of conservation for a quantity per unit mass to a quantity per unit volume can be derived using mass conservation.

Continuity equation:

$$\frac{\partial \rho A}{\partial t} + \nabla \cdot \rho A v = \rho \frac{DA}{Dt} \tag{5}$$

RANS equation:

$$\rho uj \frac{\partial ui}{\partial xj} = \rho fi + \partial\, \partial xj \left[-p\delta ij + \mu\left(\frac{\partial ui}{\partial xj} + \frac{\partial \mathrm{uj}}{\partial \mathrm{xi}}\right) - \rho u_i' u_j'\right] \tag{6}$$

The variables S, μui for liquid density, kg/mm^3, μ for turbulent viscosity, and p for static pressure, measured in Pa, are all related to the Reynolds stress term. The rotating coordinate system of the propeller is used in the computation, which is performed under stable conditions. The governing equations are the incompressible Newtonian fluid continuity equation and the Reynolds-averaged Navier-Stokes equations. Fluent version 2021 R2, a commercial CFD package, was used as the solver. The following equations express the k-ε Shear Stress Transfer (SST) turbulence model used in this study:

$$\rho \frac{Dk}{Dt} = \frac{\partial}{\partial x_i}\left[\left(\mu + \frac{\mu_t}{\sigma_k}\right)\frac{\partial k}{\partial x_i}\right] + G_k + G_b - \rho\varepsilon - Y_M \tag{7}$$

$$\rho \frac{D\varepsilon}{Dt} = \frac{\partial}{\partial x_i}\left[\left(\mu + \frac{\mu_t}{\sigma_k}\right)\frac{\partial \varepsilon}{\partial x_i}\right] + C_1\frac{\varepsilon}{k}(G_k + C_3 G_b) - C_2\rho\frac{\varepsilon^2}{k} \tag{8}$$

where k represents the energy of turbulent kinetics, reflects the rate of turbulent dissipation, is the amount of kinetic energy that is turbulent due to buoyancy, and is the energy released during turbulent turbulence when a fluid particle's average velocity gradient changes. While the constant coefficients are C_1, C_2, and C_3, YM denotes the influence of turbulent fluctuation expansion on the overall dissipation rate. The viscosity coefficient of the turbulence is represented by. Open-water numerical models were used to determine the propeller's hydrodynamic and hydroacoustic characteristics, which were later confirmed by the propeller's hydrodynamic performance [20]. The current computational approach for forecasting the hydrodynamic performance of cavitating and non-cavitating propellers in open water situations is accurate and reliable [21].

The hydrodynamics of propellers are computed numerically and contrasted with available experimental data. Then, the propeller's hydrodynamic force is applied using the finite element approach in open water, and the axial strain and corresponding force of propellers made of various materials are calculated along with their size and distribution. This information can serve as a theoretical foundation for propeller design optimization [22].

2.4. Boundary Conditions

CFDs modeling of open water tests serves as the boundary condition for this study. There are B-5 propellers, rotating domains, and static domains in these boundary conditions. And condition the position of the intake and outlet of the seawater. Compared with employing a reduced scale, the results are more accurate when the size of the modeling is made in accordance with the original or true scale, which brings the modeling closer to real conditions.

Three domains are identified in the initial development of this boundary condition: rotating domain, static domain, and propeller with hub. The static and rotating domains were originally joined to create space for the rotating domain. Because this domain is fluid, it is essentially used as a stream of water. Use vacuum or empty domains in static domains with hubs and rotating domains themselves to replicate open-water testing conditions found in real life. Figure 3 shows a comprehensive domain determination.

Velocity-inlet is the zone name that has been set on the meshing and previously in the inlet boundary conditions.

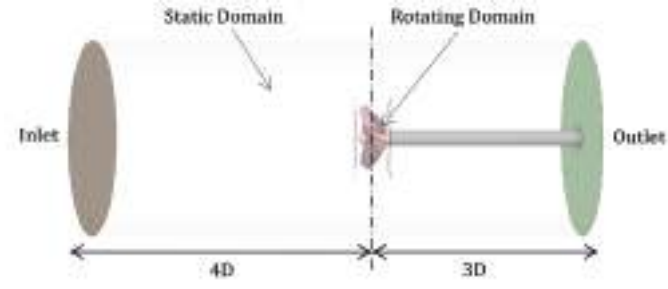

Figure 3. *Geometry of the computational domain of the B-5 propeller*

Therefore, it is filled in by inputting the flow velocity value in meters per second (m/s). In this case, the speed value is derived from the value of Va (advanced Velocity). Va can be a parameter that is entered as the initial Va at a speed of 0 m/s because this open-water test inputs variations in the value of Va based on the value of J.

Since this output is the consequence of the propeller's motion, the pressure at the outlet is set to 0, and the CFD solver computes the value. Considering that the propeller's diameter is four times the outlet's maximum seawater discharge. Fluent adapts to 1 atm conditions for operational conditions. The mesh configuration on the propeller and the domain is shown in Figure 4.

2.5. Fluid Structure Interaction

Therefore, loads and stresses must be computed simultaneously using hydrodynamic and structural analyses to precisely predict the performance of composite propellers. This relationship is called fluid-structure interaction analysis [23].

In the third section, the propeller hydrodynamics are estimated numerically. In contrast to the experimental evidence that has been published. The strength research and computation are then completed by applying the hydrodynamic force to the propeller using the FEM.

Utilizing the fluid-solid interaction analysis methodology, which combines a CFD approach based on the RANS equation with a FEM method for composite structures, the composite propeller's mechanical performance analysis is finished. Using the pressure-based solver and the k-w SST model, the CFD technique analyzes the propeller's hydrodynamic performance in all simulations. A fluid-solid interface is how the blade's surface is set up.

2.6. Materials Assignment

The material used in this study is epoxy carbon fiber, with two comparisons, namely unidirectional and woven fabric. First, epoxy (EP) matrix, high-strength carbon fiber unidirectional tape prepreg, quasi-isotropic laminate (0/+45/-45/90) s (unidirectional tape prepreg, fiber Vf: 0.55-0.65, autoclave cure at 115-180 °C, 7-6 bar) (Table 2).

Figure 4. *Meshing configuration of the B-5 propeller*

Second material, epoxy (EP) matrix, high-strength carbon fiber woven fabric prepreg, quasi-isotropic laminate (0/90/+45/-45) s (woven fabric prepreg, fiber Vf: 0.48-0.58, autoclave cure at 120-180 °C, 6-7 bar). The material properties can be seen in Table 3, these two materials will also be compared with two other materials such as titanium alloy and copper alloy. The properties of the materials are shown in the table below. Therefore, in this analysis, 2 of the lightest carbon fiber materials were taken, namely epoxy carbon fiber UD and epoxy carbon fiber Woven with mass of 8.65E-02 kg and 8.71E-02 kg respectively. When compared to metallic materials such as copper alloys with non-metallic materials such as epoxy carbon fiber UD, obtained a ratio value of 1: 5. The material comparison is illustrated in Figure 5.

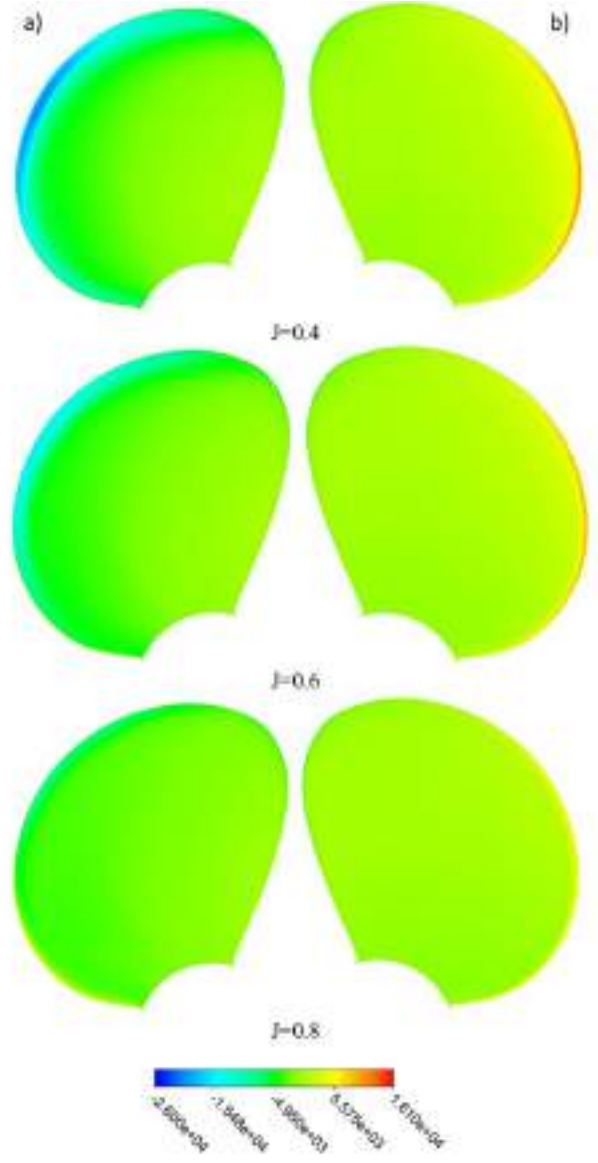

Figure 5. *Pressure distribution on a) pressure surface and b) suction surface*

3. Results and Discussion

The B-5 propeller was subjected to CFDs simulations. A sequence of modifications, ranging from J=0 to J=1, yielded pressure distribution data on the propeller, with particular attention paid to the blade, which will require additional analysis to determine the impact of the pressure on the material on the blade.

The results of the open-water simulation with the CFD method obtained results in the form of pressure distribution, which will then be used as input from structural analysis. Figure 6 shows the pressure distribution that was produced by the CFD simulation. with a pressure surface and a suction. Furthermore, data analysis was carried out by comparing the simulation results on open water with the CFDs method with data on the Wageningen B-Series Propellers curve. The results are obtained in Figure 7. Experimental data were obtained using calculations to validate numerical results. Non-dimensional thrust and torque coefficients, efficiency values, and cavity patterns on the blades are examples of such parameters.

Table 2. *Carbon fiber Ply angle*

Unidirectional tape prepreg	Woven fabric prepreg
0 Ply	0 Ply
+45 Ply	90 Ply
-45 Ply	+45 Ply
90 Ply	-45 Ply

Testing by comparing several lightweight materials like carbon fiber has been carried out. This is useful for choosing the lightest carbon fiber material and will be used as a sample in this study. There are metallic and non-metallic materials such as bronze, titanium alloy, copper alloy, epoxy carbon fiber UD, and epoxy carbon fiber Woven and carbon fiber.

Therefore, in this analysis, two of the lightest carbon fiber materials were taken, namely, epoxy carbon fiber UD and epoxy carbon fiber Woven, with masses of 8.65 E-02 kg

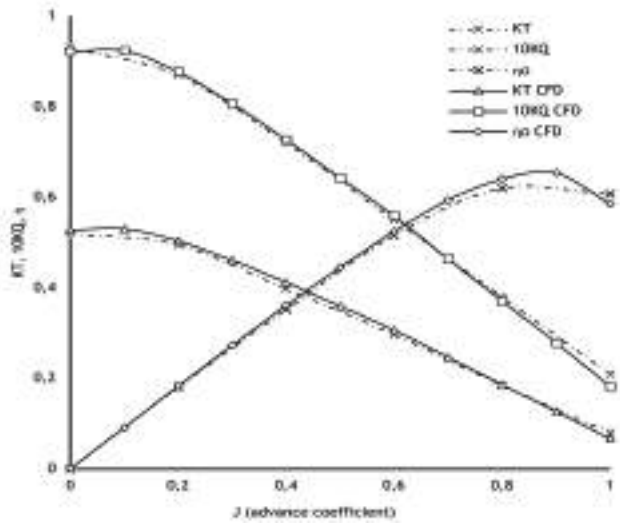

Figure 6. *Open-water test comparisons between the numerical and experimental results for propeller propulsion performance*

Table 3. *Properties of material assignment (ANSYS engineering data)*

Properties of the materials	Composite, epoxy/CF, UD prepreg, QI		Composite, epoxy/CF, woven prepreg, QI	
Density	1565	kg/mm³	1575	kg/mm³
Young's modulus	5.465e+10	Pa	4.616e+10	Pa
Poisson's ratio	0.306		0.337	
Bulk modulus	4.695e+10	Pa	4.7198e+10	Pa
Shear modulus	2.0923e+10	Pa	1.7263e+10	Pa
Isotropic secant coefficient of thermal expansion	1.203e-06	1/°C	1.27e-05	1/°C
Tensile ultimate strength	6.667e+08	Pa	5.402e+08	Pa
Tensile yield strength	6.667e+08	Pa	5.402e+08	Pa
Properties of the materials	**Titanium alloy**		**Copper alloy**	
Density	4620	kg/mm³	8300	kg/mm³
Young's modulus	9.6e+10	Pa	1.1e+11	Pa
Poisson's ratio	0.36		0.34	
Bulk modulus	1.1429e+11	Pa	1.1458e+11	Pa
Shear modulus	3.5294e+10	Pa	4.1045e+10	Pa
Isotropic secant coefficient of thermal expansion	9.4e-06	1/°C	1.8e-05	1/°C
Tensile ultimate strength	1.07e+09	Pa	4.3e+08	Pa
Tensile yield strength	9.3e+08	Pa	2.8e+08	Pa

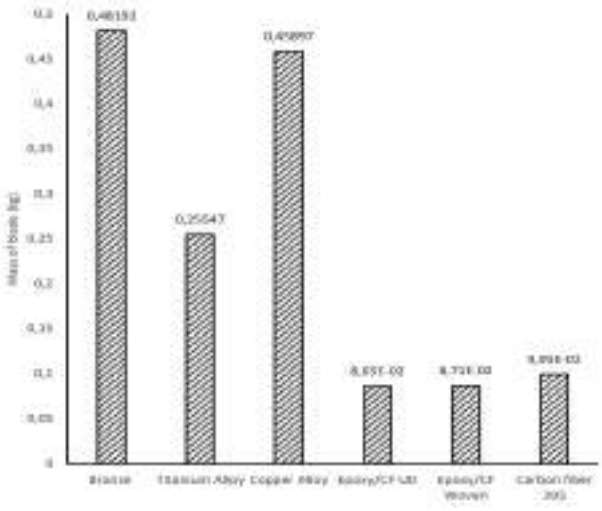

Figure 7. Material weight comparison of propeller blades

and 8.71 E-02 kg, respectively. When compared to metallic materials such as copper alloys with non-metallic materials such as epoxy carbon fiber UD, a ratio value of 1:5 was obtained.

Two varieties of carbon fiber were used in this investigation for each parameter by the result of. Using materials that have been dispersed in CFD simulations as pressure loads on open-water tests at values J=0 to J=1, the first parameter simulates testing with loads in the form of pressure. Epoxy carbon fiber UD and epoxy carbon fiber Woven are the materials. In addition, the outcomes of both material types will be shown in J values in accordance with the ship's operating conditions.

3.1. Blade Deformation

The results of these two materials are compared with the deformation of two metallic materials, titanium alloy and copper alloy, as a reference for comparison of the total deformation values. In Figure 8, compared to four materials

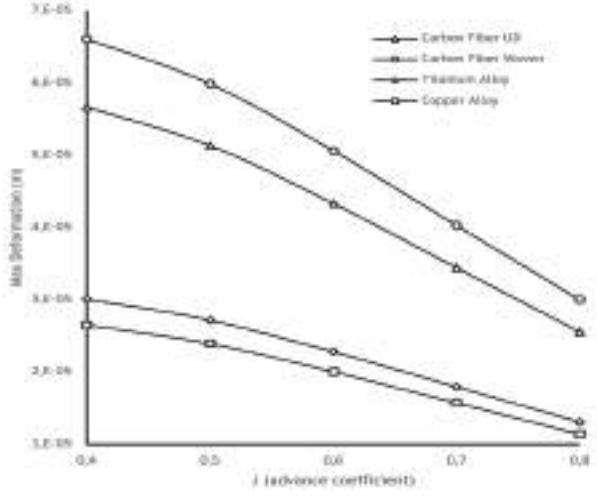

Figure 8. Maximum deformation curve

in the curve in the range of J=0.4-0.8. From metallic materials, the deformation value of copper alloy is smaller than that of titanium alloy, while in non-metallic materials, the deformation value of the epoxy carbon fiber UD material is lower than that of the epoxy carbon fiber Woven. In general, both non-metallic materials have a relatively similar deformation trend when compared to metallic materials; in other words, these non-metallic materials have a reasonable deformation value because of their properties.

Deformation on the blade is then analyzed on the basis of the blade section, with a range of numbers 1-15 corresponding to Figure 9. Starting from blade section 1 is the largest deformation value, then continuing down until blade section 15 is the smallest value. On the curve, the deformation value is displayed on the basis of the blade section for four comparison materials. The curve in metallic materials tends to slope compared with non-metallic materials or carbon fibers, which have a significant difference in deformation values in each blade section. Of course, this is a consideration in analyzing propellers with carbon fiber material using metallic material references. This is only limited to analyzing and detailing the results of blade deformation in the adjusted section, and the deformation results will be displayed in the form of contour only.

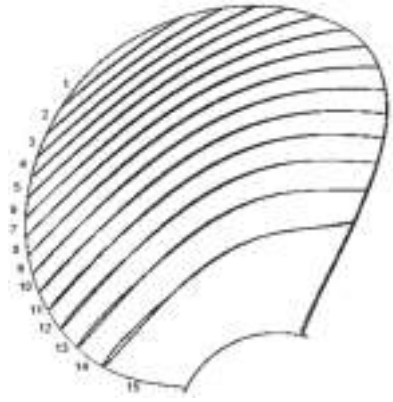

Figure 9. Blade section of the propeller

Furthermore, the results of this deformation are depicted on Figure 10-14 illustrates how variations in the form of carbon fibers impact the strength of the blades under load, causing these two materials maximum total deformation at the blade tips to differ. From the results of structural analysis with a fluid structure interaction approach, the largest deformation value was obtained in epoxy carbon fiber woven material at a value of J=0.4 of 6.81E-05m. and the lowest deformation value was in copper alloy material at J=0.8 of 1.34E-05m. When compared to non-metallic materials, the deformation value of epoxy carbon fiber UD is quite low, with a difference of 4.44E-06m, compared to epoxy carbon fiber woven at J=0.8.

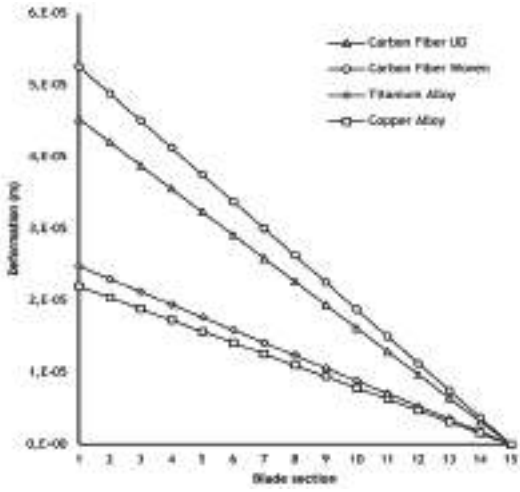

Figure 10. *Maximum deformation by blade section at J=0.6*

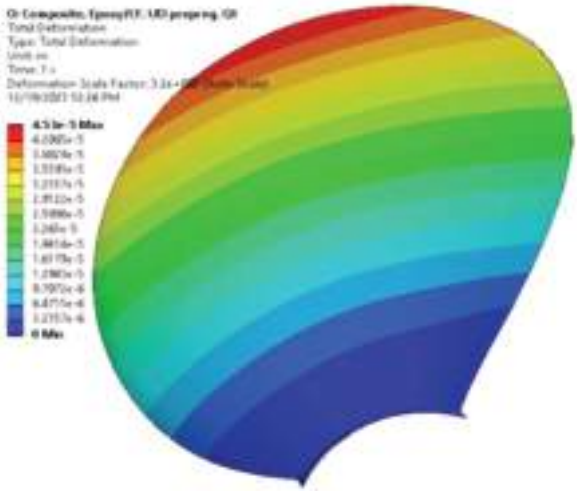

Figure 11. *Maximum deformation c/f UD at J=0.6*

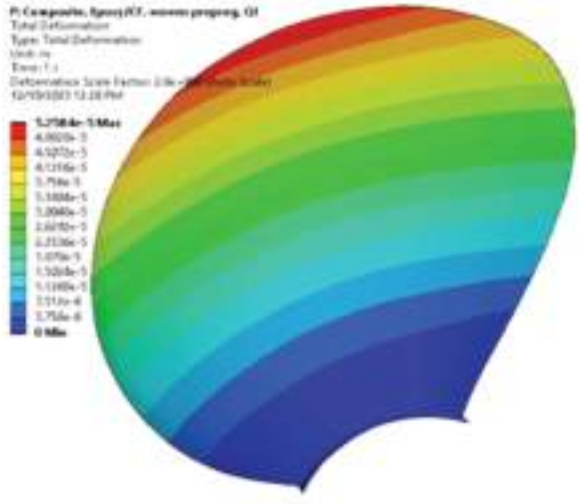

Figure 12. *Maximum deformation c/f woven at J=0.6*

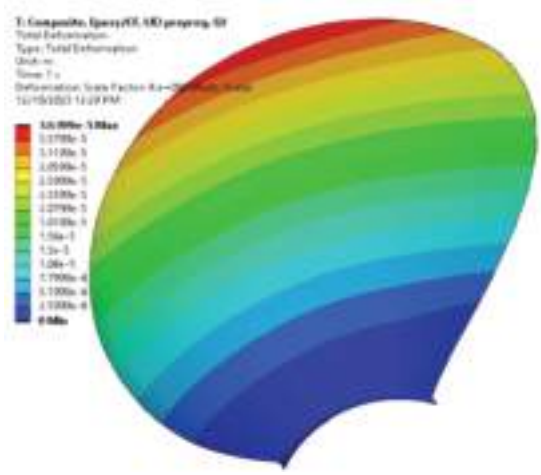

Figure 13. *Maximum deformation c/f UD J=0.7*

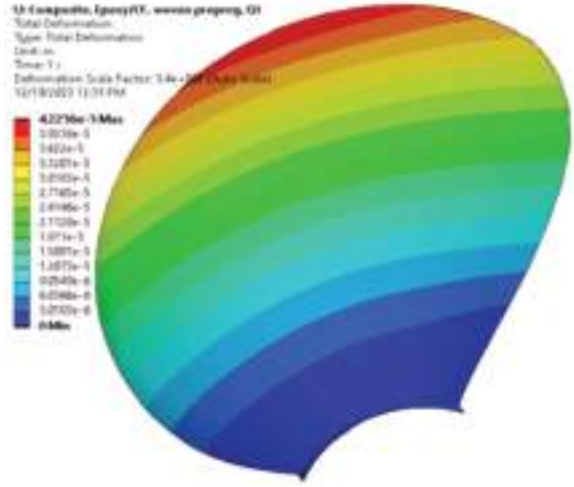

Figure 14. *Maximum deformation c/f woven at J=0.8*

It is clear from the data in the table and curve that woven and carbon fiber UD deformation is significantly greater than that of metallic materials like copper and titanium alloys.

Maximum blade deformation occurs in a carbon fiber woven material, with an illustration of comparison with solid materials that do not deform according to the illustration in Figure 15.

Blade stress analysis was carried out by inputting data from the results of the open water test in the form of pressure at conditions J=0.4 to J=0.8. Figure 16 illustrates how the data comparison is produced as a curve. The curve above show that UD carbon fiber has a low value, ranging from J=0.4 to J=0.8. This suggests that these two materials respond differently to loads.The results of equivalent (von-misses) stress tend to be identical in results. each J value. For carbon

fiber materials, there is a maximum equivalent (von-misses) stress that is different from the two materials above. The difference occurs with a fairly large difference in value between 4.43E+06 Pa and 4.51E+06 Pa, the minimum value between 37170 Pa and 41713 Pa. This greater value for the carbon fiber woven material indicates that the response to the load received by this material has a greater value. Here, there is a difference between the maximum value and the minimum value.

Additionally, the maximum equivalent (von-misses) stress values for metallic materials values of maximum equivalent (von-misses) stress are 4.60E+06 Pa and 4.52E+06 Pa respectively and minimum values are 32870 Pa for Titanium Alloy and 33482 Pa for Copper Alloy. Compared with previous results at J=0.6, the minimum stress distribution value has a relatively small difference. At both the pressure surface and suction surface positions, which are dominated by the minimal stress value throughout nearly the entire blade surface, the stress distribution patterns in the image are identical to one another. Figure 17 to Figure 20 illustrates the difference in maximum equivalent (von-misses) stress

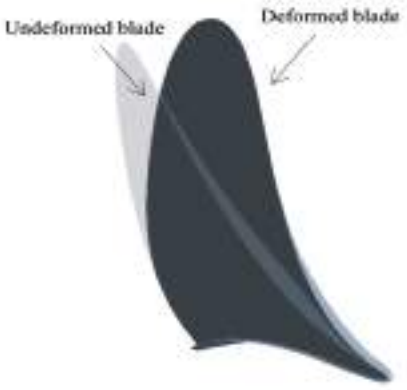

Figure 15. *Undeformed and deformed blade carbon fiber woven material under maximum load*

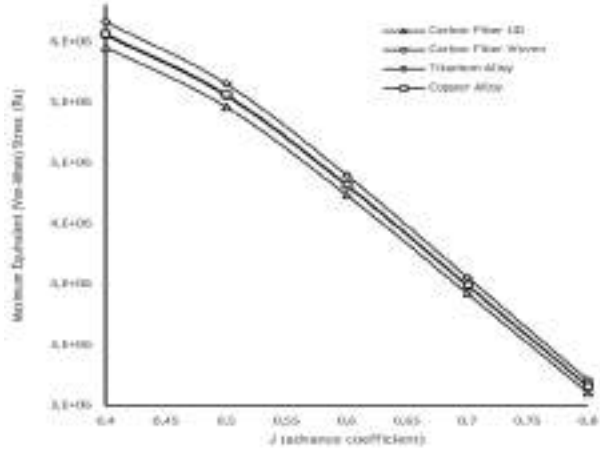

Figure 16*. Maximum equivalent (von-misses) stress curve*

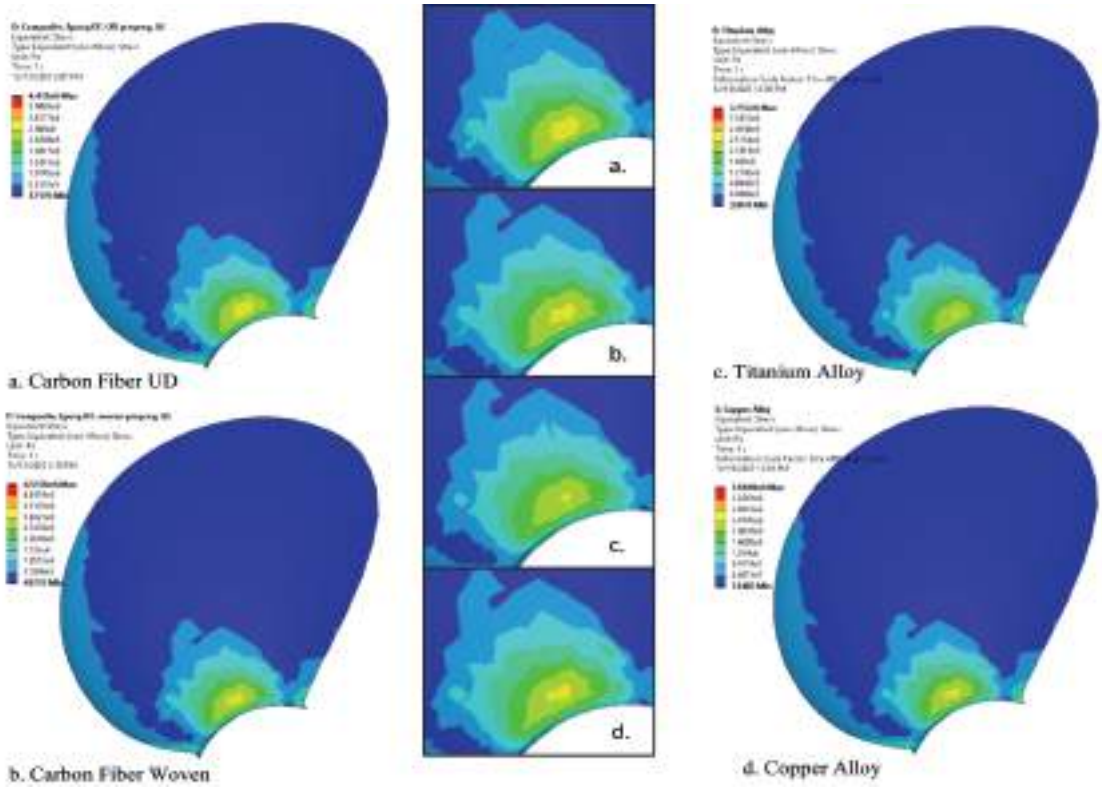

Figure 17. *Equivalent (von-misses) stress at J=0.6 carbon fiber materials, suction surface*

Figure 18. *Equivalent (von-misses) stress at J=0.6 metallic materials suction surface*

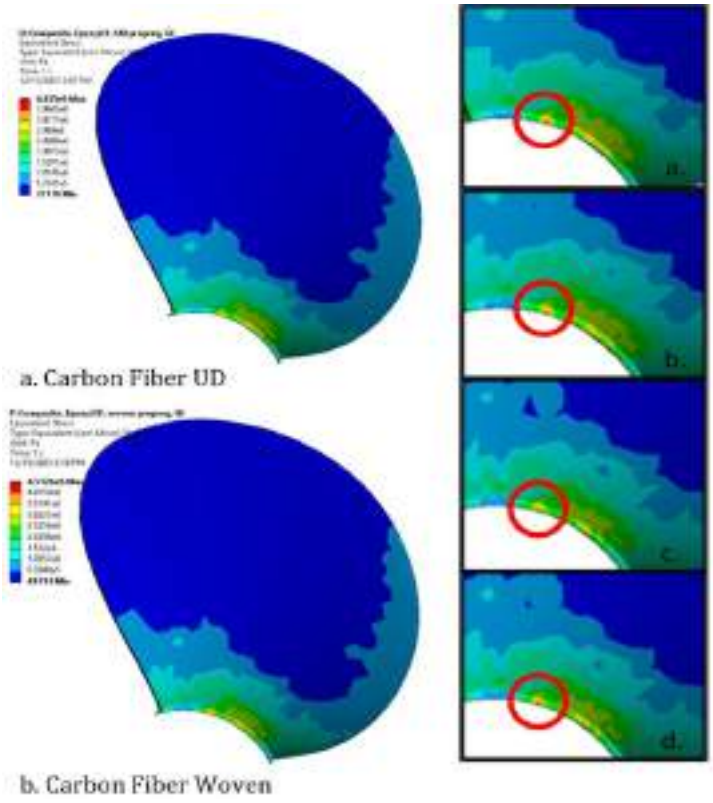

Figure 19. *Equivalent (von-misses) stress at J=0.6 carbon fiber materials, pressure surface*

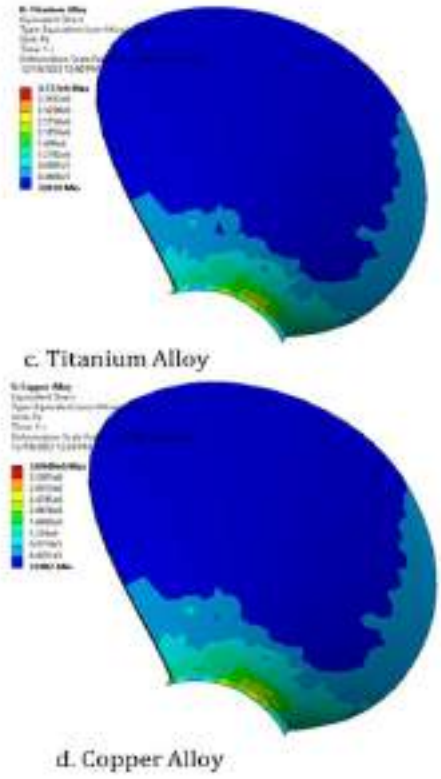

Figure 20. *Equivalent (von-misses) stress at J=0.6 metallic materials, pressure surface*

in carbon fiber UD and carbon fiber woven materials by comparing them with metallic materials such as titanium alloy and copper alloy. The stress distribution on the UD carbon fiber material is often smaller than that on the woven carbon fiber material.

The equivalent (von-misses) stress results at J=0.6 for both materials tend to follow the same pattern at the propeller's pressure and suction surface locations, with the minimal stress distribution coefficient being the determining factor. Looking at Table 2, it is clear that the maximum equivalent (von-misses) stress can still be tolerated; therefore, even if it is at the bottom of the limit, it is not an issue.

4. Conclusion

In this study, a series of simulations on the use of carbon fiber in a B-5 propeller were carried out. The research has been completed with the following conclusions. From the results of the comparison of metallic and non-metallic materials, it can be concluded that the mass of the blade for epoxy carbon fiber material, both UD and woven, is five times lighter than that of copper alloy material, which has the advantage of the mass of the blade material being much lighter.

Thus, the use of this material can certainly be an alternative choice of material in marine propellers. It can be concluded that the epoxy carbon UD material is better and has a low deformation and equivalent (Von-Mises) stress value when compared to epoxy carbon fiber woven material. It is highly recommended to use the epoxy carbon UD prepreg material for marine propeller use. Deformation of the blade is caused by the pressure received by the propeller blade, so the influence of pressure affects the value of deformation in the blade. This can be used as a further analysis of the optimum design laminate of carbon fiber on the blade propeller.

Of course, this research can still be developed further by examining how deformation or deflection affects the propeller's operational efficiency, whether the effects of deformation interfere with performance or can increase the energy efficiency of the propeller, or in other words, improve the performance of the propeller compared to general propeller materials. Additionally, deformation of the propeller blades will result in deflections, which will undoubtedly impair the marine propeller's operational performance in future analysis.

In addition, the deformation of the propeller will result in deflection, which will undoubtedly affect the operational performance of the marine propeller, whether to further increase or decrease the propeller's performance in future analysis.

Acknowledgment

We express our sincere gratitude to the Marine Power and Propulsion Laboratories, Department of Marine Engineering, Institut Teknologi Sepuluh Nopember.

Authorship Contributions

Concept design: F. I. Ahsan, I. M. Ariana, and A. Z. M. Fathallah, Data Collection or Processing: F. I. Ahsan, Analysis or Interpretation: F. I. Ahsan, I. M. Ariana, and A. Z. M. Fathallah, Literature Review: F. I. Ahsan, I. M. Ariana, and A. Z. M. Fathallah, Writing, Reviewing and Editing: F. I. Ahsan, I. M. Ariana, and A. Z. M. Fathallah.

Funding: The authors declare that no funds, grants, or other support was received during the preparation of this manuscript.

References

[1] Derek Hull. Engineering with fibre-polymer laminates: By peter powell. chapman & hall, london, 1994 (441 pp.+ xvii). isbn 0 412 496100 (hb). Greene, E. (1997). Design Guide for Marine Applications of Composites, SSC-403, Jan 1997.

[2] Y. L. Young, J. W. Baker, and M. R. Motley, "Reliability-based design and optimization of adaptive marine structures". *Composite Structures,* vol 92, pp. 244-253, Jan 2010.

[3] B.-G. Paik, et al. "Investigation on the performance characteristics of the flexible propellers". *Ocean Engineering,* vol. 73, pp. 139-148, Nov 2013.

[4] Y. L. Young, M. R Motley, R. Barber, E. J. Chae, and N. Garg, "Adaptive composite marine propulsors and turbines: progress and challenges". *Applied Mechanics Reviews,* vol. 68, 060803, Nov 2016.

[5] I. M. Ariana, R. B. Prihandanu, D. W. Handani, and A. A. B. Dinariyana, "Investigation of the effects of the pre-duct in a ship on propeller–hull interactions using the CFD method". *CFD Letters,* vol. 15, pp. 17-30, 2023.

[6] I. Fikry, I. M. Ariana, and C. Kusuma, "Propeller performance analysis on the modification of trailing edge shape as anti-singing". *IOP Conference Series: Earth and Environmental Science*, vol. 1166, 012005, 2023.

[7] A. Purwana, I. M. Ariana, and W. Wardhana, "Numerical study on the cavitation noise of marine skew propellers". *Journal of Naval Architecture and Marine Engineering,* vol. 18, pp. 97-107, Dec 2021.

[8] J. W. Cohen. *On stress calculations in helicoidal shells and propeller blades*. Waltman, 1955.

[9] P. Atkinson, "On the choice of method for the calculation of stress in marine propellers". *Trans RINA,* vol. 110, pp. 447-463, 1968.

[10] S. Paboeuf, B. Collier, P. Berthelot, F. Le Lay, and L.-A. Vialle, "Composite blade propeller: a design assessment approach". *chez 4th International Conference on Mechanics of Composites*, 2018.

[11] F. Zhang, and J. Ma, "FSI analysis the dynamic performance of composite propeller". Conference: ASME 2018 37th International Conference on Ocean, Offshore and Arctic Engineering, Jun 2018.

[12] R. Vijayanandh, K. Venkatesan, M. Senthil Kumar, G. Raj Kumar, P. Jagadeeshwaran, and R. Raj Kumar,"Comparative fatigue life estimations of marine propeller by using FSI". *Journal of Physics: Conference Series,* vol. 1473, 012018, 2020.

[13] G. Yang, X. Ying, and H. Zheng, "Computation of composite propeller's two-way fluid-structure coupling". *Ship Science and Technology,* vol. 37, pp. 16-20, 2015.

[14] Z. Huang, Y. Xiong, and H. T. Sun, "Thicken and pre-deformed design of composite marine propellers". *Journal of Propulsion Technology,* vol. 38, pp. 2107-2114, 2017.

[15] Z. Huang, Y. Xiong, and G. Yang, "A fluid-structure coupling method for composite propellers based on ANSYS ACP module". *Jisuan Lixue Xuebao/Chinese Journal of Computational Mechanics,* vol. 34, pp. 501-506, Aug 2017.

[16] Z. Huang, Y. Xiong, and G. Yang, "A comparative study of one-way and two-way fluid-structure coupling of copper and carbon fiber propeller". *J Nav Univ Eng,* vol. 29, pp. 31-35, 2017.

[17] S. Han, H. Lee, M.C. Song, Chang, B. J. Investigation of hydro -elastic performance of marine propellers using fluid-structure interaction analysis, ASME Int. Mech. Eng. Congr. Expo. Proc. 7A –2015.

[18] H. Lee, M. C. Song, S. Han, B. Chang, and J.-C. Suh, "Hydro-elastic aspects of a composite marine propeller in accordance with ply lamination methods". *Journal of Marine Science and Technology,* vol. 22, pp. 479-493, Jan 2017.

[19] J. Carlton, *Marine propellers and propulsion*. Elsevier Science, 4th edition, 2012.

[20] Ö. K. Kınacı, and C. Delen, "Advancing computational hydroacoustics for marine propellers: investigating the limits of incompressible solvers in far-field noise prediction". *Journal of ETA Maritime Science*, vol. 11, pp. 110-118, Jun 2023.

[21] Ş. Bal, "Numerical investigation of propeller skew effect on cavitation". *Journal of ETA Maritime Science*, vol. 7, pp. 127-136, Jun 2019.

[22] K. Yu, P. Yan, and J. Hu, "Numerical analysis of blade stress of marine propellers". *Journal of Marine Science and Application,* vol. 19, pp. 436-443, Oct 2020.

[23] M. R. Motley, Z. Liu, and Y. L. Young, "Utilizing fluid–structure interactions to improve energy efficiency of composite marine propellers in spatially varying wake". *Composite Structures,* vol. 90, pp. 304-313, Oct 2009.

ORIGINAL RESEARCH (AR) DOI: 10.4274/jems.2024.54926

Journal of ETA Maritime Science 2024;12(3):287-294

Correlation of the Dielectric Constant and Conductivity of Marine Motor Oils

Oksana Synashenko[1], Evgenia Rabenok[2], Mikhail Gapanovich[2], Nikolay Sinyavsky[1]

[1]Kaliningrad State Technical University, Department of Physics, Kaliningrad, Russia
[2]Federal Research Center of Problems of Chemical Physics and Medicinal Chemistry RAS, Chernogolovka, Russia

Abstract

The study of marine lubricants using modern methods for quality control and diagnostics of engine conditions is an important task. The solution to this task determines the technical condition of ships, their performance, and accident-free operation in maritime transport. In this study, the properties of several marine motor oils were studied using broadband dielectric spectroscopy. The complex dielectric constant, conductivity, and loss tangent of base oil, Shell Rimula 15W40 oil fresh and used for 250 and 500 h were studied. The influence of the test voltage frequency and temperature on the selected electrical parameters was determined. In used oils, the DC conductivity decreases slightly, which is apparently due to the depletion of additives. The increase in the conductivity of all studied oils with increasing current frequency is caused by the displacement current. It is shown that dielectric losses increase with frequency as long as the polarization has time to follow the change in the field. A shift in the frequency at which the maximum loss occurs with a change in temperature was discovered. The activation energies of polarization and conductivity were determined. The thermal activation energies obtained from the conductivity and dielectric constant are not significantly different. For the first time, the distributions of the dielectric constant relaxation times for the studied lubricating oils have been obtained. The dielectric relaxation time distribution function depends on the composition of additives in the oil, wear particles, contaminants, and the chemical degradation of the oil during operation. For the first time, correlations have been established between conductivity and dielectric constant at different temperatures and frequencies. These correlations can be used to select frequency ranges that provide stable parameter values and maximum diagnostic ability.

Keywords: Dielectric constant, conductivity, dielectric loss tangent, marine motor oils

1. Introduction

Motor oils are based on base oil and additive systems to reduce wear of parts, protect against gearboxes, remove contaminants, heat removal, and primary foam formation. Lubricating oil undergoes gradual degradation under the influence of high temperatures, water, air, and acidic contaminants (oil oxidation products). Accurate monitoring of oil wear is necessary for both technical and economic reasons.

Standard physicochemical testing methods used to control the quality and safety of motor oils are typically labor-intensive, expensive, destructive, and require multiple sampling. Electrical methods have some advantages over other methods: speed of measurement, low cost, and high testing efficiency. The electrical properties of technical materials are among the least studied. Several research centers around the world deal specifically with this area of research [1].

Kardoš and Pietriková [2] showed interest in monitoring the condition of motor oils from the point of view of determining degradation factors and diagnostics. The use of sensors and systems for real-time characteristic monitoring to control engine oil aging. For analysis, the dielectric constant and conductivity were examined. These characteristics are discussed as the basis for continuous oil diagnostics.

Schober et al. [3] investigated the conductivity of insulating oil, which is an important quantity for the design, diagnosis, and evaluation of the insulation condition of high-voltage DC systems. The paper presents and discusses conductivity estimates for the condition of insulation systems at various

Address for Correspondence: Oksana Synashenko, Kaliningrad State Technical University, Department of Physics, Kaliningrad, Russia
E-mail: oksanasynashenko@gmail.com
ORCID iD: orcid.org/0009-0004-3149-0345

Received: 13.02.2024
Last Revision Received: 17.05.2024
Accepted: 05.06.2024

To cite this article: O. Synashenko, E. Rabenok, M. Gapanovich, and N. Sinyavsky, "Correlation of the Dielectric Constant and Conductivity of Marine Motor Oils." *Journal of ETA Maritime Science*, vol. 12(3), pp. 287-294, 2024.

temperatures, field strengths, and for various types of oils. It has been established that electrical insulating oil has conductivity that depends nonlinearly on field strength, temperature, water content, and aging. In addition, its conductivity depends on time because of the drift of charge carriers.

Measurements of fresh and old oil are compared and taken into account when diagnosing oil-filled HVDC systems. Baturlya et al. [4] presented the results of a study of used motor oils using dielectric spectroscopy. A method for diagnosing oil using capacitive sensors is proposed, which is also suitable for mobile units.

Xu et al. [5] investigated the electrical conductivity of an oil film used in displays. Their study showed that the electrical conductivity of the oil film varies from pixel to pixel. This work shows that it is possible to characterize oil film resistance and heterogeneity using electrical impedance spectroscopy.

Barnoss et al. [6] studied the mechanisms of electrical conductivity of nanofluids based on motor oil saturated with graphite and multi-walled carbon nanotubes in different concentrations by the impedance spectroscopy method. The measurements were carried out at temperatures of 300-400 K in the frequency range 100 Hz-1 MHz. This work shows that the presence of carbon nanotubes significantly affects the electrical properties of motor oil. Analysis of the temperature dependence of direct current conductivity and relaxation time showed that the addition of carbon nanotubes increases the activation energy.

Popov et al. [7] proposed some criteria that can be used to check the analytical results of an expression describing data related to complex conductivity. It is shown that the polarization of the electrode is indirectly related to the relaxation phenomenon. The theoretical and experimental foundations of dielectric spectroscopy were considered by Sidambarompoulé et al. [8]. The main focus here is on insulating liquids and the study of diffusion and ion mobility.

Wolak et al. [9] assessed the suitability of the capacity and conductivity of fresh motor oils tested in a wide range of frequencies to determine the quality of the oil and its identification by physicochemical properties. Frequency ranges that provide maximum diagnostic efficiency have been identified.

Polarization caused by the injection current was studied by Zhou et al. [10]. A new model was proposed that considers the injection current. The frequency responses of the three different types of mineral oil were measured, and this new polarization model was used to interpret the experimental data. The new model allows us to better understand the phenomenon of electrical conductivity in mineral oil.

Izmestyev and Konyaev [11] the dielectric characteristics of some automotive motor oils were studied in the frequency range from 100 Hz to 3 MHz. The maximum in the frequency dependence of the dielectric loss tangent of used oil is due to the oxidation of hydrocarbons and is proposed to be used as a rejection indicator.

The polarization, conductivity, and dielectric losses of synthetic motor oils were studied by Izmest'ev and Kozhevnikova [12]. It is concluded that these oils are non-polar dielectrics in which electronic polarization occurs at high frequencies. In this study, the activation energy of conductivity, which depends on both viscosity and the presence of additives, is determined.

A review of studies of fresh and used marine motor oils conducted at the Kaliningrad Technical University using various optical and radio spectroscopic methods is given by Sinyavsky [13]. The possibilities of diagnosing a marine engine based on the characteristics of the used oil and the presence of wear products in it are discussed. Sinyavsky et al. [14] analyzed the distributions of dielectric relaxation times of some fresh and used marine motor oils. A connection between the distributions, the content of additives, and the presence of wear particles has been established. Thus, from a review of the literature, the electrical parameters of fresh and used motor oils can be successfully used to determine their physicochemical properties and diagnose their condition.

The purpose of this study was to assess the possibility of using the dielectric constant, spectrum of relaxation times, conductivity, and loss tangent measured over a wide frequency range to assess the quality of marine motor oil and its identification. A key step toward achieving this goal is to determine the effect of frequency on electrical parameters and to test whether there is a correlation between these parameters at different frequencies and temperatures. This will allow determining the optimal frequency range of the test voltage in future research.

2. Experimental Technique

The measurements were performed on a broadband dielectric spectrometer "Novokontrol" in the frequency range $f=10^{-2}$-10^{5} Hz and at temperatures from -30 to 200 °C. The sample temperature during the measurements was controlled with an accuracy of 0.5 °C. The measuring cell consisted of two gold-plated copper electrodes. The gap between the electrodes was 50 μm and was fixed using quartz spacers. The diameter of the electrodes was 20 mm. The voltage between the electrodes was 1 V.

For simple liquids, polarization decreases with increasing frequency with one characteristic relaxation time. In this case, the Debye equation for the complex relative dielectric constant has the following form [1]:

$$\varepsilon^* = \varepsilon' - i\varepsilon'' = \varepsilon_\infty + \frac{\varepsilon_s - \varepsilon_\infty}{1 + i\omega T_r} \quad (1)$$

where ω - cyclic frequency, ε_∞ - dielectric permittivity at $\omega \to \infty$, ε_s - dielectric permittivity at $\omega \to 0$, T_r - dielectric relaxation time.

Motor oil is a complex mixture of dipole molecules that relax with different relaxation times. If the distribution function of these relaxation times is denoted as $G(T_r)$, the real dielectric permittivity for motor oil can be written as follows:

$$\varepsilon'(\omega) = \int_0^\infty G(T_r) \frac{\varepsilon_s + \varepsilon_\infty \omega^2 T_r^2}{1 + \omega^2 T_r^2} dT_r \quad (2)$$

The spectrum of dielectric relaxation times G(Tr) is determined both by the degradation of oil hydrocarbons, the additive package, and the presence of wear products. The function G(Tr) was obtained by finding the inverse transformation of Equation (2), similar to [14].

3. Results and Discussion

Fresh motor oils are non-polar dielectrics. The polar component occurs after the oxidation of oil hydrocarbons. The temperature and frequency dependence of the dielectric permittivity contain information about the polarization mechanisms and their relative contribution to the resulting polarization of the medium.

The dependence of the real part of the dielectric constant on frequency at different temperatures for the four oils is shown in Figure 1. At low frequencies of voltage applied to the sample, molecular dipoles follow changes in the electric field.

Motor oils contain several additives, and the charge carriers can be ions formed as a result of the dissociation of hydrocarbon molecules or impurity molecules. As the degree of dissociation increases, the dielectric permittivity increases. However, ionic electrical conductivity is determined mainly by additives because dissociation of the main oil molecules is unlikely. When oil degrades, its conductivity increases because of moisture absorption, formation of polymerization products, and oil oxidation.

The dependence of the real part of the conductivity and the loss tangent on the frequency at different temperatures are illustrated in Figure 2 and 3. On the graph $\log(\sigma') = \varphi(\log(f))$a plateau is observed in the low frequency range. As the

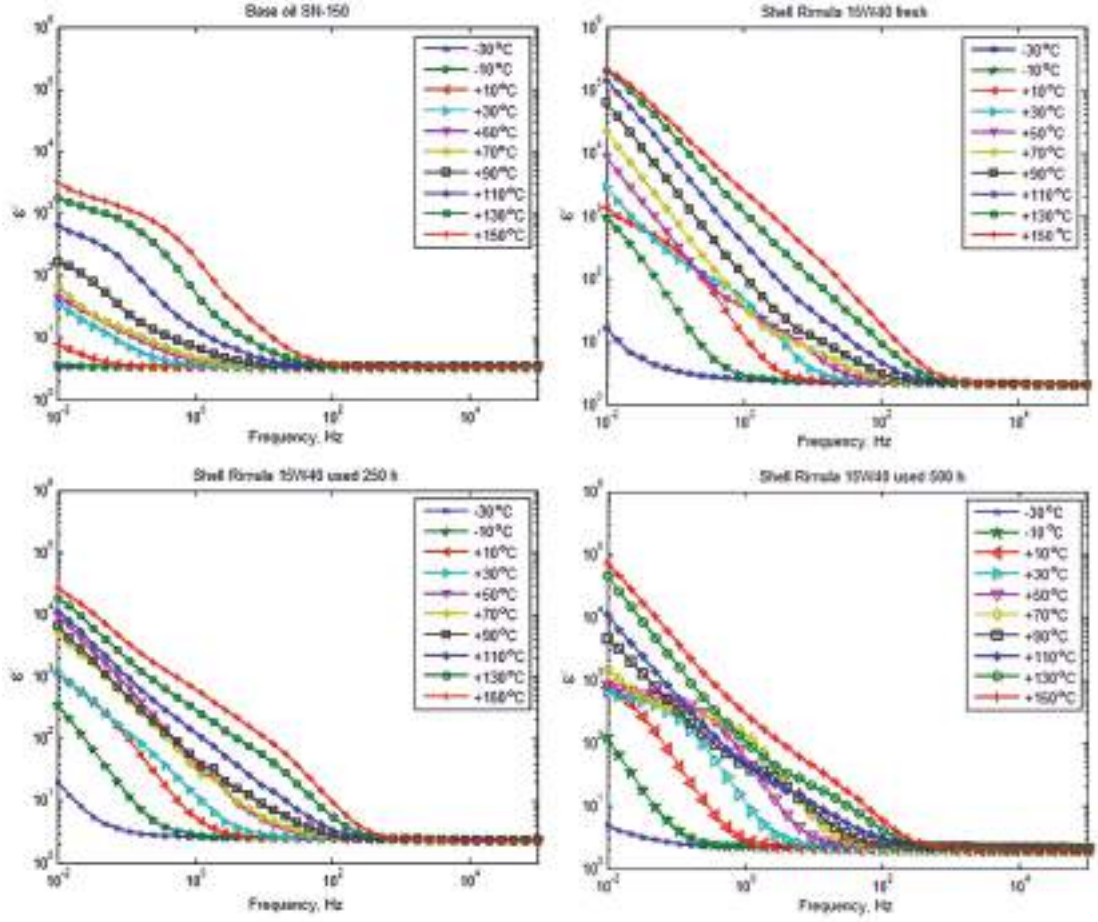

Figure 1. *Dependences of the real part of the complex dielectric permittivity ε' of oils with frequency for different temperatures*

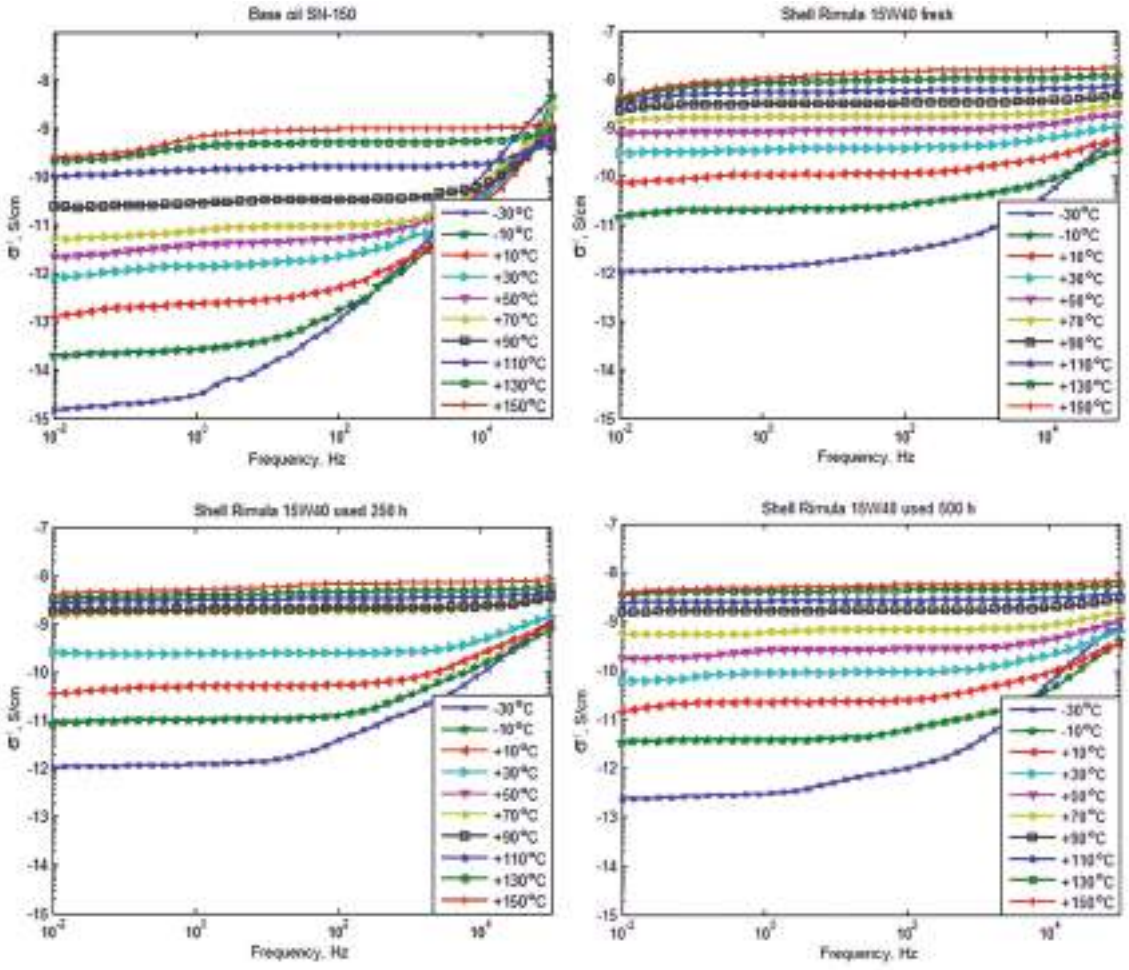

Figure 2. *Dependence of the real part of the specific conductivity σ/ of oils on the frequency at different temperatures*

temperature increases, the plateau also extends into the high-frequency region. The presence of a plateau is related to the transport of free charges [15,16]. The transition from a plateau to a change in σ'_{ac} from frequency indicates a change in the conduction mechanism. By observing the dielectric constant of oil ε' in the low frequency region, where it is constant, it is possible to determine the static conductivity σ_s.

Figure 2 shows the effect of temperature on the conductivity of the oil samples at different current frequencies. At temperature (t=30 ºC), the conductivity of the base oil is much lower than that of fresh ShellRimula 15W40 oil and gradually increases with temperature. This is due to the presence of a package of improving additives in ShellRimula 15W40 oil. One would expect the conductivity of used oils to increase because of waste metal wear particles and soot (carbon) particles, but this does not happen. In used oils, the DC conductivity decreases somewhat, which is apparently due to the depletion of additives. At low frequencies, the behavior of electrical conductivity is almost independent of frequency and is described by direct current conductivity. The increase in the conductivity of all studied oils with increasing current frequency is caused by the displacement current. In addition, at high frequencies, electrical conductivity occurs as a result of translational motion with sudden jumps in the electron. As the temperature increases, the polar group of the molecules becomes oriented, which facilitates the transfer of electrons, leading to an increase in conductivity.

In an alternating electric field, oil losses depend on frequency as follows. At low frequencies, they decrease with increasing frequency. As the frequency increases, losses increase, reach a maximum, and decrease, tending to low values.

In polar dielectrics, power dissipation is mainly determined by frictional losses due to the orientation of the dipole molecules. Therefore, dielectric losses increase with frequency until the polarization has time to follow the change in the field, and tgδ also increases (Figure 3). When the frequency becomes so high that the dipole molecules no longer have time to completely orient themselves in the direction of the field, tgδ drops and the losses become constant.

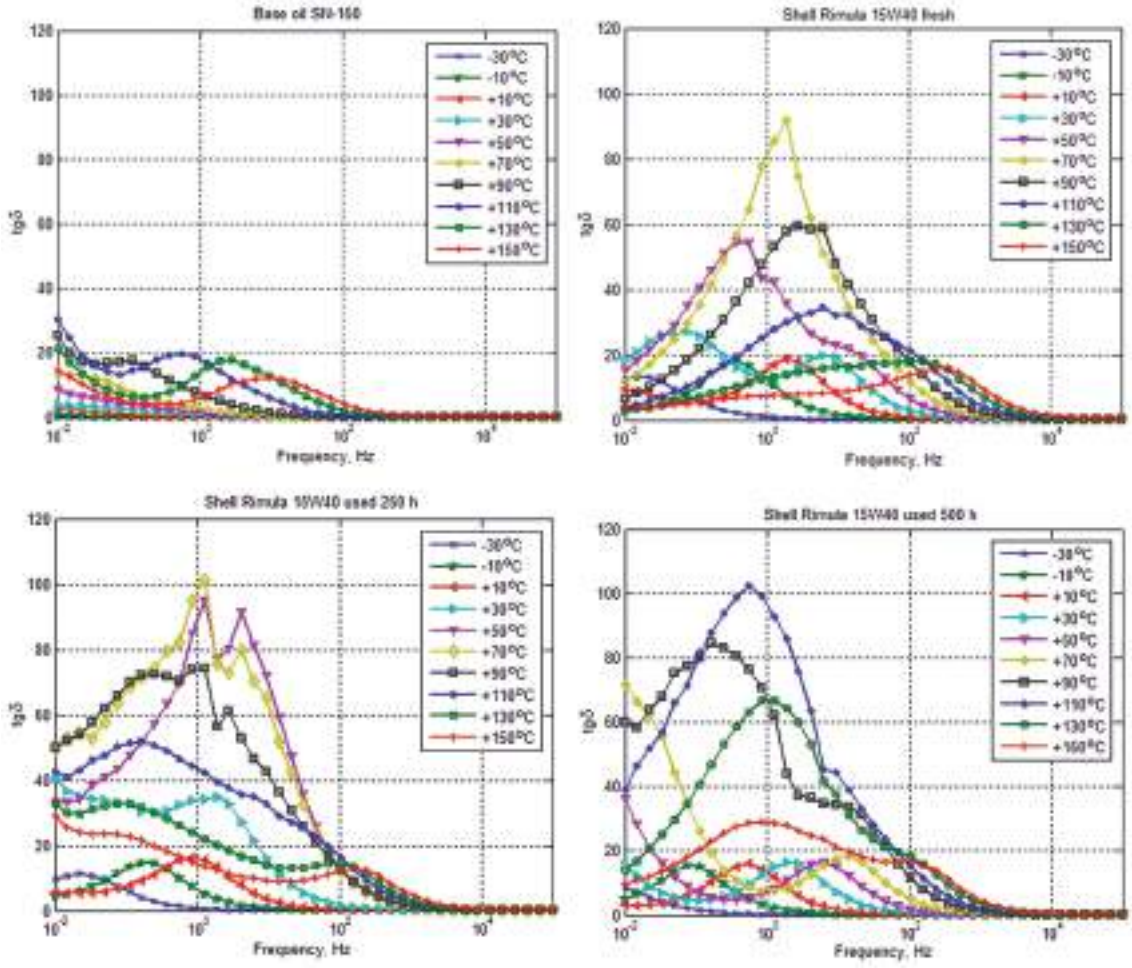

Figure 3. *Dependence of the dielectric loss tangent tg(δ) of oils on frequency at different temperatures*

The dielectric loss tangent for the Debye model can be written as follows:

$$\mathrm{tg}\delta(\omega) = \frac{\varepsilon''}{\varepsilon'} = \frac{(\varepsilon_s - \varepsilon_\infty)\omega T_r}{\varepsilon_s + \varepsilon_\infty \omega^2 T_r^2} \quad (3)$$

The frequency at which the maximum dielectric loss occurs is found from Equation (3) and has the form:

$$\omega_{max} = \frac{1}{T_r}\sqrt{\frac{\varepsilon_s}{\varepsilon_\infty}} \quad (4)$$

A shift in the frequency at which the maximum losses occur with a change in temperature is observed in all graphs in Figure 3. For the base oil, the tgδ(ω) spectra are single-humped; for Shell Rimula 15W40 oil, at some temperatures, they are more complex because of the presence of several relaxation times for different oil components. The dielectric loss tangent is determined by the presence of acidic and alkaline additive ions. With increasing oil operating time, the value of the Debye loss maximum increases and shifts to lower frequencies, which is caused by the appearance of dipole molecules and an increase in their content.

All oils are non-polar dielectrics with ionic conductivity and an exponential increase in conductivity with increasing temperature.

The polarization of non-polar dielectrics occurs as a result of charge displacement under the influence of an applied voltage. As can be seen from the experiments, with increasing temperature, the real part of the dielectric constant increases.

The activation energy of conductivity at direct current is determined using the Arrhenius formula:

$$\sigma_s = \sigma_{s0}\exp\left(-\frac{E_{a\sigma}}{kT}\right) \quad (5)$$

The activation energy of polarizability (dielectric constant) is determined using a formula similar to (5). Figure 4

shows the plots used to fit the linear equation to the above equation. On the conductivity graph, we can observe that changes occur at the critical temperature T_c= 400 K, which indicates a transition in the conductivity mechanism. On the one hand, the thermal activation energies obtained from the conductivity and dielectric constant do not differ significantly.

However, the conductivity activation energy of used oils increases from 0.389 eV to 0.480 eV compared with fresh oil (Table 1). In contrast, the activation energy of the dielectric constant of waste oils decreases from 0.423 eV to 0.394 eV. The activation energy of conductivity below 0.5 eV indicates that the samples have higher electrical conductivity than ionic conductivity [6].

The activation energies of ionic conductivity in the studied oils are determined not only by the viscosity of the dispersion medium, which limits the mobility of electric current carriers, but also by the dissociation energy of additives [13].

Application of Equation (3) and inversion of the integral transformation made it possible to find the distribution functions $G(T_r)$ of dielectric relaxation times for all studied oils at different temperatures (Figure 5). The relaxation time distribution functions are unimodal only at low temperatures. With increasing temperature, the distributions become multimodal because of the appearance of different polar molecules after the oxidation of oil hydrocarbons. These molecules have different relaxation rates, which are also found in the complex form of Debye peaks in the tgδ(ω) dependence (Figure 3).

By excluding the frequency ω from the dependence σ(ω) and ε(ω), we can obtain a relationship between σ and ε for Shell Rimula 15W40 oil fresh and used at different temperatures (Figure 6).

From Figure 6 it can be seen that in various dielectric constants ε, conductivity σ does not depend on ε. The only exceptions are very small and numerous values of ε. The dependence curves for fresh and used oils at different temperatures are similar.

Excluding temperature from the dependences σ(T) and ε(T), we obtain a relationship between σ and ε for Shell Rimula 15W40 oil fresh and used at different current frequencies (Figure 7). Here, the conductivity also changes sharply only at large and small values of ε. At intermediate values of ε, the conductivity changes, but not so much. The curves for fresh and used oils are similar to shape.

In the future, it is planned to study the concentration of wear particles in used motor oil using proton NMR spectroscopy and determine the elemental composition of oils using atomic emission spectroscopy for engine diagnostics.

4. Conclusion

Using broadband dielectric spectroscopy, the electrical characteristics of marine diesel lubricants were determined

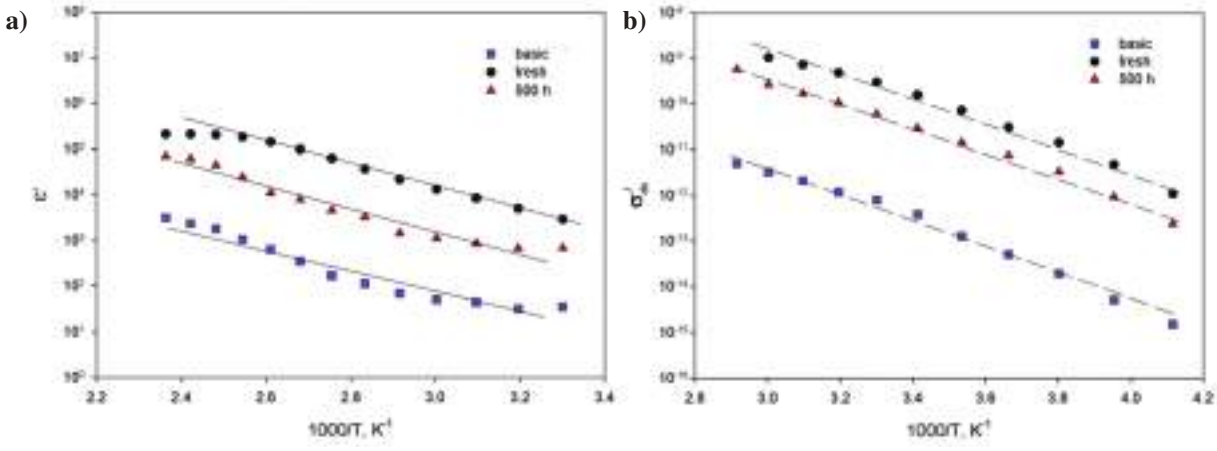

Figure 4. *Dependences of dielectric constant εs (a) and specific conductivity σs (b) on temperature for base oil SN-150 (1), oil Shell Rimula 15W40 fresh (2), and oil Shell Rimula 15W40 used for 500 h (3)*

Table 1. *Activation energies of the DC conductivity and polarizability of oils*

No	Activation energy	Base oil SN-150	Shell Rimula 15W40 fresh	Shell Rimula 15W40 used 250 h	Shell Rimula 15W40 used 500 h
1	$E_{a\sigma}$, эВ	0.605±0.019	0.525±0.020	0.406±0.030	0.480±0.015
2	$E_{a\varepsilon}$, эВ	0.466±0.036	0.431±0.020	0.293±0.023	0.394±0.028

at different temperatures and frequencies. The methods used in this study made it possible to study changes in the electrical parameters of used motor oil and establish a correlation between them.

- The presented results show good agreement with the available literature data and confirm the contribution that the proposed methods can make to the study of the characteristics of dielectric liquids.

- Analysis of the data obtained in the work made it possible to determine the distributions of the dielectric constant, electrical conductivity, and dielectric loss tangent.

- The correlations identified during the study can be used to select frequency ranges that will provide stable parameter values and maximum diagnostic ability.

- Establishing a connection between electrical and physicochemical parameters will allow us to create an effective algorithm for testing motor oils.

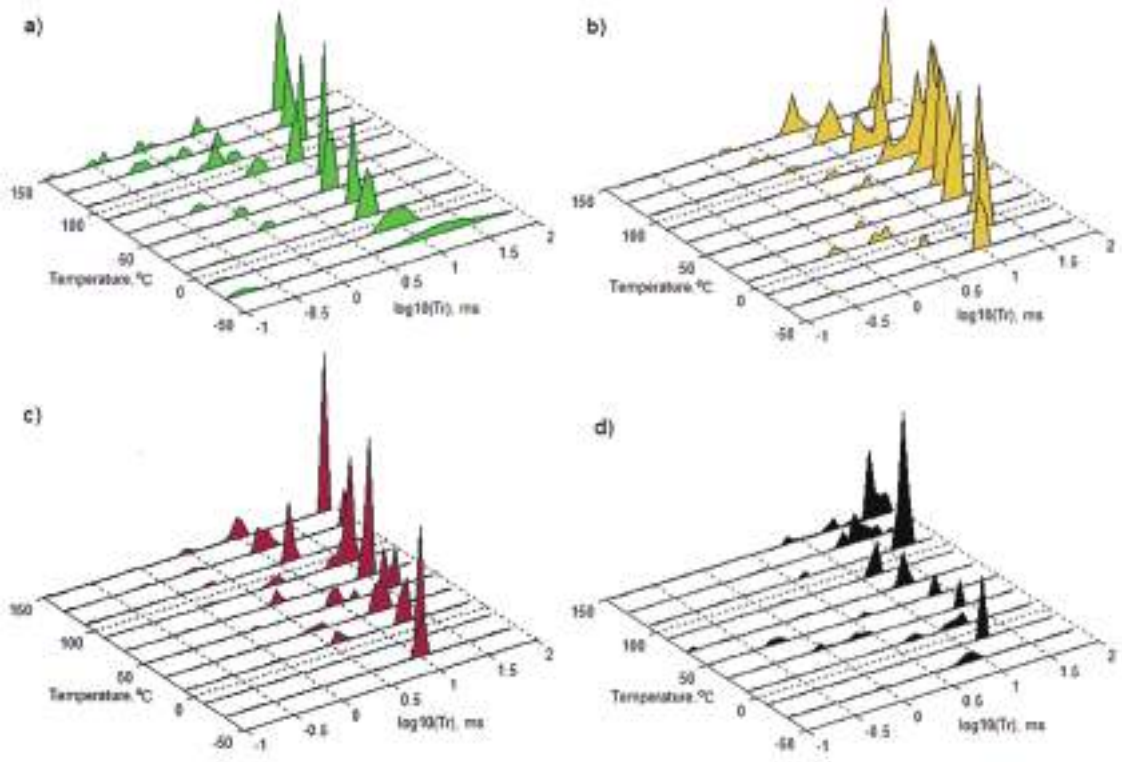

Figure 5. *Distributions of relaxation times Tr depending on temperature: base oil SN-150 (a), Shell Rimula 15W40 fresh (b), Shell Rimula 15W40 used for 250 h (c), Shell Rimula 15W40 used for 500 h (d)*

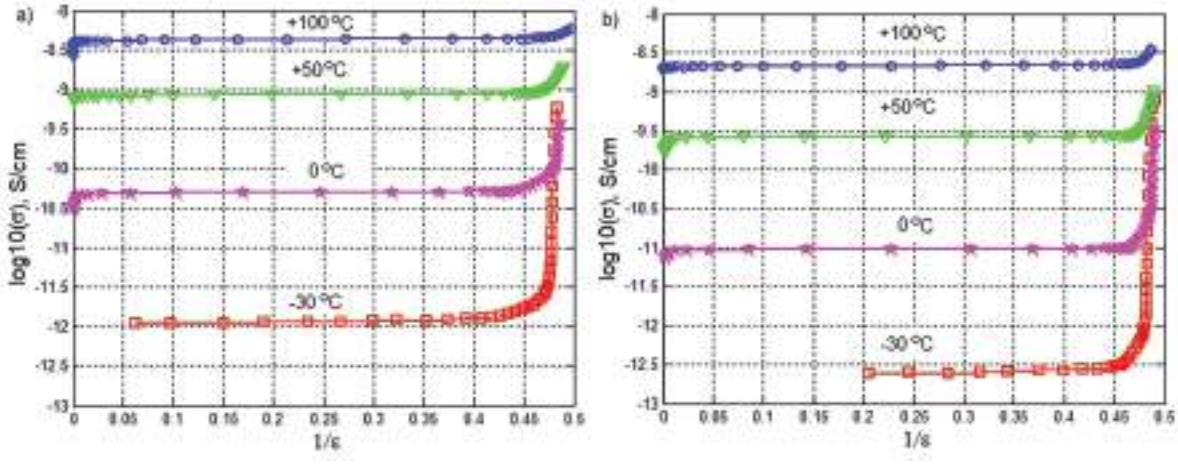

Figure 6. *Relationship between the specific conductivity and dielectric constant for oil Shell Rimula 15W40 fresh (a) and used for 500 h (b) at different temperatures*

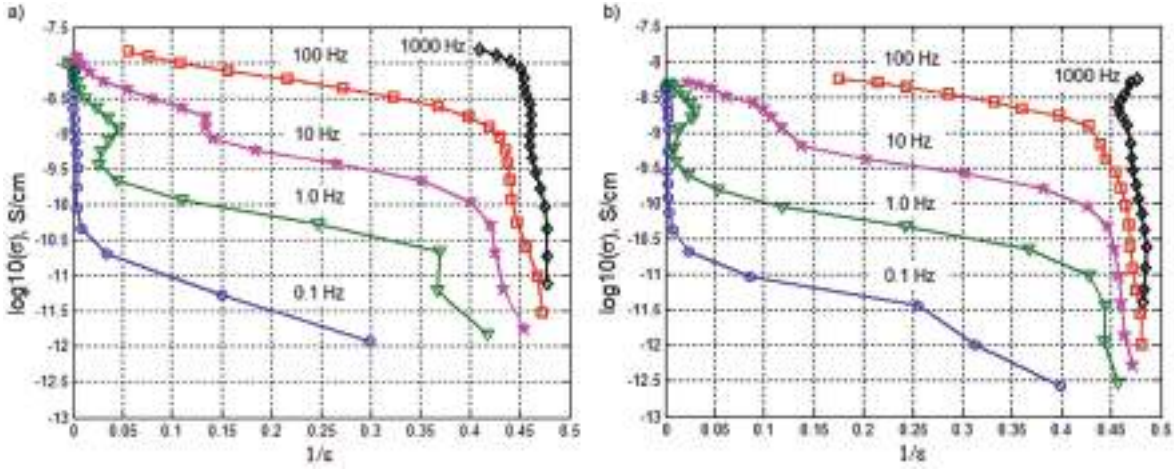

Figure 7. *Relationship between the specific conductivity and dielectric constant for oil Shell Rimula 15W40 fresh (a) and used for 500 h (b) at different frequencies*

Authorship Contributions

Concept design: M. Gapanovich, Data Collection or Processing: E. Rabenok, Analysis or Interpretation: O. Synashenko, E. Rabenok, M. Gapanovich, and N. Sinyavsky, Literature Review: N. Sinyavsky, Writing, Reviewing and Editing: N. Sinyavsky.

Funding: The research was conducted with the financial support of the Federal Agency for Fisheries of the Russian Federation (project no.: 122030900056-4) and state assignment no FFSG-2024-0003.

References

[1] F. Kremer, and A. Schönhals, *Broadband dielectric spectroscopy,* Springer Berlin Heidelberg, 2003.

[2] S. Kardoš, and A. Pietriková, "Evaluation of motor oil characteristics and degradation factors for possibilities of continuous diagnostics". *Acta Electrotechnica et Informatica,* vol. 16, pp. 20-24, Jun 2016

[3] F. Schober, A. Küchler, and C. Krause. "Oil conductivity - an important quantity for the design and the condition assessment of HVDC insulation systems". *FHWS Science Journal,* vol. 1, pp. 59-78, 2013.

[4] I. V. Baturlya et al. "Dielectric characteristics of engine oils for power units, as measured by a capacitive sensor". *Reports of BSUIR (Belarusian State University of Informatics and Radioelectronics),* vol. 3, pp. 103-106, 2016.

[5] B. Xu, et al. "Impedance analysis of oil conductivity and pixel non-uniformity in electrowetting displays". *Results in Physics,* vol. 18, 103223, Sep 2020.

[6] S. Barnoss, B. Melo, M. El Hasnaoui, M. Graça, M. Achour, and L. Costa, "Investigation of dielectric relaxation phenomena and AC electrical conductivity in graphite/carbon nanotubes/engine oil nanofluids". *Journal of Reinforced Plastics and Composites,* Aug 2020.

[7] I. I. Popov, R. R. Nigmatullin, A. A. Khamzin, and I. V. Lounev, "Conductivity in disordered structures: Verification of the generalized Jonscher's law on experimental data". *Journal of Applied Physics,* vol. 112, 094107, Nov 2012.

[8] X. Sidambarompoulé, P. Notingher, T. Paillat, J.-C. Laurentie, and P. Leblanc, "Study of electrical properties and estimation of average mobility and diffusion coefficients in several insulating liquids by dielectric spectroscopy". *International Journal of Plasma Environmental Science and Technology,* vol. 14, pp. 1-18, Dec 2020.

[9] A. Wolak, R. Z˙ywica, J. Molenda, and J. K. Banach, "Electrical parameters as diagnostics of fresh engine oil condition—correlation with test voltage frequency". *Sensors,* vol. 23, 3981, Apr 2023.

[10] Y. Zhou, M. Hao, G. Chen, G. Wilson, and P. Jarman, "Study of the dielectric response in mineral oil using frequency-domain measurement". *Journal of Applied Physics,* vol. 115, 124105, Mar 2014.

[11] I. V. Izmestyev, S.A. Konyaev, Changes in the dielectric properties of some motor oils during their destruction, Bulletin of Perm University, 2012 Series: Physics Vol. 1 (19) pp. 85-90.

[12] Izmest'ev I.V., Kozhevnikova O.A. Polarization and electrical conductivity of some motor oils as dispersed systems // Bulletin of Perm University. Series: Physics. 2016. No. 1 (32). pp. 43–50. doi: 10.17072/1994-3598-2016-1-43-50.

[13] N. Ya. Sinyavsky, Study of marine motor oils by radio spectroscopic and optical methods, Materials of the VIII International Baltic Maritime Forum: in 6 volumes. Volume 1. Kaliningrad, 2020, Publisher: Kaliningrad State Technical University (Kaliningrad).

[14] N. Sinyavsky, O. Synashenko, and N. Kostrikova, "Application of relaxation times distribution of dielectric permittivity for marine engine oils analysis". *Journal of Eta Maritime Science,* vol. 11, pp. 209-216, Sep 2023.

[15] G. F. Novikov, E. V. Rabenok, Ya. I. Estrin, Yu. A. Olkhov, E. R. Badamshina, "Influence of low concentrations of carbon nanotubes on the electrical conductivity of polyurethane elastomer". *Journal of Physical Chemistry*, t. 88. No. 10, pp. 1605-1609, 2014.

[16] G. F. Novikov, E. V. Rabenok, L. M. Bogdanova, and V. I. Irzhak, "Dielectric properties of epoxy Ag-ED20 nanocomposite films synthesized in situ. Temperature dependence of through conductivity, "High-molecular compounds. Series A". *Macromolecular Compounds (Series A)*, vol. 59, pp. 711-720, 2017.

ORIGINAL RESEARCH (AR) DOI: 10.4274/jems.2024.44711

Journal of ETA Maritime Science 2024;12(3):295-309

Modeling Investigation of Potential Sea Level Rise Effect on Hydrodynamics and Sediment Transport in Hyères Bay, France

Minh Tuan Vu[1], Yves Lacroix[2], Viet Thanh Nguyen[3]

[1]Institute of Port and Maritime Techniques, Hanoi University of Civil Engineering, Hanoi, Vietnam
[2]SeaTech, University of Toulon, Toulon, France
[3]Faculty of Civil Engineering, University of Transport and Communications, Hanoi, Vietnam

Abstract

Global climate change increases storm frequency and Sea Level Rise (SLR). This leads to an increased risk of coastal flooding, reduced effectiveness of protective structures, and intensified coastal erosion and retreat. The Bona and Ceinturon beaches, two beautiful sandy beaches with low-lying topography along the eastern branch of the Giens double tombolo on the western coast of Hyères Bay, have high tourist value. These areas are very vulnerable to SLR, which is believed to reduce the effectiveness of the shore protection structures built on these sandy beaches. The effects of SLR on changes in the hydrodynamic characteristics of these water bodies need to be quantified. This may help clarify the relationship between SLR and coastal erosion. This study investigated the variation of wave height and current speed due to SLR at the Bona and Ceinturon beaches using a coupled numerical model. The performance of this model was calibrated by comparing the model results with the in situ measured data. The research results are the basis for assessing the impact of SLR due to climate change on this area and provide a useful solution for coastal management in the future.

Keywords: Giens tombolo, SLR, numerical model, hydrodynamic, sediment transport rate

1. Introduction

According to the report of IPCC [1], the melting of glaciers and ice sheets in the polar regions and in the high mountains and the global spatial expansion due to climate change are the main causes of global sea level rise. However, within the Mediterranean Sea, a semi-enclosed basin, atmospheric forcing changes, and ocean circulation mainly cause the sea level to rise. This sea has been experiencing sea level rise differently from the global mean [2]. The mean sea level in the Mediterranean Sea increased at a rate (1.1-1.3 mm/year) lower than the global mean sea level (1.8±0.5 mm/year) during the 20th century [3]. Through satellite altimetry, Cazenave et al. [4] found that the mean sea level in the area from Marseille to Menton increased at a rate of approximately +2.2 mm/year during 1993-2013. In the 21st century, Galassi and Spada [5] predicted that future sea level changes in the Mediterranean Sea in 2040-2050 compared with 1990-2000 would be 9.8 cm in the minimum scenario and 25.6 cm in the maximum scenario. Specifically, a sea level rise rate of about 1.26±0.05 mm/year is estimated by a linear regression method based on sea level data measured at Marseille station in the period of 1885-2012. On the other hand, the sea level of Marseille station in 2040-2050 is forecasted to rise by about +1.2 mm/year in the minimum scenario and +4.2 mm/year in the maximum scenario.

The coastal areas are home to more than 50% of the world's population. However, these regions could suffer severe impacts if the global sea level rises by approximately 44 cm by 2100 [6]. Sea level rise typically entails many severe risks to coastal areas, including increased volume of sediment lost along the coast and offshore, flooding or submergence of coastal marshes and lowlands, increasing saltwater intrusion into estuaries, rivers, and aquifers, exacerbating the problem of environmental pollution in urban areas as well as damage from storms and floods [7], and displacing existing coastal animal communities and plants, significantly degrading

Address for Correspondence: Minh Tuan Vu, Institute of Port and Maritime Techniques, Hanoi University of Civil Engineering, Hanoi, Vietnam
E-mail: tuanvm@huce.edu.vn
ORCID iD: orcid.org/0000-0002-6099-0603

Received: 20.11.2023
Last Revision Received: 01.06.2024
Accepted: 03.06.2024

To cite this article: M. T. Vu, Y. Lacroix, and V. T. Nguyen. "Modeling Investigation of Potential Sea Level Rise Effect on Hydrodynamics and Sediment Transport in Hyères Bay, France." *Journal of ETA Maritime Science*, vol. 12(3), pp. 295-309, 2024.

the meadows of Posidonia oceanica [8]. Furthermore, the protective effectiveness of existing coastal structures such as breakwaters, groynes, seawalls, and sea dikes could be reduced by wave overtopping or submergence due to SLR [9]. In the study area, SLR may not only have as significant an impact on the lives of local communities as in other densely populated coastal cities in the world, but it can also be vulnerable to the tourism industry. The tourism industry in this coastal region has an annual turnover of approximately 4.6 billion euros and contributes to one-fifth of the total sales of the French tourism industry [10]. Therefore, the decline or disappearance of the beaches here induced by SLR would have a substantial negative impact on the economy of this area.

Among the negative impacts of SLR, coastal erosion is a global and topical problem. Brunel and Sabatier [10] conducted a survey of the beaches of Hyères Bay. These are pocket-beaches bounded by cliffs or scarps above the backshore. It was concluded that these beaches lost an average of 40% (±10%) of their surface area due to coastal erosion, which equates to an average retreat of approximately 12.1 (±3.5) m from 1896 to 1998. The average shoreline retreat of 5.8 (±3.5) m was caused by a relative SLR of +11 cm during this period. In addition, Brunel and Sabatier [10] predicted that nearly a quarter of the surveyed pocket-beaches would likely lose at least 75% (±10%) of their present surface area with an average retreat of -20 (±2) m if SLR is increased to +44 cm due to global climate change by 2100. Using the integration of satellite remote sensing and GIS techniques, Tuan et al. [11] showed that the Bona and Ceinturon beaches were most severely eroded, with maximum erosion rates of 0.44 and 0.77 m/yr, respectively. Moreover, they predicted that the trend of shoreline retreat would continue to occur at these beaches until 2050.

The trend of global warming, along with SLR, is hard to reverse, and global climate change will not be under control in the near future. Hence, it is essential to focus more on investigating the adverse consequences of climate change. In the present study, the authors focus on simulating the changes in the hydrodynamic field around the Ceinturon beach in the eastern branch of the Giens double tombolo, considering the SLR.

2. Study Area

The Giens double tombolo is situated in the small town of Hyères city, the southernmost point of France on the Mediterranean Sea (Figure 1). The phenomenon of wave refraction and diffraction on the island of Giens is attributed to the main cause of this tombolo formation [12,13]. It consists of two sand spits separated by a salt marsh in the middle. The eastern sand spit of the Giens double tombolo

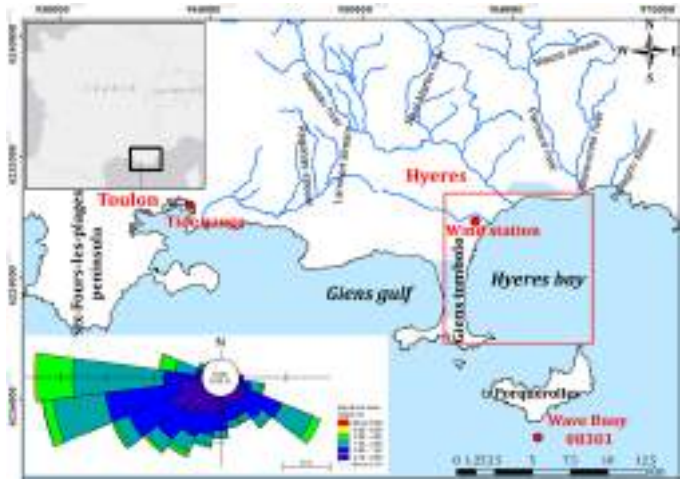

Figure 1. *Wave rose and the location of the study area*

facing Hyères Bay is bounded by the mouth of the Gapeau River to the north and the Cape of Esterel to the south. However, this sand spit is being eroded due to both natural causes and human impacts, especially Bona and Ceinturon beaches [14].

Field wind data were collected from Hyères station from 1999 to 2018. There are three main wind directions that generate waves approaching the beaches along the eastern branch of the Giens tombolo: northeast, east, and southeast morphological winds. They account for more than 28% of the total uptime. The east wind, with a frequency of 10.58%, has the highest speed of 20.31 m/s. Natural factors have the greatest influence on morphological changes in the study area [15].

Offshore wave data measured by buoy 08301 at a depth of 90 m south of Porquerolles Island (Figure 1) revealed that the waves come from three main directions. The most frequent direction is the west waves with about 36.92% of the total regime. Nevertheless, these waves do not affect the study area much and are quite difficult to penetrate into Hyères bay, as most of them are reflected or changed in the direction by the Six-Fours-les-Plages peninsula before approaching the Gulf of Giens. The second most frequent direction is west-southwest with a frequency of 28.84%. Similar to western waves, these waves are very difficult to penetrate into the study area because it is shielded by the Giens tombolo. The third dominant wave direction is east-southeast with a frequency of 19.1% of the total regime. They can spread into the study area and influence the shoreline evolution of the beaches along the eastern Giens tombolo. Wave is also the main factor affecting the hydrodynamic process in the study area because tidal fluctuations are negligible [16].

The Gapeau River, located 6 km north of the Giens tombolo, is the main source of sediment for the formation of the Giens tombolo and Hyères Bay [17] (Figure 1).

Measured discharge data were collected at the Sainte Eulalie station located approximately 6 km upstream from the mouth of the Gapeau River. The annual discharge of the Gapeau river is approximately 4 m^3/s and that of the dry season is approximately 0.5 m^3/s. Furthermore, the discharges of the decadal, tri-decadal, semi-centennial, and centennial floods are forecasted approximately 180 m^3/s, 220 m^3/s, 300 m^3/s, and 600 m^3/s, respectively [18,19].

Most of the seabed in Hyères Bay is covered with sand from organic production and Posidonia seagrass, a well-known endemic plant of the Mediterranean Sea. Sand is concentrated mainly in coastal areas. The grain size of the sand is distributed depending on the longshore current and tends to decrease from north to south. Specifically, coarse sand with a diameter of 0.55 mm occurs on the northern beaches of the study area, whereas fine sand with a diameter of 0.2 mm is observed on the southern beaches of the study area [18]. Meanwhile, Posidonia seagrass has taken over the remains of the seabed. It plays a crucial role in the hydrodynamic process and sediment transport in Hyeres Bay in general and Giens tombolo in particular [20]. Posidonia appears at very close distances from the coast. It ranges from a depth of 0 to a water depth of 30 m, covering 9200 ha in the bay of Hyères, from the south of the Giens tombolo up to Bormes-les-Mimosas [21].

3. Materials and Methods

3.1. Field Measurements

The process model calibration and validation were carried out using the in situ measurement data at La Capte beach supported by Meulé [22] and E.O.L [23]. These data are summarized here.

a. Bathymetry

Differential Global Positioning System technology has been applied to survey the bathymetry along the western and eastern parts of the double Giens tombolo from 2000 to 2010. The survey range extends approximately 500 m from the shoreline to the sea. The EOL bathymetry has zero elevation as the Lowest Astronomical Tide and uses the Nouvelle triangulation de la France horizontal coordinate reference system with the projection in Lambert III (France Sud) [23]. The bathymetry of the study area is shown in Figure 2.

b. Hydrodynamics

To obtain data on waves and currents, a measurement campaign was carried out in March 2009 by Meulé [22], where five stations with measuring devices were immersed. The five stations from SCAPT1 to SCAPT5 were installed perpendicular to the coast on a single line to understand the cross-shore hydrodynamics. They cross the geotubes furthest out to sea, and the Posidonia seagrass meadow. In total, there were four turbidity probes (OBS), four acoustic Doppler velocimeters, an acoustic Doppler current profiler (ADCP 600Khz RDI), and an electromagnetic current meter (S4DW) fixed on the five submerged stations illustrated in Figure 3.

Five stations had different measurement periods and were at different depths. Therefore, the SCAPT2 station was located at a depth of 3 m, SCAPT3 at a depth of 1.8 m, and SCAPT5 (5-1 and 5-2) was located at 1.6 m depth. On the other hand,

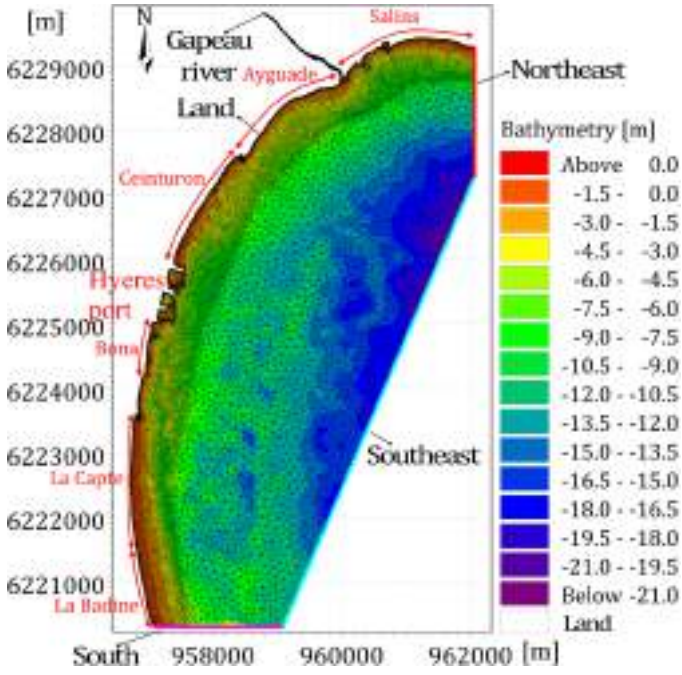

Figure 2. *Computational domain and bathymetry*

Figure 3. *Location of wave measuring stations in La Capte beach [22]*

the SCAPT1 station is located at a depth of 7.5 m, and the SCAPT4 station is less than 1 m deep. Three stations of SCAPT2, SCAPT3, and SCAPT5 started measuring from 12th to 17th March 2009, while two stations of SCAPT1 and SCAPT4 monitored from 13th March to 22nd April 2009 [22].

Data of currents (magnitude and direction) and waves (significant height) will thus be recorded over a period of one and a half months. However, only the data of SCAPT3 and SCAPT4 located in the seaward and landward directions of the geotube submerged breakwater are used to calibrate and validate in this work.

Concerning SCAPT3, the wave directions are the same as those in SCAPT1 and SCAPT2. Nonetheless, the significant wave heights averaged about 0.2 and 0.4 m during the two periods of bad weather (Figure 4a). The highest wave height in this measurement period reached 0.38 m, corresponding to a wave period of 5.2 s at 11 AM on 16th March. There is an asymmetry of waves resulting from waves approaching the coast. The average wave period at this station is approximately 6.2 s.

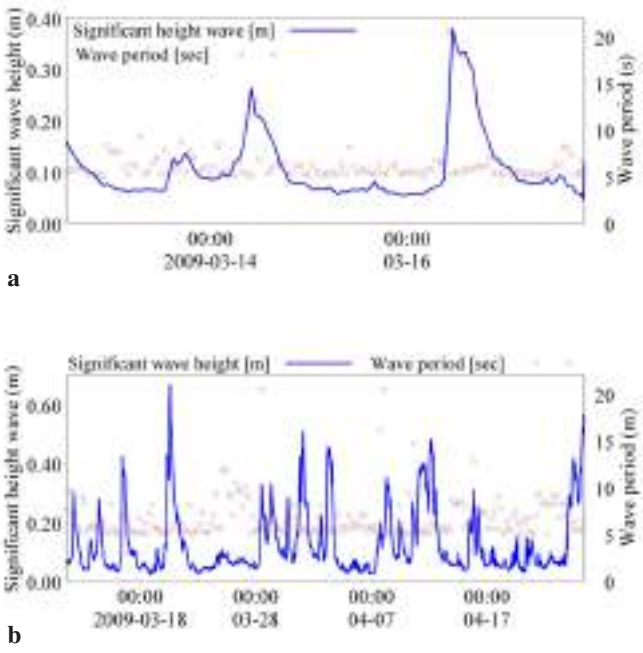

Figure 4. *Measured wave height and wave period at La Capte in 2009 [22]*

a) SCAPT3 station, b) SCAPT4 station

The measurement of the wave at the SCAPT4 station located 120 m seaward of the shoreline was carried out in the longest period from 13th March to 22nd April, 2009. The average significant wave height is approximately 0.12 m, but many variations are observed, with the highest wave height of up to 0.67 m. Hence, during this period, the number of waves that exceeded the height threshold of 0.4 m was reached nearly eight times, as depicted in Figure 4b. The wave period at this station varies from 5 to 20 s and averages approximately 6.6 s.

The current data were measured at the SCAPT4 station from 13th March to 22nd April, 2009. During the measurement period, the northern and southern currents were mostly observed, but the northbound currents were still dominant and stronger than those in other directions (Figure 5a). There are two main components of velocities, cross-shore and longshore (Figure 5b). The cross-shore velocities are positive when they are directed shoreward. Conversely, they are negative when they move seaward. It is noted that the currents moving toward the coast are faster than those moving toward the sea, but only extend over a short period. Particularly, from 18th to 28th March 2009, the seaward currents were relatively weak, while the shoreward currents

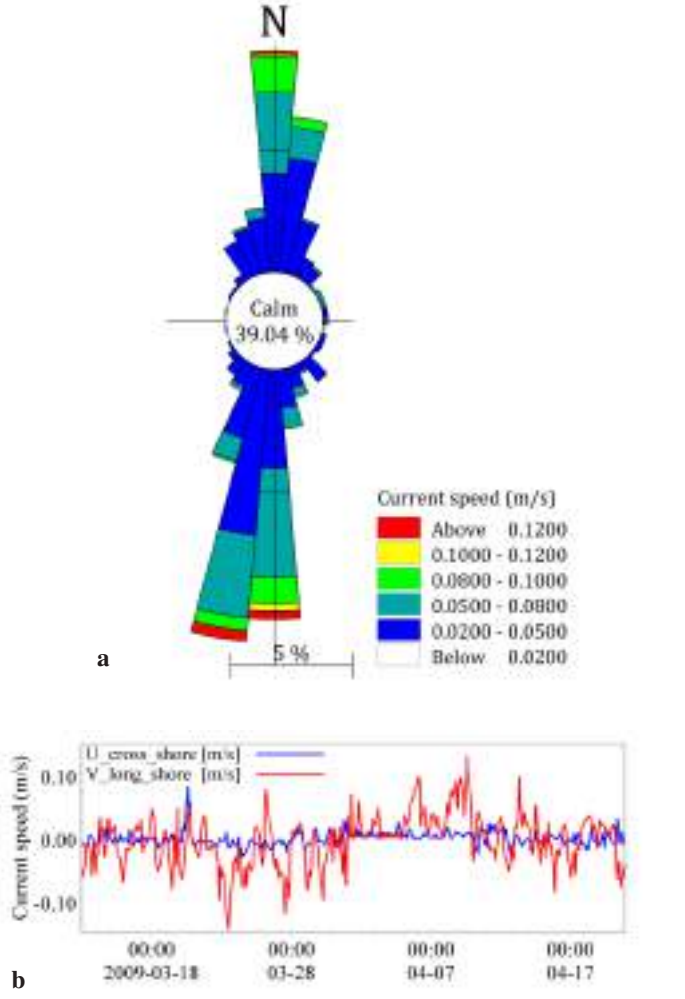

Figure 5. *Nearshore current data from the SCAPT4 station at La Capte beach in 2009 [22]*

a) Current rose, b) Velocity component

became stronger between 1st and 4th April, 2009. The main cause of this phenomenon can be attributed to wave action. It is easy to see that the largest cross-shore flow velocities occur at the time of the largest wave heights. In other words, high waves induce cross-shore currents to move shoreward, whereas weak cross-shore currents direct seaward due to small waves. The maximum cross-shore current speed is 0.09 m/s shoreward, whereas the longshore current speed reaches the highest value of 0.14 m/s northward [22].

3.2. Numerical Model Descriptions

The impact of SLR on the hydrodynamics and sediment movement process along the Bona and Ceinturon beaches in the eastern Giens double tombolo was investigated and uncovered using the MIKE21 numerical package [24]. Specifically, the MIKE 21 Spectral Waves (SWs) model is applied to reproduce the swell and wind-induced wave field. The wave-generated currents and water level fluctuation can be simulated in the MIKE 21 Hydrodynamic (HD) model, where the MIKE 21 Sand Transport (ST) model is used to describe the sediment transport and bathymetry change.

The mathematical models will be solved on a computational grid of approximately 30 square kilometers. This grid extends from Salins beach (about 2 km north of the Gapeau river mouth) to La Badine beach (about 9 km south of the Gapeau river mouth). It has three open-sea boundaries in the east, southeast, and south, and a shoreline-land boundary in the west (Figure 2). The southeast open-sea boundary of this domain is 2 km from the coastline. Furthermore, the main flow input, namely the Gapeau river, has also been included in the study domain. The length of this river ends at the Sainte Eulalie station, where no tides are reaching. All these boundaries must be located far enough to ensure that their spurious effect is kept outside the area of interest. The computational grid is built with 13,620 nodes and 22,960 elements. This is also the result of the sensitivity analysis of 15 grids with different resolutions [25]. The smallest grid cell area is approximately 9 m^2 inside the Gapeau river and along the beaches, whereas the largest is approximately 12,000 m^2 in the offshore zone (Figure 2).

3.3. Calibration Parameters

Model calibration is essentially the process of adjusting the governing parameters so that the model can reproduce the physical problem. Nikuradse's roughness height (ks) is used for the SW model to adjust the wave parameters. The distribution of Manning's number (M) in the entire study area is the main factor affecting the water level and current speed in the Hydrodynamic model. In addition, the ST model is calibrated using the median grain size (D_{50}). However, in the study area, the seafloor material is heterogeneous. Specifically, the area near the shore is characterized by sand, whereas the remaining area is covered with Posidonia seagrass interspersed with rocks. Therefore, the parameters of this model calibration will also be determined according to different formulas suitable for each type of seabed material. Details on the calibration procedure of these models are proposed by Vu et al. [20], Liu [26], and Nguyen [27].

This calibration process is performed for periods or events in which the best-fitted observed data are available within the computational domain. In this study, the HD and the SW models are calibrated by the observation data in March and April 2009, whereas the calibration of the ST model is done during the period from November 2007 to November 2008. As recommended by some researchers [26,28-34], the performance evaluation of numerical models is performed using coefficients, including the Root Mean Square error (RMSE), scatter index (SI), and squared multiple correlation coefficient (R^2). In addition, the Brier Skill Score (BSS) is suggested to access the numerical simulation of coastal morphology by Van-Rijn et al. [35], Roelvink et al. [34], Pender and Karunarathna [36].

3.4. Study Scenarios

The input parameters of the simulations that consider the SLR are summarized in Table 1. For normal cases that consider changes in wind direction, the sea level is calculated

Table 1. *Input data of simulation cases for the Ceinturon and Bona beaches*

Case	Sea level (m)	Wind data		Wave data		
		Speed (m/s)	Direction (deg)	$H_{1/3}$ (m)	T_p (s)	MWD (deg)
Annual (A1)	0.5	8.50	60 (NE)	2.18	7.43	115
Annual (A2)		6.48	90 (E)			
Annual (A3)		5.22	120 (SE)			
Decadal storm (S1)	1.30	12.55	90	6.56	9.12	110
Tri-decadal storm (S2)	1.35	19.83	90	7.10	10.3	110
Semi-centennial storm (S3)	1.50	29.59	90	7.34	11	110
Centennial storm (S4)	1.85	36.43	90	7.64	12	110

as the value of the multi-year mean sea level plus (+0.39 m) with the minimum sea level change rate in the Marseille area in the period 2040-2050 (0.11 m) [10]. Meanwhile, the calculated sea level in the storm scenarios is determined by the estimated sea level under these conditions plus the 35 cm increase due to SLR during 2010-2060 [2]. Wind parameters were taken according to the frequency of occurrence from recorded wind data at the Hyères station from 1979 to 2015. The wave parameters used in the simulations were collected from the reports of ERAMM [11] and CEREMA [12].

4. Results and Discussion

In this study, changes in sea level are simulated along with changes in wind direction and stormy variation, thus assessing the impact of these changes on hydrodynamics and sediment dynamics in the area of interest. The values of significant wave height, current speed, sediment transport rate, and bed level change were extracted and compared in a direction perpendicular to the shoreline of Ceinturon and Bona beaches, which are subjected to severe erosion [11]. To quantify the difference between scenarios, these hydrodynamic and sediment transport values at 1.5 m depth at both beaches were also calculated.

4.1. Calibration of the Model

The simulation results of significant wave height and wave period at the SCAPT3 and SCAPT4 stations were extracted and compared with the measurement data. Figures 6 and 7 express the goodness of fit between the field data and the model results. The RMSE ranges between 0.06 and 0.12 m, with a difference between 53% and 98% for wave height at SCAPT3 and SCAPT4 points, respectively. Moreover, the comparison of the wave periods at SCAPT3 and SCAPT4 shows a good fit between the observation and the simulation. The simulation results obtained from the SW model run were then applied across the entire computational domain for the HD model run in March 2009, when the wave radiation varied in time and space. Figure 7c shows a comparison of the observed and simulated current speeds at the SCAPT4 station. It was found to be in good agreement between the observation and simulation. The goodness of fit statistics had an R-square of 0.35, RMSE of 0.03 m/s, and a difference of 90%. In addition, the U and V components of the modeled current velocities are extracted and presented in Figure 8. The trends of the simulated flow velocity components are quite consistent with the results measured by Meulé [22] (Figure 5b). After successfully simulating the real hydrodynamics along the eastern Giens tombolo, the ST model was used to reproduce the sediment dynamics during the 1-year duration (November 2007-2008). The bathymetry of the study area surveyed in 2007 will be used as the input

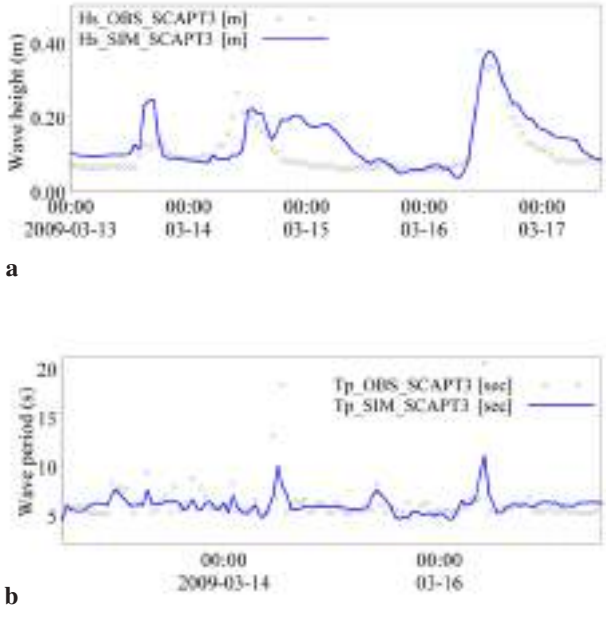

Figure 6. *Time-series plot of the observed (OBS) and simulated (SIM) wave paremeters of the SCAPT3 station*

a) Wave height, b) Wave period

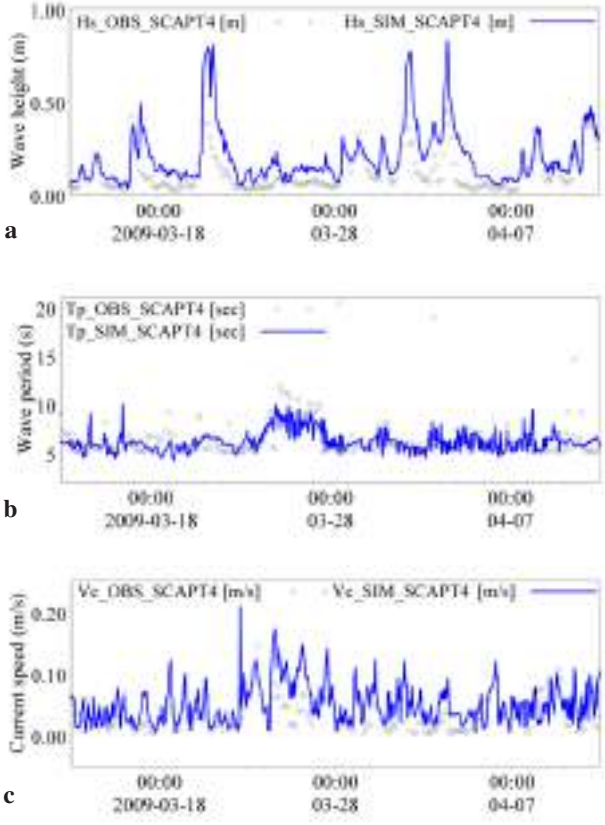

Figure 7. *Time-series plot of the observed (OBS) and simulated (SIM) hydradynamic parameters at the SCAPT4 station*

a) Wave height, b) Wave period, c) Current speed

for this model. A comparison of observed and simulated beach profiles in the south of Ceinturon beach is presented in Figure 9. The statistical error of this comparison (BSS) is found to be 0.61. This confirms that the ST model accurately describes the morphological evolution of the study area [35]. The final set of parameters including Nikuradse roughness height (k_s), Manning's number (M), and median grain size (D_{50}) will be obtained by the calibration processes (Figure 10).

4.2. Impacts of the SLR on Wave Transformation

Due to their geographical location, the beaches located on the eastern branch of the Giens tombolo are directly affected by NE, E, and SW wind-generated waves. In the sea level rise scenario, any change in wind parameters in the three directions mentioned above can cause a large variation in the wave field in the study area. Figure 11a shows the change in wave height in the cross-shore direction under different wind directions at

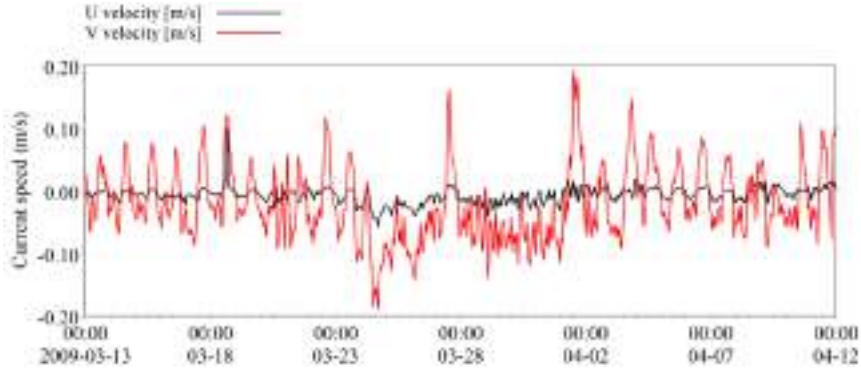

Figure 8. *Time-series plot of the U and V components of the modeled current velocities of the SCAPT4 station*

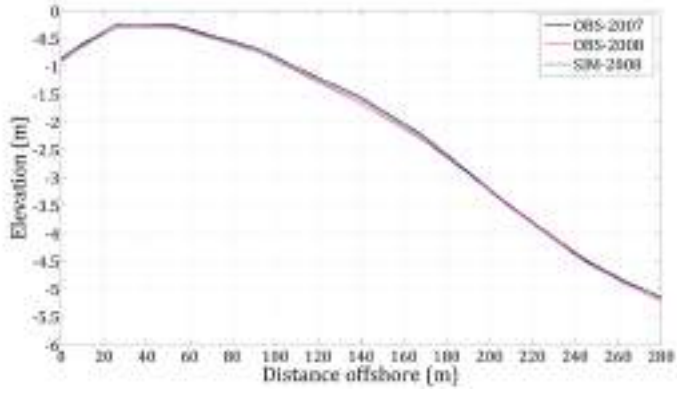

Figure 9. *Comparison of the cross-shore profiles at the Aeroport beach (the south part of the Ceinturon beach)*

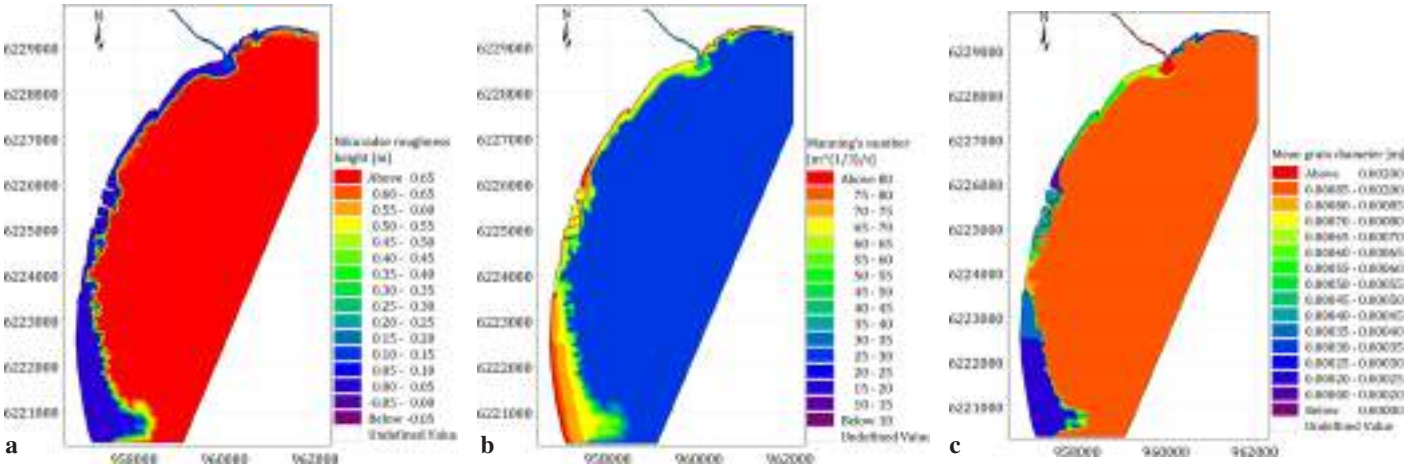

Figure 10. *Spatial distribution of calibration parameters*

a) Nikuradse's roughness height, b) Manning's number, c) Median grain size

Bona beach, while the variation in cross-shore wave height at Ceinturon beach in the annual scenarios is presented in Figure 11b. It is noticeable that the highest waves occurring off the coast of Bona beach are induced by the NE waves, where the E winds produce the highest waves off the coast of Ceinturon beach. As these waves approach shallow water, their energy is dissipated by the effect of bottom friction and gradually decreases in height. This height reduction differs between the wave directions. In the nearshore area, the NE wind-driven waves are highest at the Bona and Ceinturon beaches. Specifically, the highest significant wave heights appear at the Bona and Ceinturon beaches in the case of northeasterly winds and have values of 0.622 m and 0.682 m, respectively (Table 2). In addition, the results in this table also reveal that the NE winds not only cause the highest waves but also produce the largest radiation stresses (S_{xx}, S_{yy} and S_{xy}). Sea level rise increases the mean wave height in all wind directions at both Ceinturon and Bona beaches by 1.34-2.41% and 1.18-2.86%, respectively. Nevertheless, the magnitude of the increase in wave height is different for each wind direction and beach. Specifically, the NE winds induced the largest increase in wave height of approximately 2.86% at Bona beach, while the largest increase in wave height of approximately 2.41% was found at Ceinturon beach due to the E winds. The main cause of this increase in wave height can be an increase in water depth due to sea level rise, leading to high waves breaking near the shore [37]. Figure 11a illustrates this comment, especially with regard to SE winds. In addition, sea level rise also increases radiation stresses [38]. If SLR is about 11 cm, radiation stresses will increase by about 1-5% for all wind directions at both beaches.

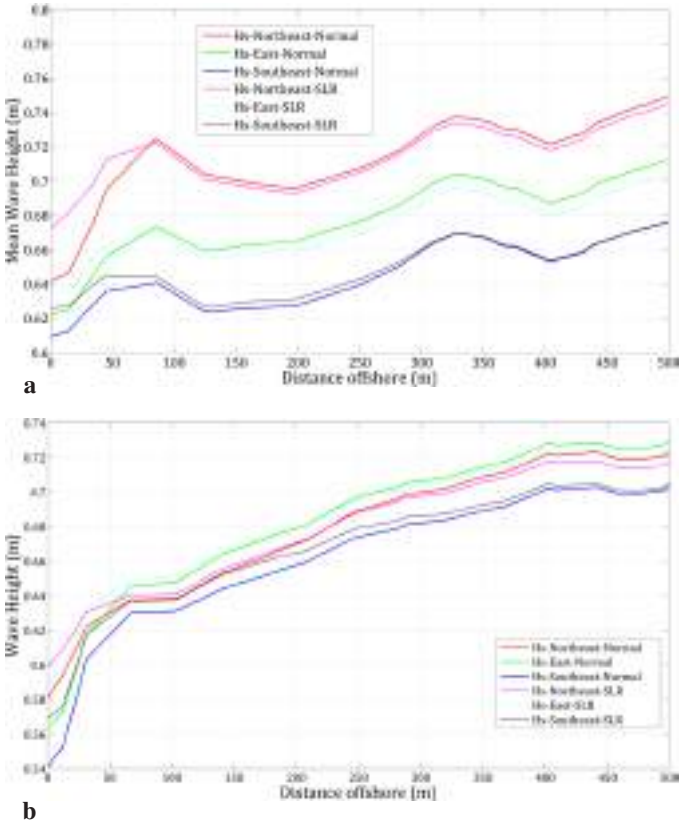

***Figure 11**. Comparison of cross-shore wave heights in different annual cases*

a) The Bona beach, b) The Ceinturon beach

Many extreme events, viz. storms, and rough seas, occur in the winter and attack the Giens tombolo. According to a study conducted by Capanni [19], this is one of the main factors causing coastal erosion on the beaches along the eastern branch of the Giens tombolo. Sea level rise due to climate change and storm surges will facilitate stormy waves that can attack the higher part of the beach and aggravate the problem of coastal erosion in vulnerable beaches [39]. Therefore, the impact of severe storms needs to be investigated in the study area. The change in cross-shore wave heights at the Bona and Ceinturon beaches due to the combined impact of SLR and storms with different frequencies is illustrated in Figure 12. Obviously, the lower the frequency of the storm, the higher

***Table 2.** Comparison of values of hydrodynamic and sediment dynamics parameters extracted at Ceinturon and Bona beaches under different scenarios*

	Scenario	Ceinturon beach						Bona beach					
		H_s (m)	S_{xx} (m^3/s^2)	S_{xy} (m^3/s^2)	S_{yy} (m^3/s^2)	V_c (m/s)	Q ($m^3/s/m$)	H_s (m)	S_{xx} (m^3/s^2)	S_{xy} (m^3/s^2)	S_{yy} (m^3/s^2)	V_c (m/s)	Q ($m^3/s/m$)
Normal condition	NE	0.622	0.232	-0.064	0.158	0.13	5.05E-05	0.682	0.337	-0.026	0.152	0.103	5.24E-05
	E	0.618	0.228	-0.064	0.155	0.08	3.12E-05	0.649	0.306	-0.028	0.140	0.163	7.35E-05
	SE	0.604	0.216	-0.061	0.147	0.08	3.88E-05	0.631	0.289	-0.029	0.132	0.171	7.57E-05
	Decadal	0.941	0.505	-0.131	0.322	0.16	2.05E-04	1.079	0.803	-0.061	0.352	0.242	4.47E-04
	Tri-decadal	1.027	0.566	-0.149	0.360	0.28	3.73E-04	1.304	1.110	-0.070	0.462	0.205	5.68E-04
	Semi-centennial	1.113	0.648	-0.157	0.380	0.36	6.97E-04	1.393	1.234	-0.050	0.487	0.062	3.99E-04
	Centennial	1.254	0.806	-0.191	0.461	0.37	7.98E-04	1.512	1.412	-0.069	0.563	0.054	4.63E-04

Table 2. *Continued*

	Scenario	Ceinturon beach						Bona beach					
		H_s (m)	S_{xx} (m^3/s^2)	S_{xy} (m^3/s^2)	S_{yy} (m^3/s^2)	V_c (m/s)	Q ($m^3/s/m$)	H_s (m)	S_{xx} (m^3/s^2)	S_{xy} (m^3/s^2)	S_{yy} (m^3/s^2)	V_c (m/s)	Q ($m^3/s/m$)
Sea-level rise	NE	0.631	0.237	-0.065	0.161	0.13	4.93E-05	0.702	0.354	-0.026	0.159	0.081	4.47E-05
	E	0.633	0.237	-0.066	0.161	0.09	3.48E-05	0.656	0.311	-0.028	0.142	0.133	5.79E-05
	SE	0.618	0.227	-0.064	0.155	0.06	2.90E-05	0.641	0.296	-0.029	0.137	0.154	6.60E-05
	Decadal	1.020	0.596	-0.157	0.383	0.13	1.81E-04	1.141	0.923	-0.063	0.389	0.049	1.84E-04
	Tri-decadal	1.142	0.703	-0.180	0.433	0.25	3.54E-04	1.404	1.264	-0.083	0.529	0.184	5.27E-04
	Semi-centennial	1.215	0.766	-0.193	0.461	0.31	5.56E-04	1.487	1.374	-0.066	0.556	0.071	4.59E-04
	Centennial	1.350	0.920	-0.219	0.522	0.33	6.74E-04	1.584	1.531	-0.087	0.620	0.056	5.18E-04
Difference (%)	NE	1.34	2.11	1.88	2.06	2.09	-2.49	2.86	4.97	1.03	4.36	-24.0	-14.63
	E	2.41	4.22	3.38	3.53	4.35	11.35	1.18	1.83	-1.41	1.66	-18.4	-21.15
	SE	2.35	4.83	4.66	4.99	-21.0	-25.13	1.61	2.64	0.21	3.34	-9.87	-12.83
	Decadal	8.36	18.04	19.71	18.93	-22.0	-11.42	5.82	14.96	2.64	10.31	-79.8	-58.89
	Tri-decadal	11.23	24.07	20.3	20.43	-9.16	-5.35	7.65	13.91	19.6	14.5	-10.4	-7.25
	Semi-centennial	9.12	18.19	22.48	21.29	-13.3	-20.35	6.78	11.35	31.05	14.09	15.24	15.2
	Centennial	7.65	14.19	14.49	13.31	-10.9	-15.57	4.8	8.41	25.68	10.23	4.18	11.86

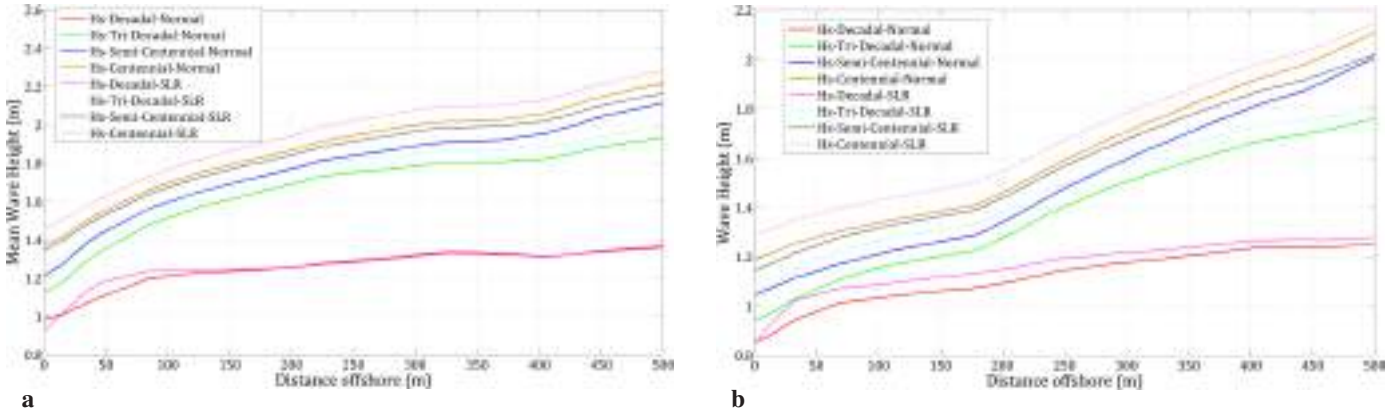

a b

Figure 12*. Comparison of cross-shore wave heights in the different stormy cases*
a) The Bona beach, b) The Ceinturon beach

the waves will be generated in both the case with and without sea level rise. Specifically, the significant wave height at Bona beach increased from 1.08 m in a decadal storm to 1.51 m in a centennial storm (Table 2), regardless of sea level rise due to climate change. Meanwhile, the significant wave height at the Ceinturon beach increased from 0.94 m in a decadal storm to 1.25 m in a centennial storm without considering SLR due to climate change. In addition, the simulation results demonstrate that higher waves often attack Bona beach instead of Ceinturon beach during the same storm. The average wave height during storms at Bona beach is greater than that at the Ceinturon beach by about 14.7-27% in conditions without SLR and 11.9-22.9% in conditions of SLR. The cause of this difference may be due to seabed bathymetry. Specifically, the bottom bathymetry at Bona beach is steep and deep, whereas the bottom bathymetry at Ceinturon beach is quite gentle and shallower (Figure 2). Therefore, higher waves can aproach and break closer to Bona beach than to Ceinturon beach. Table 2 also reveals that the nearshore significant wave height is enhanced by about 8.41-14.96% at Bona beach and by about 7.65-11.23% at Ceinturon beach when considering the impact resonance of sea level rise due to climate change and storms. Consequently, the radiation stress will also be increased proportionally to the wave height. Specifically, the radiation stress at the Bona and Ceinturon beaches increased to about 2.64-31.05% and

about 13.31-24.07%, respectively, when compared with scenarios excluding sea level rise due to climate change. This confirms that climate change-induced sea level rise and storm surge increase water depth and reduce wave energy dissipation due to bottom friction, resulting in higher waves reaching the beaches. In the condition of a centennial storm, the radiation stresses increased to relative minima, probably due to the sharp increase in water volume as a result of the submergence of the shore.

4.3. Impacts of the SLR on Current Speed

The simulation results of the cross-shore current speeds generated by different wind directions at the Bona and

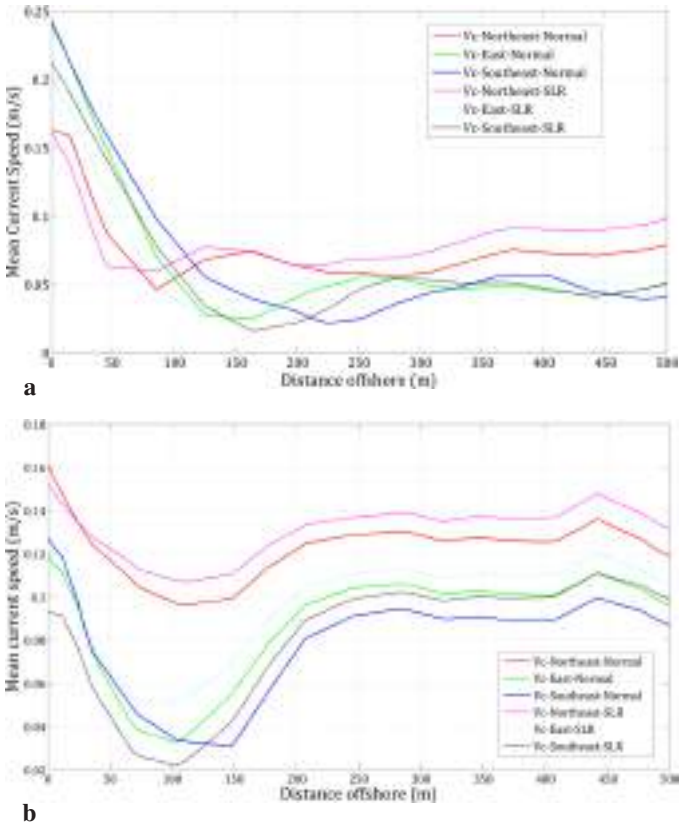

***Figure 13**. Comparison of cross-shore current speeds in the different annual cases*

a) The Bona beach, b) The Ceinturon beach

Ceinturon beaches are shown in Figure 13. It can be easily seen that the offshore current speed in the study area is greatly influenced by the NE winds when sea level rise is not considered. However, the degree of influence of wind directions in the surf zone in the study area changed because of the location of these beaches and the depth of the seabed. Specifically, the NE winds produced the highest mean current speed of 0.128 m/s, approximately 58% higher than other wind directions at the Ceinturon beach. Conversely, the NE winds generate lower currents than the E and SE winds, about 58-66% (Table 2). The breakwaters of the port of Hyères are the main cause of this discrepancy. The longshore currents induced by the NE winds move along the coast from Salins beach to Hyères port, and then they have to change direction and flow seaward after meeting with the breakwaters of Hyères port [18].

As a result, the speed of these currents is reduced much more after reaching Bona beach right downstream of the structures. Meanwhile, the currents generated by the E and SE winds approach this beach without any obstacles. In Bona beach, the highest current speed was induced by SE winds, whereas NE winds generated the largest waves. This proves that wind factors mainly influence nearshore currents. At the same time, waves play only a minor role in the development of these currents. SLR causes offshore currents (from a depth of about 150 m to offshore) to be stronger than those in scenarios excluding sea level rise. In contrast, nearshore currents under normal sea level conditions are higher than those in sea level rise scenarios. Table 2 reveals that the nearshore current speed caused by the SE winds at the Ceinturon beach decreased by 21% if the sea level increased. At Bona beach, the nearshore current speeds in all wind directions are reduced by 9.87-24% compared with the cases excluding sea level rise. The decrease in current speed has been attributed to the local expansion of water volumes due to the SLR and inundation of low-lying beaches. The current speed can decrease from depths 50 m offshore at Ceinturon beach and from depths 100 m offshore at Bona beach in both seasonsThe current speed maintains a reduction trend from a depth of 50 m offshore at Ceinturon beach and from a depth of 100 m offshore at Bona beach in both the normal water level and sea level rise scenarios. Then, the cross-shore currents increase sharply before they reach the shoreline. This increase in current speed in these areas can be attributed to the breaking wave energy [38]. The swift reduction in the current speed at these positions was caused by sand bars and troughs (Figure 2). Incoming waves break when they pass over the sand bars. Subsequently, the presence of troughs causes a decrease in wave-induced radiation stresses due to increased water depth. When the breaking waves approach the shore, accompanied by decreased water depth, the radiation stresses intensify again. This results in a sharp increase in current speed close to the shore.

Figure 14 shows the change in cross-shore current speed at the Bona and Ceinturon beaches under the combined impacts of sea level rise and different storm levels (decadal storm, tricadal storm, semi-centennial storm, and centennial storm). Stronger storms generate higher speed currents at Ceinturon beach. Indeed, the higher the storm level, the greater the wave height. As a result, higher wave heights result in faster current speeds. In particular, the current

speed during decadal, tri-decadal, semi-centennial, and centennial storms was recorded as 0.164, 0.276, 0.36, and 0.371 m/s at this beach, respectively. In addition, the current speed at Ceinturon beach is often greater than that at Bona beach during the same storm, regardless of sea level rise. Specifically, the current speed values extracted from Bona beach in the decadal, tri-decadal, semi-centennial, and centennial storm scenarios are 0.242, 0.205, 0.062, and 0.054 m/s, respectively. Similar to the annual scenarios, the main cause of this phenomenon is the appearance of the Hyeres port breakwater, which causes the speed of longshore currents to decrease as they approach Bona beach. At Ceinturon beach, although the current speed is generally reduced, the strong storms still induce high nearshore current speeds (Figure 14b). However, the current field in the surf zone at Bona beach is completely different from that at Ceinturon beach. It is easy to see that the current speeds in all storms are accelerated in the surf zone at the Ceinturon beach (Figure 14a), whereas most of the currents induced by storms occurring at the Bona beach tend to decrease before approaching the shore (Figure 14b). If sea levels rise due to climate change, most of the current speeds during storms are reduced by about 10.4-79.8% at Bona beach and about 9.16-22% at Ceinturon beach. Except for the semi-centiennial and centennial storm scenarios, the current speed near Bona beach increased by 15.24% and 4.18%, respectively (Table 2).

4.4. Impacts of the SLR on Sediment Transport and Beach Morphology

Many researchers [13,15,18,19] have found that the longshore currents generated by the oblique waves approaching the coast govern the law of sediment transport in Hyères Bay. These authors also showed a decrease in sediment grain size in the flow direction from north to south and from east to west. However, the longshore currents and the sediment dynamics field have been modified by cross-shore structures, viz. jetties, breakwaters, and groynes, which were built along the eastern branch of the Giens double tombolo. These structures have caused differences in sediment dynamics between the beaches, especially between Ceinturon beach (upstream of the Hyeres harbor breakwater) and Bona beach (located between the Hyeres harbor breakwaters and the La Capte groyne). The cross-shore changes in sediment transport rates under the dual action of NE, E, and SE winds and sea level rise at the Ceinturon and Bona beaches are shown in Figure 15. It is easy to see that the high sediment transport

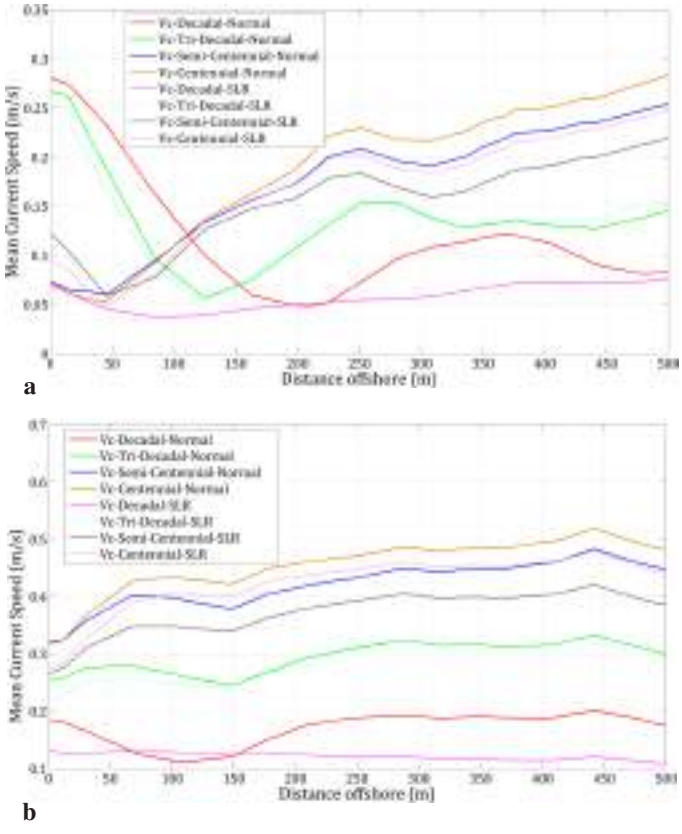

***Figure 14**. Comparison of cross-shore current speeds in the different stormy cases*

a) The Bona beach, b) The Ceinturon beach

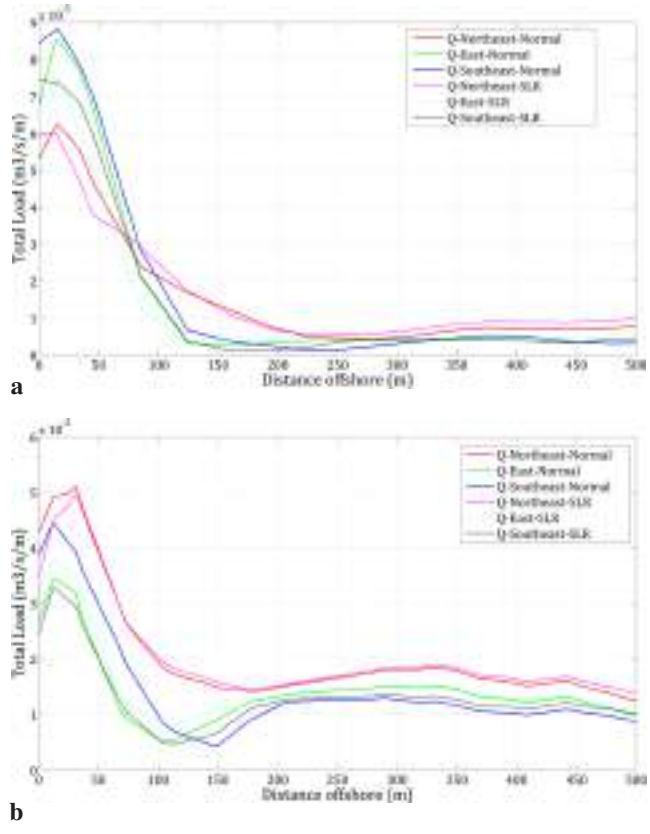

***Figure 15**. Comparison of cross-shore sediment transport rates in the different annual cases*

a) The Bona beach, b) The Ceinturon beach

rates are concentrated mainly between the shoreline and the 150 m offshore location. The main causes of this phenomenon are due to high wave-induced radiation stresses and current speeds (Figure 13). For the area from a depth of 150 m from shore to offshore, the impact of sediment transport is most strongly influenced by the NE winds in both normal and sea level rise scenarios. The highest sediment transport rates at Bona and Ceinturon beaches were observed in the NE winds. In addition, northeasterly winds continue to govern the sediment transport in the area from the shoreline to a depth of approximately 150 m offshore at the Ceinturon beach. In addition, in this area, the highest total load of more than $5x10^{-5}$ $m^3/s/m$ was recorded in the NE winds. In contrast, the highest total load of about $9x10^{-5}$ $m^3/s/m$ was triggered by the SE winds at Bona beach. Meanwhile, the NE winds generate the total minimum load in the nearshore area under both normal and sea level rise conditions. The current speed field greatly influences this cross-shore sediment transport distribution (Figure 13). When taking into account the occurrence of sea level rise, the total sediment transport load decreased in the area from the shoreline to a depth of approximately 150 m, but increased significantly in the area from the shoreline depth of 150 m out to offshore at both beaches in all wind directions. Table 2 reveals that the total nearshore sediment transport load is reduced by 12.83-21.15% at Bona beach and 2.49-25.13% at Ceinturon beach, respectively, due to SLR. The main cause may be a decrease in coastal current speed as water depth increases.

Similar to the current and wave fields, the sediment dynamics in the study area are greatly influenced by extreme weather events, especially storms. The extent of the impact of storms is increasing with the appearance of sea level rise due to global climate change. This could be explained by the increased frequency of bigger storms with sea level rise, resulting in larger waves approaching higher beach areas and wave-driven currents moving more sediment volume. Figure 16 illustrates the cross-shore variation of the sediment transport rate at the Bona and Ceinturon beaches due to the impact of stormy scenarios. It is noticeable that high sediment transport rates are observed in the 100-250 m offshore area at Bona beach (Figure 16a). In contrast, high sediment transport rates occur in the coastal area along the shoreline from 50 m to 150 m at Ceinturon beach (Figure 16b) both with and without regard to SLR. In addition, the centennial storm caused the highest sediment transport rates at both beaches (above $1.1x10^{-3}$ $m^3/s/m$). As sea levels rise, most sediment transport rates at the Ceinturon and Bona beaches decrease. Specifically, the sediment transport rate at Ceinturon beach decreased from 5.35% to 20.35% in all storms (Table 2). Meanwhile, the sediment transport rate at Bona beach decreased in the decadal and tri-decadal storm scenarios but increased by about 11.86-15.2% in the semi-centennial and centennial storm conditions. The decrease in sediment transport rates can be mainly attributed to the decrease in current speed as the sea level rises.

The consequence of sea level rise is that the river mouth and estuaries tend to enlarge, and the speed of fluvial currents will also be reduced by further intrusion of sea currents into the inland; the sediment is deposited right in the river mouth and estuaries [40]. This leads to a shortage of sediment in the downstream zones. The dual effect of this low sediment supply rate and rapid sea level rise is likely to increase the risk of shoreline erosion. To illustrate the change in beach bathymetry under the influence of sea level rise and change in wind direction, beach profiles at Ceinturon and Bona beaches are extracted and are shown in Figure 17. The change in bed level is usually observed at a distance from the shoreline to a depth of -2.5 m at the Ceinturon beach and from the shoreline to a depth of -5.0 m at the Bona beach in both normal and sea level rise scenarios. In addition, northeast winds caused the largest beach profile change in both Ceinturon and Bona beaches. When the sea level rises, the nearshore beach profile is eroded deeper than in normal sea-level cases. This may be due to the impact of the higher waves and higher radiation

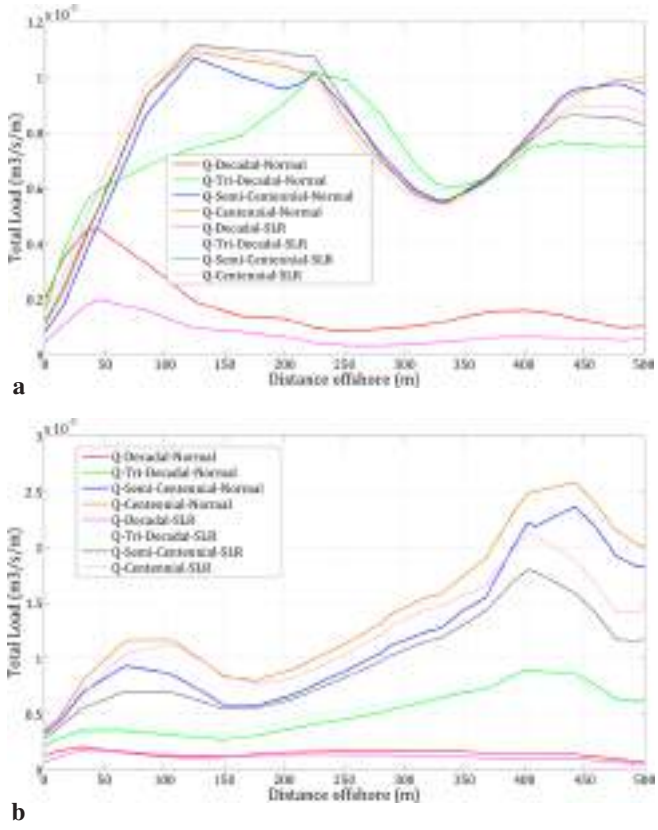

***Figure 16**. Comparison of cross-shore sediment transport rates in the different stormy cases*

a) The Bona beach, b) The Ceinturon beach

stresses generating stronger cross-shore currents, which extract sediment and are suspended by the waves and carried offshore.

The dual impact of storms and SLR will intensify the problem of coastal erosion occurring on the Ceinturon and Bona beaches. The beach profile variation of the Bona beach mainly occurs in the distance from the shoreline to offshore, approximately 150 m (Figure 18a). Meanwhile, the beach profile variation of Ceinturon beach is mainly concentrated in the distance from the shoreline to offshore, about 330 m (Figure 18b) in both cases, with and without considering SLR. The storms induce high waves, which extract sediment near the shoreline and carry them offshore. The presence of SLR provokes coastal erosion more severely than that in the no SLR scenarios, especially in nearshore zones on both beaches. The comparison of beach profile changes also demonstrates that the severity of coastal erosion depends on the storm level.

Additionally, the erosive mode at Bona beach is more severe than that at Ceinturon beach. The eroded area extends from the shoreline to a depth of 4.5 m offshore at Bona beach. The main reason may be that its location is exposed to storm waves, so higher waves can easily reach this beach. At the same water depth of 1.5 m, the wave heights observed at Bona beach are larger than those at Ceinturon, about 14.67-26.97% without sea-level rise and about 11.86-22.94% with SLR (Table 2).

5. Conclusion

The influence of the SLR on the hydrodynamic field around the Ceinturon and Bona beaches in the eastern Giens double tombolo has been successfully quantified using numerical models. The numerical simulation results confirmed that the presence of SLR could increase wave height but decrease current speed in the surf zone. The increase in wave height under storm conditions is much larger than that under annual conditions. In addition, under annual conditions, NE winds have the greatest influence on wave height in the study area. Under stormy conditions, significant wave heights near shore increased from 7.65% to 11.23% in Ceinturon beach and from 8.41% to 14.96% in Bona beach under stormy conditions. Simultaneously, it only increased by about 1.34-2.41% in Ceinturon beach and 1.18-2.86% in Bona beach in annual scenarios due to SLR. By contrast, a decrease in current speed of about 9.87-24% and 9.16-79.8% is observed at both beaches in the annual and stormy scenarios, respectively, in the case of SLR. The decrease in current speed is attributed as the main cause of the 2.49-25.13% reduction in sediment transport rate, regardless of wave conditions. Although the total load and the mean current speed reduce when the sea level rises, the beach erosion rate is higher than without a rise in the sea level.

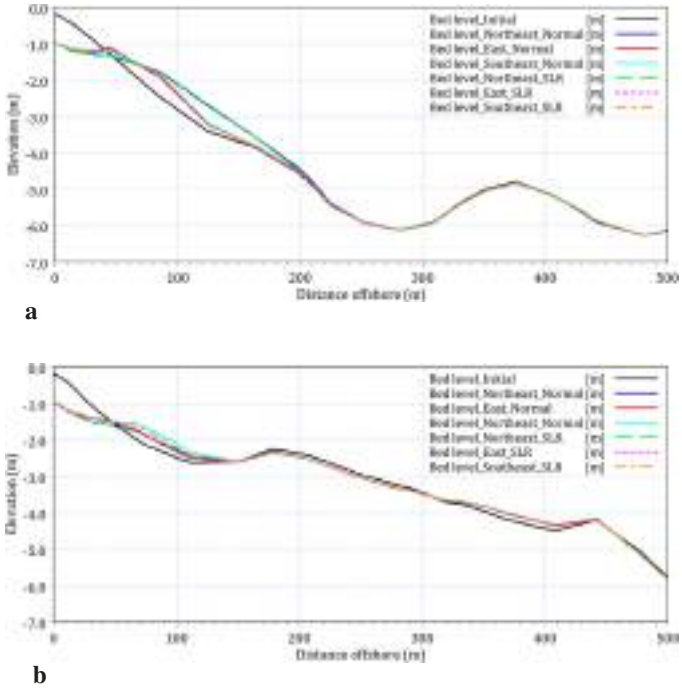

***Figure 17**. Comparison of beach profile changes in the different annual cases*

a) The Bona beach, b) The Ceinturon beach

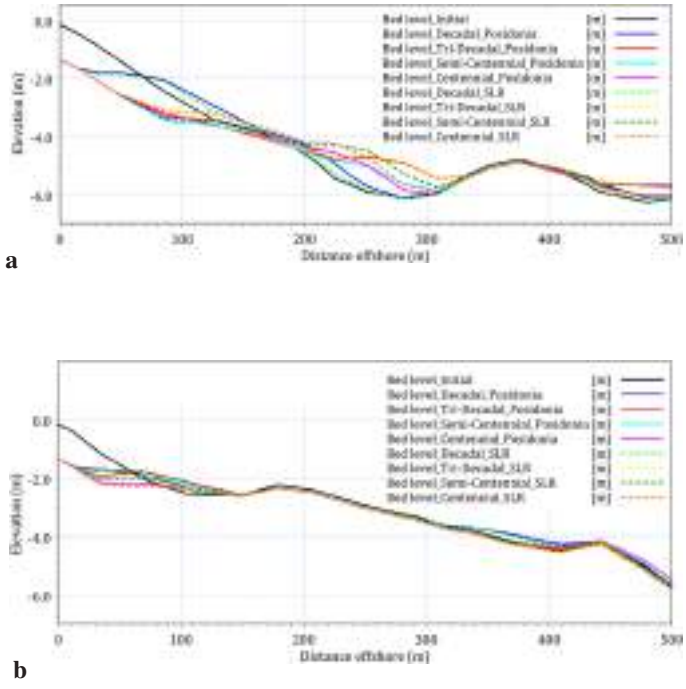

***Figure 18**. Comparison of beach profile changes in the different stormy cases*

a) The Bona beach, b) The Ceinturon beach

With the above-mentioned conclusions, sea level rise due to climate change has a very significant impact on the hydrodynamic mechanism and sediment transport along the Ceinturon and Bona beaches. This makes the erosion of these beaches more serious. Therefore, solutions to adapt to sea level rise and limit the impact of this phenomenon on beach stability need to be considered in future studies.

Acknowledgements

The authors would like to express their sincere gratitude to the Ministry of Education and Training, Vietnam (grant no.: 911) for financial support. The authors are equally thankful to Mr. Samuel Meule, OL, CETMEF, CEREMA, SHOM, and REFMAR for sharing the measured data and to DHI for generously providing MIKE software for research purposes.

Authorship Contributions

Concept design: M. T. Vu, and Y. Lacroix, Data Collection or Processing: M. T. Vu, and Y. Lacroix, Analysis or Interpretation: M. T. Vu, and V. T. Nguyen, Literature Review: M. T. Vu, Y. Lacroix, and V. T. Nguyen, Writing, Reviewing and Editing: M. T. Vu, and V. T. Nguyen.

Funding: Financial support was received from the Ministry of Education and Training, Vietnam (grant no.: 911).

References

[1] IPCC, "The Physical Science Basis", 2021.

[2] M. Tsimplis, M. Marcos, S. Somot, and B. Barnier, "Sea level forcing in the Mediterranean Sea between 1960 and 2000". *Global and Planetary Change,* vol. 63, pp. 325-332, Nov 2008.

[3] D. Gomis, et al. "Sea level rise and its forcing in the Mediterranean Sea". *MedCLIVAR – Mediterranean CLImate VARiability,* 2011.

[4] A. Cazenave, C. Cabanes, K. Dominh, M. C. Gennero, and C. Provost, "Present-day sea level change: observations and causes". in *Earth Gravity Field from Space — From Sensors to Earth Sciences: Proceedings of an ISSI Workshop 11–15 March 2002, Bern, Switzerland*, G. Beutler, M. R. Drinkwater, R. Rummel, and R. Steiger, Eds. Dordrecht: Springer Netherlands, 2003, pp. 131-144.

[5] G. Galassi, and G. Spada, "Sea-level rise in the Mediterranean Sea by 2050: Roles of terrestrial ice melt, steric effects and glacial isostatic adjustment". *Global and Planetary Change,* vol. 123, Part A, pp. 55-66, Dec 2014.

[6] R. P. Paskoff, "Effects of sea-level rise on coastal cities and residential areas". In *Climate Change, Human Systems and Policy*. vol. 2, A. Yotova, Ed., ed: Eolss Publishers Co. Ltd.,, 2009, pp. 1-16.

[7] P. Vellinga and S. P. Leatherman, "Sea level rise, consequences and policies". *Climatic Change,* vol. 15, pp. 175-189, 1989.

[8] N. R. Council, D. E. L. Studies, O. S. Board, B. E. S. Resources, and O. W. Committee on Sea Level Rise in California, *Sea-Level Rise for the Coasts of California, Oregon, and Washington: Past, Present, and Future*: National Academies Press, 2012.

[9] R. Ranasinghe, "Assessing climate change impacts on open sandy coasts: A review". *Earth-Science Reviews,* vol. 160, pp. 320-332, Sep 2016.

[10] C. Brunel, and F. Sabatier, "Potential influence of sea-level rise in controlling shoreline position on the French Mediterranean Coast". *Geomorphology,* vol. 107, pp. 47-57, Jun 2009.

[11] V. M. Tuan, Y. Lacroix, and V. Q. Hung, "Assessment of the Shoreline Evolution at the Eastern Giens Tombolo of France". In *Proceedings of the International Conference on Innovations for Sustainable and Responsible Mining*, Cham, 2021, pp. 349-372.

[12] J. J. Blanc, «Phénomènes d'érosions sous-marines à la Presqu'île de Giens (Var),» *CR Acad. Sci. Paris,* vol. 278, pp. 1821-1823, 1974.

[13] A. J. D. Grissac, "Dynamic sedimentology of the Hyères and Giens bays (Var). Planning problems," Ph.D. dissertation, University of Aix-Marseille II, Marseille, 1975.

[14] Y. Lacroix, M. T. Vu, V. V. Than, and V. T. Nguyen, "Modeling the effect of geotextile submerged breakwater on hydrodynamics in La Capte beach". In *Vietnam-Japan Workshop on Estuaries, Coasts and Rivers*, Hoi An, Vietnam, 2015.

[15] M. T. Vu, Y. Lacroix, and V. T. Nguyen, "Empirical equilibrium beach profiles along the Eastern Tombolo of Giens". *Journal of Marine Science and Application,* vol. 17, pp. 241-253, Jun 2018.

[16] M. T. Vu, Y. Lacroix, and V. T. Nguyen, "Investigating the effects of sea-level rise on morphodynamics in the western Giens tombolo, France". *IOP Conference Series: Earth and Environmental Science,* vol. 167, 012027, Jul 2018.

[17] J. J. Blanc, "Recherches sédimentologiques sur la protection du littoral à la presqu'ile de Giens (Var)". Rapport final 1973.

[18] J. Courtaud, "Geomorphological dynamics and coastal risks case of the tombolo of Giens (Var, southern France)". Ph.D. dissertation, University of Aix-Marseille I, 2000.

[19] R. Capanni, "Study and integrated management of sediment transport in the Gapeau river/ Hyères bay system". Ph.D., University of Aix Marseille 1, 2011.

[20] M. T. Vu, Y. Lacroix, and V. T. Nguyen, "Investigating the impacts of the regression of Posidonia oceanica on hydrodynamics and sediment transport in Giens Gulf". *Ocean Engineering,* vol. 146, pp. 70-86, Jan 2017.

[21] J. M. Sinnassamy, and C. Pergent-Martini, "Localisation et état de l'herbier de Posidonies sur le littoral P.A.C.A: Var". D.R.A.E. & G.I.S. Posidonie 1990.

[22] S. Meulé, «IMplantation d'Atténuateur de Houle en GEOtextile: Suivi scientifique de la plage de La Capte, Hyères, Var : Instrumentation, Modélisation,» Hyères, Rapport final2010.

[23] E.O.L, "Monitoring of the evolution of the beaches of the commune of Hyères-les-palmiers," Municipality of Heres-Les-Palmiers, Rapport final 2010.

[24] DHI, "MIKE 21 & MIKE 3 FLOW MODEL FM - Hydrodynamic and Transport Module - Scientific Documentation," 2014.

[25] M. T. Vu, "A numerical Approach for the design of coastal protection works in the oriental Tombolo of the Giens Peninsula," Université de Toulon, 2018.

[26] Z. Liu, "Hydrodynamic and Sediment Transport Numerical Modelling and Applications at Tairua Estuary, New Zealand" Doctor of Philosophy, University of Waikato, 2014.

[27] V. T. Nguyen, "Morphological evolution and back siltation of navigation channel in Dinh An Estuary, Mekong River Delta: understanding, simulating and soluting," Doctor of Philosophy, Hohai University, 2012.

[28] M. Hsu, A. Kuo, J. Kuo, and W. Liu, “Procedure to calibrate and verify numerical models of estuarine hydrodynamics”. *Journal of Hydraulic Engineering,* vol. 125, pp. 166-182, Feb 1999.

[29] W. Liu, M. Hsu, and A. Kuo, “Modelling of hydrodynamics and cohesive sediment transport in Tanshui River estuarine system, Taiwan”. *Marine Pollution Bulletin,* vol. 44, pp. 1076-1088, Oct 2002.

[30] H. S. Mashriqui, “Hydrodynamic and Sediment Transport Modeling of Deltaic sediment processes,” Doctor of Philosophy, Department of Civil and Environmental Engineering, Louisiana State University, 2003.

[31] J. Sutherland, A. H. Peet, and R. L.Soulsby, “Evaluating the performance of morphological models”. *Coastal Engineering,* vol. 51, pp. 917-939, 2004.

[32] J. Sutherland, D. J. R. Walstra, T. J. Chesher, L. C. van Rijn, and H. N. Southgate, “Evaluation of coastal area modelling systems at an estuary mouth". *Coastal Engineering,* vol. 51, pp. 119-142, 2004.

[33] C. Brière, S. Abadie, P. Bretel, and P. Lang, “Assessment of TELEMAC system performances, a hydrodynamic case study of Anglet, France,” *Coastal Engineering,* vol. 54, pp. 345-356, 2007.

[34] D. Roelvink, A. Reniers, A. van Dongeren, J. van Thiel de Vries, R. McCall, and J. Lescinski, “Modelling storm impacts on beaches, dunes and barrier islands". *Coastal Engineering,* vol. 56, pp. 1133-1152, Nov-Dec 2009.

[35] L. C. Van-Rijn, D. J. R. Walstra, B. Grasmeijer, J. Sutherland, S. Pan, and J. P. Sierra, “The predictability of cross-shore bed evolution of sandy beaches at the time scale of storms and seasons using process-based profile models". *Coastal Engineering,* vol. 47, pp. 295-327, 2003.

[36] D. Pender, and H. Karunarathna, “A statistical-process based approach for modelling beach profile variability”. *Coastal Engineering,* vol. 81, pp. 19-29, Nov 2013.

[37] C. D. Storlazzi, E. Elias, M. E. Field, and M. K. Presto, “Numerical modeling of the impact of sea-level rise on fringing coral reef hydrodynamics and sediment transport". *Coral Reefs,* vol. 30, pp. 83-96, 2011.

[38] S. K. Liu, “Using coastal models to estimate effects of sea level rise". *Ocean & Coastal Management,* vol. 37, pp. 85-94, 1997.

[39] R. J. N. Devoy, “Coastal Vulnerability and the Implications of Sea-Level Rise for Ireland". *Journal of Coastal Research,* vol. 24, pp. 325-443, 2008.

[40] P. D. Komar, *Beach Processes and Sedimentation*: Prentice Hall, 1998.

ORIGINAL RESEARCH (AR) DOI: 10.4274/jems.2024.45822

Journal of ETA Maritime Science 2024;12(3):310-318

Increased Availability Risk-Based Maintenance ROV's Hydraulic System

Leonardo Braga[1], Igor De Souza Pinto[2], Paulo Apicelo De Souza Pereira[2], Mateus Carvalho Amaral[2], Rodolfo Cardoso[2]

[1]Miguel Ângelo Da Silva Santos Faculty, Department of Production Engineering, Rio de Janeiro, Brazil
[2]Fluminense Federal University, Institute of Science and Technology, Rio de Janeiro, Brazil

Abstract

In the contemporary landscape characterized by heightened competitive pressures, adept maintenance management assumes a pivotal and strategic role in cost mitigation and profit augmentation. This paper applies the risk-based maintenance (RBM) methodology to the hydraulic system of a remotely operated vehicle (ROV) owned by an oil and gas services company. To achieve this, it was necessary to gather information on the system failures, followed by determining the critical subsystems. By analyzing the frequency and severity of identified failures, a risk matrix could be constructed. Using the "5 Whys" technique, an analytical framework was used to uncover the root causes of the failures observed in the handlers and propellant subsystems. Subsequently, a risk matrix is formulated again after the implementation of the RBM and the mitigation measures adopted by the authors to elucidate the discernible impact of the maintenance methodology on improving the availability of the ROV and the incidence of failures outlined in the study.

Keywords: RBM, ROV, Failures, Availability

1. Introduction

Petrochemicals is the most expressive and dynamic branch of the multi-faceted national and international chemical industry. It is clear that oil represents the world's main energy source, accounting for around 31.5% of the matrix [1]; when we think of Brazil, this average remains close at around 33.1%. Oil is conceived as a fundamental good for the development of society. Within this context, the management of oil and petrochemical production is quite broad and challenging because it correlates several processes, such as input control, equipment management, and personnel training.

Maintenance activities have become one of the most important areas of the industry because of their remarkable participation in the achievement of objectives in an increasingly competitive environment. This increase in competitiveness implies an even greater need to establish appropriate strategies for the security of processes in force in modern industry that take into account factors such as the reliability and availability of these systems [2]. Adequate maintenance can ensure a satisfactory level of operability for systems and equipment over a certain period [3].

Experts from various fields have been discussing better maintenance strategies that, in addition to being able to reduce their costs, are also able to assess system conditions to manage factors such as reliability, safety, and availability of their assets [4]. The increasing use of fault management-focused maintenance strategies can reduce costs, increase productivity, and maintain the high reliability, availability, and safety of critical systems [5]. One of the approaches that has been discussed in the literature and industry is risk-based maintenance (RBM).

RBM analyses the probability and consequences of failures to prioritize maintenance actions [6]. RBM is a quantitative analysis methodology guided by financial aspects and aimed at continuous improvement, as well as at defining opportunities for the abovementioned process improvement.

Address for Correspondence: Paulo Apicelo De Souza Pereira, Fluminense Federal University, Institute of Science and Technology, Rio de Janeiro, Brazil
E-mail: pauloapicelo@id.uff.br
ORCID iD: orcid.org/0000-0002-7765-3961

Received: 25.01.2024
Last Revision Received: 30.04.2024
Accepted: 24.06.2024

To cite this article: L. Braga, I. D. S. Pinto, P. A. D. S. Pereira, M. C. Amaral, and R. Cardoso. "Increased Availability Risk-Based Maintenance ROV's Hydraulic System." *Journal of ETA Maritime Science*, vol. 12(3), pp. 310-318, 2024.

The approach is capable of analyzing financial risks given the occurrence of a failure, as well as assessing the cost/benefit of its elimination. The concept of RBM was developed to inspect high-risk components and to achieve acceptable risk criteria. The proposed methodology provides a tool for maintenance planning and decision-making to reduce the probability of equipment failure and the consequences of failure [7].

One of the equipment used in the exploration and production of oil and gas, which was the object of this study, is a remotely operated vehicle (ROV). This equipment consists of a robot responsible for performing underwater interventions and assisting in activities such as equipment installation and de-installation, inspection, and monitoring. As important equipment for exploration activities, there is a need for the ROV to have maximum availability and to meet the needs of the client, which reinforces the importance of an efficient maintenance plan [8].

These underwater vehicles supervise the preparation and installation of oil exploration and production equipment in depth [9]. The underwater ROV enables the remote contemplation of the ocean floor and underwater structures. An umbilical cord allows two-way communication (between operators and machines) and the transmission of energy to the ROV.

Hydraulic failures are critical because, in addition to resulting in considerable damage to the equipment, there is a great chance that oil will leak into the sea. That is, in addition to the cost of the asset being unavailable, fines and downtime may occur due to environmental damage. Professional ROV pilots can also engage in safety operations, underwater engineering inspections, and underwater rescue missions; therefore, they assist in the work of these professionals, especially when there is a risk [10].

The high time for the completion of maintenance, the various operational failures due to inadequate maintenance management, the delay in the treatment of recorded anomalies, the low availability of ROV, and the slow acquisition of spare parts are just some of the challenges encountered in the practical management context of these pieces of equipment. The objective of this study was to apply a RBM methodology to the critical subsystems of ROV systems.

2. Theoretical Reference

Maintenance management was conceptualized simply as planning and resource management based on the expected workload. Currently, the concept has expanded, and the maintenance organization is focused on managing and solving production problems, which makes a company remain competitive in the market. Maintenance is a structured activity of the company that is integrated into other activities to provide solutions that maximize results [11].

To achieve more efficient maintenance management, it is necessary to perform a consolidated fault analysis, which allows the root causes of unwanted events to be searched. Failure is when the operation or performance of a particular asset is interrupted at various levels: system, subsystem, and components [12]. Failures occur for different reasons. An example is that machines can break due to design errors, customer actions, supplier issues, and product manufacturing process difficulties, and so on [13].

Regarding the classification of failures, [14] stated that it is possible to observe failures from various aspects, such as their origin, time, extent, and criticality. For reliability, failures are classified according to their effect on a function of the system to which they belong. The root cause of failure analysis is a method performed in equipment to search for the causes of problems and determine specific actions to prevent their recurrence [11]. By prioritizing resources to deal with those who have higher operational risks, the maintenance team can achieve more satisfactory financial and safety results [3].

The RBM methodology provides a tool for maintenance planning and decision-making to reduce the probability of equipment failure and the consequences of failure [7]. Maintenance optimization is a possible technique to reduce maintenance costs while improving reliability. Companies must seek to implement new strategies for more effective maintenance techniques and programs to manage inspections and maintenance activities.

The RBM aims to select maintenance policies in the most different areas by using risk analysis concepts and techniques. In recent decades, maintenance engineering has experienced several profound changes that have integrated RBM into the full planning of industrial activities. Such changes began with the addition of reliability concepts in maintenance planning in the 1980s, and these changes are known as the “third generation of maintenance”. As a subsequent phase of maintenance management development, there was the integration of risk analysis concepts, which is known as the “fourth generation of maintenance” [15].

In the final opinion of a given project or process, a risk mitigation decision is made by adding factors such as cost [16]. When the process of this step is included, this concept is capable of denoting RBM. Figure 1 shows the general RBM procedure in detail.

Figure 1 illustrates the main steps of the RBM methodology, which begin with the collection of failure data. Subsequently, consequences and probability must be assessed to prioritize the risks present in the analyzed system. The development

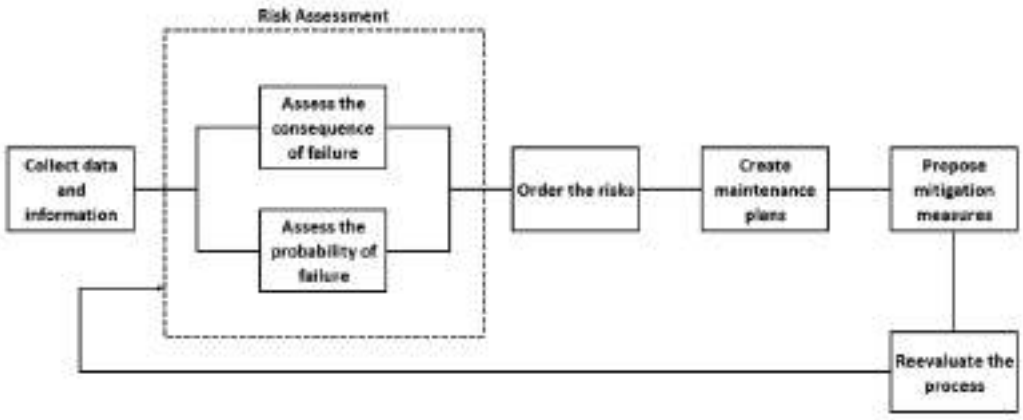

Figure 1. *RBM steps*

Adapted from Sakai [16]

RBM: Risk-based maintenance

of a maintenance plan along with proposals for mitigation measures is necessary so that a new evaluation of the process can be conducted to compare the current state after the implementation of the RBM steps with the state before the application of the methodology. These steps were used during this article and form the basis of the work conducted by the authors.

For ROV systems, there is a planned maintenance system, with emphasis on preventive techniques, developed according to the manufacturer's guidance, to reduce the possibility of failures before the expected or unnecessary disassembly of equipment still in good operating condition. However, even with a manufacturer-driven maintenance plan, significant corrective maintenance is performed, which may result in deviations from the maintenance plan used.

3. Methods

The classification of this article in terms of its nature is applied because it aims to aggregate practical knowledge used to solve problems. As to how the problem is addressed, the article is classified as quali-quantitative; quantitative, since the data of the failures were represented in numbers and classified to identify the subsystems with the highest level of criticality; and qualitative, due to the subjectivity and interpretation of the data obtained with the approach used to identify the root causes of the events that occurred.

A temporal cut-off was performed limiting the data collection period and the interval was established between June 2019 and June 2021. The work was carried out in an oil and gas sector company located in the city of Macaé, state of Rio de Janeiro (Brazil), presented here as "Delta". The Pipe Laying Support Vessel (PLSV) type vessel is also highlighted, where the ROV is installed is called "Deep X", even following a preventive maintenance plan based on the manufacturer's specifications, representing a significant period of unavailability.

Figure 2 shows the four steps responsible for characterizing the proposed method.

The ROV hydraulic system was defined and later divided into subsystems (Step 1) to collect and classify the data of the obtained failures (Step 2), which made it possible to organize the data using the analysis of Pareto. From this organization and application of the Pareto analysis, we were able to prioritize the critical ROV subsystems that presented the greatest occurrences of failure (Step 3). Subsequently, a risk matrix was developed to classify the risk of failure present in each subsystem. The subgroups that presented the highest risk were submitted to root causes of failure analysis (Step 4), and with the solution found, a new risk matrix was created to support the discussion of the results.

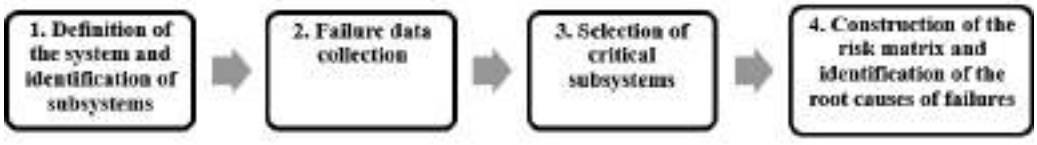

Figure 2. *Method steps*

4. Development

4.1. Description of System Analyzed

ROVs are submersible vehicles operated remotely by an operator, either on land or on a vessel. The submarine is an unmanned submarine whose main objective is to support oil well operations. These underwater vehicles supervise the preparation and installation of oil exploration and production equipment in depth [9]. The underwater ROV enables the remote contemplation of the ocean floor and underwater structures.

The use of ROVs allows long-term operation in deep water, which is not feasible in the case of diver use. It can also be operated in contaminated water, which poses a threat to the health and life of a diver, for example. ROVs are also widely used in underwater research, including shipwreck research and underwater archeological research [10].

ROVs have several classes and models that vary according to the type of operation. On the Deep X vessel, the ROV installed was class 3, and the model was Triton XLX (Figure 3) from the manufacturer Forum Energy Technologies extracted in [17]. The hydraulic, main, and auxiliary systems work essentially in the same manner; that is, a hydraulic pump coupled to an electric motor generates pressure on the system components and valves. For example, the pump supplies pressure to the manifold control valves. These valves provide pressure for various controlled components (thrusters, hydraulic tools, handlers, Pan&Tilt, etc.). The control valves on the manifolds are actuated by a surface control system through a local valve controller (LVC) plate located on each manifold. The LVC provides an electrical control interface with the valves.

Figure 3. *Triton XLX [17]*

A command is sent from the surface to the LVC that properly acts by controlling the valves that control the thrusters, tools, or other components. When any device is activated, there is an increase in the hydraulic pressure demand and consequently a pressure drop in the system. This drop is "felt" by the pump control circuits. The pump control circuits act so that there is an increase in the flow, which increases the system pressure, bringing it back to balance. The pump control system works continuously to balance the flow and pressure so that the output reaches the demand as it increases or decreases.

The main functions of the ROV hydraulic system served as a reference for this research by creating categories for the classification of faults that occurred. Name: (1) Thrusters, which are responsible for the ROV displacement; (2) handlers, which are the hands and arms of the submarine robot capable of lifting, connecting, and disconnecting; (3) Pan&Tilt, which provide movement to the cameras; (4) Motor/pump, which provide hydraulic power to the entire system; (5) Manifolds, which is the place where the control valves are installed; (6) reservoirs, where hydraulic fluid is stored; and (7) filters, which are responsible for keeping the fluid in healthy operating conditions.

4.2. Data Collection and Organization

The data collection process was carried out by Delta, specifically in a ROV installed in a PLSV vessel called Deep X. With one of its operational bases located in the city of Macaé, Brazil, Delta is a world leader in projects, technologies, systems, and services for the oil and gas industry. The company is capable of offering everything from individual products and services to fully integrated solutions, providing experience across the segments: Subsea, onshore/offshore, and surface projects.

To maintain asset functionality, the ROV has a strict preventive maintenance plan based on the manufacturer's specifications that indicates the replacement of parts, checking the wear of specific items, and hydraulic fluid conditions used. All system maintenance is managed by software called InforEAM© which is used for enterprise asset management to optimize maintenance operations and maximize equipment reliability. In addition to maintenance, the software has inventory control along with the purchasing system, simplifying procurement processes. The failure data recorded between June 2019 and June 2021 were exported from the software to a spreadsheet, classified according to subsystem, and quantified.

4.3. Quantification of Faults and Analysis of Pareto

From the hydraulic system division into 7 subsystems (Propellers, Handlers, Pan&Tilt, Motor/Pump, Reservoirs, Manifolds, and Filters), the exported failures of the InforEAM© software, comprising the period June 2019 to

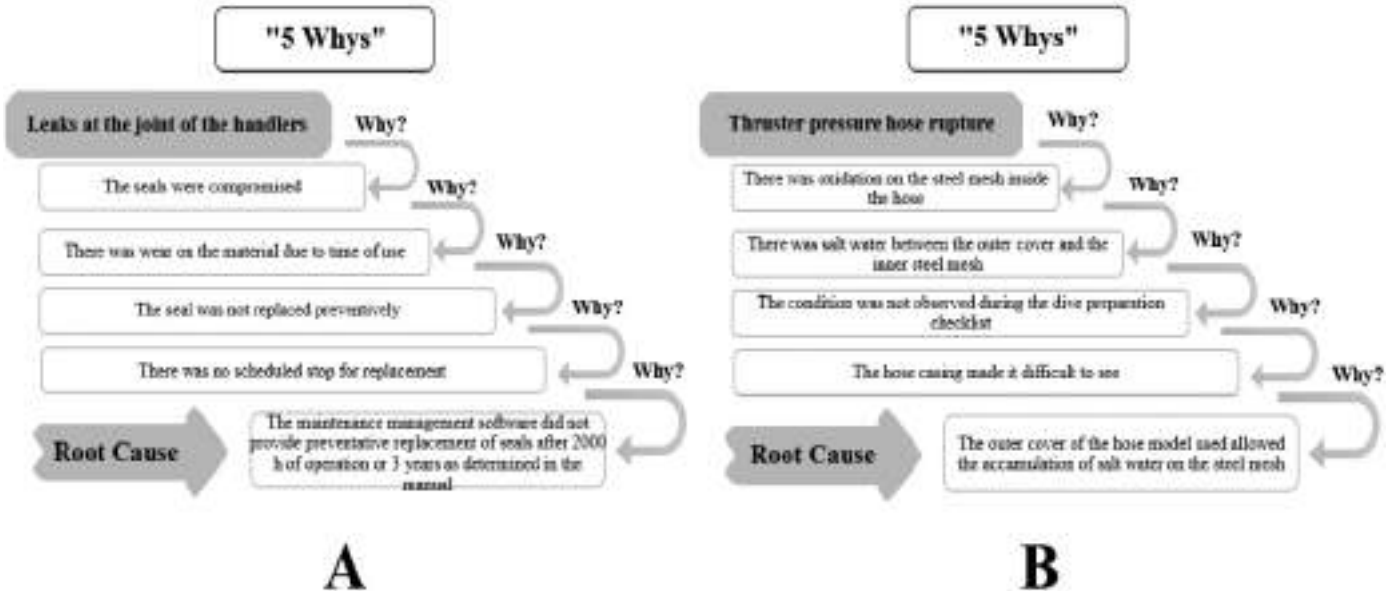

Figure 4. *Whys "Handlers (A)/Propellants (B)"*

June 2021, the relative and accumulated percentages for each subsystem shown in Table 1 below are also shown and classified according to their respective subsystem, together with the classification:

With the help of the table, it was possible to observe that in the period a total of 56 hydraulic failures occurred, and 73.21% of the events belonged to the subsystems of the manipulator and thrusters, thus representing the main causes of ROV unavailability due to hydraulic problems with a total of 41 of the 56 occurrences. All failures involving the hydraulic system were addressed by the ROV sector of the Deep X vessel in a corrective manner [18]. Dividing the system into categories and organizing the data combined with the risk matrix helped illustrate the impacts.

4.4. Criticality Analysis and Construction of A Risk Matrix

The risk matrix was developed to classify groups based on the relationship between the frequency of analysis failures and their severity. Table 2 lists the severity levels adopted in this study. The severity levels are described in Appendix A. Such levels of frequency and severity were determined in collaboration with ROV specialists from the operation and maintenance department of Delta Co.

Categories A, B, C, and D in Table 3 represent each level of criticality, i.e., how critical the respective group is for the hydraulic system, given its representativeness regarding the total number of events that occurred due to severity. Table 3 lists the criteria for each category.

Table 1. *Rov subsystems pareto analysis*

Description	Subsystem	Qty.	%Rel	%Acum
Handlers' failures	Handlers	28	50.00%	50.00%
Failures of thrusters	Propellants	13	23.21%	73.21%
Failures in Pan&Tilt	Pan&Tilt	4	7.14%	80.36%
Failures in the valve control block	Manifolds	3	5.36%	85.71%
Failures in the reservoirs	Reservoirs	3	5.36%	91.07%
Failures in the filtration system	Filters	3	5.36%	96.43%
Failures in hydraulic power generation systems	Motor/pump	2	3.57%	100.00%
	Total	**56**		

Source: Elaborated by the authors

4.5. Analysis of Root Cause of Failure in Selected Subsystems

In the risk matrix, the Pan&Tilt, Manifolds, Reservoirs, Filters, and Motor/Pump subsystems were positioned at level C in the criticality category, i.e., they are tolerable and, without additional measures required, can only be monitored according to the preventive maintenance plan already carried out by the ROV industry and as approached [19]. On the other hand, the subgroups of the handlers and thrusters were at level A, which represents the need for intervention to fall into acceptable categories.

Table 2. Frequency category

Level	Designation	Description
5	Very high	Represents over 50% of all failure occurrences
4	High	Represents 20-50% of all failure occurrences
3	Moderate	Represents 15-20% of all failure occurrences
2	Low	Represents 10-15% of all failure occurrences
1	Very low	Represents less than 10% of all failures
Source: Elaborated by the authors		

Table 3. Criticality category

Level	Designation	Criteria
A	Intolerable	Alternative methods must be considered to reduce the probability of occurrence and its consequences so that the criticality can be reduced to acceptable categories.
B	Undesirable	Additional measures should be evaluated to reduce criticality by implementing measures considered practicable.
C	Tolerable	No additional measures are required. Monitoring is required to ensure that criticality is maintained.
D	Negligible	No additional measures are required.
Source: Elaborated by the authors		

The 28 failures that occurred in the handler subsystem during the aforementioned period were arranged in a spreadsheet. According to the observed data, the events that occurred were due to leaks in the seals of the joints of the arms. To find the primary cause of these leaks, the technique used to analyze the root cause of failure [11].

The 13 failures in the thruster subsystem were also arranged in a spreadsheet. Based on the observed data, the events occurred mainly due to rupture of the pressure hoses connected to the propellers.

Based on the technique described by [20], to verify that the analysis was performed well, it is possible to replace the "Why" with "then" in the opposite direction, i.e., the root cause of the problem, and thus check the consistency of the analysis. The 41 failures in the handler and thruster subsystem during the period mentioned in the method section were arranged in a spreadsheet. According to the observed data, the events that occurred were due to leaks in the seals of the arms joints (case of the manipulators); and to find a primary cause of these leaks, the technique used was analysis of the root cause of failure [11].

Defined the parameters for the development of the risk matrix, each subsystem was classified, and for the Handlers group, the analysis of Pareto represented 50% of all hydraulic failures. The frequency and severity analysis resulted in level A (represented by "X") in the category of criticality, which can be observed in the risk matrix shown in Figure 5.

On the other hand, the Propellants subsystem represented 23.21% of the total occurrences in the frequency category, where it obtained level 4. Regarding severity, the group also obtained level 4, resulting in category A of criticality (represented by "X" too), as shown in Figure 5.

Figure 5. Risk matrix of "Handlers and Propellants"

Figure 6. *Post RBM risk matrix: Handlers and Propellants*

RBM: Risk-based maintenance

Since hydraulic failures represent a high severity scale, the solution according to the RBM methodology was to reduce the frequency at which these events occur, such as what happens in the filter group, so the risk matrix exposes a high severity of failure. Nevertheless, because the frequency is low, this group occupies category C in the risk scale, without the need for intervention, and only for monitoring.

When dealing with the two subsystems that had the greatest occurrence of failure and were more critical, it was possible to identify the two primary causes that were directly related to the high frequency of the failures. For the Handlers subsystem, the root cause was the failure to perform preventive maintenance as provided for in the manufacturer's manual, which states that the seals of the joints must be replaced every 2000 hours of operation or every 3 years.

The root cause of the Propellants subsystem was the type of hose used by the system. The hoses installed in the pressure lines were of a model that allowed the accumulation of salt water in the internal steel mesh, which caused oxidation in the mesh and broke with hydraulic pressure. The solution proposed for this failure was to replace the hose with a rubberized external cover that did not allow water to enter. In addition, this replacement and the check for corrosion or water accumulation in the hose should be inserted into the pre-operation checklist, and if there is still a propellant in the old hose, it should be replaced with a new one.

To illustrate the improvement in the RBM implementation, Figure 6 shows the new risk category of the Handlers and Propellants group.

5. Conclusion

This article aimed to apply the RBM methodology to the hydraulic failures of ROVs, and to achieve this objective, a case study developed for a Delta company vessel that operates in the oil and gas sector was used. Data extracted from the InforEAM© software were recorded in a spreadsheet, organized with the help of a Pareto chart, and classified according to the risk matrix. The ROV hydraulic system was detailed and divided into subsystems, where the elaborated matrix highlighted two subsystems with high levels of risk. With the analysis of the failures, it was possible to determine the root causes.

The solution found by the analysis resulted in a jump in the risk category in the two subsystems, and the proposal to improve the pre-operation checklist and update the preventive maintenance plan for the handlers has reinforced the importance of RBM for the company by highlighting the decrease in the frequency of failure occurrence. Due to the complexity of the other systems that make up the ROV, this research was based on only the hydraulic system. With this in mind, it is suggested for future studies that all ROVs be mapped according to the risks and analyses, and that maintenance plans and checklists be updated not only with the manufacturer's specifications but also with the RBM methodology.

The proposed solution for the failures identified in the handlers was to insert a 2000-hour preventive measure in the maintenance plan and a half-yearly inspection independent of the operating time to identify possible wear that the seals may present. With this proposed solution based on the RBM methodology, the authors expect that there will be a reduction in the number of failures that occur with fences. This implies an increase in the availability of the ROV of the Deep X vessel and a reduction in the costs that the Delta company has for the non-operability of the system. On the propellers, the solution proposed by the authors went through the replacement of the hose commonly used by another model with rubberized external cover, which was capable of blocking the water inlet, thus reducing the existence of corrosion in the equipment.

Authorship Contributions

Concept design: L. Braga, P. A. D. S. Pereira, M. C. Amaral, and. R. Cardoso, Data Collection or Processing: L. Braga, Analysis or Interpretation: L. Braga, and P. A. D. S. Pereira, Literature Review: L. Braga, I. D. S. Pinto, and P. A. D. S. Pereira, Writing, Reviewing and Editing: L. Braga, I. D. S. Pinto, and P. A. D. S. Pereira.

Funding: The authors declare that no funds, grants, or other support was received during the preparation of this manuscript.

References

[1] EPE, "National Energy Matrix", *Empresa de Pesquisa Energética*, 2018. [Online]. Available: https://www.epe.gov.br/pt/publicacoes-dados-abertos/publicacoes/balanco-energetico-nacional-2018. [Accessed: Oct. 2, 2021].

[2] Y. Jiang, and S. Yin, "Recent advances in key-performance-indicator oriented prognosis and diagnosis with a MATLAB toolbox: DB-KIT", *IEEE Transactions on Industrial Informatics,* vol. 15, pp. 2849-2858, May 2019.

[3] P. A. de Souza Pereira, "Risk-based maintenance applied in subsea equipments". *Brazilian Journal of Development*, vol. 9, pp. 18178-18197, May 2023.

[4] V. Atamuradov, K. Medjaher, P. Dersin, B. Lamoureux, and N. Zerhouni, "Prognostics and health management for maintenance practitioners - review, implementation and tools evaluation". *IJPHM*, vol. 8, pp. 1-31, Nov 2020.

[5] D. Galar, M. Palo, A. Van Horenbeek, and L. Pintelon, "Integration of disparate data sources to perform maintenance prognosis and optimal decision making". *Insight - Non-Destructive Testing and Condition Monitoring,* vol. 54, pp. 440-445, Aug 2012.

[6] J. Lima, A. Santos, and R. Sampaio, "Sistemas de gestão da manutenção - Uma revisão bibliográfica visando estabelecer critérios para avaliação de maturidade.", *Enegep*, Oct 2010.

[7] N. S. Arunraj, and J. Maiti, "Risk-based maintenance—Techniques and applications". *Journal of Hazardous Materials*, vol. 142, pp. 653-661, Apr 2007.

[8] P. Pereira, M. Amaral, R. Bella, and L. Ribeiro, "Reliability centered maintenance applied to an ROV system". *Brazilian Journal of Development*, vol. 9, Jul 2023.

[9] G. Lorosa, "*Sistemas elétricos de um veículo de operação remota (ROV): análise técnica funcional e operacional*", 2015.

[10] N. Bouchonneau, et al. "Study of expanded polymers water absorption for buoyancy modulus development of a submarine mini-robot". *Polimeros,* vol. 20, pp. 181-187, 2010.

[11] A. Kardec and J. Nascif, *Manutenção: função estratégica*. Rio de Janeiro: Qualitymark Petrobras, 2013.

[12] NASA, "Reliability centered maintenance guide for facilities and collateral equipment". *National Aeronautics and Space Administration,* Final, Sep 2008. [Online].

[13] N. Slack, S. Chambers, and R. Johnston, *Administração da Produção*. São Paulo: Atlas, 2002.

[14] P. Siqueira, *Manutenção Centrada na Confiabilidade: Manual de Implementação*. Rio de Janeiro: Qualitymark Editora, 2014.

[15] F. I. Khan, and M. Haddara, "Risk-based maintenance (RBM): A new approach for process plant inspection and maintenance", *Process Safety Progress*, vol. 23, pp. 252-265, Nov 2004.

[16] S. Sakai, "Risk-based maintenance". *JR East Technical Review,* Tokyo, 2010.

[17] ROV Solutions for Power & Telecom, "ROVOP: Global ROV specialist". *ROV Solutions for Power & Telecom*, 2019. [Online]. Available: https://www.rovop.com. [Accessed: Jun 5, 2023].

[18] M. Pereira, *Engenharia de Manutenção – Teoria e Prática*. Rio de Janeiro: Ciência Moderna Ltda., 2009.

[19] M. Pego, *Fundamentos da Engenharia de Manutenção*. *[S.l]*: *[S.n],* 2018.

[20] E. Bassan, *Gestão da Qualidade: Ferramentas, técnicas e métodos*. Curitiba: Clube de Autores, 2018.

Appendix A. *Severity category*

Level	Designation	Assets	Environment	Customer	Operability
5	Catastrophic	Material damage whose economic values for repair actions are very high compared to acquisition costs.	Environmental impact is difficult to reverse, even with mitigating actions, and of great magnitude and extent (beyond the limits of the enterprise) with the potential to affect stakeholders.	Direct impact on customer relationship. Contract interruption.	More than 24 hours of average downtime.
4	Critical	Material damage whose economic values for repair actions are high compared to acquisition costs.	Impact of great magnitude, reversible with mitigating actions, but restricted to adjacent areas of the unit.	Direct impact on customer relationship. Project shutdown.	Between 12 and 24 hours of average downtime.
3	Moderate	Material damage whose economic values for repair actions are moderate compared to acquisition costs.	Impact of considerable magnitude, but reversible with mitigating actions, affecting only internal areas of the unit.	Possible impact on the customer with a chance to affect the project and other operations.	Between 6 and 12 hours of average downtime.
2	Marginal	Material damage whose economic values for repair actions are reduced compared to acquisition costs.	Impact of negligible magnitude, but reversible with mitigating actions, affecting only internal areas of the unit.	Possible impact on the customer with a chance to affect the project.	Between 1 and 6 hours of average downtime.
1	Negligible	Material damage whose economic values for repair actions are negligible compared to acquisition costs.	Impact of negligible magnitude for the environment/restricted to the occurrence site, fully reversible with immediate actions, does not affect stakeholders.	No impact on the customer.	Up to 1 hour of average downtime.

ORIGINAL RESEARCH (AR) DOI: 10.4274/jems.2024.59862

Journal of ETA Maritime Science 2024;12(3):319-331

Simulation Modeling Frameworks for Single-Cycling and Double-Cycling Strategies in Container Terminals

Gonca Tuncel[1], Özgür Yalçınkaya[2], Elvan Deniz[3], Soner Esmer[4]

[1]Dokuz Eylül University, Department of Industrial Engineering, İzmir, Türkiye
[2]Dokuz Eylül University, Graduate School of Natural and Applied Sciences, İzmir, Türkiye
[3]Çanakkale Onsekiz Mart University, Çan Higher Vocational School, Çanakkale, Türkiye
[4]Kocaeli University, Department of Maritime Business Administration, Kocaeli, Türkiye

Abstract

Container terminals are among the most critical parts of transportation systems. Reducing the ship turnaround time increases terminal efficiency and enhances global trade volumes. Such time reductions can be achieved by improving the operational efficiency of major resources at container terminals. Quay crane operating strategies are crucial for assessing the performance of container terminals. Simulation models are effective and reliable methods for interpreting and improving complex systems. This study proposes simulation models that include container loading and unloading tasks in marine container terminals implementing single-cycling and double-cycling strategies. Double-cycling is a quay crane operating strategy that attempts to improve container handling efficiency. The system was modeled using ARENA simulation software. The implementation results of the single-cycling and double-cycling strategies were compared in terms of the performance criteria, such as the utilization rates of the quay crane and yard trucks, ship turnaround time, and operating cost.

Keywords: Container terminal, Quay crane, Double-cycling, Simulation

1. Introduction

Container terminals are service businesses located over global distribution systems, and they are particularly concentrated on main trade routes serving global supply chains. Most container terminals have three types of handling equipment: quay cranes (QCs), yard cranes (YCs), and yard trucks (YTs). QCs, which are the basic equipment of the handling process and are located on the quay wall, significantly affect the operational efficiency of container terminals. Potential disruptions, such as the inefficient operation of QCs in any logistic process at the port, can affect the speed of handling operations and increase the turnaround time of the ships. Ships waiting at the quay prevent cargo owners from receiving their cargo at the scheduled time and also increase container terminal costs. Single-cycling and double-cycling strategies can be applied in the operation of QCs. Container terminals require a flexible decision-support tool that includes logistical processes related to handling, port transportation, and storage, can measure the performance of terminal equipment, provide timely information regarding bottlenecks, and evaluate different alternatives. Changing parameters in real-life systems, such as container terminals, carries some risks. Instead, it is much more advantageous to model the system and conduct experiments on the system model. Simulation can be used as an analysis method in planning and developing processes by conducting experiments on models [1]. This study consists of two parts that align to develop flexible simulation models applicable to all terminals by measuring the performance of container terminal handling operations using simulation models. The terminal operating system includes a QC and a Rubber Tyred Gantry (RTG) YC working with YTs. The first simulation model was implemented with the single-cycling strategy, and the second simulation model was implemented with the double-cycling strategy. Although a growing number of researchers have addressed the problems

Address for Correspondence: Gonca Tuncel, Dokuz Eylül University, Department of Industrial Engineering, İzmir, Türkiye
E-mail: gonca.tuncel@deu.edu.tr
ORCID iD: orcid.org/0000-0003-0389-5594

Received: 10.01.2024
Last Revision Received: 30.07.2024
Accepted: 03.08.2024

To cite this article: G. Tuncel, Ö. Yalçınkaya, E. Deniz, and S. Esmer, "Simulation Modeling Frameworks for Single-Cycling and Double-Cycling Strategies in Container Terminals." *Journal of ETA Maritime Science*, vol. 12(3), pp. 319-331, 2024.

of port design and operation, quite little attention has been given to investigating different QC operating strategies to improve the productivity of container handling components such as QCs, RTG cranes, and YTs.

In this paper, after an overview of the literature, single-cycling and double-cycling strategies are described. The simulation models developed for single-cycling and double-cycling cases are then presented. In addition, system performance concerning the considered measures was examined. Finally, the conclusions of this study and possible research directions are discussed.

2. Literature Review

"The QC double-cycling problem" (QCDCP) is well-known as the "QC scheduling problem" (QCSP), whose main issue is to find an entire QC working schedule that typically aims to reduce the operation time of the ship. The first scientific research on sequencing problems in double-cycling (or dual-cycling) operations was initiated by Goodchild and Daganzo [2]. The authors introduce a model expressed as a two-machine flow-shop SP to determine the permutation of stacks for a double-cycling operation flow. In their next study, the authors [3] presented the double-cycling effect on port operations, including crane, ship, and berth efficiency. The proximal stack strategy was described for double-cycling, and its effectiveness was assessed. The impact of the double-cycling strategy on the landside transportation operations was then evaluated. The authors report that double-cycling can decrease processing time by 10% by improving ship, crane, and berth efficiency. Zhang and Kim's study [4] expanded the problem to include multiple hatches. The objective of this study was to minimize the processing cycles of QC during loading/unloading operations in a ship bay. This is, of course, possible by maximizing the number of double-cycling operations. The authors developed a mixed IP (MIP) model for this purpose. A hybrid heuristic method was used to resolve this problem. Implementing a double-cycling strategy in terminals requires only functional changes without the need to purchase additional equipment. In addition, the YT operation method must be altered from the assigned system to the pooling system. The following year, some other authors studied the same problem involving YCs and YTs. Nguyen and Kim [5] used a modified MIP model and a heuristic algorithm to minimize the empty move seconds of YTs by the QC double-cycling method. A simulation technique was employed to evaluate the effect of unloading and loading schedules and storage plans for unloaded containers on the system efficiency, including the percentage of double-cycling operation of YTs. The authors note that the process type of QCs has a significant impact on the performance of YT processes. They considered the unloading of vehicles (YTs). Nevertheless, the unified scheduling of vehicle routes, YC processes, and QC processes can be considered in future studies. Additionally, the storage spaces of loaded containers should be considered in the context of YTs. By considering the features of double-cycling operations, Meisel and Wichmann [6] studied the problem of container sequencing for reshuffles in a shipping bay. An integer programming (IP) model and a heuristic solution method were used to arrange crane operations in internal reshuffles. The results provided insights into the performance enhancement of internal reshuffles associated with a single application of double crane cycling. The QCSP and other SPs in seaside planning and operation have been intensively reviewed by Bierwirth and Meisel [7,8]. Another study, which considered a more complex scenario considering hatch covers, was conducted by Lee et al. [9]. Liu et al. [10] investigated models and algorithms for general QCDCP with internal reshuffles. The integrated DCP of QCs and YCs was considered by Zhang et al. [11]. The aim was to minimize the processing time of QC and YC. They formulated a MIP model for the two-stage double-cycling process of container terminals. Numerical exercises showed that the specified model and algorithm were more efficient in terms of lower bounds presented in previous studies. In the same year, Zeng et al. [12] developed a scheduling model and designed algorithms for QCDCP. A MIP model was formulated to develop a stacking plan for outbound containers and the process order of QCs to increase the performance progress of the QCDC. Double-cycling QCSP was also investigated by Wang and Li [13]. The problem is presented as a two-machine non-permutation flow-shop scheduling model, and a composite heuristic for the problem is described. Zhang et al. [14] proposed "a mixed storage strategy" for horizontal transportation associated with the QCDCP to enhance the performance of yard processes. The authors discussed the impact of the mixed storage strategy on QC double-cycling operations. In light of the numerical results, the authors report that using a hybrid storage strategy and double-cycling can decrease the number of YTs per QC, the operation time of the YC, and the length of the YT travel. Although double-cycling increases the port capacity, some ports are reluctant to implement this strategy. In the same year, Ku and Arthanari [15] considered the multi-QCDCP. The problem was formulated as a MIP model and a two-stage hybrid heuristic approach was presented for double-cycling QCSP in numerous hatches. The process involves two stages: intra-phase and inter-phase sequencing. A mathematical model was presented by Chu et al. [16] for the "multiple-QC sequencing problem" with the strategy of double-cycling. An algorithm was designed based on Lagrange relaxation to solve the model. In addition, Kamble et al. [17] investigated the implementation barriers of a double-cycling strategy in

Indian ports. The authors concluded that the ability to use information technologies in ports and to integrate with other ports and partners is the primary barrier to implementation. On the other hand, Zhang et al. [18] focused on the complete handling efficiency and system strength of container terminals. The performance of double-cycling operations based on different equipment variations is analyzed using Tianjin port data. Tang et al. [19] developed "an agent-based simulation model" to define QCs, YCs, and YT operation processes. They concluded that peak shaving is a promising strategy for QC double-cycling. Ahmed et al. [20], presented a container handling strategy to improve terminal operations and minimize unit cost by applying double-cycling of YTs. The authors developed simulation models based on a real-life case study considering the uncertainties in the work task duration. Zhang et al. [21], proposed an automated guided vehicle (AGV) SP with multi-QC by employing the double-cycling strategy. The main objective was to minimize the total waiting time of AGVs and propose an AGV scheduling model with a high loading rate. A container planning sequence based on the Hybrid Particle Swarm Optimization algorithm with a penalty function was obtained for a time interval to the arrival of AGVs at the quayside. Minimizing the empty AGV trips could improve the container terminal transporting efficiency in terms of time. Zhu et al. [22], applied a mixed storage strategy for port-handling operations to accommodate double-cycle scheduling plans in container terminals. Fontes and Homayouni [23] investigated the joint SP of QCs and speed-adjustable AGVs under the double-cycling strategy. The authors address the energy consumption of seaports. In the same year, Wei et al. [24], investigated the energy efficiency optimization problem of automated QC operation sequences with time window constraints. A corresponding MIP model was established by decomposing the automated QC operations. The proposed double-cycle model was not combined with internal truck scheduling. Yue et al. [25] addressed the block allocation problem for inbound and transshipment containers based on a multi-ship block-sharing strategy, which can enhance the double-cycling of AGVs and YCs. The authors presented a two-stage MIP model that minimizes the handling cost. Cai et al. [26], presented a MIP model for the integrated SP of QCs, YCs, and intelligent guided vehicles under the double-cycling mode in a U-shaped container terminal. Li et al. [27] investigated the multiple-equipment integrated SP (MISP) in automated container terminals. The authors focus on optimizing the equipment scheduling and container job sequence in MISP by employing the double-cycling strategy. Tan et al. [28] considered the storage space allocation problem in a container yard under the double-cycle operation mode for internal YTs. Wang et al. [29] studied an integrated SP for automated stacking cranes and AGVs considering direct, buffer, and hybrid modes for transferring containers. The authors developed a genetic algorithm to solve this problem. Based on the double-cycle operations for AGVs, Zhang et al. [30] applied a branch and bound algorithm to assign container tasks to YCs, where two crossover YCs move on different rails.

Although the single-cycling strategy is more commonly employed in practice, a growing body of literature exists on the incorporation of the double-cycling mode in recent years. However, most previous studies only analyzed the YT transportation or the efficiency of equipment, such as QCs and YCs, independently. Scheduling the handling components separately is considered impractical because they involve mutual work tasks [20]. On the other hand, few studies analyzed both QC and YT operations or, in an integrated way, QCs, YCs, and AGVs in automated container terminals. Due to the very different conditions in container terminals, there is still a gap between the requirements of real configuration problems and the status of research. This study aims to develop flexible simulation models that can be applied to all container terminals by modifying only the system parameters for analyzing the handling performance. The first of the simulation models was applied to a single-cycling strategy, and the second was applied to a double-cycling strategy. This study differs from the literature in terms of measuring the loaded and unloaded travel time ratios of the YTs for both strategies.

3. Modeling QC Operating Strategies

3.1. Single-Cycling Strategy

Single-cycling strategy is an operating technique in which containers are loaded in the ship bay after the QCs complete unloading tasks. With the single-cycling strategy applied using a single QC and a single bay, the handling operation starts with the arrival of the ship. The QC starts the container handling process from the related pre-planned bay. It loads the related container onto the YT, which takes it to the stockyard. The RTG stacks the containers in the stockyard, and the YT is released. The QC performs either loading or unloading activities in each cycle, covering the crane's round trip between the ship and the shore. After the unloading tasks are completed, the containers to be transported to the same ship are loaded onto the YTs by the RTG in the relevant stockyard. The YT is released once a container is delivered to the QC. The QC then loads the container onto the ship and completes the handling operation in a single cycle.

3.2. Double-Cycling Strategy

Double-cycling strategy is an operating technique in which QCs simultaneously perform their loading and unloading tasks in the same ship bay. In the double-cycling strategy

implemented using a single QC and a single bay, the QC starts the container handling process from the relevant bay and loads the related containers onto the YTs, which transport them to the stockyard. The RTG then unloads the YTs and stacks the containers in the yard blocks. Unlike single-cycling, the released YTs do not return empty. Instead, they are directed to the nearest stockyard where the containers are loaded. The containers to be transported by the ship are loaded onto the YTs by the RTG in the yard. Once the QC picks up the container, the YT is released. The container is then loaded onto the ship by the QC, and the handling process is completed in the same crane cycle. The double cycle continues until the handling of the ship bay is completed. Single-cycling and double-cycling strategies are compared in Figure 1.

4. Simulation Modeling Frameworks

We developed two simulation models for a case study based on a real container terminal. Single-cycling and double-cycling strategies are employed in each model. The main resources defined in these models are QC and RTG cranes. In addition, the use of one or more YTs is allowed in the process. The process flows of the single-cycling and double-cycling strategies are presented in Figures 2 and 3, respectively.

The parameter values were set based on the work-study conducted during terminal visits and interviews with operation managers. After data collection and evaluation, simulation models are created depending on the determined processes and identified routes. The operation of the considered simulation model is based on the following assumptions:

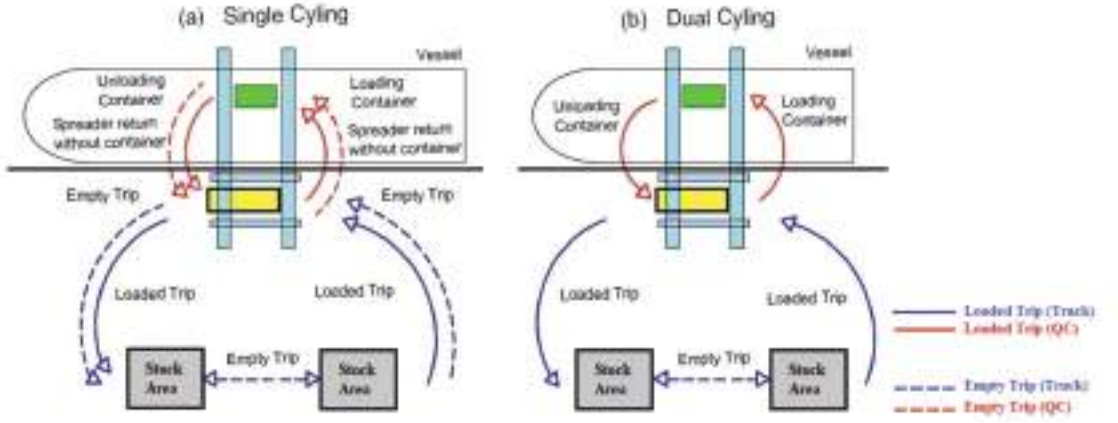

Figure 1. *Comparison of single-cycling and double-cycling strategies [31]*

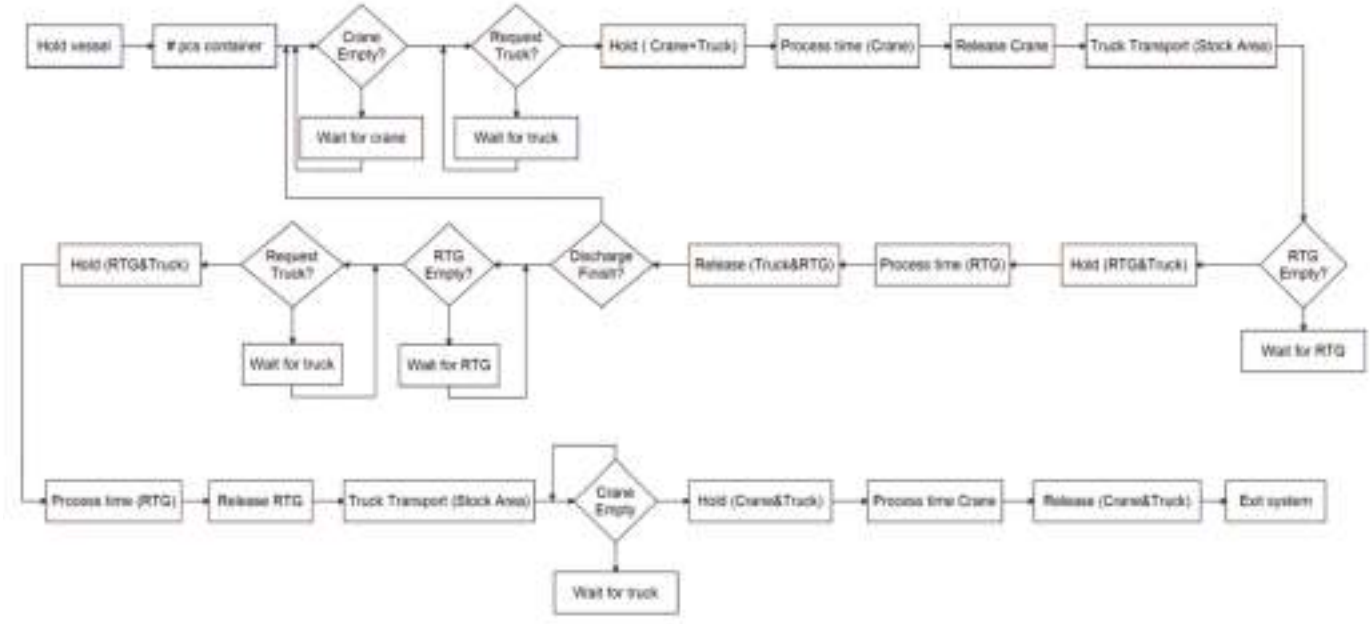

Figure 2. *Flow chart of the single-cycling strategy*

• One QC, one RTG crane, and one or more YTs are in the system.

• Containers to be loaded or unloaded during ship operation are 40 feet.

• The handling time of work tasks by the QC is generated from a uniform distribution with a range, [2 min.+uniform (0;0.5)], and the processing time for unloading/loading by the RTG is also generated from a uniform distribution with a range, [5 min.+uniform (0;1)].

• The YT velocity was assumed to be 20 km per hour.

We used ARENA 14.0 simulation software to build the simulation models for the container terminal. The developed models are generic and can be easily adapted to changing operating conditions. The elements of the simulation models are given in Figures 4 and 5 for the single-cycling and double-cycling models, respectively.

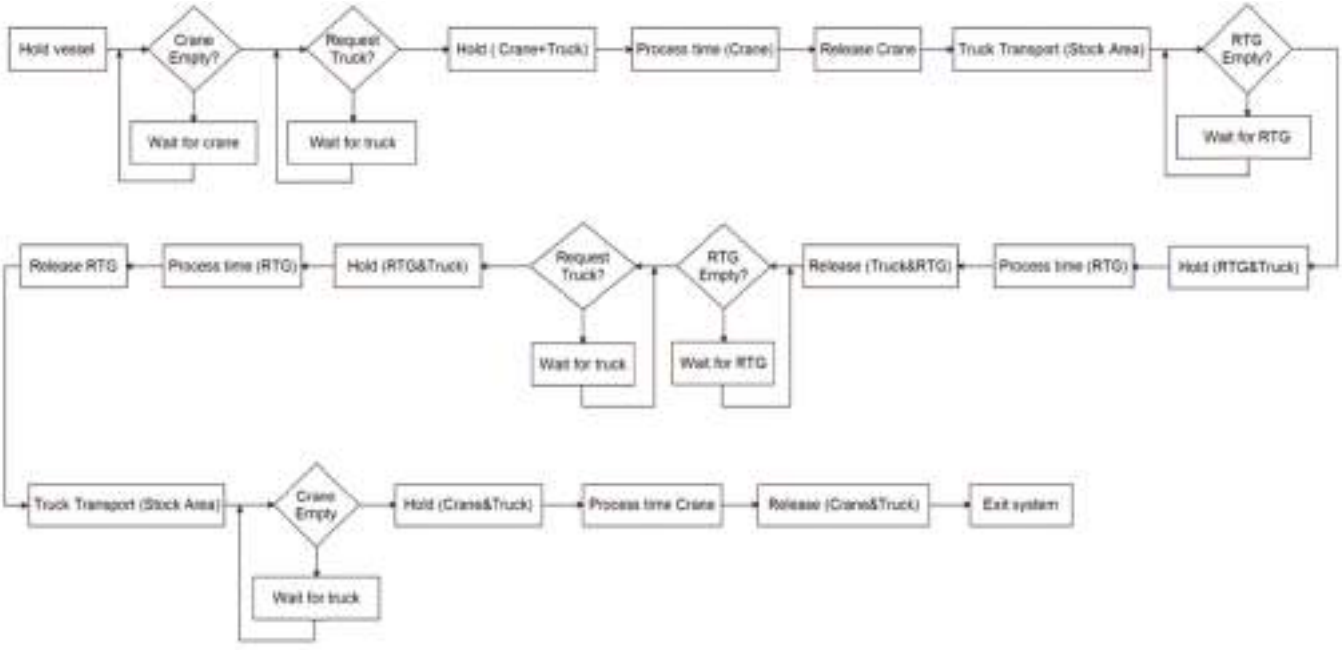

Figure 3. *Flow chart of the double-cycling strategy*

Variables	Attributes	Resources	Transporters	Replicate	Dstats
ConNum	Timein	Crane	Trucks		nq(TruckqL1)
Loaded	Unload	RTG			nq(TruckqL3)
	Truck#				nq(CraneqL1u)
					nq(CraneqL1l)
					nq(RTGqL2)
					nq(RTGqL3)
					nr(Crane)
					nr(RTG)
					nt(Trucks)
					it(Trucks,1)
					Loaded(1)
					it(Trucks,1)-Loaded(1)
					it(Trucks,2)
					Loaded(2)
					it(Trucks,2)-Loaded(2)
					it(Trucks,3)
					Loaded(3)
					it(Trucks,3)-Loaded(3)

Queues	Tallies	Stations	Distances
CraneqL1u	OverallflowtimeU	L1	Map1
TruckqL1	OverallflowtimeL	L2	
RTGqL2		L3	
CraneqL1l			
TruckqL3			
RTGqL3			

Figure 4. *Elements of the single-cycling model*

4.1. Elements

Attributes; Timein is the record of the loading and unloading service times of the containers, and Unload is the record of the YTs' loading and unloading service times.

Resources; The following two resources were defined in the simulation model:

- Crane
- RTG

Queues; The following nine queues were defined in the simulation model:

- Craneq
- RTGq
- Truckq
- CraneqL1u
- RTGqL2
- TruckqL1
- CraneqL1l
- TruckqL3
- RTGqL3

Variables; ConNum is implemented as a counter to determine the number of containers unloaded from the ship.

Loaded is a variable used to determine the container-loaded YT rate.

Dstats; Statistics on the utilization rate of each resource, and the average number of containers waiting in each queue are recorded.

Tallies; Tallies are defined as the record of the overall flow time of containers and the time spent on containers (loading and unloading).

Replicate; The replication number was set to 10.

Transport; The transporter element describes the operating characteristics of the transporters used in the model. A transporter type (YT) is identified in the simulation model.

Distances; The distance between all stations is shown on the transporter's system map.

Stations; The three stations L1, L2, and L3 were defined in the simulation model.

4.2. Blocks

The effectiveness of the QC operating strategies was tested using the simulation models. The first simulation model was developed by applying the single-cycling strategy, where the loading tasks of the containers onto the ship started after the unloading of the ship was completed. In the second simulation model, handling operations are carried out simultaneously by unloading the inbound containers from the ship and loading the corresponding outbound containers onto the ship in a double cycle. The entities in the proposed models represent 40' containers.

Figure 6 shows the blocks of the single-cycling model. Container/Entity arrivals are defined in the "Create" block for containers. Each created entity is transferred to the "Assign" block with m attributes and is unloaded. Then, they join the L1 station, and their handling operations (loading or unloading) are checked in the "Branch" block. Containers join the QC queue for unloading operations, are seized by

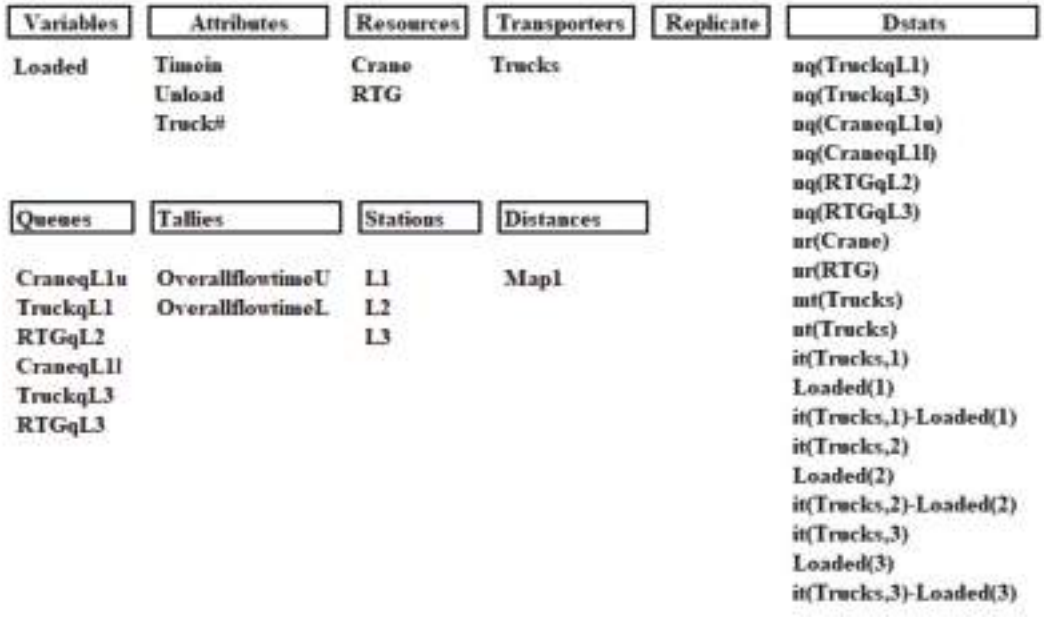

Figure 5. *Elements of the double-cycling model*

the QC, and spend operation time in the "Delay" block. The QC then releases the containers. YTs are requested for containers from the L1 station to the L2 station by the "Request" block. After the loaded variables are assigned in the "Assign" block, the YTs transport the containers in the "Transport" block. The containers join the RTG queue after seizing the RTG and spend the operation time in the "Delay" block. Later, the container releases the RTG and YT. The loaded and ConNum variables are assigned in the "Assign" block. In the "Branch" block, containers are unloaded from the ship. After joining the "Tally" block, which records the handling operation times, the container exits the system via the "Dispose" block. If the container's ConNum is equal to the number of containers in the "Branch" block, the container joins the "Duplicate" block. Containers are created in the "Duplicate" block to start the loading process. Unload, Timein, and m (enter systems) are assigned in another "Assign" block. Then, the RTG is seized and the operation time is spent in the "Delay" block. Afterward, the RTG is released. YTs are requested to be transported from the L3 station to the L1 station by the "Request" block. The loaded variables are assigned in the "Assign" block after the YTs are transported from the L3 station to the L1 station in the "Transport" blocks. Containers join the QC queue for loading, seize the QC, and spend operation time in the "Delay" block. Then, the QC is released by the "Release" block and the YT is set free. After the "Tally" block records the handling operation times, the container exits the system via the "Dispose" block.

Figure 7 shows blocks of the double-cycling model. The entities created in the first "Create" block leave the system by the "Dispose" block after the signal codes are generated and defined in the "Signal" block. In the second "Create" block, entities representing containers are created and entered into the system. Each created entity is transferred to the "Assign" block with *m* attributes and unloaded, as in the single-cycling model. Then, the related container is redirected to the L1 station, which is assigned to the "Station" block. The container arriving at the "Branch" block is put into the QC queue by activating the "Queue" block according to the probability of unloading=1 if it is unloaded from the ship and the probability of unloading=0 if it is loaded onto the

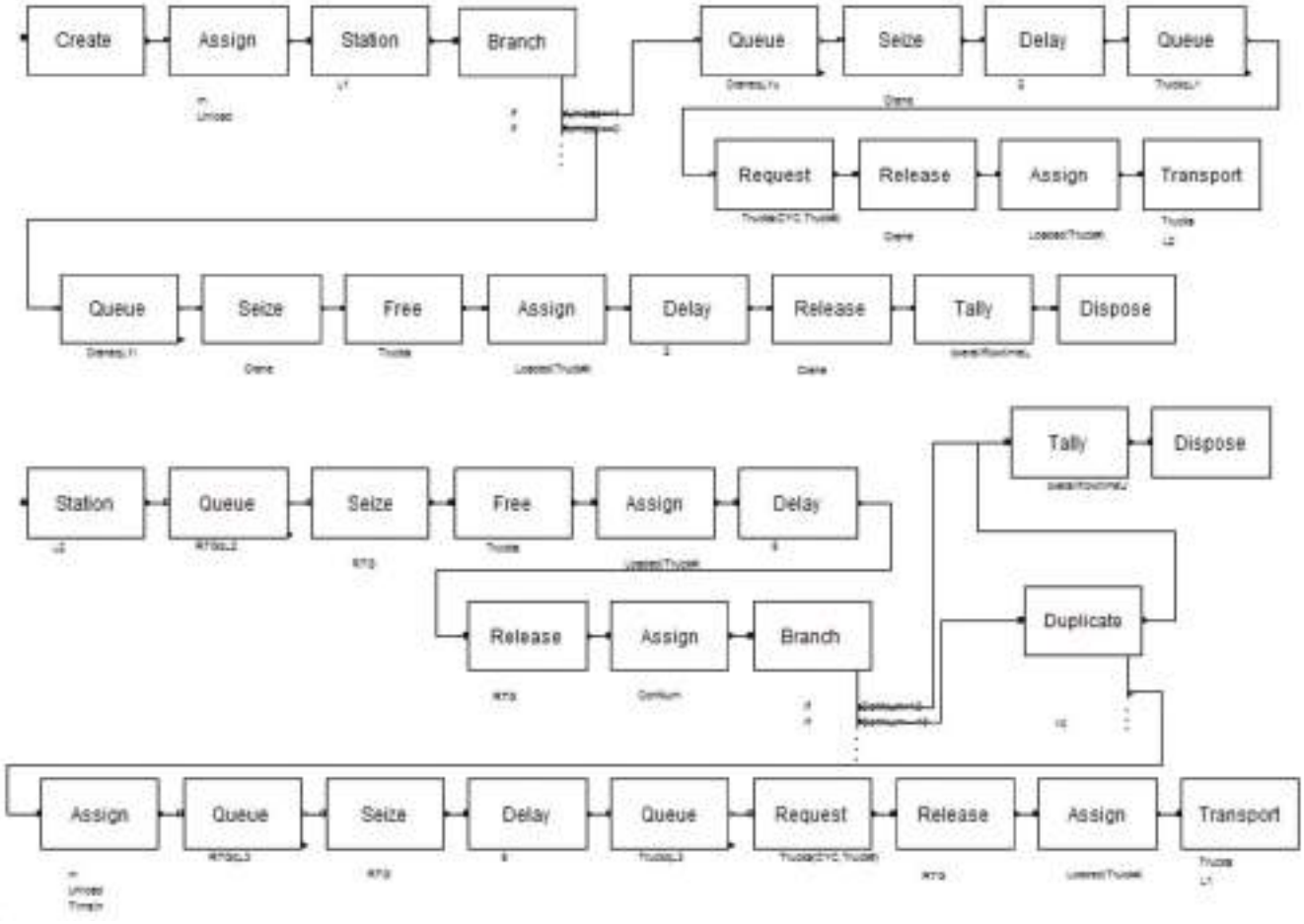

Figure 6. *Blocks of the single-cycling model*

Figure 7. *Blocks of the double-cycling model*

ship. Then, the "Wait" block keeps the movements of the container on hold until the signal code arrives from the "Signal" block. In the meantime, the container seizes the QC by the "Seize" block to initiate the unloading process and releases the source (QC) it holds by the "Release" block at the end of the operation time in the "Delay" block. The YT is requested through the "Request" block, and the arriving YT joins the queue. After the loading task is executed, the value of the loaded variable is incremented in the "Assign" block. The YT transports the container by the "Transport" block to the relevant station. The loaded YT arriving at the L2 station waits in the RTG queue. The container released with the signal code in the "Signal" block, seizes the RTG by the "Seize" block. The YT is released in the "Free" block by reducing the value of the loaded variable, which acts as a counter, after activating the "Assign" block. At the end of the operation time in the "Delay" block, the container releases the source (RTG) it holds by the "Release" block. After the "Tally" block records handling operation times, the container exits the system via the "Dispose" block.

In the third "Create" block, entities are also defined as containers. They enter the system and are directed to the "Assign" block. After joining the L3 station (Stock Yard Area) and the RTG queue, the containers wait for the signal in the "Wait" block and then seize the RTG. It spends the operation time in the "Delay" block and then releases the RTG. Next, the YT is requested to travel from the L3 station to the L1 station by the "Request" block. Loaded variables are assigned in the "Assign" block, and the "Transport" block transports the containers by YTs. The containers join the QC queue, send the signal in the "Signal" block, seize the QC, and spend the operation time in the "Delay" block. Then, it releases the QC and sets the YT free. After the "Tally" block records handling operation times, the container exits the system via the "Dispose" block.

5. Implementation Results

The system performance was measured in the following ways:

• Time periods are defined and constituted using the tally element,

• Resource, transporter, and queue statistics are determined using the Dstats element,

Two tally variables were defined: Overall Flow Time (Overall_Flow_TimeU and Overall_Flow_TimeL) and replication ended time. Statistics regarding the utilization rate of each YT and source in the Dstats element and the average number of containers waiting in the queue were also recorded and displayed as simulation results based on the changes in the Tally variables and the discrete change variables. The implementation results of the single-cycling and double-cycling models are summarized in Figures 8-15.

Figure 8 shows the total operation time of the single-cycling model. The total operation time decreased from 242.53 to 119.02 minutes.

As can be seen in Figure 9, the total operation time decreased from 263.12 minutes to 119.02 minutes in the double-cycling model. Note that the total operation time achieved with ten YTs in the single-cycling model is achieved with four YTs in the double-cycling model.

The average utilization of the QC for the single-cycling model decreased from 53.65% to 33.61% when the number of YTs increased from 1 to 10 (see Figure 10).

Figure 11 shows the average utilization rate of the QC for the double-cycling strategy. The average utilization rate increased from 15.20% to 33.61% as the number of YTs increased.

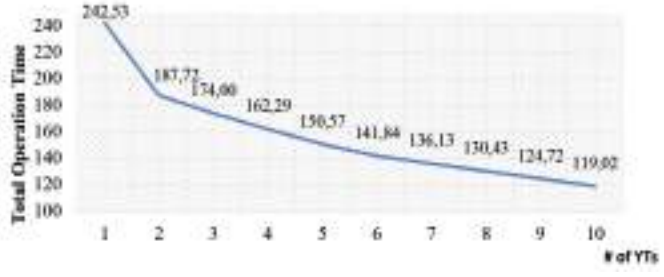

Figure 8. *Total operation time of the single-cycling model*

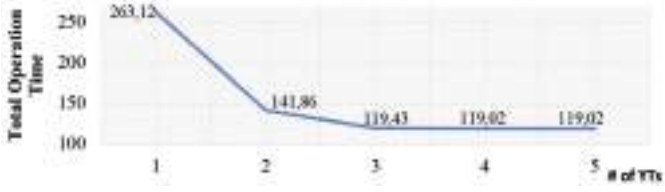

Figure 9. *Total operation time of the double-cycling model*

In Figure 12, another discrete-change variable called the average utilization of YTs is given. It can be seen that the average utilization of the YTs for a single-cycling model is 94.23% for one YT and that the minimum average utilization of the YTs is 21.69% for ten YTs.

As shown in Figure 13, when the number of YTs increases from 1 to 5, the average YT utilization rate decreases from 46.79% to 42.75%.

Loaded and unloaded travel times were measured in the single-cycling model simulated from one YT to 10 YTs.

Figure 10. *Average utilization rate of the QC in the single-cycling model*

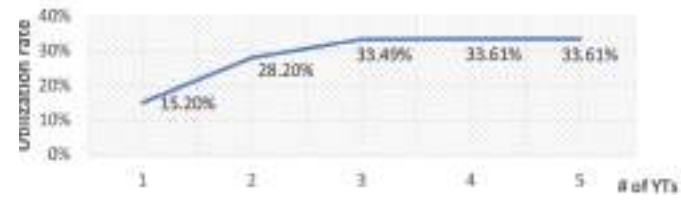

Figure 11. *Average utilization rate of the QC in the double-cycling model*

Figure 12. *Average utilization rate of the YTs in the single-cycling model*

Figure 13. *Average utilization rate of the YTs in the double-cycling model*

Table 1. *Average travel time ratios of loaded and unloaded YTs in the single-cycling model*

Number of YTs in the system	Average travel time ratios of loaded YTs in the single-cycling model	Average travel time ratios of unloaded YTs in the single-cycling model
1	0.4953	0.4470
2	0.3280	0.2576
3	0.2531	0.1628
4	0.2266	0.1129
5	0.2233	0.0818
6	0.2292	0.0586
7	0.2299	0.0400
8	0.2272	0.0253
9	0.2219	0.0131
10	0.2144	0.0025

Table 2. *Average travel time ratios of loaded and unloaded YTs in the double-cycling model*

Number of YTs in the system	Average travel time ratios of loaded YTs in the double-cycling model	Average travel time ratios of unloaded YTs in the double-cycling model
1	0.4565	0.0114
2	0.4526	0.0106
3	0.4691	0.0084
4	0.4574	0.0063
5	0.4224	0.0051

Table 1 shows the average travel time ratios of loaded and unloaded YTs in the single-cycling model for each number of YTs operating in the system. When the table is examined, it can be seen that as the number of YTs increases, the general averages of the loaded and unloaded travel time ratios tend to decrease. However, the difference between the average loaded travel time rates after the number of YTs exceeded four is insignificant. On the other hand, the reduction in the overall average unloaded travel time ratio was much more noticeable.

According to Figure 14, as the number of YTs used in the system increases, a significant reduction in the average unloaded travel time ratio is observed for each number of YTs.

Furthermore, loaded and unloaded travel time ratios were measured in the double-cycling model simulated from one to ten YTs. Table 2 gives the average loaded and unloaded travel time ratios for each number of YTs operating in the system. As the table shows, the average loaded travel time ratios of the YTs have an irregular tendency with minor differences in the double-cycling model. Besides, it is seen that as the number of YTs increases, the average unloaded travel time ratio of the YTs decreases significantly.

As shown in Figure 15, the average unloaded driving time ratio for each number of YTs was negligible compared to the

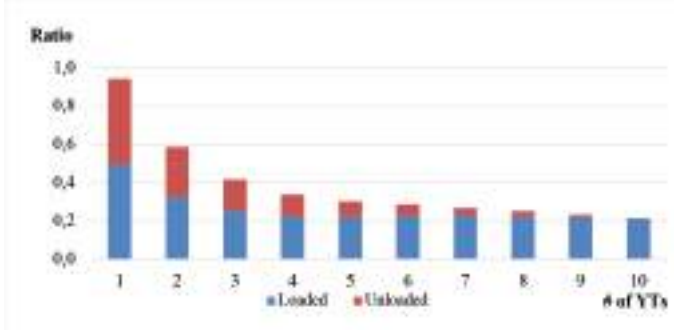

Figure 14*. Average loaded and unloaded travel time ratios for each number of YTs in the single-cycling model*

single-cycling model. The implementation results showed that the unloaded driving time ratio for each number of YTs was higher in the single-cycling model than in the double-cycling model. The double-cycling model has been shown to reduce travel rates for empty YTs. Moreover, in terms of the total operation time, four YTs for completing the handling operation employing the double-cycling strategy would be a preferred choice, whereas ten YTs would be the preferred choice for the single-cycling strategy.

Table 3 summarizes the performance analysis results of the single-cycling strategy for one to ten YTs and the double-

Table 3. *Performance analysis results of implementation scenarios*

Number of YTs	Single-cycling			Double-cycling			Productivity improvement		Time saved		Cost saved	
	Productivity rate (TEUs/hr)	Average turnaround time (hrs)	Operating cost (US$)	Productivity rate (TEUs/hr)	Average turnaround time (hrs)	Operating cost (US$)	TEUs/ hr	%	hrs	%	US$	%
1	2.47	242.53	195.77	2.28	263.12	117.64	-0.19	-7.83	-20.59	-8.49	78.12	39.91
2	3.2	187.71	156.59	4.23	141.86	94.17	1.03	32.32	45.85	24.43	62.42	39.86
3	3.45	174.00	147.51	5.02	119.43	96.21	1.58	45.7	54.58	31.37	51.30	34.78
4	3.70	162.29	141.02	5.04	119.02	104.38	1.34	36.36	43.27	26.66	36.64	25.98
5	3.98	150.57	135.55	5.04	119.02	110.08	1.06	26.52	31.56	20.96	25.47	18.79
6	4.23	141.84	131.68									
7	4.41	136.13	127.95									
8	4.60	130.43	123.21									
9	4.81	124.72	117.46									
10	5.04	119.02	110.72									

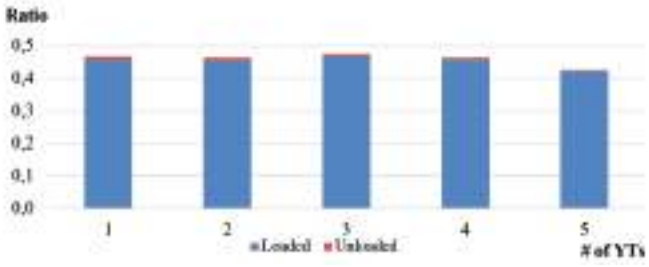

Figure 15*. Average loaded and unloaded travel time ratios for each number of YTs in the double-cycling model*

cycling strategy for one to five YTs. When the number of YTs exceeds these values, there is no significant increase in efficiency. The operating cost includes the cost of the QC, RTG, and YTs based on their utilization rates, the operator cost, the hourly fuel cost, and the maintenance and repair cost. We draw the following conclusions from the implementation results;

• We note that for the double-cycling strategy to work effectively in this system, at least two YTs must complete the container handling process.

• Compared with the single-cycling strategy, we observe a 45.70% increase in productivity, a 31.37% decrease in the average turnaround time of ships, and a 34.78% decrease in the cost when using three YTs in the double-cycling strategy.

• On the other hand, the highest productivity rate and the shortest ship turnaround time were achieved in the double-cycling strategy when 4 and 5 YTs were used and in the single-cycling strategy when 10 trucks were used. This is consistent with the general expectation; a higher number of YTs will result in quicker responses to the QC unloading and loading cycles and, thus, better performance. However, when we consider the cost of additional YTs as well as the operating cost and the traffic problems that may occur due to the movement of many YTs in the system, the double-cycling strategy is more advantageous.

• Considering productivity and operating costs, the double-cycling strategy employing three YTs is the preferred option for this case study. We can see that increasing the number of YTs does not always increase productivity or reduce costs because inadequate QCs and RTGs increase the idle time of YTs and other handling equipment. Beyond additional YTs, further improvements can be achieved by increasing the number of QCs and RTG cranes, especially when dealing with large ships [20]. It should also be noted that although a double-cycling strategy does not require significant capital investments, increasing the number of cranes requires additional financial resources.

Minimizing empty YT trips and reducing the ship turnaround time can improve terminal productivity in terms of reasonable time and cost. The results of the application study demonstrate the cost and performance differences between handling operations using single-cycling and double-cycling strategies. When the two operational strategies are compared, double-cycling can be seen to provide a remarkable improvement in terms of performance criteria as a cost-effective option.

6. Conclusion

Operational efficiency at container terminals has become one of the most discussed topics in recent years. Global container operators are constantly increasing their ship capacities due

to economies of scale. Today, mega ships with a capacity of 24 thousand TEU serve on world maritime routes. Such an increase in ship capacities has also increased the port efficiency expectations. For this reason, ports have had to develop many strategies. At this point, the modernization of equipment is not enough. Operational strategies also need to be reviewed and improved. This paper is a technical study based on these efficiency concerns in ports. QC operation efficiency is one of the vital criteria used to evaluate the performance of terminal operating systems. We developed simulation models for single-cycling and double-cycling strategies to plan QC operations. The simulation results were analyzed in terms of the average driving time for each loaded and unloaded YT, total operation time, and productivity rate. When the two models are compared in terms of the total operation time, the lowest total operation time is achieved when four YTs are used in the double-cycling model and ten YTs are used in the single-cycling model. We note that four YTs with the double-cycling strategy handle the same number of containers in the container terminal. From the viewpoint of firms, the handling operation is carried out by using six YTs less with the double-cycling strategy, which is significantly advantageous in terms of investment and cost. As a result of the implementation study, we observed that the productivity rate in the double-cycling model is higher than that in the single-cycling model. Furthermore, the double-cycling strategy reduced the total cost by decreasing the number of YTs and increasing the efficiency of the cranes and YTs. Therefore, double-cycling operations can be implemented to achieve cost savings and efficient operation in container terminals. One limitation of this study is that it is based on the operating strategies of a single QC in a container terminal layout. It would be insightful to consider multiple QCs operating in different container terminal layouts, such as parallel and U-shaped layouts. The other possible development following this research is to incorporate the breakdown and repair process of the equipment used in the handling process so that realistic factors can be better addressed. Furthermore, Port 4.0, an extension of the Industry 4.0 paradigm to the port and maritime industry, is a growing trend that has the potential to significantly improve efficiency and competitiveness compared to traditional terminals. Automation and integration of container terminals reduce operator workload and minimize human error and delays at ports. In addition, occupational health and safety measures will be provided using intelligent technologies, such as artificial intelligence, and an environmentally friendly structure will be created. As a further research area, similar studies can be conducted by integrating these smart technologies with optimization methods.

Authorship Contributions

Concept design: G. Tuncel, Ö. Yalçınkaya, and S. Esmer, Data Collection or Processing: G. Tuncel, Ö. Yalçınkaya, E. Deniz, and S. Esmer, Analysis or Interpretation: G. Tuncel, Ö. Yalçınkaya, E. Deniz, and S. Esmer, Literature Review: G. Tuncel, and E. Deniz, Writing, Reviewing and Editing: G. Tuncel, and E. Deniz.

Funding: The authors declare that no funds, grants, or other support was received during the preparation of this manuscript.

References

[1] A. Wisniewska, M. Deja, M, Dobrzynski, and M. Siemiatkowski. "Simulation studies into quayside transport and storage yard operations in container terminals". *Polish Maritime Research,* vol. 24, pp. 46-52, May 2017.

[2] A. V. Goodchild, and C. F. Daganzo, "Double-cycling strategies for container ships and their effect on ship loading and unloading operations". *Transportation Science,* vol. 40, pp. 473-483, Nov 2006.

[3] A. V. Goodchild, and C. F. Daganzo, "Crane double cycling in container ports: Planning methods and evaluation". *Transportation Research Part B: Methodological,* vol. 41, pp. 875-891, Oct 2007.

[4] H. Zhang, and K. H. Kim, "Maximizing the number of dual-cycle operations of quay cranes in container terminals". *Computers & Industrial Engineering,* vol. 56, pp. 979-992, Apr 2009.

[5] V. D. Nguyen, and K. H. Kim, "Minimizing empty trips of yard trucks in container terminals by dual cycle operations". *Industrial Engineering and Management Systems,* vol. 9, pp. 28-40, Mar 2010.

[6] F. Meisel, and M. Wichmann, "Container sequencing for quay cranes with internal reshuffles". *OR Spectrum*, vol. 32, pp. 569-591, Dec 2010.

[7] C. Bierwirth, and F. Meisel, "A survey of berth allocation and quay crane scheduling problems in container terminals". *European Journal of Operational Research,* vol. 202, pp. 615-627, May 2010.

[8] C. Bierwirth, and F. Meisel, "A follow-up survey of berth allocation and quay crane scheduling problems in container terminals". *European Journal of Operational Research,* vol. 244, pp. 675-689, Aug 2015.

[9] C. Y. Lee, M. Liu, and C. Chu, "Optimal algorithm for the general quay crane dual-cycling problem". *Transportation Science,* vol. 49, pp. 957-967, Nov 2014.

[10] M. Liu, S. Wang, C. Chu, and F. Zheng, "A branch-and-price framework for the general double-cycling problem with internal-reshuffles", in *IEEE 12th International Conference on Networking. Sensing and Control (ICNSC),* 09-11 April 2015, Taipei, Taiwan [Online] Available: IEEE Xplore, https://ieeexplore.ieee.org [04 June 2015].

[11] R. Zhang, Z. Jin, Y. Ma, and W. Luan, "Optimization for two-stage double-cycle operations in container terminals". *Computers & Industrial Engineering,* vol. 83, pp. 316-326, May 2015.

[12] Q. Zeng, A. Diabat, and Q. Zhang, "A simulation optimization approach for solving the dual-cycling problem in container terminals". *Maritime Policy & Management,* vol. 42, pp. 806-826, May 2015.

[13] D. Wang, and X. Li, "Quay crane scheduling with dual cycling". *Engineering Optimization,* vol. 47, pp. 1343-1360, 2015.

[14] X. Zhang, Q. Zeng, and Z. Yang, "Modeling the mixed storage strategy for quay crane double cycling in container terminals". *Transportation Research Part E: Logistics and transportation Review*, vol. 94, pp. 171-187, Oct 2016.

[15] D. Ku, and T. S. Arthanari, "On double cycling for container port productivity improvement". *Annals of Operations Research*, vol. 243, pp. 55-70, Aug 2016.

[16] Y. Chu, X. Zhang, and Z. Yang, "Multiple quay cranes scheduling for double cycling in container terminals". *PLoS One,* vol. 12, pp. e0180370, Jul 2017.

[17] S. S. Kamble, A. Gunasekaran, and R. D. Raut, "Analysing the implementation barriers of dual cycling in port container terminal using interpretive structural modeling-Indian context". *International Journal of Logistics Research and Applications*, vol. 22, pp. 119-137, 2019.

[18] X. Zhang, Q. Zeng, and J. B. Sheu, "Modeling the productivity and stability of a terminal operation system with quay crane double cycling". *Transportation Research Part E: Logistics and Transportation Review,* vol. 122, pp. 181-197, Feb 2019.

[19] G. Tang, M. Qin, Z. Zhao, J. Yu, and C. Shen, "Performance of peak shaving policies for quay cranes at container terminals with double cycling". *Simulation Modelling Practice and Theory*, vol. 104, pp. 102129, Nov 2020.

[20] E. Ahmed, M. S. El-Abbasy, T. Zayed, G. Alfalah, and S. Alkass, "Synchronized scheduling model for container terminals using simulated double-cycling strategy". *Computers & Industrial Engineering,* vol. 154, pp. 107118, Apr 2021.

[21] H. Zhang, L. Qi, W. Luan, and H. Ma, "Double-cycling AGV scheduling considering uncertain crane operational time at container terminals". *Applied Sciences,* vol. 12, pp. 4820, May 2022.

[22] Zhu, Z. Tan, Z. Yang, and L. Cai, "Quay crane and yard truck dual-cycle scheduling with mixed storage strategy". *Advanced Engineering Informatics,* vol. 54, pp. 101722, Oct 2022.

[23] D.B.M.M. Fontes and S.M. Homayouni, "A bi-objective multi-population biased random key genetic algorithm for joint scheduling quay cranes and speed adjustable vehicles in container terminals". *Flexible Services and Manufacturing Journal,* vol. 35, pp. 241-268, Mar 2023.

[24] M. Wei, J. He, C. Tan, J. Yue, and H. Yu, "Quay crane scheduling with time windows constraints for automated container port". *Ocean & Coastal Management,* vol. 231, pp. 106401, Jan 2023.

[25] L.-J. Yue, H.-M. Fan, and H. Fan, "Blocks allocation and handling equipment scheduling in automatic container terminals". *Transportation Research Part C - Emerging Technol,* vol. 153, 104228, Aug 2023.

[26] L. Cai, W. Li, B. Zhou, H. Li, and Z. Yang, "Robust multi-equipment scheduling for U-shaped container terminals concerning double-cycling mode and uncertain operation time with cascade effects". *Transportation Research Part C,* vol. 158, 104447, Jan 2024.

[27] Y. Li, Z. Sun, and S. Hong, "An exact algorithm for multiple-equipment integrated scheduling in an automated container terminal using a double-cycling strategy". *Transportation Research Part E: Logistics and Transportation Review,* vol. 186, 103565, Jun 2024.

[28] C. Tan, T. Qin, J. He, Y. Wang, and H. Yu, "Yard space allocation of container port based on dual cycle strategy". *Ocean & Coastal Management,* vol. 247, 106915, May 2024.

[29] Y.-Z. Wang, Z.-H. Hu, and X.-D. Tian, "Scheduling ASC and AGV considering direct, buffer, and hybrid modes for transferring containers". *Computers & Operations Research,* vol. 161, 106419, Jan 2024.

[30] X. Zhang, H. Li, and J.-B. Sheu, "Integrated scheduling optimization of AGV and double yard cranes in automated container terminals". *Transportation Research Part B: Methodological,* vol. 179, 102871, Jan 2024.

[31] E. Deniz, G. Tuncel, O. Yalcinkaya, and S. Esmer, "Simulation of multi-crane single and dual cycling strategies in a container terminal". *International Journal of Simulation Modelling,* vol. 20, pp. 465-476, 2021.

ORIGINAL RESEARCH (AR) DOI: 10.4274/jems.2024.67689

Journal of ETA Maritime Science 2024;12(3):332-345

Combined Effects of Axial Flow and High System Rotation on the Fluid Dynamics of Taylor-Couette-Poiseuille Flow

Taner Çoşgun, Nurten Vardar

Yıldız Technical University Faculty of Naval Arthitecture and Maritime, Department of Naval Architecture and Marine Engineering, İstanbul, Türkiye

Abstract

Taylor-Couette-Poiseuille (TCP) flow, characterized by the flow through an inner rotating shaft and an outer stationary cylinder, is a fundamental flow system in many industrial applications, including ship stern tubes, turbomachinery, journal bearings, and offshore drilling. Understanding the hydrodynamics of the TCP flow offers significant benefits for ensuring the robust design and operational efficiency of such systems. This paper presents the numerical modeling of turbulent TCP flow to assess the combined effects of two key control parameters-axial Reynolds number (10000-30000) and Taylor number ($2.2x10^7$-$3.1x10^9$)-on the fluid dynamics within the system. Using Reynolds Stress Modeling, this study investigates the behavior of TCP flow at high Reynolds numbers, which is relevant to real-world rotating machinery. The results indicate that the interaction between rotation and axial flow is not linear, with high rotation rates showing distinct behavior from low rotation rates, especially in the throughflow effects. At low and moderate rotation numbers (N), both the mean and turbulent variables display strong dependence on the rotational velocity and axial flow rate. However, further increases in N lead the flow field to be increasingly dominated by the contribution of rotation, and mean flow variables become relatively independent of the imposed flow rate. Furthermore, systematic deviations from the log-law in the boundary layer velocity profiles further emphasize the need to account for the combined effects of rotation and axial flow in the TCP flow system design and operation.

Keywords: Taylor-Couette-Poiseuille flow, Annular flow, Turbulence, Computational fluid dynamics, Concentric annulus, Stern tube

1. Introduction

The flow within the annular cavity between rotating concentric cylinders, also known as Taylor-Couette (TC) flow, is a great area of interest in fluid dynamics research. Beyond its role as a fundamental flow system in many industrial applications [1,2], TC flow can also serve as an important test case in turbulent flow studies [3].

TC flow is a closed system in which a moving cylinder wall creates flow within the cavity. Introducing an axial flow to an open-ended TC system creates a configuration known as Taylor-Couette-Poiseuille (TCP) flow. The presence of axial flow significantly complicates the fluid behavior by adding a second key parameter (throughflow) that influences the flow field [4]. In such a flow, the balance between the additional body forces induced by inner cylinder rotation and the pressure-driven axial flow is shaped by the flow field dynamics. The arrangement of concentric rotating cylinders is a common feature in various engineering applications, including ship stern tubes, journal bearings, turbomachinery, cooling systems for electrical devices, drilling operations, and fluid filtration devices… etc. Therefore, a deeper understanding of the TCP flow field is beneficial not only for the theory of turbulent flow in rotating systems but also for the reliable design and operation of such systems.

The superposition of the axial and rotational flows in the TCP system is not a linear combination of TC and annular Poiseuille flows; thus, each pair of axial rotational velocities induces a different flow field. In other words, the characteristics of the turbulent flow field can vary between canonical flows. The influence of two main flow parameters (rotational and axial velocities) on the features of the turbulence has already

Address for Correspondence: Taner Çoşgun, Yıldız Technical University Faculty of Naval Arthitecture and Maritime, Department of Naval Architecture and Marine Engineering, İstanbul, Türkiye
E-mail: tcosgun@yildiz.edu.tr
ORCID iD: orcid.org/0000-0002-1364-0133

Received: 13.06.2024
Last Revision Received: 22.07.2024
Accepted: 03.08.2024

To cite this article: T. Çoşgun, and N. Vardar. "Combined Effects of Axial Flow and High System Rotation on the Fluid Dynamics of Taylor-Couette-Poiseuille Flow." *Journal of ETA Maritime Science*, vol. 12(3), pp. 332-345, 2024.

been motivated by several studies. Nouri and Whitelaw [5] experimentally measured the mean velocities and turbulence stresses of a flow in a concentric annulus with a rotating inner cylinder. They observed an enhancement of the turbulence statistics with inner wall rotation compared to those of the non-rotating case. They also concluded that the same rotation rates of the inner cylinder affected the flow field, depending on whether the imposed axial flow was laminar or turbulent. Escudier and Coulson [6] investigated the TCP flow in a similar experimental arrangement. Their results emphasized that an increase in axial Re diminishes the magnitude of the tangential velocity of inner cylinder rotation, especially in the central region of the annulus. Also, the turbulence fluctuations are suppressed at higher axial flow rates. Chung et al. [7] applied direct numerical simulation to the flow through an annular gap between concentric cylinders without inner wall rotation. They reported that the annular flow between concentric pipes has the general characteristics of fully developed internal flows like channel and pipe flows. At a later date, they performed a large-eddy simulation (LES) to examine the effects of inner cylinder rotation under the same geometrical configuration and axial flow conditions [8]. They showed an increase in the overall turbulence statistics with inner wall rotation. They found that the flow became more isotropic, and the increasing tendency of the turbulence statistics was more apparent at high rotation rates. The authors addressed the destabilizing effect of inner wall rotation on the alteration of the turbulent field. Liu and Lu [9] investigated the near-wall turbulence features of both stationary and moving walls in TCP flows. Jung and Sung [10] conducted direct numerical simulations to examine the turbulent boundary layers in a concentric annulus with a rotating inner wall. They clarified the modifications in the near-wall turbulent structures with the centrifugal force induced by the rotation of the inner cylinder. Hadžiabdić et al. [11] studied the effect of outer cylinder rotation in an annular flow. They revealed that the variation trend of the turbulence features with increasing rotational wall velocity can be reversed after a critical value of rotation number. They also used the Ta/Re2 ratio as a dynamic representative of the ratio of the centrifugal to axial inertial forces, instead of the rotation number Poncet et al. [12] studied the TCP flow in a narrow gap cavity with six different combinations of axial and rotational flow conditions using an LES. They found that inner wall rotation dominated the mean tangential velocity profile, and the fluid rotated nearly in solid body rotation, especially in the core region. In addition, turbulence is mostly concentrated in the boundary layers.

Due to the significant resemblance of TCP flow to many engineering systems, investigations of hydrodynamic features like skin friction, rotating cylinder torque, pressure drop, and heat transfer are important for industrial applications. Thus, several researchers have focused on such hydrodynamic properties in TCP flows. Yamada [13] measured the resistance of an annular flow with a rotating inner cylinder. Their results showed that lowers the inner cylinder resistance to a certain level, while a further increase in Re raises the resistance. Manna and Vacca [14] numerically investigated the torque reduction behavior under a superimposed axial pressure gradient in a TCP flow. A detailed flow field analysis in the study indicates that the torque reduction is associated with the modification of the large-scale coherent structures, as imposed by the axial flow. Oshawa et al. [15] investigated the contributions of Reynolds stress terms to torque variations under diabatic conditions. The experimental study by Woo et al. [16] showed that the pressure loss of TCP flow increases with inner cylinder rotation. Chong et al. [17] measured the pressure drop in an annular passage with a rotating inner cylinder to investigate the flow entry effects in the rotor-stator gap of electrical machines. Various authors have investigated the heat transfer mechanism in TCP flow including [18-22]. A review of heat transfer studies can be found in the extended literature review by Fénot et al. [4]. They concluded that more data on the hydrodynamic field should be provided to eliminate the many question marks concerning TCP heat transfer.

The literature review reveals that TCP flow has been exhaustively studied over the last few decades. Table 1 summarizes the primary findings and investigated ranges of the relevant literature. It can be seen that most previous research, especially those focused on the hydrodynamic and turbulent fields, considered relatively lower rotation numbers. The parameter range in some heat transfer studies can reach higher values, but they are generally focused on the measurement/prediction of the thermal field. Reference [4] highlighted the importance of understanding the flow physics associated with TCP heat transfer. On the other hand, under real operating conditions in industrial applications, very high rotational and axial velocities. Poncet et al. [12,19] pointed out the need for reliable data at high rotation rates, which is also the motivation of the present work. The last author performed numerical simulations to understand the hydrodynamical behavior and heat transfer under the real operating conditions of electrical machinery. Nevertheless, their studies concerned a narrow gap cavity and gap height, which play important roles in the dynamics of annular flows [7,23]. The purpose of the present study was to investigate the mean and turbulent field in a middle-gap TCP flow over a wide range of rotational numbers from low to very high. The 15 different combinations of rotational and axial velocities in the parameter space of the study provided a rich data field to examine the fluid dynamics of the system. The second aim of this work was to study the effects of superimposed axial flow at high system rotation.

Table 1. *Summary of relevant literature in the investigated ranges. Throughout the literature, scaling the system rotation does not have unity in both the selection of the parameter that is used to quantify the rotational velocity of the inner cylinder and the definition of that parameter itself. In addition, it is not possible to convert them to a single parameter. Hence, the flow control parameters of the summarized papers are presented in the following sections. The parameter range of the present study is 10000-30000 for axial Reynolds number and $2.2x10^7$-$3.1x10^9$ for Taylor Number.*

Ref.	Type	r	Axial flow parameters	Range	Rotational flow parameter	Range	Primary findings
[24]	Exp.	0.8	$Re = 2sU/\nu$	0-12000	$Ta = \frac{\omega^2 r_o (r_o - r_i)^3}{\nu^2}$	0-330000	Temperature measurements over a wide range of flow parameters. A regimen map is created for diabatic and adiabatic flows.
[13]	Exp.	0.89-0.98	$Re = sU/\nu$	0-30000	$Re_\omega = \omega R_i s / \nu$	0-30000	Flow resistance measurements at six gap heights and various combinations of axial and rotational velocities. The friction coefficient was found to be unaffected when the axial flow was laminar. Beyond a certain level of rotational velocity the resistance increases.
[25]	Exp./ Num.	0.5	$Re = sU/\nu$	0- 150	$Ta = \omega s^2 / \nu$	0-170	The linear stability of the spiral flow was investigated. The observed critical Taylor numbers were compared with the theoretical predictions.
[26]	Exp.	0.71	$Re = 2sU/\nu$	0-137	$Ta = \frac{(\omega r_i^{1/2} s^{3/2} / \nu)}{1.43}$	255	Visual observations of the vortex structure. Complete vortex destruction after Re/Ta > 0.55
[27]	Exp.	0.8	$Re = 2sU/\nu$	500-1250	$Ta = \omega R_i s / \nu$	0-500	The heat and mass transfer observations were performed. The mass transfer coefficients were enhanced at high rotational velocities.
[28]	Exp.	0.85	$Re = 2sU/\nu$	0-37	$Ta = \omega R_i s / \nu$	0-2900	Seven intermediary flow regimes were identified by optical techniques. A stability map for the TCP flow is generated.
[5]	Exp.	0.5	$Re = 2sU/\nu$	950, 9000, 26600	rpm/ $Re_\omega = \omega R_i s / \nu$	0,300/ 0,398	Mean flow and Reynolds stresses in Newtonian and non-Newtonian fluids. Turbulence enhancement is observed with rotation.
[6]	Exp.	0.5	$Re = 2sU/\nu$	1200, 2700, 7400	rpm/ $Ta = (\omega s / \nu)^2 r_i s^3$	126/ $8.78x10^5$	LDA measurements of mean flow and Reynolds stresses in Newtonian and shear-thinning fluids. An increase in the axial flow reduces the mean tangential velocity and fluctuations.
[29]	Exp.	0.83	$Re = sU/\nu$	1.6-23	$Ta = \omega R_i s / \nu$	100-215	PIV measurements in the meridional plane of the annulus. The vortex behavior was investigated in detail at low axial flow rates.
[30]	Num.	0.83	$Re = sU/\nu$	1.6-23	$Ta = \omega R_i s / \nu$	100-215	Experimental stability analysis of (Wereley & Lueptow, 1999) was numerically validated. The axial flow stabilizes the flow field and reduces the torque coefficient on the inner cylinder.
[8]	Num.	0.5	$Re = 2sU/\nu$	8900	$N = V_\omega / U$	0.214, 0.429, 0.858	Destabilization of the near-wall turbulent structures due to the rotation of the inner cylinder was revealed using the LES. Various turbulence statistics were investigated.

Table 1. Continued

Ref.	Type	r	Axial flow parameters	Range	Rotational flow parameter	Range	Primary findings
[9]	Num.	0.5	$Re = sU_t/\nu$	640	$N = 2\omega s / U$	0-20	The turbulence statistics and TKE budget in the TCP flow were investigated in detail using the LES. Significant change in the radial and azimuthal turbulence intensities with rotation, as well as an increasing Coriolis term in the TKE budget.
[16]	Exp.	0.52	$Re = 2sU/\nu$	100-12000	rpm	0-600	Pressure losses and skin friction coefficients were measured for water and non-Newtonian fluids. Critical Re was found to decrease with increasing rotation rate, whereas the pressure loss increased.
[31]	Num.	0.5	$Re = 2sU/\nu$	8900	$N = U_a / U$	0.171, 0.257	The combined effects of buoyancy and inner wall rotation on the mixed convection in TCP flow were demonstrated. Rotation suppresses the heat-reducing effects on the turbulence statistics.
[32]	Exp.	0.9	$Re = sU/\nu$	30-1200	$Re_\omega = \omega R_i s / \nu$	0-2922	The effect of longitudinal ribs mounted on the rotating inner cylinder on the heat transfer characteristics of TCP was investigated. Significant heat transfer enhancement was observed with ribs.
[14]	Num.	0.98	$Re = sU/\nu$	0-400	$Ta = \omega R_i s / \nu$	1000-15000	The torque reduction behavior at low axial velocities was confirmed using DNS. The relationship between torque reduction and large-scale coherent structures was revealed.
[19]	Num.	0.96	$C_W = Q/\nu r_o$	0-30000	$Re_i = \omega R_i s / \nu$	3744-37443	The effects of flow parameters on heat transfer characteristics are presented. Correlations for the averaged Nusselt numbers along both cylinders are provided.
[33]	Exp.	0.99	$Re = 2sU/\nu$	2140-6425	$Re_r = V_r s / \nu$	1750-35000	Heat transfer in a TCP system with a slotted inner cylinder is investigated. The importance of the axial ratio and entrance velocity profile on heat transfer is presented.
[11]	Num.	0.5	$Re = 2sU/\nu$	12500	$N = U_a / U$	0.5- 4	LES modeling of the influence of outer cylinder rotation. A critical N was determined at which the effect of rotation on turbulence is reversed.
[34]	Num.	0.5, 0.89	$Re = sU/\nu$	50-200	$Re_\omega = \omega R_i s / \nu$	127-296	The combined effects of eccentricity and axial velocity on the TCP stability were investigated. Eccentricity stabilizes the system regardless of the axial flow rate.

Table 1. Continued

Ref.	Type	r	Axial flow parameters	Range	Rotational flow parameter	Range	Primary findings
[12]	Num.	0.88	$Re = sU/\nu$	3745, 5617	$N = Re_{ax}/Re_{\theta}$ $(N = \omega R_i / U)$	2.24-4.47	Investigation of mean flow, turbulent field, and near-wall flow in a wide range of flow parameters using LES. The boundary layers along the inner and outer walls are governed by the effective Re and are found to be two-dimensional. The non-isothermal case was also studied.
[20]	Exp.	0.88	$Re = 2sU/\nu$	7490-11200	$Ta = \omega^2 R_i s^3 / \nu^2$	$8.8\text{x}10^6$-$7.9\text{x}10^7$	Velocity and temperature measurements over a wide range of flow parameters. A correlation is provided for the Nusselt number on the rotating wall.
[35]	Exp./ Num.	0.78	$Re = sU/\nu$	7589	$Ta = \omega^2 R_i s^3 / \nu^2$	$3.2\text{x}10^8$	Heat transfer and power loss (drag force) were studied at high rotation speeds. RANS methodology. Nusselt number correlation was proposed.
[36]	Exp.	0.85	$Re = 2sU/\nu$	1.49-120	$Ta = \frac{\omega r_i s}{\nu}\sqrt{\frac{s}{r_i}}$	46-680	PIV investigation of the vortex field. Vortex formation under different flow conditions was demonstrated.
[21]	Num.	0.5	$Re = 2sU/\nu$	9000	$N = \omega R_i / U$	0.21, 0.86	The influence of rotation on heat transfer in the TCP flow was also investigated. The destabilizing effect of rotation enhances mixing and Nusselt number.
[37]	Num.	0.85	$\beta = sU/\nu$	0-40	$Ta = \omega R_i s / \nu$	110-150	Stability analysis of TCP flow on permeable surfaces using DNS. Three different configurations were tested: radial flow injection, extraction, and cross-flow.
[38]	Num.	0.77	$Re = sU/\nu$	1500, 7500	$Re_i = \omega R_i s / \nu$	$3.7\text{x}10^4$-$1.5\text{x}10^5$	The effect of contracting the outer cylinder on the pressure field was investigated. Counter-rotating Taylor vortex pairs cause pressure oscillations. A prediction model was developed.
[39]	Num.	0.93	$Re = d_h U/\nu$	5000-65000	$Re_i = \omega R_i d_h / \nu$	160-1900	The thermal performance of various outer cylinder shapes was investigated. Heat transfer characteristics and pressure drop values were obtained for three cavity shapes.
[40]	Num.	0.8	$Re = 2sU/\nu$	2100-2400	$Ta_m = \frac{\omega^2 R_{av} s^3}{\nu F_R}$	30000-90000	Thermal performance analysis of the TCP flow with longitudinal and helical ribs mounted on the inner cylinder. Ribs induce more vorticity and turbulence and enhance heat transfer.
[41]	Num.	0.83	$Re = 2sU/\nu$	730-14600	$Ta = \omega^2 R_i s^3 / \nu^2$	10^5-10^9	The effect of the imposed radial flow through the inner cylinder surface on heat transfer was investigated. The thermal efficiency of the radial flow case was superior to that of the axial flow case.
[42]	Num.	0.5	$Re = 2sU/\nu$	10000	$N = U_a / U$	0-4	Numerical predictions were performed using the LES and RANS methodologies. The effects of high rotation rates on the turbulence statistics and mean flow were investigated.

With this object in mind, the same set of rotational parameters was tested for different axial Reynolds numbers. Thus, numerical results were presented separately in terms of rotation and axial velocity to observe the effects of varying operating conditions on the mean flow features, turbulent field, and boundary layer structure.

2. Numerical Modeling

2.1. Geometry and Flow Conditions

Figure 1 shows the schematic view of the TCP flow configuration. The solution domain is composed of a stationary outer cylinder with radii r_o and an inner cylinder with radii r_i which is rotating around its axis with constant angular velocity ω. The radius ratio of the cylinders is r_i/r_o=0.506. The cavity length in the streamwise direction is L=10s (where $s = r_0 - r_i$).

Three values of the axial velocity and five values of the rotation rate of the inner cylinder were considered in this study.

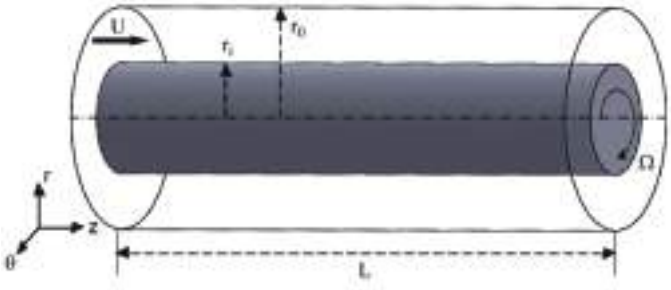

Figure 1. *Schematic of the problem*

The ranges of the flow control parameters are given in Table 2. The assumed throughflow is characterized by the axial Reynolds number based on the hydraulic diameter, $\mathrm{Re} = 2sU/\nu$, where U is the bulk velocity at the inlet and ν is the kinematic viscosity. The rotational Reynolds number, $\mathrm{Re}_\omega = \omega r_i s/\nu$, donates the rotating velocity of the inner wall. The equivalent Taylor number Ta and rotation number N are also given in Table 2, for comparison with similar studies. The Taylor number is defined as $Ta = \omega^2 r_i s^3/\nu^2$ and the rotation number is $N = U_\Omega/U$, where $U_\Omega = \omega r_i$. The rotation number is widely used in studies of rotating annular flows to provide ratios of the axial and rotational velocities. However, varying the imposed flow rate resulted in different N values for the same rotation rate of the inner cylinder. The present work aimed to report the effect of the axial and rotational flow control parameters separately. Thus, inner cylinder rotational velocities are symbolized as Ω_1 - Ω_5 for a clear representation of the results.

2.2. Numerical Details

A finite volume method-based commercial computational fluid dynamics code Simcenter Star-CCM+ was utilized to solve the governing equations, Reynolds Averaged Navier-Stokes Equations, of the transient incompressible flow. The Spatial derivatives are discretized by a second-order accurate central difference scheme. In the same way, a second-order implicit Euler scheme is used for time advancement. The SIMPLE algorithm is employed for velocity-pressure coupling. The no-

Table 2. *Summary of flow control parameters*

Axial velocity	Rotational velocity			*N*		
Re	**Ω**	**Re_Ω**	**Ta**	**For Re=10000**	**For Re=20000**	**For Re=30000**
10000 20000 30000	Ω_1	4704	2.16×10^7	0.94	0.47	0.31
	Ω_2	9446	8.71×10^7	1.89	0.94	0.63
	Ω_3	18854	3.47×10^8	3.77	1.89	1.26
	Ω_4	37784	1.39×10^9	7.55	3.77	2.52
	Ω_5	56600	3.13×10^9	11.32	5.66	3.77

Table 3. *Numerical details for different rotational velocities. Three values in each cell of the table correspond to the axial Reynolds number of 10,000, 20,000, and 30000, respectively*

	$N_r x N_\theta x N_z$	Δr_i^+	$r_i \Delta\theta^+$	Δz_i^+	CFL
Ω_1	64x140x127	0.34, 0.41, and 0.50	25, 31, and 38	32, 40, and 48	0.33, 0.43, 0.38
Ω_2	64x140x127	0.49, 0.54, 0.61	37, 41, and 46	47, 52, and 59	0.31, 0.34, and 0.35
Ω_3	97x180x192	0.33, 0.35, 0.36	40, 41, 53	58, 60, 63	0.26, 0.35, 0.22
Ω_4	97x180x192	0.60, 0.60, and 0.62	72, 73, and 89	105, 106, and 107	0.30, 0.30, 0.24
Ω_5	97x220x242	0.85, 0.85, and 0.86	84, 84, 85	117, 118, 118	0.30, 0.34, and 0.39
CFL: Courant-Friedrichs-Lewy					

slip condition is valid at all walls in the computational domain. A fixed tangential velocity component is assigned to the rotating inner cylinder. To ensure that the calculations were independent of the inflow conditions, periodic boundary conditions were applied in the axial direction. The same approach has been successfully implemented by several researchers to achieve fully developed flow conditions [12,15,21]. The results were checked with solutions in a relatively longer domain to ensure that the domain length was sufficiently long for large-scale turbulent structures.

Turbulence modeling is based on the low-Reynolds-number elliptic-blending Reynolds Stress Transport model (RSM). The model formulation was presented in Manceau and Hanjalić [43] and was not repeated here. The Reynolds stress model is free of the eddy viscosity assumption and accounts for the anisotropy of the Reynolds stress tensor. Thus, it can serve as a more realistic turbulence model for flows that includes swirling motion and rapid changes in the strain rate. It has been successfully applied to complex flow fields like vortex flows [44], rotating pipes [45], and TCP flows [19,40,46].

2.3. Grid Resolution

The computation grid was uniform in the axial and circumferential directions. In the wall-normal direction, the grid points were clustered near the inner and outer cylinders to achieve fine grid resolution near the walls. The first grid point was placed to keep the r^+ $\left(r^+ = u_\tau \Delta r/\upsilon\right)$ value below 1. The grid structure is detailed in Table 3. The mesh distribution between the cylinders can also be seen in Figure 2 (for 64x140x127 mesh). N_r , N_θ , and N_z donates the number of grid points in the radial, tangential, and axial directions, respectively. The grid structures presented in the table are obtained by conducting a systematic grid dependency study (which is presented in the following section). The initial grid was structured similarly to that in [12]. The number of grid points was refined for higher rotation rates because finer grids were needed in the axial direction to resolve the flow for increasing N [8]. Although the implemented implicit solution algorithm relieves the CFD restriction, relatively small time steps were selected to maintain the mean Courant-Friedrichs-Lewy (CFL) value (CFL = $U\Delta t/\Delta x$) around 1, to increase the accuracy. The maximum CFL value was 0.43 in all cases.

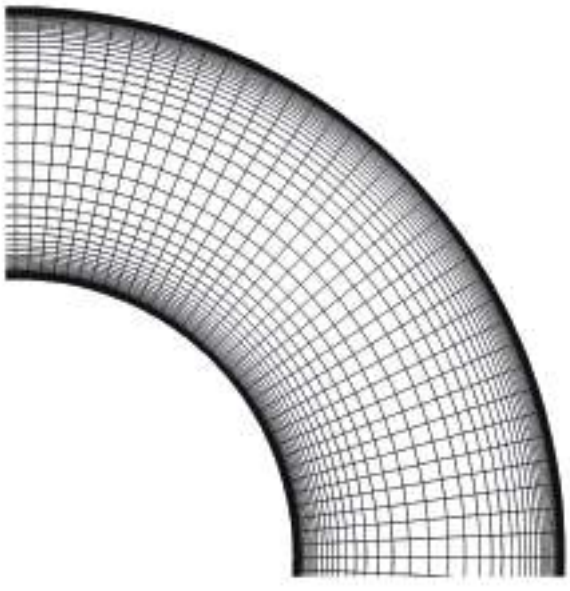

Figure 2. *Mesh distribution between the cylinders*

3. Numerical Accuracy Evaluation

The present calculations are compared with the experimental results of Escudier and Coulson [6] to validate the numerical methodology. Results of the validation case were obtained under the same conditions as the experiment, which are Re=7400 and Ω=126 rpm. This flow configuration resulted in a Taylor Number of Ta=8.75x10^5 and a rotation number N=0.25. Before comparing the numerical results with the experimental data, we studied the mesh dependency of the numerical predictions. To examine the impact of the mesh structure on the numerical results, the mesh distribution was changed separately in all directions, and variations in the results were observed. It's worthy of mention that the mesh density in the radial direction seems to have a greater influence on the tangential velocity distribution. Considering these findings and previous studies in the literature, the final mesh distribution was determined. Once the optimal mesh distribution was determined, the overall mesh count was parametrically changed in all directions to examine the mesh dependency of the numerical results (Figure 3). The validation case was selected for the mesh dependency study. Here, the medium mesh refers to the mesh distribution in the first row of Table 3 due to the similarity of the flow conditions. The coarse, medium, and fine mesh counts were 0.6, 1.14, and 2.55 million, respectively. When the results were examined, the coarse mesh structure was observed to underestimate the tangential velocity distribution along the radial gap, whereas

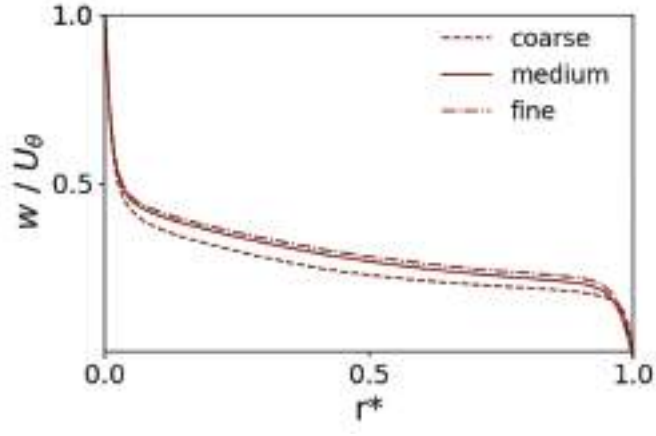

Figure 3. *The effect of mesh density on the numerical results*

the medium and fine mesh structures produced very similar results to each other. Therefore, considering computational time and accuracy together, the study was continued with a medium mesh structure.

Figure 4 compares the present results with those of Escudier and Coulson [6] for the mean axial and tangential velocity components. The predicted mean axial and tangential velocity profiles are non-dimensionalized by the bulk and inner cylinder rotational velocities, respectively. r^* represents the radial location $\left(r^* = r - r_i / s\right)$. The numerical predictions are in good agreement with the experimental ones. The velocity profiles in both the boundary layers and the core region were very similar to those obtained in the experiment. The predicted tangential velocity values are smoother and slightly higher than the measurements; nevertheless, the slope of the curve in the core region is successfully captured.

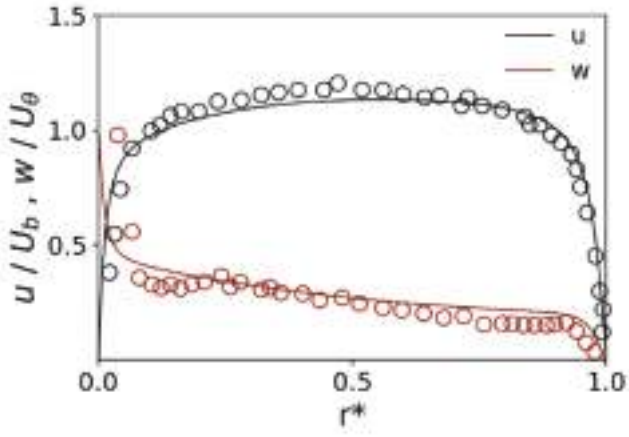

Figure 4. *Comparison of calculated mean velocity components (straight lines) with experimental data (symbols) along the radial direction*

The predicted axial and tangential turbulent fluctuations compared with the experimental data are plotted in Figure 5. The variation in the normal components of the Reynolds stress tensor along the radial direction was generally in good agreement with the measurements. In most parts of the radial distance, the tangential velocity fluctuation, w', calculations correspond well to the experimental results but exhibit a smoother profile. The turbulence intensity in the axial direction, u', is in the same tendency as in the experiment. The calculated turbulence levels in the core region and boundary layer along the outer cylinder were in the same magnitude as the measurements. However, some differences can be seen in the peak values of the fluctuations in the boundary layer along the inner cylinder. The same features were observed for near-wall velocity fluctuations in the RSM predictions of Poncet et al. [19] against the same measurements and the LES results of Chung and Sung [8] and DNS of Jung and Sung [10] against the experimental data of Nouri and Whitelaw [5]. Overall, it can be concluded that the flow field in the annular gap can be accurately predicted using the present numerical methodology.

4. Numerical Results

Detailed calculations were carried out for the parameter spaces summarized in Table 2. In Figure 6, we observe the distribution

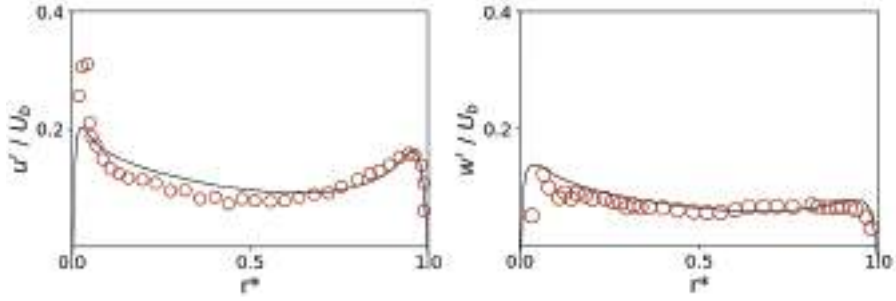

Figure 5. *Comparison of calculated axial and tangential velocity fluctuations (straight lines) and experimental data (symbols) along the radial direction*

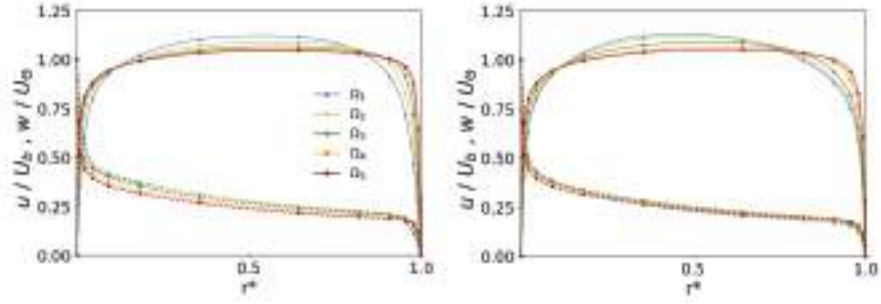

Figure 6. *Effect of rotation on distribution of mean axial (solid line) and tangential (dashed line) velocity components (left: Re=10000, right: Re=30000)*

of mean axial and tangential velocities normalized to the inlet bulk velocity and inner cylinder rotational velocity, respectively, across two different flow rates. Regardless of the axial velocity, all cases exhibit turbulent flow profiles. The increasing inner cylinder rotational speed flattens and slightly shifts the velocity profiles toward the outer wall, which is particularly evident at lower rotational speeds. Higher Reynolds numbers yield similar results. Rotation influences the normalized tangential velocity primarily near the inner cylinder, thinning the boundary layer and decreasing the slope of the core region profile, as previously pointed out by Poncet et al. [12]. It is worth noting that Poncet et al. [12] reported a solid body-like rotation in the core region with a decreasing slope of the tangential velocities toward zero. Their calculations consider a very narrow gap with a radius ratio of $r_1/r_2 = 8/9$. On the other hand, in the present results, the angular momentum is still almost constant, but the tangential velocity curves never show such a flatter profile in the center region. Similar variations in normalized tangential velocities can be observed in the LES results of Chung and Sung [8] with $r_1/r_2 = 0.5$. At higher axial flow rates, changes in the rotational speed have less impact on the tangential velocity profiles because of the limited rotation number variation. Increasing the flow rate prioritizes the axial velocity, diminishing the influence of rotation under the same rotational parameters.

The influence of the imposed flow rate on the distribution of the mean velocity components can be seen in Figure 7, for the highest and lowest rotational speeds of the inner cylinder. The axial velocity profiles showed slight deviations with flow rate variations. An increase in Re reverses the effect of rotation, and the axial velocity profiles start to have lower gradients near the outer stationary wall at low rotational speed (Figure 7-left). The effect of the imposed flow rate on the tangential velocity is more apparent. Tangential velocity values exhibit a progressive decrease nearly in the entire flow field with increasing Re. As stated by Nouri and Whitelaw [5], increasing the axial flow rate limits the penetration of the influence of rotation through the inner parts of the annular gap. For the higher rotational speed (Figure 7-right), the imposed flow rate seems to have no considerable influence on the mean velocity components. It is worth noting that N varies in the range of 0.31-0.94 for Ω_1 and 3.77-11.32 for Ω_5. Even when the change in N was larger, the case with higher rotation was almost not affected by the variation in the imposed flow rate. It can be concluded that rotation determines the flow field; thus, the influence of the imposed flow rate on the mean velocity components diminishes, as the Ω increases.

The response of low and high rotational speeds to changes in the axial flow rate, regardless of the variation in N, prompts an examination of the mean velocity balance across the annular gap (Figure 8). Cross-stream velocity remains nearly zero across all cases, while the normalized axial velocity exhibits minimal variation with changing flow conditions. Notably, variations in the rotational and/or axial flow control parameters primarily affect the tangential velocity distribution. At low rotational speeds (Figure 8a), the axial velocity dominates the flow field, with the velocity magnitudes decreasing from the axial to the tangential to the cross-stream components. Increasing the rotational speed (in the meantime N) augments the tangential velocity, particularly in the first half of the radial distance (where $0<r<0.5$). At low Re, the same amount of change in the rotational speed results in higher N, thereby enhancing the tangential velocity. As previously mentioned for the numerical results in Figure 6, axial flow limits the penetration of the effect of the rotation through the inner parts of the flow field for the same rotational speed (e.g. Figure 8b, f, j).

Another remarkable feature of the velocity distributions for different axial/rotational velocity pairs is the balance near the inner rotating cylinder. After a certain value of N (approximately $1.89<N<2.52$ in the investigated range), the tangential velocity becomes dominant in the near region of the inner cylinder. These findings provide some insights into Figure 7, where the

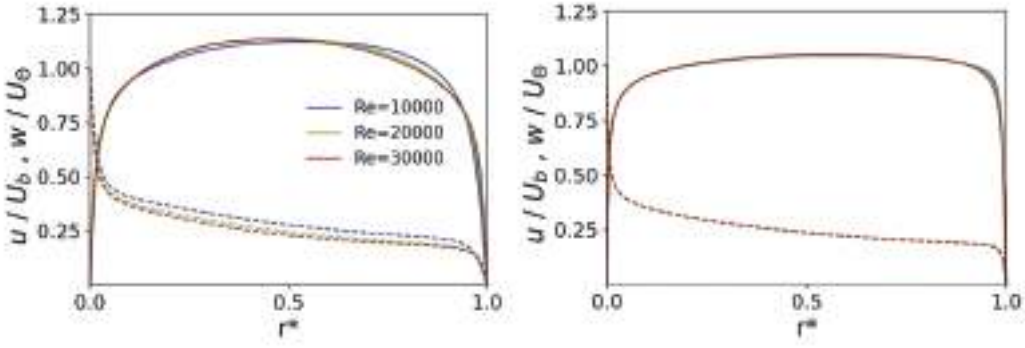

Figure 7. *Effect of axial velocity on distribution of mean velocity components. dashed: mean axial velocity; Straight line: mean tangential velocity (left:Ω_1, right: Ω_5)*

higher rotation case shows minimal sensitivity to changes in the imposed flow rate despite larger variations in N. When the rotational speed of the inner cylinder is relatively low (e.g. $\Omega_1$or Ω_2), axial velocity is dominating the flow field (see Figure 8a, e, i). On the other hand, beyond a certain N value, the tangential velocity becomes dominant near the inner cylinder, thereby influencing the flow-field balance. This dominance persisted even with varying Re (see Ω_5 at Figure 8d, h, l). The results thus far suggest that beyond a threshold N value, rotation dominates near the inner cylinder, and the contribution of rotation becomes

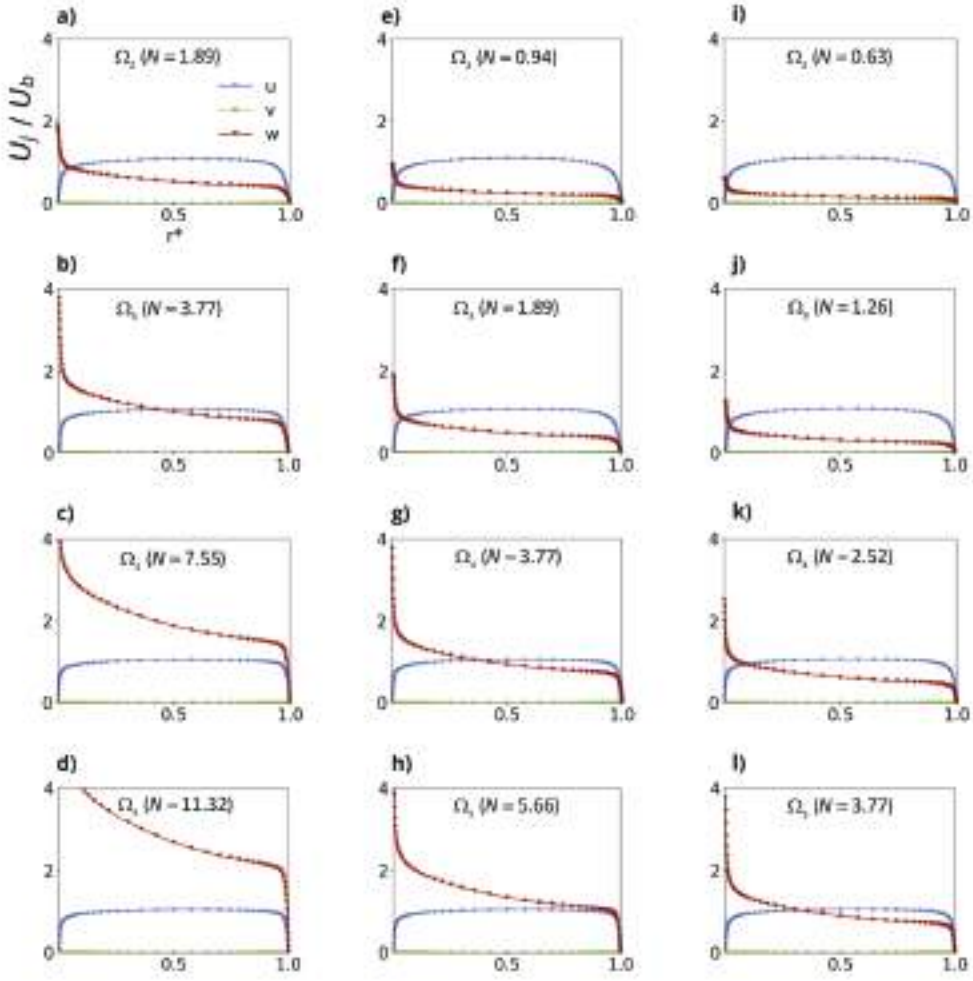

Figure 8. *Distribution of mean velocity components normalized by Ub along the radial gap (left column: Re=10000, middle: Re=20000, right: Re=30000)*

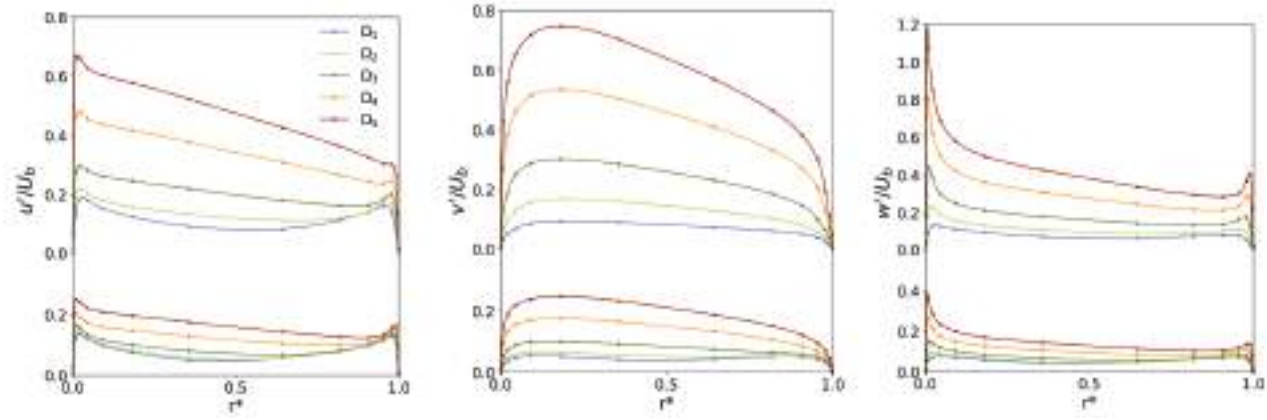

Figure 9. *Effect of rotation on distribution of normal components of Reynolds stress tensor (lower: Re=30000, lifted: Re=10000)*

superior, making mean flow variables less sensitive to changes in the axial flow rate within the specified N range.

Figure 9 presents the effect of rotation on the distribution of normal components of the Reynolds stress tensor. The inner cylinder rotation triggers turbulence, which results in the rapid growth of all turbulence intensities as the rotational speed increases. Turbulence enhancement is limited at high Re. *u*' stress shows a profile with a peak centered at the boundary layer. The magnitude of the *u*' stress in the core region increased with the rotational speed; nevertheless, the peak values were still in the near region of the inner cylinder. *w*' stress retains the general behavior with high values in the boundary layers in all cases. The cross-stream component of the Reynolds stress tensor, *v*', distinctly has higher values in the core region and vanishes toward the walls. All profiles of turbulence intensities are highly asymmetric, which is attributed to the destabilizing effect of centrifugal forces, as noted by Chung and Sung [8]. The asymmetry becomes more apparent with the increase in Ω , akin to similar studies in the literature with the same radius ratio [8,21]. However, Poncet et al. [12] predicted notably weaker asymmetry with a narrow-gap annulus with a radius ratio of $r_i/r_o = 8/9$ within the range of rotational parameters 1.49<N<6.71. Despite the low curvature effect, it can be attributed to the close proximity of the rotating and stationary walls in narrow gap systems.

Figure 10 shows the effect of the axial flow on the distribution of normal stresses at the highest and lowest inner cylinder rotation speeds. In general, an increase in the axial flow rate suppresses the turbulence in the entire flow field. This effect is clearer near the inner cylinder at high rotation rates. The axial flow independence of higher rotation rates noted earlier in the mean velocity profiles (see Figure 7) is not observed for the turbulence variables. The turbulence stresses still exhibit a dependence on both the axial flow rate and the system rotation. The change in the imposed flow rate alters the turbulence stress components in a similar way for low and high rotation speeds of the inner cylinder, except that the results at higher rotation rates vary over a wider range of values.

The velocity profiles in the boundary layer along the inner cylinder are plotted against the law of the wall in Figure 11. It can be seen that rotation causes no significant change in the velocities of the viscous sublayer. However, the profiles in the buffer and log-law regions differed considerably from the wall law. Furthermore, the level of this discrepancy depends

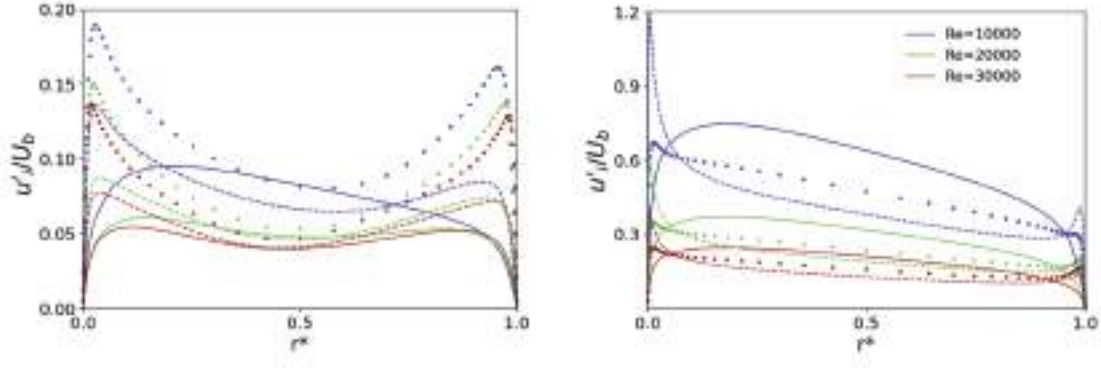

Figure 10. *Effect of axial flow on normal components of Reynolds stress tensor. Symbols donate u', straight line v', and dashed line w' (left: Ω_1, right:Ω_5)*

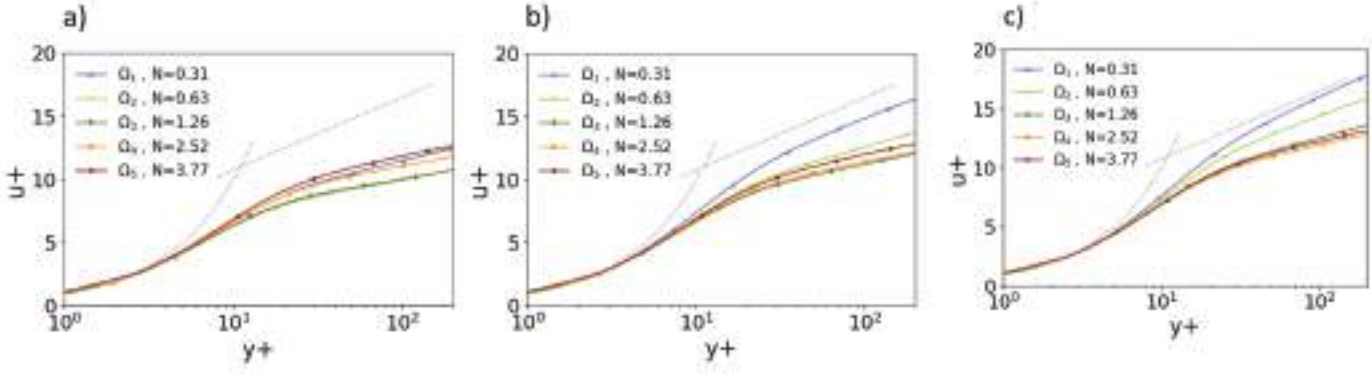

Figure 11. *Boundary layer velocity distribution under the law of the wall (a: Re=10000, b: Re=20000, c: Re=30000)*

on the value of N. For instance, in Figure 11a, velocities in the boundary layer diverge from the standard log-law as the rotational speed of the inner cylinder increases up to Ω_2 . However, a further increase in rotation shifts the profiles closer to that of the law of the wall. The value of N at which the effect of rotation is reversed is 1.89<N<2.52 in the investigated range. This value also coincides with the range where the mean tangential velocity dominates the near-wall region of the inner rotating cylinder at Figure 8. Note that the increment rate of the rotational speed of the inner cylinder causes the values N to jump from one value to another, and determining intermediate values requires many more cases to solve. This is the reason why the present study suggests ranges instead of exact values of N. The results are in accordance with those of other studies in the literature. Schneider et al. [21] and Chung and Sung [8] reported an increasing discrepancy between the boundary layer velocity profiles and those of the law of the wall with increasing N from 0 to 0.858. However, in the LES results of Poncet et al. [12], the velocities in the logarithmic region approached the log-law with increasing N from 2.24 to 6.71.

The effect of the axial flow on the law of the wall for boundary layer velocity is shown in Figure 12. At low cylinder rotation, an increase in the axial flow rate suppresses the influence of rotation and decreases the discrepancy of the velocity profiles with the log-law (see Figure 12-left). However, the axial flow seems to have no considerable effect on the boundary layer velocity profiles at high rotational speeds, even though N varies in a wider range (see Figure 12-right). Note that the mean velocity profiles in Figure 7 were also nearly unaffected by the axial flow at high system rotation. Here, the same feature that is explained in Figure 8, the superior value of the tangential velocity near the rotating wall, which is thought to be the reason why the effect of the imposed flow is considerably limited in Figure 12-right.

5. Conclusion

This study conducted a numerical investigation of a fully developed turbulent flow within a concentric annular channel. A RSM-based numerical procedure was employed to examine the effects of the inner wall rotational velocity and imposed axial flow rate on the flow dynamics. The numerical predictions were first validated against experimental data by Escudier and Coulson [6]. Subsequently, various flow control parameters were investigated. This research focused on the behavior of the TCP system at high Reynolds numbers. The key findings are summarized below:

• The influence of flow control parameters on the mean flow variables differed between high and low system rotation. At higher rotational speeds, the mean flow variables are nearly independent of the changes in the imposed flow rate, regardless of the rotation number (N) variation.

• The balance between the mean velocity components across the radial gap exhibits a significant dependence on both rotation and the imposed axial flow. As expected, increasing rotation increased the tangential velocity, particularly in the first half of the radial gap near the inner wall. Beyond a certain value of N, the tangential velocity becomes dominant in the flow field between the inner wall and core region. At even higher N values, the flow field is likely to be more dominated by the contribution of rotation. This phenomenon explains the observed independence of mean flow features from axial flow at high rotational speeds.

• In general, the imposed flow and rotation have opposing effects on the turbulence behavior. Inner wall rotation significantly enhanced the turbulence statistics, whereas axial flow suppressed the destabilizing effect of rotation. Unlike the mean flow variables, the turbulence intensities decreased with increasing axial flow rate at any rotational speed.

• Rotation has a non-monotonic effect on the agreement of the boundary layer velocity profiles with the law of the wall. As the rotational speed increases, the discrepancy of the boundary-layer velocities with the log law initially increases but then decreases. The rotation rate at which this behavior

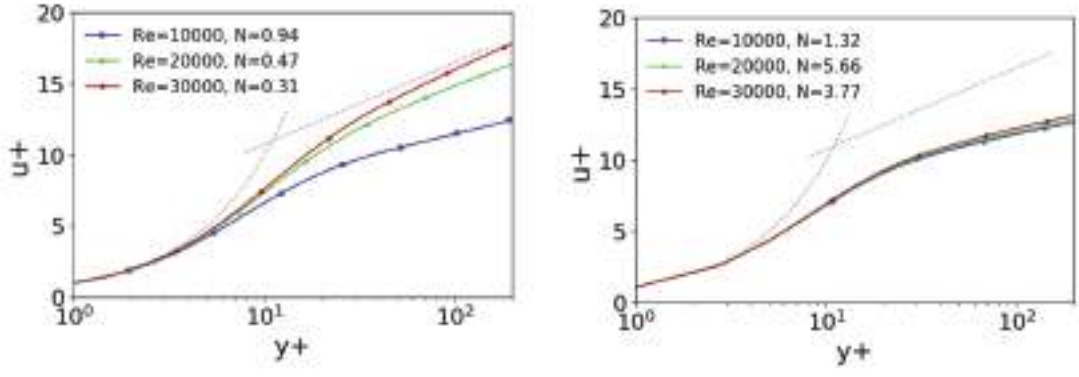

Figure 12. *Effect of axial flow on the velocity distribution in the boundary layer (left:* Ω_1*, right:*Ω_5*)*

shift coincides with the range in which the tangential velocity dominates the flow field.

These results provide valuable insights into the complex interplay between rotation and axial flow in TCP systems. This knowledge can be used to optimize the design and operation of various engineering applications.

Authorship Contributions

Concept Design: T. Çoşgun, N. Vardar, Data Collection or Processing: T. Çoşgun, Analysis or Interpretation: T. Çoşgun, Literature Review: T. Çoşgun, N. Vardar, Writing, Reviewing and Editing: T. Çoşgun, N. Vardar.

Funding: The authors received no financial support for the research, authorship, and/or publication of this article.

References

[1] D. L. Cotrell, "Flow Between a Cylinder and a Rotating Coaxial Cylinder, Axisymmetric Shaft With Axially-Periodic Radius Variation, or Screw," University of Illinois at Urbana-Champaign, vol. 112, pp. 153-161, Jun 2003.

[2] M. Bilson, and K. Bremhorst, "Direct numerical simulation of turbulent Taylor-Couette flow". *Journal of Fluid Mechanics,* vol. 579, pp. 227-270, May 2007.

[3] S. Grossmann, D. Lohse, and C. Sun, "High-Reynolds number taylor-couette turbulence". *Annual Review of Fluid Mechanics,* vol. 48, pp. 53-80, 2016.

[4] M. Fénot, Y. Bertin, E. Dorignac, and G. Lalizel, "A review of heat transfer between concentric rotating cylinders with or without axial flow". *International Journal of Thermal Sciences,* vol. 50, pp. 1138-1155, Jul 2011.

[5] J. M. Nouri, and J. H. Whitelaw, "Flow of newtonian and non-newtonian fluids in a concentric annulus with rotation of the inner cylinder," *Journal of Fluids Engineering,* vol. 116, pp. 821-827, Dec 1994.

[6] M. P. Escudier and I. W. Gouldson, "Concentric annular flow with centerbody rotation of a Newtonian and a shear-thinning liquid". *International Journal of Heat and Fluid Flow*, vol. 16, pp. 156-162, Jun 1995.

[7] S. Chung, G. Rhee, and H. Sung, "Direct numerical simulation of turbulent concentric annular pipe flow: Part 1: Flow field". *International Journal of Heat and Fluid Flow*, vol. 23, pp. 426-440, 2002.

[8] S. Y. Chung, and H. J. Sung, "Large-eddy simulation of turbulent flow in a concentric annulus with rotation of an inner cylinder". *International Journal of Heat and Fluid Flow,* vol. 26, pp. 191-203, 2005.

[9] N. S. Liu, and X. Y. Lu, "Large eddy simulation of turbulent flows in a rotating concentric annular channel". *International Journal of Heat and Fluid Flow,* vol. 26, pp. 378-392, Jun 2005.

[10] S. Y. Jung, and H. J. Sung, "Characterization of the three-dimensional turbulent boundary layer in a concentric annulus with a rotating inner cylinder". *Physics of Fluids,* vol. 18, 2006.

[11] M. Hadžiabdić, K. Hanjalić, and R. Mullyadzhanov, "LES of turbulent flow in a concentric annulus with rotating outer wall". *International Journal of Heat and Fluid Flow*, vol. 43, pp. 74-84, Oct 2013.

[12] S. Poncet, S. Viazzo, and R. Oguic, "Large eddy simulations of Taylor-Couette-Poiseuille flows in a narrow-gap system". *Physics of Fluids*, vol. 26, pp. 1070-6631, Oct 2014.

[13] Y. Yamada, "Resistance of a Flow through an Annulus with an Inner Rotating Cylinder". *Bulletin of JSME*, vol. 5, pp. 302-310, 1962.

[14] M. Manna, and A. Vacca, "Torque reduction in Taylor-Couette flows subject to an axial pressure gradient". *Journal of Fluid Mechanics,* vol. 639, pp. 373-401, Nov 2009.

[15] A. Ohsawa, A. Murata, and K. Iwamoto, "Through-flow effects on Nusselt number and torque coefficient in Taylor-Couette-Poiseuille flow investigated by large eddy simulation". *Journal of Thermal Science and Technology,* vol. 11, pp. JTST0031-JTST0031, Jun 2016.

[16] N. S. Woo, Y. J. Kim, and Y. K. Hwang, "Experimental study on the helical flow in a concentric annulus with rotating inner cylinder". *Journal of Fluids Engineering*, vol. 128, pp. 113-117, 2006,

[17] Y. C. Chong, D. A. Staton, M. A. Mueller, and J. Chick, "An experimental study of rotational pressure loss in rotor-stator gap". *Propulsion and Power Research*, vol. 6, pp. 147-156, Jun 2017.

[18] S. Huang, and C. H. Chun, "A numerical study of turbulent flow and conjugate heat transfer in concentric annuli with moving inner rod". *International Journal of Heat and Mass Transfer,* vol. 46, pp. 3707-3716, Sep 2003.

[19] S. Poncet, S. Haddadi, and S. Viazzo, "Numerical modeling of fluid flow and heat transfer in a narrow Taylor-Couette-Poiseuille system". *International Journal of Heat and Fluid Flow*, vol. 32, pp. 128-144, 2011.

[20] A. Aubert, S. Poncet, P. Le Gal, S. Viazzo, and M. Le Bars, "Velocity and temperature measurements in a turbulent water-filled Taylor-Couette-Poiseuille system". *International Journal of Thermal Sciences*, vol. 90, pp. 238-247, 2015.

[21] M. Schneider, B. A. Younis, and B. Weigand, "Large-eddy simulations of flow and heat transfer in heated concentric annulus with inner cylinder rotation". *International Journal of Heat and Mass Transfer,* vol. 114, pp. 1248-1262, Apr 2017.

[22] J. M. Lopez, F. Marques, and M. Avila, "Conductive and convective heat transfer in fluid flows between differentially heated and rotating cylinders". *International Journal of Heat and Mass Transfer,* vol. 90, pp. 959-967, Nov 2015.

[23] J. Kaye, and E. C. Elgar, "Modes of adiabatic and diabatic fluid flow in an annulus with an inner rotating cylinder". *Transactions of the ASME*, vol. 80, pp. 753-765, Apr 1958.

[24] K. M. Becker, and J. Kaye, "Measurements of diabatic flow in an annulus with an ınner rotating cylinder". *ASME Journal of Heat and Mass Transfer,* vol. 84, pp. 97, May 1962.

[25] D. I. Takeuchi, and D. F. Jankowski, "A numerical and experimental investigation of the stability of spiral poiseuille flow". *Journal of Fluid Mechanics,* vol. 102, pp. 101-126, Jan 1981.

[26] Z. H. Gu, and T. Z. Fahidy, "Characteristics of Taylor vortex structure in combined axial and rotating flow". *The Canadian Journal of Chemical Engineering,* vol. 63, pp. 710-715, Oct 1985.

[27] M. Molki, K. N. Astill, and E. Leal, "Convective heat-mass transfer in the entrance region of a concentric annulus having a rotating

inner cylinder". *International Journal of Heat and Fluid Flow*, vol. 11, pp. 120-128, Jun 1990.

[28] R. M. Lueptow, A. Docter, and K. Min, "Stability of axial flow in an annulus with a rotating inner cylinder". *Physics of Fluids*, vol. 4, pp. 2446-2455, Nov 1992.

[29] S. T. Wereley, and R. M. Lueptow, "Velocity field for Taylor-Couette flow with an axial flow". *Physics of Fluids*, vol. 11, pp. 3637-3649, 1999.

[30] J.Y. Hwang and K.S. Yang, "Numerical study of Taylor-Couette flow with an axial flow". *Computers & Fluids,* vol. 33, pp. 97-118, Jan 2004.

[31] S. Y. Jung, and H. J. Sung, "Large-eddy simulation of turbulent mixed convection in a vertical annulus with a rotating inner cylinder". *Journal of Turbulence*, vol. 8, pp. N5, Jan 2007.

[32] T. M. Jeng, S. C. Tzeng, and C. H. Lin, "Heat transfer enhancement of Taylor-Couette-Poiseuille flow in an annulus by mounting longitudinal ribs on the rotating inner cylinder". *International Journal of Heat and Mass Transfer,* vol. 50, pp. 381-390, Jan 2007.

[33] M. Fénot, E. Dorignac, A. Giret, and G. Lalizel, "Convective heat transfer in the entry region of an annular channel with slotted rotating inner cylinder". *Applied Thermal Engineering,* vol. 54, pp. 345-358, May 2013.

[34] C. Leclercq, B. Pier, and J. F. Scott, "Temporal stability of eccentric taylor-couette-poiseuille flow". *Journal of Fluid Mechanics*, vol. 733, pp. 68-99, Sep 2013.

[35] K. R. Anderson, J. Lin, C. McNamara, and V. Magri, "CFD study of forced air cooling and windage losses in a high speed electric motor". *Journal of Electronics Cooling and Thermal Control,* vol. 5, pp. 27-44, Jan 2015.

[36] W. Abassi, F. Aloui, S. B. Nasrallah, and J. Legrand, "Use of the PIV and electrochemical techniques to experimentally characterize the couette-taylor-poiseuille flow ınstabilities". *Journal of Applied Fluid Mechanics,* vol. 9, Special Issue 1, pp. 59-68, 2016.

[37] N. Tilton, and D. Martinand, "Taylor-Couette-Poiseuille flow with a weakly permeable inner cylinder: Absolute instabilities and selection of global modes". *Journal of Fluid Mechanics*, vol. 849, pp. 741-776, Aug 2018.

[38] G. Luo, Z. Yao, and H. Shen, "Mechanism of pressure oscillation in Taylor-Couette-Poiseuille flow with abruptly contracting and expanding annular gap". *Physics of Fluids*, vol. 31, pp. 075105, Jul 2019.

[39] A. Nouri-Borujerdi and M. E. Nakhchi, "Prediction of local shear stress and heat transfer between internal rotating cylinder and longitudinal cavities on stationary cylinder with various shapes". *International Journal of Thermal Sciences,* vol. 138, pp. 512-520, Apr 2019.

[40] S. Gokul, and M. Deepu, "Fluid flow and heat transfer in an annulus with ribs on the rotating ınner cylinder surface". *International Journal of Heat and Mass Transfer*, vol. 12, 041026, Aug 2020.

[41] I. Mochalin, E. Shi-Ju, D. Wang, and J.-C. Cai, "Numerical study of heat transfer in a Taylor-Couette system with forced radial throughflow". *International Journal of Thermal Sciences*, vol. 147, pp. 106142, Jan 2020.

[42] A. Gavrilov, and Y. Ignatenko, "Numerical simulation of taylor-couette-poiseuille flow at re = 10,000". *Fluids*, vol. 8, pp. 1-17, 2023.

[43] R. Manceau, and K. Hanjalić, "Elliptic blending model: A new near-wall Reynolds-stress turbulence closure". *Physics of Fluids,* vol. 14, pp. 744-754, Feb 2002.

[44] S. Lardeau, and R. Manceau, "Computations of complex flow configurations using a modified elliptic-blending Reynolds-Stress model". *10th International ERCOFTAC Symposium on Engineering Turbulence Modelling and Measurements*, 2014.

[45] N. Ashton, J. Davis, and C. Brehm, "Assessment of the elliptic blending reynolds stress model for a rotating turbulent pipe flow using new DNS data". *American Institute of Aeronautics and Astronautics (AIAA),* Jun 2019.

[46] J. L. V. Neto, A. L. Martins, A. S. Neto, C. H. Ataíde, and M. A. S. Barrozo, "CFD applied to turbulent flows in concentric and eccentric annuli with inner shaft rotation". *The Canadian Journal of Chemical Engineering,* vol. 89, pp. 636-646, Aug 2011.

ORIGINAL RESEARCH (AR) DOI: 10.4274/jems.2024.79027

Journal of ETA Maritime Science 2024;12(3):346-356

Parameter Optimization for Model-Based Design and Control of the KVLCC2 Tanker Ship

Emre Sayin, Ismail Bayezit

İstanbul Technical University Faculty of Aeronautics and Astronautics, Department of Aeronautical Engineering, İstanbul, Türkiye

Abstract

This article provides a model-based design method for heading control based autonomous trajectory tracking of a KVLCC2 ship. Kinematics, dynamics, and hydrodynamic force subsystems are used to represent the ship's motion equations. By contrasting the outcomes with experimental data received from the maneuvering modelling group, the accuracy of the model is confirmed. Heading angle of the ship is controlled by a linear cascade controller, and the settings of the controller are modified by using two separate heuristic optimization techniques: particle swarm optimization and genetic algorithm. The comparison of the findings demonstrates that the particle swarm optimization approach is computationally more effective than the genetic algorithm. Performance in the presence of disturbance has been investigated using the controller parameters discovered using particle swarm optimization. A suitable guidance algorithm is incorporated into the architecture of a trajectory tracking system to establish the necessary heading angle for travel between waypoints. We use a real-time simulator to visualize the ship motion on a graphical environment.

Keywords: Ship heading control, Cascade control, Model-based simulation, Genetic algorithm, Particle swarm optimization

1. Introduction

In the ever-evolving landscape of maritime transportation, the efficient and precise control of vessels remains a pivotal challenge. The utilization of modern control strategies, grounded in model-based design, presents an avenue of exploration to enhance the performance of vessels like the KVLCC2 tanker. The central focus of this study revolves around the implementation and advantages of cascade control approach and optimization of controller parameters, a crucial facet in achieving optimal control outcomes. Leveraging the innovative paradigms of particle swarm optimization (PSO) and genetic algorithms (GAs), this research delves into the synergy between advanced control methodologies and state-of-the-art optimization techniques. By combining the principles of model-based control, cascade control architecture, and the potency of optimization, this study offers insights into the broader realm of complex systems optimization as well as contributing to the emerging field of the maritime control engineering.

By analyzing the system dynamics, it is possible to design a controller that can transform a manually controlled system into an autonomously controlled one. Most control systems are closed-loop systems that use feedback from the system's output to generate an error signal, which is then compensated by using a controller to implement certain algorithms.

Scope of this work is the simulation of the dynamics of the ship motion, design and implementation of a linear cascade controller within the model-based design and simulation environment, and to satisfy the autonomous heading tracking performance. The control methodology for the system is chosen as in the cascade control scheme using a deterministic approach. This control method involves the utilization of various control loops, in which, each loop is responsible for controlling a specific aspect of the system's behaviour. The output of one control loop is used as the input to the next control loop, resulting in a hierarchical control structure that can be finely tuned to achieve the desired system behaviour. The aforementioned control

Address for Correspondence: Ismail Bayezit, İstanbul Technical University Faculty of Aeronautics and Astronautics, Department of Aeronautical Engineering, İstanbul, Türkiye
E-mail: bayezit@itu.edu.tr
ORCID iD: orcid.org/0000-0001-9345-5108

Received: 30.04.2024
Last Revision Received: 07.08.2024
Accepted: 11.08.2024

To cite this article: E. Sayın, and İ. Bayezit. "Parameter Optimization for Model-Based Design and Control of the KVLCC2 Tanker Ship". *Journal of ETA Maritime Science*, vol. 12(3), pp. 346-356, 2024.

algorithm also allows the fast rejection of disturbance since one loop perceive the disturbance prior to other loop and obtains chance to compensate the disturbance before it propagates [1]. Cascade control is commonly used in complex systems where a single control loop may not be sufficient to achieve the desired level of performance. Several studies have been done on the ship heading control by using cascade approach. In [2], Kula designs a heading control system by using a cascade system and internal model control approach. Li and Wang [3] propose a hybrid approach for ship dynamic positioning control that uses piecewise and cascade controllers. However, they do not make any tuning of controller parameters [3]. Tao and Ma [4] design a robotic arm for steering wheel control of the ship. They use as cascade approach to control the steering angle with PID controllers. They do not utilize any tuning of the PID parameters [4]. Zhibin et al. [5] design a cascade controller for an autonomous underwater vehicle. They use PI and P controllers for inner and outer loops, respectively. They optimize the controller parameters. However, the optimization method used for tuning the controller parameters is not shared [5]. Andrija et al. [6] manufacture an unmanned surface vehicle and use PID controllers to control throttle and steering of the ship. They tune controller parameters manually [6]. Many other advanced control algorithms have been presented for ship control such as LQR [7] MPC [8-10] neural network-based controllers [11,12] sliding mode controller [13-15], non-linear adaptive control [16] and so on.

Additionally, studies on the path following of KVLCC2 tanker are also abundant. Paramesh and Rajendran investigate the PID controlled KVLCC2 tanker for heading control. They use a Line-of-Sight (LOS) guidance algorithm to navigate between given waypoints [17]. Adams et al. [18] proposes an MPC, PID and LQR based heading control of KVLCC2 tanker. They also use LOS guidance algorithm and compare the performances of controllers [18]. Sandeepkumar et al. [19] design a non-linear MPC for the KVLCC2 tanker. They develop a 3 DoF Maneuvering model and design an MPC to control the heading angle in the presence of regular waves [19]. Wang et al. [20] develops a control approach using Deep Reinforcement Learning technique in order to execute the path following of 7 meters scaled version of KVLCC2 tanker ship. They use Adaptive LOS guidance method to convert waypoints into heading angle commands. Different controller methods are also compared in the study [20].

The rest of this paper is organized as follows: In the second chapter, the equations of motion that are essential for the development of the model are discussed and validated. In the third chapter, the control strategy used to regulate the ship's heading angle is described in detail, including the application of optimization methods for controller parameter tuning and comparison of these tuning techniques. The fourth chapter focuses on the implementation of a path tracking system and real-time simulation. Lastly, in the fifth chapter, the study has been concluded and strategies for future research are proposed.

2. Equations of Motion

The coordinate systems used to analyze the ship motion is given in Figure 1. The three degrees-of-freedom (DoF) motion of a ship (including yaw, surge, and sway) can be given using differential relations. The non-linear equations of motion for a ship with these three DoF can be written as follows [21]:

$$\begin{bmatrix} m+m_x & 0 & 0 \\ 0 & m+m_y & x_G m \\ 0 & x_G m & I_{zz}+x_G^2 m+J_z \end{bmatrix} \begin{bmatrix} \dot{u} \\ \dot{v}_m \\ \dot{r} \end{bmatrix} = \begin{bmatrix} X+(m+m_y)v_m r+x_G m r^2 \\ Y-(m+m_x)ur \\ N_m-x_G m u r \end{bmatrix} \quad (1)$$

u and v_m are the surge and lateral velocities at the center of the ship, respectively. r is the yaw rate, m is the ship mass, m_x and m_y are the added masses for x and y axis directions. $\boldsymbol{x}_G$ is the longitudinal coordinate value of the of gravity (CoG) of the ship, I_{zG} is the ship moment of inertia calculated around CoG and J_z is the added moment of inertia. X and Y stand for surge and sway forces. N_m is the yaw moment calculated around the center of the ship excluding added mass term. This information is useful for having insight into the ship behaviour for designing control strategies to achieve a desired performance.

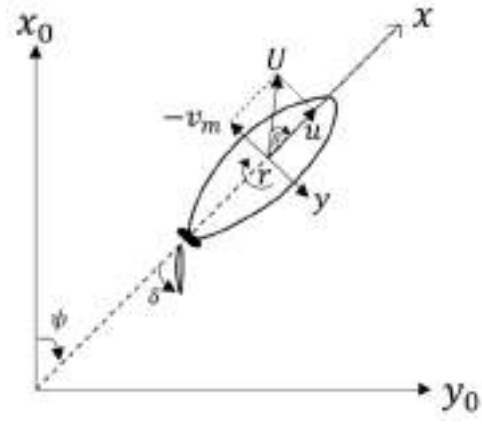

Figure 1. *Ship coordinate system*

2.1. Kinematics

The kinematics equations for a ship can be derived by using appropriate coordinate transformations. The dynamics equations, on the other hand, are typically described in a fixed-body frame, as shown in Figure 1. In this frame, the x-axis points toward the ship's bow, y-axis points toward the starboard side, and right-hand rule is used to find the z-axis,

which completes the axes. To visualize the ship motion in an inertial frame, it is necessary to convert the body-fixed coordinates into Earth-fixed inertial coordinates. The Earth-fixed inertial coordinate system has an origin fixed at the Earth's center; x-axis points toward the North, y-axis points toward the East, and the z-axis completes the right-hand rule. Both angular and linear motions of the ship must be converted into this coordinate system in order to fully describe the motion dynamics of the ship in a fixed frame of reference [22]. Proper transformations are made according to these conversions.

2.2. Hydrodynamic Forces

This section reveals the hydrodynamic forces that act on the ship as: forces that act on ship hull (H), forces due to propeller (P) and forces by steering (R). It is obvious that adding extra forces into these equations is possible for ongoing advanced studies. The forces acting on a ship can be elaborated as:

$$\begin{aligned} X &= X_H + X_R + X_P \\ N_m &= N_H + N_R \\ Y &= Y_H + Y_R \end{aligned} \tag{2}$$

where X_H and Y_H are surge and sway forces; N_H is the yaw moment calculated around the center of the ship acting on ship hull, excluding the added mass components, respectively. X_R and Y_R are surge and sway forces and N_R is the yaw moment around midship by steering. X_P represents the propeller-induced surge force. These forces are completed by using set of equations and hydrodynamic derivatives obtained experimentally.

Hydrodynamics forces acting on a ship hull can be elaborated by set of equations. For the surge, sway, and yaw motions, the forces that act on ship hull can be calculated as [21]:

$$\begin{aligned} X_H(v_m, r) &= -R_0 + X_{vv}v_m^2 + X_{vr}v_m r + X_{rr}r^2 + X_{vvvv}v_m^4 \\ Y_H(v_m, r) &= Y_v v_m + Y_R r + Y_{vvv}v_m^3 + Y_{vvr}v_m^2 r + Y_{vrr}v_m r^2 + Y_{rrr}r^3 \\ N_H(v_m, r) &= N_v v_m + N_R r + N_{vvv}v_m^3 + N_{vvr}v_m^2 r + N_{vrr}v_m r^2 + N_{rrr}r^3 \end{aligned} \tag{3}$$

where R_0 is the resistance coefficient, N_v, N_R, N_{vvv}, N_{vvr}, N_{vrr}, N_{rrr}, X_{vv}, X_{vr}, X_{rr}, X_{vvvv}, Y_v, Y_R, Y_{vvv}, Y_{vvr}, Y_{vrr}, and Y_{rrr} are the hydrodynamic derivatives on maneuvering. These coefficients can be determined both computationally by using CFD tools and experimentally. Bold usage indicates the non-dimensional form. The dimensionalized form of the coefficients X_H, Y_H, and N_H can be written as:

$$\begin{aligned} X_H &= 0.5\rho\, L_{pp} d U^2 X_H \\ Y_H &= 0.5\rho\, L_{pp} d U^2 Y_H \\ N_H &= 0.5\rho\, L_{pp}^2 d U^2 N_H \end{aligned} \tag{4}$$

where ρ, L_{pp}, d and U are the density of water, ship length, ship draft and resultant speed, respectively. Additionally, $\boldsymbol{v_m}$ and $\boldsymbol{r}$ can be found by calculating v_m/U and rL_{pp}/U, respectively.

It is assumed that the hydrodynamic force arisen from the propeller is only affecting surge movement of the ship. Thus, a surge force X_P is produced by propeller. X_P can be calculated as:

$$X_P = (1 - t_p)T \tag{5}$$

t_p is the thrust deduction factor and T is the thrust of the propeller, which can be calculated as given in [1] and [2]:

$$T = \rho n_p^2 D_p^4 K_T(J_P) \tag{6}$$

where n_p is the revolution number and D_p is the diameter value of the propeller, respectively. K_T is a 2nd order polynomial that is a function of propeller advanced ratio J_P, and can be calculated as:

$$K_T(J_P) = k_2 J_P^2 + k_1 J_P + k_0 \tag{7}$$

where $k\,0$, k_1 and k_2 are the elements of K_T polynomial. Additionally, J_P can be calculated as:

$$J_p = \frac{u(1-w_p)}{n_p D_p} \tag{8}$$

where w_p is the wake coefficient at propeller position during maneuvering, which is calculated as:

$$w_p = 1 - (1 - w_{p0})\left(1 + \left(1 - e^{-C_1|\beta_p|}\right)(C_2 - 1)\right) \tag{9}$$

w_{p0} is the propeller position wake coefficient during straight motion, β_p is the geometrical inflow angle to propeller for maneuvering motions, C_1 and C_2 are the experimental constants that stand for wake characteristics in maneuvering.

Due to presence of rudder, there also exists a hydrodynamic force acting on surge, sway and yaw motions. Hydrodynamic forces by steering can be formulated as [3]:

$$\begin{aligned} X_R &= -(1 - t_R)F_N \sin\delta \\ Y_R &= -(1 + a_H)F_N \cos\delta \\ N_R &= -(x_R + a_H x_H)F_N \cos\delta \end{aligned} \tag{10}$$

where F_N and $t\,R$ are the normal force of the rudder and the steering resistance deduction factor, respectively. The increase factor of the rudder force, the rudder position longitudinal coordinate, the longitudinal coordinate value of acting point of the additional lateral force, and the rudder angle are given with a_H, x_R, x_H, and δ, respectively. F_N can also be calculated as:

$$F_N = 0.5\rho A_R U_R^2 f_\alpha \sin\alpha_R \tag{11}$$

where $A\,R$ is the profile area value of the movable part of mariner rudder, f_α is the lift gradient coefficient of the

rudder, α_R is the effective inflow angle to rudder and U_R is the resultant inflow velocity to the rudder. U_R can be calculated as:

$$U_R = \sqrt{(u_R^2 + v_R^2)} \tag{12}$$

where u_R is the longitudinal and v_r is the lateral inflow velocity components to rudder. Additionally, α_R can be calculated from:

$$\alpha_R = \delta - tan^{-1}\left(\frac{v_R}{u_R}\right) \tag{13}$$

v_R can be calculated from:

$$v_R = U\gamma_R\beta_R \tag{14}$$

where γ_R and β_R are the flow straightening coefficient and the effective inflow angle to rudder for maneuvering motions, respectively. β_R can be calculated as:

$$\beta_R = \beta - l_R \tag{15}$$

where β and l_R are the hull drift angle at midship and the dimensionless effective longitudinal coordinate value of the rudder position, respectively. Additionally, u_R can be calculated from:

$$u_R = \epsilon u(1 - w_p)\sqrt{\eta\left\{1 + \kappa\left(\sqrt{1 + \frac{8K_T}{\pi J^2}} - 1\right)\right\}^2 + (1 - \eta)} \tag{16}$$

where, ϵ is the ratio between the wake fraction at rudder position and propeller position, w_p is the propeller position wake coefficient for maneuvering motions, η is the ratio between the diameter of the propeller and rudder span. κ is an experimental constant.

2.3. Model Validation

Validation of the model is verified by conducting turning and zig-zag maneuvering tests. Parameters of the ship used in the model are taken from 7 meters KVLCC2 model [21]. Initial surge velocity is chosen as 1.179 m/s and propeller revolution is kept constant as 11.86 rps. In the turning maneuver test, a 35 degree of rudder angle is applied to the system after 1 second of ship movement. The resulting dimensionless trajectory of the ship and experimental data taken from [21] are compared and shown in Figure 2. The dimensional trajectories for turning maneuver tests with ±35 degree rudder angles are shown in Figure 3. It is resulted that the surge velocity (u) stabilizes to a value of 0.544 m/s whereas the yaw rate (r) stabilizes to a value of 0.063 rad/s (given in Figure 4). By using the basic equation for circular motion, the standard turning diameter can be calculated to be approximately 17.27 meters, which is consistent with the trajectory shown in Figure 3. Comparison of non-dimensional turning maneuver parameters with experimental data taken from [21] are given in Table 1.

Additionally, we conducted a zig-zag maneuver test. The performed zig-zag maneuver test simulation is given in Figure 5. Comparison of zig-zag maneuver test overshoot angles (OSA) with experimental data taken from [21] is given in Table 2. These tests allowed for the assessment of the model's accuracy and the identification of any discrepancies between the simulated and actual ship behaviour.

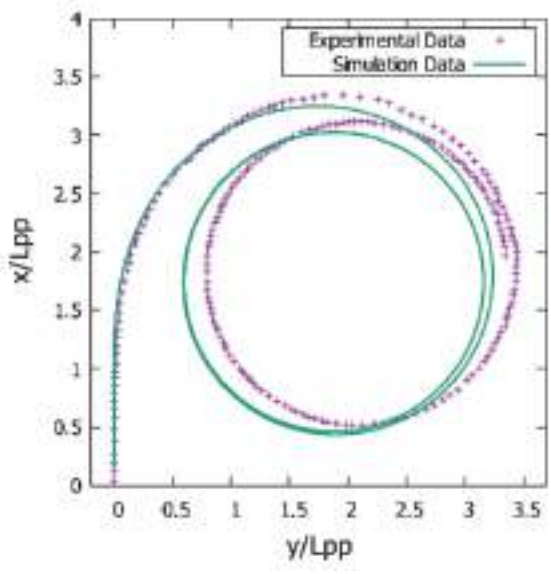

Figure 2. *Data comparison*

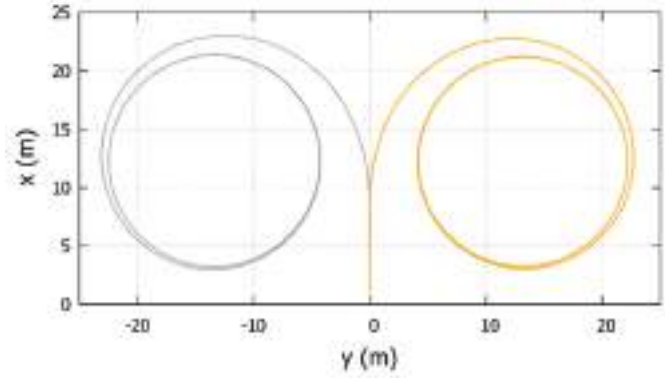

Figure 3. *±35 degree turning maneuver*

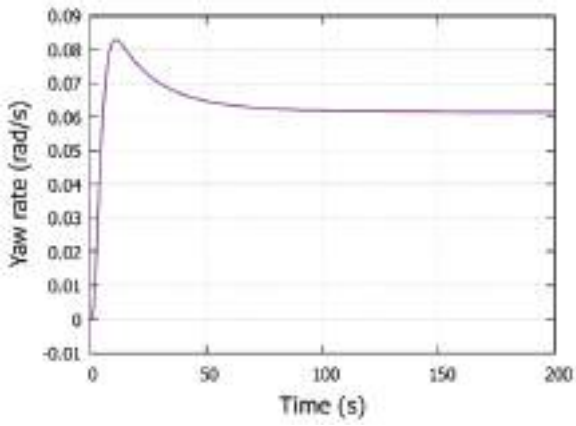

Figure 4. *Yaw rate change for turning maneuver*

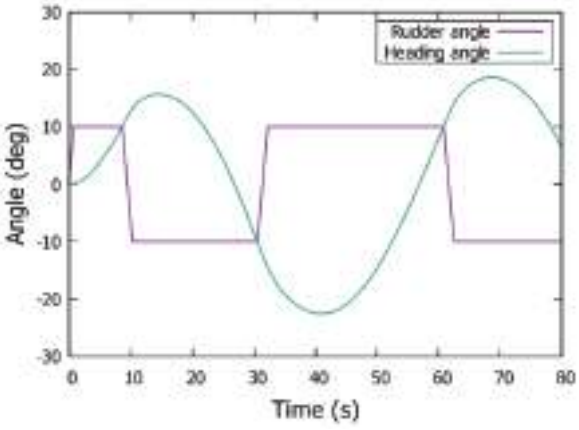

Figure 5. *Zig-zag maneuver test*

Table 1. *Turning maneuver comparison between numerical and experimental data*

Parameter	Experimental value	Simulation value	Error (%)
Advance (β = 35°)	3.25	3.19	2
Transfer (β = 35°)	1.7	1.31	23
Tactical Diameter (β = 35°)	3.34	3.18	5
Advance (β = -35°)	3.11	3.22	4
Tactical Diameter (β = -35°)	1.95	1.33	32

Table 2. *Zig-zag maneuver comparison between numerical and experimental data*

Parameter	Experimental value	Simulation value
1st OSA	8.2	5.61
2nd OSA	21.9	12.63

It is possible to extrapolate that the model accurately represents the behaviour of the ship with regards to its trajectory based upon the comparison of the simulated and experimental data. The similarity between simulated results and experimental data suggests that the

3. Control Strategy

A cascade control scheme is chosen to satisfy the heading stability of the ship. Both yaw rate and yaw angles are controlled in this approach. The outer loop stabilizes the ship's yaw angle, while the inner loop controls the yaw rate. The control structure used in system is given in Figure 6.

In the cascade control approach, it is important to ensure that the inner control loop response is faster than the outer control loop, as this allows the system to be more resistant to disturbances. It is generally recommended that the inner control loop to be at least 3 times faster than the outer control loop in order to achieve this [25]. To check this condition, two tests are conducted without controller gains. In the first test, the inner loop is closed and the outer loop is opened. A step input is applied to the inner loop, and the response of the inner loop is measured. Rise time of the inner loop is determined as 1.01 sec. In the second test, the primary loop is closed and the secondary loop is opened. A step input is applied to the outer loop, and the rise time of the outer loop is determined as 11.11 sec. It is observed that the rise time of the inner loop is approximately 11 times smaller than the rise time of the outer loop. This meets the criteria that requires for secondary loop to be at least three times faster than the primary loop in a cascade control system, as it demonstrates that the inner loop has a significantly faster response time when comparing with the outer loop. One can say that this will develop the performance of the system by allowing the inner loop to more quickly respond to changes in the outer loop output. By assuming G_{c_1} and G_{c_2} are proportional controllers which have the coefficients k_1 and k_2, the control law of the cascade system can be written as:

$$u = k_2\left(k_1\left(\psi_{ref} - \psi_{out}\right) - r\right) \tag{17}$$

where u is the control input, G_{c_1} and G_{c_2} are the primary and secondary controllers, respectively. Proportional controllers are used as inner and outer loop controllers.

Controller parameters are optimized via GA and PSO techniques. The selection of the parameters is performed using an evaluation criterion known as the fitness function [26]. Different performance criteria were implemented in the literature such as Sum Absolute Error [27]. In our case, the fitness function is chosen as the Integrated Time Absolute Error (ITAE) to be minimized. It is a well-known control performance criterion with the advantages of

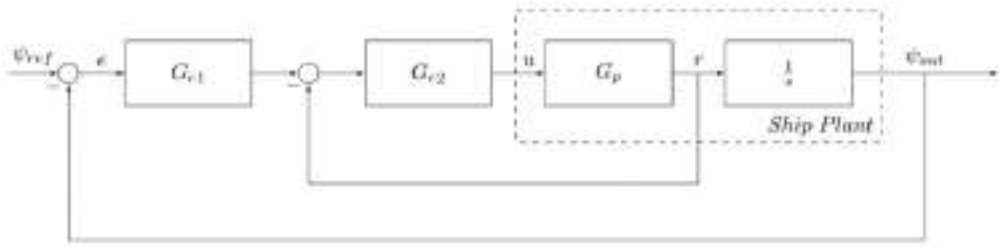

Figure 6. *Control scheme of the ship system*

obtaining smaller overshoots and oscillations than alternative performance criterions such as integral absolute error and integral square error. Mathematical representation of the ITAE can be written as [28]:

$$ITAE = \int_0^T t|e|dt \tag{18}$$

where e is the error between reference and feedback, t is the time. For the cascade loop structure, two different ITAE values obtained and added together as a single performance criterion. First ITAE value has been calculated for the difference between output heading angle and the reference heading angle whereas the second one has been calculated between the yaw rate of the ship and heading angle error multiplied by the controller. The objective function J can be written as [29]:

$$J = ITAE_1 + ITAE_2 \tag{19}$$

where $ITA\,E_1$ and $ITA\,E_2$ are obtained from the outer loop and inner loop, respectively.

3.1. GA-Based Tuning

GA is a well-known optimization technique used to find extremum value of a function. GA is inspired by the process of evolution in nature and is based on the principles of natural selection. Initial population develops as the generations pass thanks to the elimination of genetically poor individuals [30]. The GA process consists of several basic steps, including population initialization, selection, crossover, and mutation. The process is completed once the termination criterion is met. Controller parameters are k_1 for primary and k_2 for the secondary loop. Parameters of the GA function are given in Table 3.

Table 3. *Genetic algorithm implementation parameters*

Population size	50
Lower boundary	[0 0]
Upper boundary	[100 100]
Number of max. generations	500
Stop criterion	1e-3
Crossover fraction	0.8
Mutation function	Gaussian

The iteration process for GA can be explained as follows [31,32]:

1. Initialize population with random numbers for controller gains, k_1 and k_2. Members of the population are called chromosomes.
2. Calculate the function value of each chromosome.
3. Select the best chromosomes as to be having higher chance for the next generation.
4. Crossover randomly selected chromosomes.
5. Mutate the population for next generation.
6. If the stop criterion is satisfied, choose k_1 and k_2 as the best controller parameters. Otherwise, return step 2.

A signal that consists of different steps is applied to the system and objective function J is minimized by the GA algorithm. After 57 Generations, the algorithm found the minimum value of J to be 34.2854 and the optimum controller parameters for this criterion are found to be $k_1 = 0.3733$ and $k_2 = 64.6377$. Reference signal and heading angle response of the system for the 5th and optimal generations are given in Figure 7. As shown in the figure, the system evolved a behaviour with lower oscillation and overshoot, which is the expected result of the optimization process. The GA showed its efficiency to obtain the optimum system parameters to achieve the desired performance.

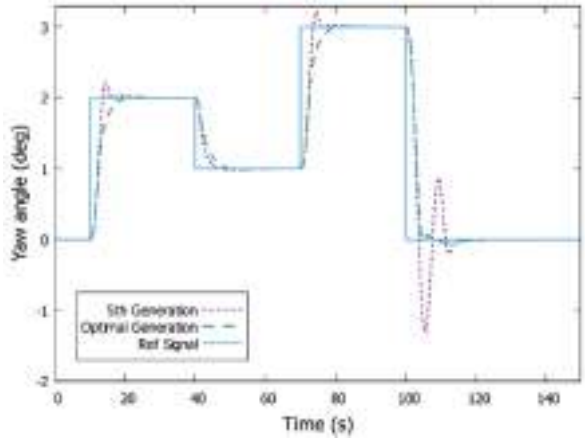

Figure 7. *Yaw angle response during different generations of GA*

GA: Genetic algorithm

3.2. PSO Based Tuning

PSO, is another nature-inspired optimization technique based on the behaviour of swarms. An initial population is set at the beginning of the algorithm that is randomly distributed in the search space. Position and velocity need to be given to every population member. During each iteration, the position and velocity of each member of the population are updated based on the best member of the population [33]. This allows the population to converge towards the optimal solution as the iterations progress.

Let us represent N possible solutions as $X = [k_1, k_2, \ldots k_N]$ whereas elements of vector $k_i = \left[k_{1_i}\ k_{2_i}\right]$ as the gains of outer and inner loops, respectively. For each step, the particles are updated according to the formula [34]:

$$x_i(t+1) = x_i(t) + v_i(t+1) \tag{20}$$

where v_i is the velocity of the particle that can be calculated from:

$$v_i(t+1) = wv_i(t) + c_1(p_i - x_i(t))R_1 + c_2(g - x_i(t))R_2 \tag{21}$$

where p_i is the best solution for that individual particle obtained so far, g is the global best, i.e. the best solution of the swarm overall, w is the inertia weight coefficient, c_1 is cognitive coefficient and c_2 is social coefficient. These coefficients regulate the magnitudes of personal and global best solutions. R_1 and R_2 are diagonal matrices between 0 and 1 that are distributed uniformly [35].

For PSO-based optimization, the same fitness and cost functions are used given in equations (18) and (19). The significant PSO parameters are listed in Table 4. To achieve an efficient solution, a swarm size value of 80 is chosen, as suggested by [36].

Table 4. *Particle swarm optimization parameters*

Swarm size	80
Lower bound	[0 0]
Upper bound	[100 100]
Stop criterion	1e-3

The optimization process took 24 iterations to reach the optimal point. The optimum parameters are found to be $k1 = 0.3737$ and $k_2 = 66.7472$. For a reference input, responses of the 1st iteration and optimum iteration are given in Figure 8, which shows the superior performance of the optimal iteration than the first one.

Additionally, disturbance rejection performance of the system is evaluated. The wave disturbance which is a dominant disturbance for a ship can be approximated linearly as an output $y(s)$ [37]:

$$y(s) = h(s)\omega(s) \tag{22}$$

where $\omega(s)$ is a Gaussian white noise that has zero-mean and unity power, $h(s)$ is the transfer function. For $h(s)$, a 2nd order transfer function approximation can be established:

$$h(s) = \frac{2\lambda\omega_0\sigma s}{s^2 + 2\lambda\omega_0 s + \omega_0^2} \tag{23}$$

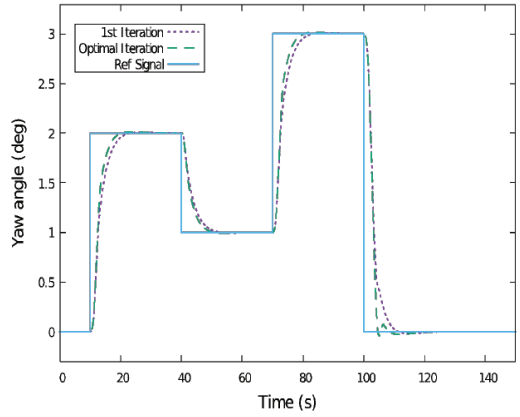

Figure 8. *Response of the PSO for different iterations*

PSO: Particle swarm optimization

where λ is the damping coefficient, σ is a constant that expresses wave density and $\omega 0$ is the dominating wave frequency.

The heading tracking behaviour of the ship is tested under different sea conditions. To mimic these conditions, wave density, σ has been changed while the other parameters, λ and ω_0 are kept constant as 0.1017 and 0.7222, respectively. The σ value has been changed as 1, 2 and 10, where the value of 10 means around maximum 40% deviation from the 1 deg. of heading angle command.

The system response under commanded reference heading signal in the presence of different wave disturbances is given in Figure 9, which demonstrates that the ship is able to track the reference input effectively despite the presence of different sea states.

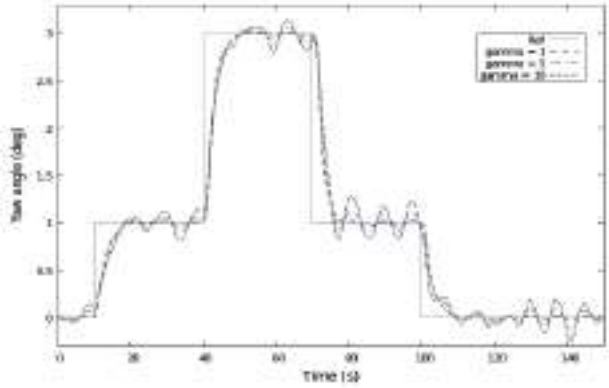

Figure 9. *Yaw angle output in the presence of disturbance*

Additionally, system response in the presence of disturbance is also evaluated for the controller parameters obtained by GA. To compare the controllers, root mean square error (RMSE) values between the output and reference angle given in Figure 9 is calculated. According to the results, RMSE value of PSO is 0.3657 whereas this value is 0.3666 for GA, which shows that PSO is slightly superior than GA in the presence of disturbance.

4. Simulation Results

4.1. Comparison of Tuning Algorithms

The computation times of both optimization algorithms, GA and PSO, are investigated. The time of computation for the GA algorithm is 47 minutes, while the time of computation for the PSO algorithm is 34 minutes. This result indicates that the PSO algorithm is approximately 1.38 times faster than the GA algorithm. Fitness function values of the algorithms during iterations are given in Figures 10 and 11. The controller parameters found by PSO algorithm have been chosen to proceed on.

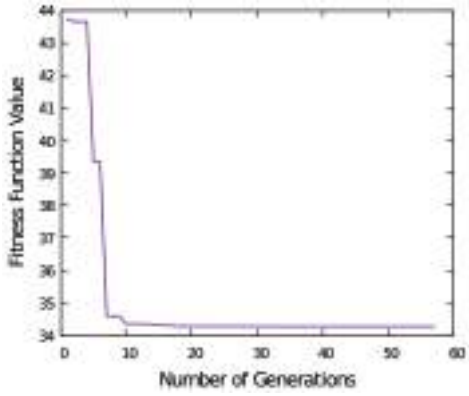

Figure 10. *Fitness function evolution for GA*

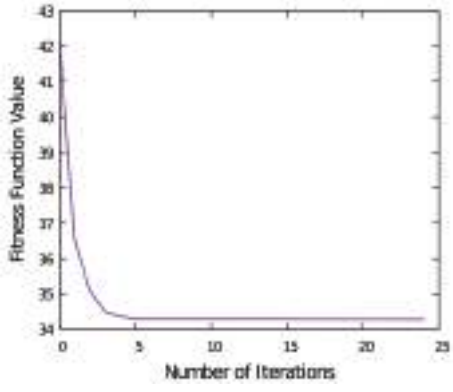

Figure 11*. Fitness function evolution for PSO*

Once the ship is able to track the given heading angle signal, it is possible to generate waypoints to determine the required path and yaw angle to navigate between points. For a given waypoint, (x, y) the required guidance equation that converts given waypoints into heading angle command, ψ_{cmd} can be written as [27,37]:

$$\psi_{cmd}(t) = atan2(y_k - y(t), x_k - x(t)) \quad (24)$$

where x_k and y_k stand for the position of the next waypoint. Equation (24) is also called the LOS guidance law. The function $atan2$ is used to assure that the $atan2(y,x)$ stay between $-\pi$ and π. To test the path tracking performance of the ship, four waypoints are given as (30,20), (50,100), (60,80), (70,30) meters, respectively. Trajectory of the ship under given waypoints is given in Figure 12, which shows that the ship has the capability of following the given waypoints accurately. Additionally, rudder deflection of the ship during the waypoint tracking process is given in Figure 13.

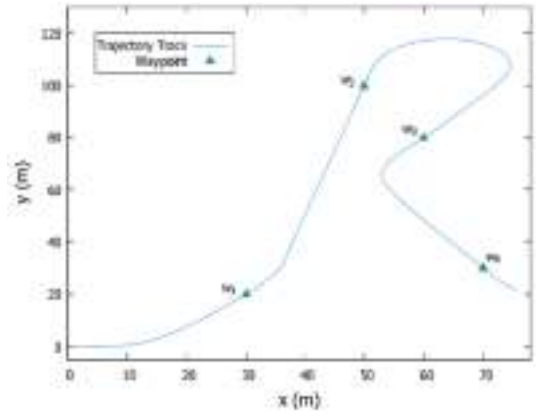

Figure 12*. Trajectory of the ship during waypoint tracking*

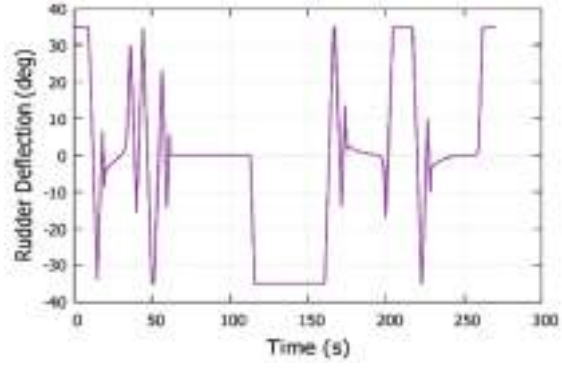

Figure 13*. Rudder deflection during the waypoint tracking*

4.2. Real-Time Simulator Design

In order to simulate the dynamics of the ship in a visual environment, an open-source flight simulator, FlightGear, is utilized. Data is transmitted to FlightGear through the utilization of the Aerospace Toolbox within MATLAB/Simulink. As shown in Figure 14, modelling and control of the ship are carried out within MATLAB/Simulink, and

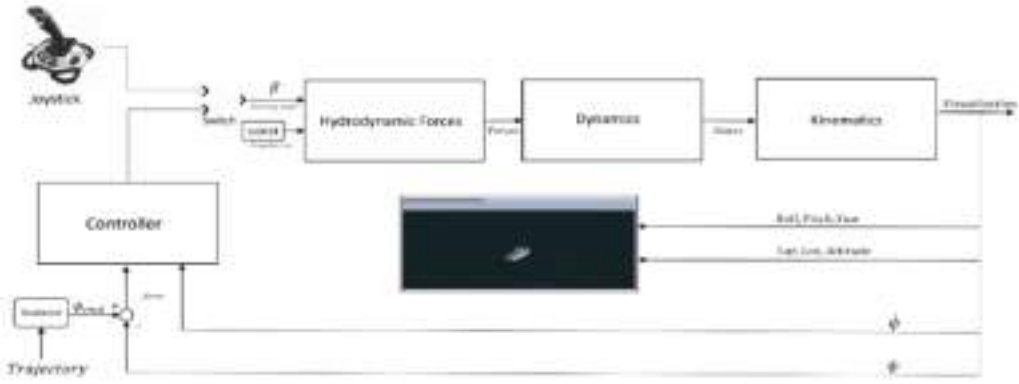

***Figure 14**. Closed loop control testing: Real-time marine simulator setup*

the three degrees of freedom data is visualized through the use of the FlightGear block within the Aerospace Blockset of MATLAB/Simulink. Latitude and longitude data are given arbitrarily, whereas altitude, roll and pitch angles are kept as zero since these states are not calculated. Data transmission to FlightGear software is provided via UDP bus. This enabled the examination of the ship's behaviour in a graphical representation.

Additionally, an optional mode is incorporated into the simulation that enables switching between manual and autonomous modes during the ship's operation. The manual mode allows for the ship to be manually controlled using a joystick given in Figure 14, while the autonomous mode is executed by providing the required waypoint for the ship to navigate to. The switching between two modes is facilitated using a joystick.

5. Conclusion

In this study, autonomous trajectory tracking of a ship has been executed by using a model-based control approach. The ship's motion is modelled using dynamics, kinematics and hydrodynamic force equations, which are subsequently validated through a turning maneuver test and comparison with experimental data. To achieve autonomous control of the ship's heading angle, a cascade control structure is employed. Controller parameters are optimized using both PSO and GA optimization methods. The cost function that is required to be minimized is the combination of integral time absolute errors of both inner and outer loops. As the most important contribution of this study, a comparison has been executed between the optimization methods in terms of computational efficiency. It has been found that the PSO is faster than the GA method to find the optimal parameters that minimizes the cost function. Afterwards, a guidance algorithm is given that determines the heading angle change for corresponding waypoints. It is shown that the ship is able to track given waypoints autonomously. A real time simulator has been employed to visualize the motion of the ship in a graphical environment.

Ongoing researches on this study may consist of designing different linear/non-linear controllers and comparing the performances of different controllers; designing an observer to filter the output of the system in the presence of noise such as Kalman filter. Additionally, the simulation may be improved by different model-based design steps such as software-in-the-loop, processor-in-the-loop and hardware-in-the-loop to achieve a real-time controlled system.

Authorship Contributions

Concept Design: E. Sayin, and I. Bayezit, Data Collection or Processing: E. Sayin, Analysis or Interpretation: E. Sayin, and I. Bayezit, Literature Review: E. Sayin, and I. Bayezit, Writing, Reviewing and Editing: E. Sayin, and I. Bayezit.

Funding: The authors declare that no funds, grants, or other support was received during the preparation of this manuscript.

References

[1] P. Dash, L. C. Saikia, and N. Sinha, "Automatic generation control of multi area thermal system using bat algorithm optimized PD–PID cascade controller". *International Journal of Electrical Power & Energy Systems*, vol. 68, pp. 364-372, Jun 2015.

[2] K. S. Kula, "Heading control system with limited turning radius based on IMC structure", in *21st International Conference on Methods and Models in Automation and Robotics (MMAR),* 29 August 2016 - 01 September 2016, Miedzyzdroje, Poland [Online]. Available: IEEE Xplore, https://ieeexplore.ieee.org [Accessed: 26 Sep 2016].

[3] H. Li, and K. Wang, "The design of ship dynamic positioning controller", in *2014 Sixth International Conference on Intelligent Human-Machine Systems and Cybernetics,* 26-27 August 2014 Hangzhou, China [Online]. Available: IEEE Xplore, https://ieeexplore.ieee.org [Accessed: 09 Oct 2014].

[4] M. Tao, and F. Ma, "Research on ship control with mechanical arms based on the PID controller", in *2021 6th International Conference on Transportation Information and Safety (ICTIS),* October 2021 Wuhan, China [Online]. Available: IEEE Xplore, https://ieeexplore.ieee.org/ [Accessed: 27 Jun 2022].

[5] J. Zhibin, L. Tiejun, X. Huixi, and W. Fuli, "Diving control of autonomous underwater vehicle based on cascade control and tracking differentiator", in *OCEANS 2016-Shanghai*, 10-13 April 2016, Shanghai, China [Online]. Available: IEEE Xplore, https://ieeexplore.ieee.org/ [Accessed: 09 Jun 2016].

[6] L. Andrija, S. Vedran, and B. Juraj, "Unmanned surface vehicle-tritor". *Brodogradnja*, vol. 73, pp. 135-150, 2022.

[7] O. S. Sahin, E. Kahramanoglu, F. Cakici, and E. Pesman, "Control of dynamic trim for planing vessels with interceptors in terms of comfort and minimum drag". *Brodogradnja*, vol. 74, pp. 1-17, 2023.

[8] Z. Li, and J. Sun, "Disturbance compensating model predictive control with application to ship heading control". *IEEE Transactions on Control Systems Technology,* vol. 20, pp. 257-265, Feb 2011.

[9] T. Asfihani, K. Chotimah, and I. Fitria, "Ship heading control using nonlinear model predictive control", in *3rd International Seminar on Research of Information Technology and Intelligent Systems (ISRITI)*, 10-11 December 2020, Yogyakarta, Indonesia [Online]. Available: IEEE Xplore, https://ieeexplore.ieee.org/ [Accessed: 13 Jan 2021].

[10] S. Subchan, A. M. Syafii, T. Asfihani, and D. Adzkiya, "Modified kalman filter-based model predictive control for ship heading control with probabilistic constraints". *Systems Science & Control Engineering*, vol. 9, pp. 109-116.

[11] T. T. Le, "Ship heading control system using neural network". *Journal of Marine Science and Technology*, vol. 26, pp. 963-972, Jan 2021.

[12] D. M. Pathan, T. Hussain, J. Daudpoto, and I. A. Memon, "Neural network steering controller for a ship". *Sindh University Research Journal-SURJ (Science Series)*, vol. 44, pp. 399-404, 2012.

[13] L. P. Perera, and C. G. Soares, "Pre-filtered sliding mode control for nonlinear ship steering associated with disturbances". *Ocean Engineering*, vol. 51, pp. 49-62, Sep 2012.

[14] L. Yuan, and H. Wu, "Simulation and design of fuzzy sliding-mode controller for ship heading-tracking". *Journal of Marine Science and Application*, vol. 10, pp. 76-81, Apr 2011.

[15] H. Zhang, X. Zhang, and R. Bu, "Radial basis function neural network sliding mode control for ship path following based on position prediction". *Journal of Marine Science and Engineering*, vol. 9, 1055, 2021.

[16] X. Lu, Z. Liu, and Z. Chu, "Nonlinear adaptive heading control for an underactuated surface vessel with constrained input and sideslip angle compensation". *Brodogradnja*, vol. 71, pp. 71-87, 2020.

[17] S. Paramesh, and S. Rajendran, "A unified seakeeping and manoeuvring model with a PID controller for path following of a KVLCC2 tanker in regular waves". *Applied Ocean Research*, vol. 116, 102860, 2021.

[18] J. Adams, A. C. Dubey, and S. Rajendran, "A model predictive based controller (MPC) for the path following of a KVLCC2 tanker in waves", in *OCEANS 2022-Chennai*, 21-24 February 2022, Chennai, India [Online]. Available: IEEE Xplore, https://ieeexplore.ieee.org/ [Accessed: 19 May 2022].

[19] R. Sandeepkumar, S. Rajendran, R. Mohan, and A. Pascoal, "A unified ship manoeuvring model with a nonlinear model predictive controller for path following in regular waves". *Ocean Engineering*, vol. 243, 110165, Jan 2022.

[20] S. Wang, X. Yan, F. Ma, P. Wu, and Y. Liu, "A novel path following approach for autonomous ships based on fast marching method and deep reinforcement learning". *Ocean Engineering*, vol. 257, 111495, Aug 2022.

[21] H. Yasukawa, and Y. Yoshimura, "Introduction of MMG standard method for ship maneuvering predictions". *Journal of Marine Science and Technology*, vol. 20, 37-52, 2015.

[22] T. Perez, and T. I. Fossen, "Ship motion control: kinematics of ship motion". *Springer*, pp. 45-58, Trondheim, Norway, 2005.

[23] O. K. Kinaci, I. Bayezit, and M. Reyhanoglu, "A practical feedforward speed control system for autonomous underwater vehicles". *Ocean Engineering*, vol. 218, 108214, Dec 2020.

[24] O. K. Kinaci, M. K. Gokce, A. D. Alkan, and A. Kukner, "On self-propulsion assessment of marine vehicles". *Brodogradnja*, vol. 69, pp. 29-51, 2018.

[25] A. C. Dimian, C. S. Bildea, and A. A. Kiss, "Chapter 15 - plantwide control". *Computer Aided Chemical Engineering,* vol. 35, pp. 599-647, 2014.

[26] S. Kumar, S. Jain, and H. Sharma, Advances in swarm intelligence for optimizing problems in computer science, *Chap. 2. Chapman and Hall/CRC, New York, USA*, 27-52, 2018.

[27] I. Bayezit, R. Bitirgen, M. Hançer, and O. K. Kinaci, "Strait of Istanbul crossing simulation of a VLCC type ship in autopilot mode". *Journal of ETA Maritime Science*, vol. 7, pp. 304-316, Dec 2019.

[28] D. Maiti, A. Acharya, M. Chakraborty, A. Konar, and R. Janarthanan, "Tuning PID and PIλ Dμ controllers using the integral time absolute error criteria", in *4th International Conference on Information and Automation for Sustainability ICIAFS*, 12-14 December 2008, Colombo, Sri Lanka [Online]. Available: IEEE Xplore, https://ieeexplore.ieee.org [Accessed: 13 Feb 2009].

[29] M. V. Sadasivarao, and M. Chidambaram, "PID Controller tuning of cascade control systems". *Journal of the Indian Institute of Science*, vol. 86, pp. 343-354, Jul-Aug 2006.

[30] O. Kramer, Genetic Algorithms. In: Genetic Algorithm Essentials. Studies in Computational Intelligence, Springer, Cham. 2017, pp. 11-19.

[31] S. Katoch, S. S. Chauhan, and V. Kumar, "A review on genetic algorithm: past, present, and future". *Multimedya Tools and Applications*, vol. 80, pp. 8091-8126, 2021.

[32] A. Lambora, K. Gupta, and K. Chopra, "Genetic algorithm-a literature review", in *International Conference on Machine Learning, Big Data, Cloud and Parallel Computing (COMITCon)*, 14-16 February 2019, Faridabad, India. [Online]. Available: IEEE Xplore, https://ieeexplore.ieee.org [Accessed: 11 Oct 2019].

[33] R. Poli, J. Kennedy, and T. Blackwell, "Particle swarm optimization". *Swarm Intelligence*, vol. 1, pp. 33-57, Aug 2007.

[34] T. Dlabač, M. Ćalasan, M. Krčum, and N. Marvučić, "PSO-based PID controller design for ship course-keeping autopilot". *Brodogradnja*, vol. 70, pp. 1-15, 2019.

[35] F. Marini, and B. Walczak, "Particle swarm optimization (PSO). A tutorial". *Chemometrics and Intelligent Laboratory Systems*, vol. 149, pp. 153-165, Dec 2015.

[36] A. P. Piotrowski, J. J. Napiorkowski, and A. E. Piotrowska, "Population size in particle swarm optimization". *Swarm and Evolutionary Computation*, vol. 58, 100718, Nov 2020.

[37] T. I. Fossen, *Marine Control Systems: Guidance. Navigation, and Control of Ships, Rigs and Underwater Vehicles*, Marine Cybernetics, Trondheim, Norway, 2002.

Reviewer List of Volume 12 Issue 3 (2024)

Abdullah Açık	Dokuz Eylül University	Türkiye
Ali Doğrul	National Defense University	Türkiye
Amellal Issam	Ensa Berrechid	Morocco
Ayşe Yüksel Ozan	Aydın Adnan Menderes University	Türkiye
Burcu Aracıoğlu	Ege University	Türkiye
Cihad Delen	İstanbul Technical University	Türkiye
Cihan Şahin	Yıldız Technical University	Türkiye
Coşkan Sevgili	Zonguldak Bülent Ecevit University	Türkiye
Dahlia El-manstrly	Sheffield University Management School	England
Doğan Kısacık	IZTECH Civil Engineering	Türkiye
Elif Arslan	Dokuz Eylül University	Türkiye
Emrah Erginer	Dokuz Eylül University	Türkiye
Emre Kahramanoğlu	İstanbul Technical University	Türkiye
Erdem Kan	Çanakkale Onsekiz Mart University	Türkiye
Erkan Çakır	Recep Tayyip Erdoğan University	Türkiye
Ferdi Çakıcı	Yıldız Technical University	Türkiye
Gökçe Çiçek Ceyhun	Bursa Technical University	Türkiye
Mahmut Ali Gökçe	Yaşar University	Türkiye
Meisam Mahboubi Niazmandi	Shiraz University of Technology	Iran
Mehmet Doymuş	Dokuz Eylül University	Türkiye
Momoko Kitada	World Maritime University	Sweden
Mouhsene Fri	Euro Mediterranean University of Fez	Morocco
Müge Büber	Dokuz Eylül University	Türkiye
Mustafa Nuran	Dokuz Eylül University	Türkiye
Mustafa Taşkın	Altınay Defense Technologies	Türkiye
Neslihan Paker	İzmir Kavram Vocational School	Türkiye
Ömer Kemal Kınacı	İstanbul Technical University	Türkiye
Özgür Kırca	İstanbul Technical University	Türkiye
Ramazan Şener	Bandırma Onyedi Eylül University	Türkiye
Samet Biçen	İstanbul Technical University	Türkiye
Serdar Kum	İstanbul Technical University	Türkiye
Serdar Turgut İnce	Yıldız Technical University	Türkiye
Simone Mancini	University Of Naples	Italy
Uğur Can	Virginia Commonwealth University	United States
Yavuz Hakan Özdemir	Çanakkale Onsekiz Mart University	Türkiye
Yunus Emre Şenol	İstanbul Technical University	Türkiye

Volume 12 Issue 3 (2024) is indexed in

JEMS's Sponsors

INCE SHIPPING GROUP

GEMLIK PILOTS

DENIZ ÇALIŞANLARI DAYANIŞMA DERNEĞI

EGE GAZ INC.

SEFİNE SHIPYARD

GÜRDESAN SHIP MACHINERY CORP.

ER SHIPPING

ONURSAN

40 YEARS

Istanbul / Türkiye

onursan@onursan.net

SAFETY FIRST

GEPA

Istanbul / Türkiye

info@gepafiberglass.com

AMERICAN MARINE SAFETY

Houston / Texas

sales@americanmarinesafety.com

ONURSAN Europe

Rotterdam / Netherlands

rotterdam@onursan.net

RINA ONV KR ClassNK CCS

GEMLIK PILOTS

Gemlik Pilotage and Tugboat Services Inc.

GEMLIK Pilotage and Tugboat Services Inc., provides the highest level of navigation and maneuvering safety, which aims to continuous training and development, in Gemlik Bay.

GEMLIK PILOTS
GEMLIK Pilotage and Tugboat Services Inc.

Adress : Ata Mh. Sanayi Cd. No:4 İç Kapı No:9
Gemlik / BURSA Phone : 0224 524 77 35 - 0224 524 77 36
Fax : 0224 524 77 64
e-mail : pilotage@geptco.com